

การผลิตแอมโมเนียไดรคาร์บอนจากนอร์แมลเฮกเซนและแก๊สโซลีนธรรมชาติ
โดยใช้ตัวเร่งปฏิกิริยาแพลเลเดียม/ ซีโอไลต์แซทเอสเอ็ม-5
และออกซิเดชันของฟีนอลบนเบดนิ่งของแอกทีฟคาร์บอน



นางสาว สมสลวย สุวรรณประสพ

สถาบันวิทยบริการ
จุฬาลงกรณ์มหาวิทยาลัย
วิทยานิพนธ์นี้เป็นส่วนหนึ่งของการศึกษาตามหลักสูตรปริญญาวิทยาศาสตรดุษฎีบัณฑิต

สาขาวิชาปิโตรเคมี

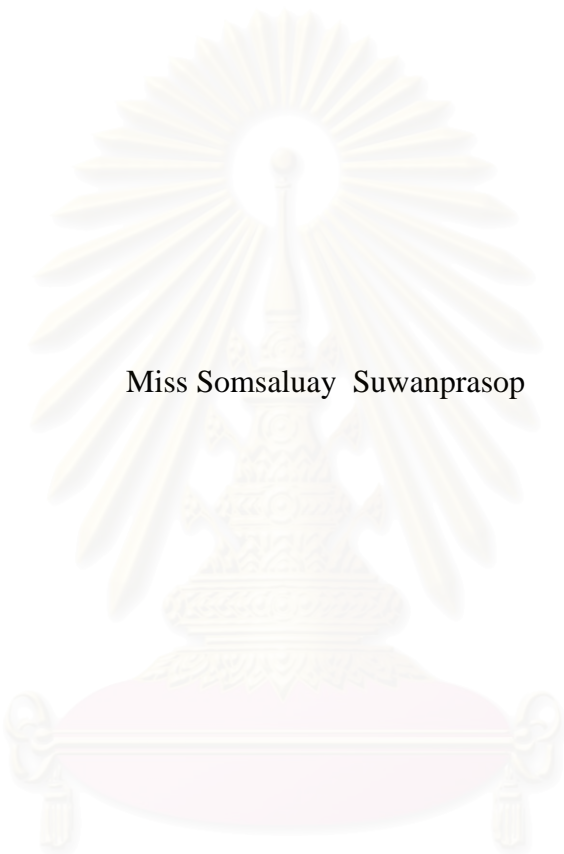
คณะวิทยาศาสตร์ จุฬาลงกรณ์มหาวิทยาลัย

ปีการศึกษา 2547

ISBN 974-17-6895-8

ลิขสิทธิ์ของจุฬาลงกรณ์มหาวิทยาลัย

PRODUCTION OF AROMATIC HYDROCARBONS FROM *n*-HEXANE AND
NATURAL GASOLINE OVER Pd/ZSM-5 ZEOLITE
AND OXIDATION OF PHENOL ON FIXED BED OF ACTIVE CARBON



Miss Somsaluay Suwanprasop

สถาบันวิทยบริการ
จุฬาลงกรณ์มหาวิทยาลัย

A Dissertation Submitted in Partial Fulfillment of the Requirements
for the Degree of Doctor of Philosophy in Petrochemistry

Faculty of Science
Chulalongkorn University

Academic year 2004

ISBN 974-17-6895-8

Thesis Title Production of aromatic hydrocarbons from *n*-hexane and natural gasoline over Pd/ZSM-5 zeolite and oxidation of phenol on fixed bed of active carbon

By Miss Somsaluay Suwanprasop

Field of Study Petrochemistry

Thesis Advisor Associate Professor Amorn Petsom, Ph.D.

Thesis Co-advisor Professor Henri Delmas, Dr.Ing.

Accepted by the Faculty of Science, Chulalongkorn University in Partial Fulfillment of the Requirements for the Doctor's Degree

.....Deputy Dean for Administrative Affairs,
Acting Dean, The Faculty of Science
(Associate Professor Tharapong Vitidsant, Ph.D.)

THESIS COMMITTEE

.....Chairman
(Professor Pattarapan Prasassarakich, Ph.D.)

.....Thesis Advisor
(Associate Professor Amorn Petsom, Ph.D.)

.....Thesis Co-advisor
(Professor Henri Delmas, Dr.Ing.)

.....Member
(Professor Somsak Damronglerd, Dr.Ing.)

.....Member
(Professor Sophon Roengsumran, Ph.D.)

.....Member
(Professor Pramote Chaiyavech, Ph.D.)

.....Member
(Assistant Professor Warinthorn Chavasiri, Ph.D.)

สมสกลวย สุวรรณประสพ: การผลิตแอรโม่ติกไฮโดรคาร์บอนจากนอร์แมลเฮกเซนและแก๊สโซลีนธรรมชาติโดยใช้ตัวเร่งปฏิกิริยาแพลเลเดียม/ซีโอไลต์แซทเอสเอ็ม-5 และ ออกซิเดชันของฟีนอลบนเบดนิ่งของแอกทีฟคาร์บอน. (PRODUCTION OF AROMATIC HYDROCARBONS FROM *n*-HEXANE AND NATURAL GASOLINE OVER Pd/ZSM-5 ZEOLITE AND OXIDATION OF PHENOL ON FIXED BED OF ACTIVE CARBON)
 อ.ที่ปรึกษา: รศ.ดร. อมร เพชรสม, อ.ที่ปรึกษาร่วม: Prof. Henri Delmas; 203 หน้า. ISBN 974-17-6895-8

เรื่องที่ 1: กระบวนการผลิตแอรโม่ติกไฮโดรคาร์บอนจากนอร์แมลเฮกเซนและแก๊สโซลีนธรรมชาติ โดยใช้ตัวเร่งปฏิกิริยาแพลเลเดียม/ซีโอไลต์แซทเอสเอ็ม-5 ในเครื่องปฏิกรณ์แบบท่อได้ถูกพัฒนาขึ้น ภายใต้สภาวะที่เหมาะสม คือ อุณหภูมิ 400 องศาเซลเซียส อัตราการไหลของสารตั้งต้น 0.4 มิลลิลิตรต่ออนาที โดยใช้ตัวเร่งปฏิกิริยาซีโอไลต์แซทเอสเอ็ม-5 ที่มีแพลเลเดียมร้อยละ 0.5 ภายใต้สภาวะนี้ ค่าการเปลี่ยนแปลงของนอร์แมลเฮกเซนและแก๊สโซลีนธรรมชาติ คิดเป็นร้อยละ 99.7 และ 94.3 ตามลำดับ (โดยมีค่าความจำเพาะต่อการเกิดแอรโม่ติกไฮโดรคาร์บอน คิดเป็นร้อยละ 92.3 และ 92.6 ตามลำดับ)

เรื่องที่ 2: ปฏิกิริยาออกซิเดชันของฟีนอลบนตัวเร่งปฏิกิริยาแอกทีฟคาร์บอน ได้ถูกศึกษาในเครื่องปฏิกรณ์แบบเบดนิ่ง ภายใต้อุณหภูมิและความดันออกซิเจนต่ำ ค่าความเข้มข้นของฟีนอลที่ออกจากรเบด ค่าความต้องการใช้ออกซิเจน และสารกึ่งกลางได้ถูกวิเคราะห์ ปฏิกิริยาออกซิเดชันของฟีนอลมีค่าเพิ่มขึ้น เมื่ออุณหภูมิในการทำปฏิกิริยา ความดันของออกซิเจน และลิกวิดสเปซไทม์ เพิ่มขึ้น ในขณะที่ทิศทางการไหลของสารตั้งต้น ส่งผลกระทบบ้างเล็กน้อยต่อปฏิกิริยา แบบจำลองที่รวมถึงค่าจลนศาสตร์แบบอินทรินสิค และค่าการถ่ายเทมวล ได้ถูกนำเสนอในงานวิจัยนี้ด้วย

สถาบันวิทยบริการ
 จุฬาลงกรณ์มหาวิทยาลัย

สาขาวิชา.....ปีโตรเคมี..... ลายมือชื่อนิสิต.....

ปีการศึกษา.....2547..... ลายมือชื่ออาจารย์ที่ปรึกษา.....

ลายมือชื่ออาจารย์ที่ปรึกษาร่วม.....

4373871723 : MAJOR PETROCHEMISTRY

KEY WORD: HEXANE / NATURAL GASOLINE / NGL / ZEOLITE / AROMATIZATION / PHENOL /
OXIDATION / ACTIVE CARBON / FIXED BED REACTOR

SOMSALUAY SUWANPRASOP: THESIS TITLE. (PRODUCTION OF AROMATIC
HYDROCARBONS FROM *n*-HEXANE AND NATURAL GASOLINE OVER Pd/ZSM-5
ZEOLITE AND OXIDATION OF PHENOL ON FIXED BED OF ACTIVE CARBON)
THESIS ADVISOR: ASSOC. PROF. AMORN PETSOM, Ph.D., THESIS COADVISOR:
PROF. HENRI DELMAS, Dr. Ing., 203 pp. ISBN 974-17-6895-8

Part I: The production of aromatic hydrocarbons from *n*-hexane and natural gasoline over Pd loaded ZSM-5 zeolite in a tubular reactor was achieved under the suitable conditions at 400 °C, and 0.4 ml/min reactant feeding rate, employing ZSM-5 (0.5% Pd content) as a catalyst. Under these conditions, *n*-hexane and natural gasoline conversions were found to be 99.7% and 94.3%, respectively (with respective aromatic selectivity of 92.3% and 92.6%).

Part II: Wet catalytic air oxidation of phenol over a commercial active carbon was studied in a three phase fixed bed reactor under mild temperature and oxygen partial pressure. Exit phenol concentration, COD, and intermediates were analysed. Oxidation of phenol was significantly improved when increasing operating temperature, oxygen partial pressure, and liquid space time, while up or down flow modes had only marginal effect. A complete model involving intrinsic kinetics and all mass transfer limitations gave convenient reactor simulation.

สถาบันวิทยบริการ
จุฬาลงกรณ์มหาวิทยาลัย

Field of study... Petrochemistry..... Student's signature.....

Academic year... 2004..... Advisor's signature.....

Co-advisor's signature.....

ACKNOWLEDGEMENTS

I would like to express my deepest gratitude to my advisors, Associate Professor Dr. Amorn Petsom and Professor Dr. Henri Delmas, for their valuable instruction, concern, and encouragement throughout this study. I am grateful to Dr. Carine Julcour-Lebiege for her kind suggestion, instruction, and great help. I would also like to acknowledge Professor Dr. Anne-Marie Wilhelm for her valuable advice and instruction. I am also thankful to Professor Dr. Frank Stüber for his valuable suggestion and great help. I would also like to acknowledge Professor Dr. Sophon Roengsumran for his kind instruction and valuable advice. I am grateful to Professor Dr. Pramote Chaiyavech for his valuable suggestion and advice. I would also like to acknowledge Professor Dr. Somsak Damronglerd for his valuable advice and suggestion.

I would like to thank the Chairman and Members of the Thesis committee for their valuable suggestion and comment.

I am grateful to the Department of Chemistry and the Institute of Biotechnology and Genetic Engineering (IBGE), Chulalongkorn University for the GC/MS and GC facilities, respectively. I am indebted to the Royal Golden Jubilee Ph.D. Program, The Thailand Research Fund for a student scholarship. I would also like to acknowledge the French Embassy in Thailand for kind support and convenient for the research work in France. My thanks also go to Dr. Prasat Kittakoop for his comments and suggestion on this thesis.

I would like to thank Lahcen, Alain, Lucien, Jean-Louis L., Jean-Louis N., Richard and Marie-Line for their help on the fixed bed set-up and the HPLC at INP. I would also like to thank Mr. Yi Yue, my colleague, for his friendship and kind help for the experiments at INP. I am thankful to Miss Elisabet Agullo, my colleague, for her experiments on the kinetic study of phenol oxidation. My thanks also go to my friend, Dr. Rojrit Rojanathanes, for the discussion on the mechanism of phenol oxidation. I am also thankful to my friends and colleagues for their friendship and encouragement.

I am grateful to my parents and my brother for their love, understanding, and great encouragement throughout this study.

CONTENTS

	PAGE
Abstract in Thai	iv
Abstract in English	v
Acknowledgement	vi
Contents	vii
List of Figures	xv
List of Tables	xx
List of Abbreviations and notations	xxii
PART I: PRODUCTION OF AROMATIC HYDROCARBONS FROM <i>n</i>-HEXANE AND NATURAL GASOLINE OVER Pd/ZSM-5 ZEOLITE	xxvi
CHAPTER	
I. INTRODUCTION	1
II. THEORY AND LITERATURE REVIEW	3
2.1 Catalysis.....	3
2.1.1 Catalysis activity.....	4
2.1.2 Catalysis selectivity.....	5
2.1.3 Catalysis deactivation.....	6
2.1.3.1 Catalyst poisoning.....	6
2.1.3.2 Fouling.....	6
2.1.3.3 Sintering.....	7
2.1.3.4 Loss of catalyst species <i>via</i> the gas phase.....	7
2.2 Classification of catalyst.....	7
2.2.1 Comparison of homogeneous catalysis and heterogeneous catalysis.....	8
2.3 Heterogeneous catalysis.....	9
2.3.1 Individual steps in heterogeneous catalysis.....	9
2.3.2 Promoters.....	10
2.4 Zeolites.....	11
2.4.1 Structure of zeolites.....	11
2.4.2 Catalytic properties of zeolites.....	14

	PAGE
2.4.2.1 Shape selectivity.....	14
2.4.3 Acidity of zeolites.....	14
2.4.4 Metal-doped zeolites.....	18
2.5 Literature review.....	19
2.6 Practical application.....	23
2.6.1 Cyclar process.....	23
2.6.2 RZ-Platforming Process.....	24
2.6.3 Alpha process	24
2.6.4 Toray TAC9 Process	25
III. EXPERIMENTAL SECTION.....	26
3.1 Materials and general methods.....	26
3.2 Aromatization reactor.....	26
3.3 Aromatization procedure.....	27
3.4 Preparation of Pd/ZSM-5 catalyst.....	28
3.4.1 Preparation of 0.2% Pd/ZSM-5 catalyst.....	28
3.4.2 Preparation of 0, 0.3, and 0.5% Pd/ZSM-5 catalyst.....	28
3.5 Characterization of Pd/ZSM-5 catalyst.....	28
3.6 Aromatization of <i>n</i> -hexane.....	28
3.6.1 Various effects on aromatization of <i>n</i> -hexane.....	28
3.6.1.1 Effect of Pd contents in ZSM-5 zeolite.....	28
3.6.1.2 Effect of reactant feeding rate and reaction temperature.....	28
3.6.2 Regeneration of spent catalyst.....	29
3.6.3 Activity of regenerated catalyst.....	29
3.7 Aromatization of natural gasoline.....	29
3.7.1 Various effects on aromatization of natural gasoline.....	29
3.7.1.1 Effect of Pd contents in ZSM-5 zeolite.....	29
3.7.1.2 Effect of reactant feeding rate and reaction temperature.....	29
3.7.2 Regeneration of spent catalyst.....	30
3.7.3 Activity of regenerated catalyst.....	30

	PAGE
3.8 Characterization of <i>n</i> -hexane and natural gasoline aromatization products.....	30
3.9 Characterization of <i>n</i> -hexane and natural gasoline.....	30
IV. RESULTS AND DISCUSSION.....	31
4.1 Characterization of ZSM-5 zeolite.....	31
4.2 Preparation of Pd/ZSM-5 catalyst by ion-exchange method.....	31
4.2.1 Preparation of 0, 0.2, 0.3, and 0.5% Pd/ZSM-5 catalysts.....	32
4.3 Aromatization of <i>n</i> -hexane.....	33
4.3.1 Various effects on aromatization of <i>n</i> -hexane.....	33
4.3.1.1 Effect of Pd contents in ZSM-5 zeolite.....	33
4.3.1.2 Effect of reactant feeding rate and reaction temperature.	34
4.3.1.3 Activity of regenerated catalyst.....	36
4.3.2 Aromatic contents in reaction product and product distributions.....	37
4.4 Aromatization of natural gasoline.....	39
4.4.1 Various effects on aromatization of natural gasoline	39
4.4.1.1 Effect of Pd contents in ZSM-5 zeolite.....	39
4.4.1.2 Effect of reactant feeding rate and reaction temperature.	41
4.4.1.3 Activity of regenerated catalyst.....	42
4.4.2 Aromatic contents in reaction product and product distributions.....	43
V. CONCLUSION.....	47
PART II: OXIDATION OF PHENOL ON FIXED BED OF ACTIVE CARBON	48
CHAPTER	
I. INTRODUCTION.....	49
II. THEORY AND LITERATURE REVIEW.....	51
2.1 Wastewater treatment.....	51
2.2 Wet air oxidation fundamental.....	53
2.3 Catalytic wet air oxidation catalysts.....	53
2.3.1 Noble metals.....	54

	PAGE
2.3.2 Metal oxides.....	55
2.3.3 Active carbon.....	55
2.4 Industrial application of Wet Air Oxidation.....	58
2.4.1 NS-LC process.....	59
2.4.2 Osaka Gas process.....	59
2.5 Three phase fixed-bed reactors	60
2.5.1 Introduction.....	60
2.5.2 Hydrodynamics of cocurrent gas-liquid fixed bed reactor.....	63
2.5.2.1 Flow regimes.....	63
2.5.2.1.1 Flow regimes of cocurrent downflow fixed bed reactor.....	63
2.5.2.1.2 Flow regimes of cocurrent upflow fixed bed reactor.....	65
2.5.2.2 Pressure drop.....	66
2.5.2.3 Liquid holdup.....	68
2.5.2.4 Axial dispersion in the gas and liquid phases.....	70
2.5.2.5 Catalyst wetting.....	71
2.5.3 Mass transfer.....	73
2.5.3.1 Gas-liquid mass transfer.....	74
2.5.3.2 Liquid-solid mass transfer.....	75
2.5.4 Heat transfer.....	76
2.5.5 Application of fixed bed reactors to the CWO of phenol.....	77
III. EXPERIMENTAL SECTION: MATERIALS AND METHOD	80
3.1 Materials	80
3.2 Characterization of products	80
3.2.1 HPLC analysis	81
3.2.2 Determination of chemical oxygen demand (COD) of reaction products	82
3.3 Catalytic reactors	82
3.3.1 Autoclave reactor	83
3.3.1.1 Description	83

	PAGE
3.3.1.2 Operating the reactor	84
3.3.2 Fixed bed reactor	85
3.3.2.1 Description	85
3.3.2.1.1 Principal circuit of reaction	85
3.3.2.1.2 Temperature control circuit	87
3.3.2.1.3 Data acquisition	88
3.3.2.2 Procedure for operating continuous oxidation reactor.....	88
3.3.2.2.1 Catalyst packing	88
3.3.2.2.2 Operating the reactor	88
3.3.2.2.3 Reactor shutdown	89
IV. RESULTS AND DISCUSSION: EXPERIMENTAL AND	
MODELLING	90
4.1 Phenol adsorption on active carbon.....	90
4.2 Kinetic study on catalytic wet air phenol oxidation on active	
carbon	94
4.2.1 Evaluation of kinetic parameters	94
4.2.1.1 Interpretation of experimental results	94
4.2.1.2 Modelling of batch reaction and evaluation of intrinsic	
kinetic parameters	97
4.2.2 Continuous oxidation in fixed bed reactor.....	101
4.2.2.1 Operating conditions and flow regimes	101
4.2.2.2 Transient profiles	103
4.2.2.3 Activity of catalyst	104
4.2.2.4 Influence of operating parameters on phenol conversion	
4.2.2.4.1 Effect of temperature	105
4.2.2.4.2 Effect of oxygen partial pressure	107
4.2.2.4.3 Effect of gas inlet velocity	108
4.2.2.5 Characterisation of reaction products	110
4.2.2.5.1 Main intermediates	110
4.2.2.5.2 Determination of chemical oxygen demand.....	116

	PAGE
4.2.2.5.3 Proposed mechanism for oxidative destruction of phenol over activated carbon in fixed bed reactor...	117
4.2.2.6 Axial temperature and concentration profiles.....	120
4.2.2.6.1 Axial temperature profiles	120
4.2.2.6.2 Axial concentration profiles	121
4.2.2.7 Considerations on scale-up of phenol oxidation over AC	123
4.3 Modelling of continuous CWO	126
4.3.1 Fixed bed model and numerical solution	126
4.3.1.1 Model equations	126
4.3.1.2 Numerical solution	131
4.3.2 Evaluation of physicochemical properties and fixed bed parameters	132
4.3.2.1 Physicochemical and thermodynamic properties.....	132
4.3.2.2 Hydrodynamic, mass, and heat transfers parameters.....	133
4.3.3 Prediction of pilot plant reactor performance	135
4.3.3.1 Axial temperature profiles	135
4.3.3.2 Outlet phenol conversions and axial concentration profiles	135
4.3.3.2.1 Upflow mode	135
4.3.3.2.1.1 Outlet phenol conversions.....	136
4.3.3.2.1.2 Axial concentration profiles	140
4.3.3.2.2 Downflow mode	143
4.3.3.2.2.1 Outlet phenol conversions.....	144
4.3.3.2.2.2 Axial concentration profiles	147
4.4 Conclusion	151
V. CONCLUSION	153
REFERENCE	155
APPENDICES	171
Appendix 1-1A XRD spectrum of zeolite ZSM-5.....	172
Appendix 1-2A XRD spectrum of fresh Pd/ZSM-5 catalyst.....	173
Appendix 1-3A: XRD spectrum of regenerated Pd/ZSM-5 catalyst.....	174

PAGE

Appendix 1-4A: Typical GC chromatogram of products from <i>n</i> -hexane aromatization.....	175
Appendix 1-5A: Typical GC chromatogram of products from natural gasoline aromatization.....	176
Appendix 1-6A: GC chromatogram of standard compounds.....	177
Appendix 1-7A: GC chromatogram of commercial mixture of benzene, toluene, and xylenes.....	178
Appendix 2-1A: Correlation for the two-phase pressure drop calculation in cocurrent downflow and upflow fixed bed reactors...	179
Appendix 2-2A: Correlation for the calculation of liquid retention or liquid saturation in cocurrent downflow and upflow fixed bed reactors	183
Appendix 2-3A: Correlation for the calculation of mass transfer volumetric coefficient and the gas-liquid interfacial area in cocurrent downflow and upflow fixed bed reactors....	186
Appendix 2-4A: Properties of Marlotherm S.....	190
Appendix 2-5A: Thermogravimetric analysis of fresh and aged activated carbon	192
Appendix 2-6A: Typical HPLC chromatogram of fast analysis for phenol	193
Appendix 2-7A: Typical HPLC chromatogram of fast analysis for phenol oxidation products	194
Appendix 2-8A: HPLC chromatogram of full analysis for standard solution (commercial compounds) including some of main phenol oxidation intermediates	195
Appendix 2-9A: Typical HPLC chromatogram of full analysis of phenol oxidation products	196
Appendix 2-10A: Proposed reaction mechanism for phenol CWAO based on the identified intermediates in the reaction products	197
Appendix 2-11A: Axial phenol concentration profiles (1).....	200

	PAGE
Appendix 2-12A: Axial phenol concentration profiles (2).....	201
Appendix 2-13A: Axial phenol concentration profiles (3).....	202
VITA	203



สถาบันวิทยบริการ
จุฬาลงกรณ์มหาวิทยาลัย

LIST OF FIGURES

FIGURE		PAGE
1-2-1	Classification of catalysts.....	7
1-2-2	Structural unit of sodalite cage in zeolite.....	12
1-2-3	Three-dimensional structure of ZSM-5.....	13
1-2-4	Bifunctionality of metal-doped zeolites: isomerization and hydrogenation.....	18
1-3-1	Reactor for continuous aromatization of <i>n</i> -hexane and natural gasoline.....	27
1-4-1	Effect of Pd contents in ZSM-5 zeolite on conversion and aromatic contents in reaction product of <i>n</i> -hexane. Conditions: reaction temperature, 400 °C; feeding rate, 0.4 cm ³ /min	34
1-4-2	Effect of the feeding rate on <i>n</i> -hexane conversion and aromatic contents in reaction product over 0.5% Pd in ZSM-5 zeolite at different temperatures (C and A represent conversion and aromatic contents in reaction product, respectively).....	35
1-4-3	Comparison of activity between fresh and regenerated catalysts on <i>n</i> -hexane conversion and aromatic contents in reaction product at different temperatures. Conditions: feeding rate, 0.4 cm ³ /min; catalyst, 0.5% Pd in ZSM-5 zeolite (C and A represent conversion and aromatic contents in reaction product, respectively).....	37
1-4-4	Effect of Pd contents in ZSM-5 zeolite on conversion and aromatic contents in reaction product of natural gasoline. Conditions: reaction temperature, 400 °C; feeding rate, 0.4 cm ³ /min.....	40

FIGURE		PAGE
1-4-5	Effect of the feeding rate on natural gasoline conversion and aromatic contents in reaction product over 0.5% Pd in ZSM-5 zeolite at different temperatures (C and A represent conversion and aromatic contents in reaction product).....	41
1-4-6	Comparison of activity between fresh and regenerated catalysts on natural gasoline conversion and aromatic contents in reaction product at different temperatures. Conditions: feeding rate, 0.4 cm ³ /min; catalyst, 0.5% Pd in ZSM-5 zeolite (C and A represent conversion and aromatic contents in reaction product, respectively).....	42
2-2-1	Schematic diagrams of three-phase packed-bed reactors	60
2-2-2	Flow regime boundaries of non-foaming liquid for cocurrent gas-liquid downflow fixed-bed reactor	64
2-2-3	Flow regime boundaries (air-water system) for cocurrent gas-liquid upflow and downflow fixed-bed reactor	66
2-2-4	Flow patterns in trickle flow regime for externally completely and partially wetted particles	72
2-2-5	Concentration profiles for the gaseous reactant A and liquid reactant B	74
2-3-1	Schematic diagram of autoclave reactor	84
2-3-2	Schematic diagram of cocurrent gas-liquid fixed bed reactor ..	86
2-4-1	Experimental and modelled breakthrough curves	92
2-4-2	Adsorption isotherms of phenol on Merck AC at room temperature	93
2-4-3	Time-evolution of phenol concentration in the liquid phase (normalized by initial phenol concentration). T = 150°C, P _{O₂} = 3.3 bar, W _{cat} = 9 g, V _{L0} = 200 ml, ω = 800 rpm	95
2-4-4	Experimental and calculated time-concentration profiles in the liquid phase	99
2-4-5	Arrhenius plot of intrinsic kinetics obtained in batch reactor ...	101

FIGURE	PAGE
2-4-6	Location of our experimental conditions in the map regimes of three phase fixed bed reactors for air-water system 103
2-4-7	Transient phenol concentration profiles for cocurrent upflow and downflow fixed bed reactors. Conditions: oxygen partial pressure 1.2 bar, oil temperature 160°C, gas flow rate 175 NI/h, and liquid flow rate 0.55 kg/h..... 104
2-4-8	Phenol conversion versus the liquid contact time for downflow (open symbols) and upflow (filled symbols) at different oil temperatures 106
2-4-9	Phenol conversion versus the liquid contact time for downflow (open symbols) and upflow (filled symbols) at different oxygen partial pressures 108
2-4-10	Phenol conversion versus gas velocity for downflow (open symbols) and upflow (filled symbols) at different operating conditions 109
2-4-11	Formic acid concentration profile after phenol conversion in both upflow and downflow fixed bed reactors 112
2-4-12	Acetic acid concentration profile after phenol conversion in both upflow and downflow fixed bed reactors 112
2-4-13	Malonic acid concentration profile after phenol conversion in both upflow and downflow fixed bed reactors 113
2-4-14	Oxalic acid concentration profile after phenol conversion in both upflow and downflow fixed bed reactors 113
2-4-15	1,4-Benzoquinone concentration profile after phenol conversion in both upflow and downflow fixed bed reactors ... 114
2-4-16	4-Hydroxybenzoic acid concentration profile after phenol conversion in both upflow and downflow fixed bed reactors ... 114
2-4-17	Comparison of measured COD values and HPLC-based COD values in both upflow and downflow fixed bed reactors..... 116
2-4-18a	Mechanism for phenol WAO according to Devlin and Harris.. 118

FIGURE	PAGE
2-4-18b	Proposed reaction pathway for phenol CWAO based on the identified intermediates in the reaction products 119
2-4-19	Axial temperature profiles for $P_{O_2} = 1.2$ bar, $T_{oil} = 140$ °C, $u_{G,inlet} = 1.1 \times 10^{-2}$ m/s ($F_G = 100$ NI/h), and $F_L = 1$ kg/h in cocurrent upflow and downflow fixed bed reactors 121
2-4-20	Axial concentration profiles for $P_{O_2} = 2.0$ bar, $T_{oil} = 140$ °C, $u_{G,inlet} = 1.1 \times 10^{-2}$ m/s ($F_G = 100$ NI/h), and $F_L = 0.5$ kg/h in cocurrent upflow fixed bed reactor 122
2-4-21	Axial concentration profiles for $P_{O_2} = 2.0$ bar, $T_w = 140$ °C, $u_{G,inlet} = 1.1 \times 10^{-2}$ m/s ($F_G = 100$ NI/h), and $F_L = 0.5$ kg/h in cocurrent downflow fixed bed reactor 123
2-4-22	Phenol concentration for downflow (open symbols) and upflow (filled symbols) oxidation over active carbon at 0.2 MPa of O_2 124
2-4-23	Outlet phenol concentrations: experimental (\diamond) and corresponding simulations for fully wetted catalyst ($D^{ad}=D^{ad}(\text{Stüber})$): $k_{Ga}=k_{La}$ (solid line), $k_{Ga}=5 \times k_{La}$ (long dotted line), and instantaneous liquid-vapour equilibrium (short dotted line)..... 138
2-4-24	Axial phenol concentration profiles: experimental (\diamond) and corresponding simulations for fully wetted catalyst: $k_{Ga} = k_{La}$ (solid line), $k_{Ga} = 5 \times k_{La}$ (long dotted line), and instantaneous liquid-vapour equilibrium (short dotted line). $D^{ad}=D^{ad}(\text{Stüber})$ 141
2-4-25	Axial phenol concentration profiles: experimental (\diamond) and corresponding simulations for fully wetted catalyst: $k_{Ga} = k_{La}$ (solid line), $k_{Ga}=5 \times k_{La}$ (long dotted line), and instantaneous liquid-vapour equilibrium (short dotted line). $D^{ad} = 4.2 \times D^{ad}(\text{Stüber})$ 142

FIGURE	PAGE	
2-4-26	Outlet phenol concentrations: experimental (\diamond) and corresponding simulations for fully wetted catalyst: $k_{Ga} = k_{La}$ (solid line), $k_{Ga} = 5 \times k_{La}$ (long dotted line), and instantaneous liquid-vapour equilibrium (short dotted line).....	145
2-4-27	Outlet phenol concentrations: experimental (\diamond) and corresponding simulations for partially wetted catalyst: $k_{Ga} = k_{La}$ (solid line), $k_{Ga} = 5 \times k_{La}$ (long dotted line), and instantaneous liquid-vapour equilibrium (short dotted line) ...	146
2-4-28	Axial phenol concentration profiles: experimental (\diamond) and corresponding simulations for fully wetted catalyst: $k_{Ga} = k_{La}$ (solid line), $k_{Ga} = 5 \times k_{La}$ (long dotted line), and instantaneous liquid-vapour equilibrium (short dotted line)	147
2-4-29	Axial phenol concentration profiles: experimental (\diamond) and corresponding simulations for partially wetted catalyst: $k_{Ga} = k_{La}$ (solid line), $k_{Ga} = 5 \times k_{La}$ (long dotted line), and instantaneous liquid-vapour equilibrium (short dotted line) ...	149

LIST OF TABLES

TABLE		PAGE
1-2-1	Comparison of homogeneous and heterogeneous catalysts.....	9
1-2-2	Characteristics of important zeolites.....	13
1-2-3	Effect of metal ion in faujasite on cumene dealkylation.....	16
1-2-4	Classification of acidic zeolite according to Si/Al ratio.....	17
1-2-5	Transformation of <i>n</i> -hexane on zeolite catalysts at 380 °C.....	18
1-2-6	Aromatization of light naphtha on zeolite catalysts at 480 °C and 2.5 bar.....	20
1-4-1	Relationship between concentrations of Pd in ZSM-5 zeolite and various ion-exchanged times.....	32
1-4-2	Comparison of expected values and experimental values of the Pd contents of the exchanged catalysts.....	33
1-4-3	Contact time between reactants (<i>n</i> -hexane and natural gasoline) and catalyst at different reactant feeding rates.....	36
1-4-4	Product distributions from continuous aromatization of <i>n</i> -hexane at the optimal conditions compare to the corresponding reactant compositions and commercial mixture of benzene, toluene, and xylenes.....	38
1-4-5	Sulfur contents in reactants (<i>n</i> -hexane and natural gasoline), fresh catalysts, and regenerated catalysts.....	42
1-4-6	Product distributions from continuous aromatization of natural gasoline at the optimal conditions compare to the corresponding reactant compositions and commercial mixture of benzene, toluene, and xylenes.....	43
2-2-1	The applications of noble metal catalysts in the CWAO.....	54
2-2-2	Influence of the oxygen partial pressure on the carbon consumption	57
2-2-3	Industrial processes of wet air oxidation	58
2-2-4	Some examples of reactions carried out in trickle-bed reactors	61

TABLE	PAGE
2-2-5	Upflow versus downflow cocurrent fixed bed reactors 62
2-3-1	Physical properties of Merck activated carbon 2514..... 80
2-4-1	Parameters of the Freundlich equation and adsorption capacity at 5 g/l 91
2-4-2	Optimised values of Freundlich “a” parameter from experimental breakthrough curve 93
2-4-3	Operating conditions of the kinetic study in batch reactor 94
2-4-4	Amounts of phenol consumed and re-adsorbed during the experimental series 96
2-4-5	Intrinsic rate constants at different temperatures from batch phenol destruction experiments with: $W_{\text{cat}} = 9$ g, stirrer speed of 800 rpm 100
2-4-6	AC bed dimensions and operating conditions for phenol oxidation in fixed bed reactor..... 102
2-4-7	Values of physical properties in the range of operating conditions 133
2-4-8	Parameter values and correlations used in up- and downflow reactor modelling of pilot plant at: $T = 140$ °C, $P_T = 6$ bar, $F_G = 100$ NI/h, $F_L = 0.5$ l/h 134
2-4-9	Influence of k_{La} , k_{Ga} and D^{ad} on upflow model conversion: comparison with reference case and experimental conversion at $T_{\text{oil}} = 140$ °C, $F_L = 0.5$ l/h, $F_G = 100$ NI/h and $P_{O_2} = 1.2$ bar.. 136
2-4-10	Influence of particle wetting efficiency on the simulated outlet phenol concentration in downflow mode: $P_{O_2} = 1.2$ bar, $T_w =$ 140 °C, $F_G = 100$ NI/h, $F_L = 0.5$ l/h, Case: k_{Ga} infinite 144

LIST OF ABBREVIATIONS AND NOTATIONS

a	reactor section area (m ²)
AC	activated carbon
BTX	benzene, toluene, and xylenes
ca.	about
C _j	concentration of compound j (mol/m ³)
C _{G,H₂O}	gas phase concentration of water vapour (mol/m ³)
C _{L,O₂} *	dissolved oxygen concentration at the gas-liquid interface (mol/m ³)
c _{pL}	liquid heat capacity (J kg ⁻¹ K ⁻¹)
c _{pG}	gas heat capacity (J kg ⁻¹ K ⁻¹)
CWAO	catalytic wet air oxidation
D _c	column (reactor) diameter (m)
d _p	catalyst particle diameter (m)
D _j	diffusion coefficient of compound j (m ² /s)
D _j ^{eff}	effective diffusion coefficient of compound j (m ² /s)
D ^{ad}	axial dispersion coefficient (m ² /s)
E	activation energy (J/mol)
Eq.	equation
f	external wetting efficiency (f = f ^d + f ^s)
FBR	fixed bed reactor
F _G	gas flow rate (Nm ³ /h or Nm ³ /s, at STP)
F _L	liquid flow rate (kg/h or l/h)
G	gas mass superficial flow rate (kg m ⁻² s ⁻¹)
GC	gas chromatography
H	Henry constant
HPLC	high-pressure liquid chromatography
h _w	wall-to-bed heat transfer coefficient (W m ⁻² K ⁻¹)
ΔH ^v	water enthalpy of vaporisation (J/mol)
ΔH _i	heat of i th reaction (J/mol)
k ₀	pre-exponential factor of rate constant (m ³ s ⁻¹ kg ⁻¹)
k _{GS}	gas-solid mass transfer coefficient of oxygen (m s ⁻¹)

k_{GA}	gas side-liquid volumetric mass transfer coefficient of water vapour (s^{-1})
k_{La}	gas-liquid side volumetric oxygen mass transfer coefficient (s^{-1})
$(ka)_{LL,j}$	dynamic-static liquid volumetric mass transfer coefficient of compound j (s^{-1})
$k_{LS,j}$	j-compound liquid-solid mass transfer coefficient (m/s)
L	liquid mass superficial flow rate ($kg\ m^{-2}\ s^{-1}$)
LHSV	liquid hourly space velocity (h^{-1})
\dot{m}_L	mass liquid flow rate (kg/s)
MS	mass spectrometry
MT/Y	metric ton per year
$\dot{n}_{G,T}$	total molar gas flow rate (mol/s)
\dot{n}_{G,H_2O}	molar water vapour flow rate (mol/s)
$P_{H_2O}^v$	water vapour pressure (Pa)
P_{O_2}	oxygen partial pressure (Pa or bar)
P_T	total pressure in the reactor (Pa or bar)
q_e	amount of phenol adsorbed per unit weight of activated carbon ($mol\ g^{-1}$)
r	particle radial dimension (m)
r_i	i^{th} reaction rate ($mol\ kg^{-1}\ s^{-1}$)
r_p	catalyst particle radius (m)
R	universal gas constant ($8.314\ J\ kg^{-1}\ K^{-1}$)
R_j	total production or destruction rate of compound j ($mol\ kg^{-1}\ s^{-1}$)
SSR	small-scaled fixed bed reactor
T	temperature (K or $^{\circ}C$)
TBR	trickle-bed reactor
T_w	reactor wall temperature (K or $^{\circ}C$)
u_L	liquid superficial velocity (m/s)
u_G	gas superficial velocity (m/s)
\dot{V}	volumetric flow rate (m^3/s)
V_R	reactor volume (m^3)
V_L	liquid volume (m^3)
WAO	wet air oxidation

W_{cat}	catalyst load (g or kg)
WHSV	weight hourly space velocity (h^{-1})
wt%	percentage by weight
x	liquid molar fraction
XRD	X-ray diffraction
XRF	X-ray fluorescence
z (or Z)	reactor axial dimension (m)

Greek

α	order of reaction of oxygen
ε_L	liquid hold up
ε_p	particle porosity
ϕ'	Weisz modulus for pore diffusion based on observed reaction rate
η_j	effectiveness factor of compound j
φ	evaporation rate based on reactor length ($\text{mol m}^{-1} \text{s}^{-1}$)
μ	viscosity (Pa s)
ρ_b	apparent bed density (kg/m^3)
ρ_L	liquid density (kg/m^3)
ρ_G	gas density (kg/m^3)
ρ_p	catalyst particle density (kg/m^3)
σ	surface tension (N/m)
τ	space time (h or min)
ω	stirrer speed (rpm)

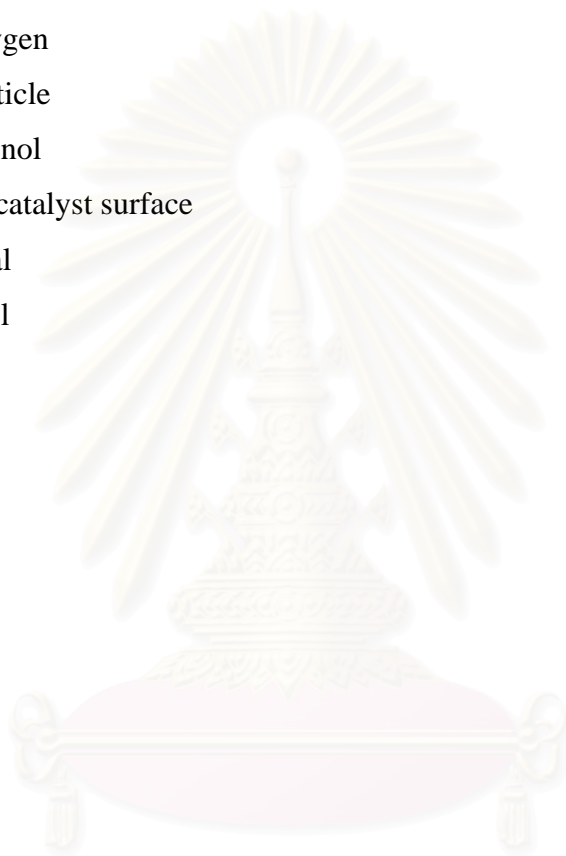
Superscripts

app	apparent
dyn	dynamic liquid
sta	static liquid

Subscripts

b	bed
---	-----

eq	at equilibrium
G	gas
H ₂ O	water
i	reaction index
j	compound index
L	liquid
O ₂	oxygen
p	particle
Ph	phenol
S	on catalyst surface
T	total
W	wall



สถาบันวิทยบริการ
จุฬาลงกรณ์มหาวิทยาลัย



PART I

**PRODUCTION OF AROMATIC HYDROCARBONS FROM *n*-HEXANE AND
NATURAL GASOLINE OVER Pd/ZSM-5 ZEOLITE**

สถาบันวิทยบริการ
จุฬาลงกรณ์มหาวิทยาลัย

CHAPTER I

INTRODUCTION

The transformation of alkanes into aromatic hydrocarbons is an area of great industrial relevance and also of academic interest for the production of benzene, toluene, xylene (BTX), and naphthalene derivatives. Aromatic hydrocarbons are important feedstock in chemical industries; for examples, benzene is an important feedstock for the production of polystyrene (PS); toluene is used as feedstock for polyurethane (PU) production; *p*-xylene is employed in poly(ethylene terephthalate) (PET) production process; and naphthalene is a substrate for the production of phthalic anhydride, an intermediate for dyestuff manufacture [1]. In general, naphtha-reforming catalysts (Pt/Al₂O₃) have been used to convert heavy naphtha (C₇–C₁₀) into aromatic hydrocarbons, but lower alkanes (C₂–C₆) are hardly transformed over these catalysts [2]. Chen and co-workers first found the ability of ZSM-5 zeolite to convert light hydrocarbons to BTX; however, these catalysts give poor results for paraffin conversion because of excessive methane and ethane formation with low selectivity to aromatics [3]. Consequently, there have been numerous reports on various ZSM-5-based catalysts for the conversion of light paraffins into aromatics. To improve the low paraffin conversion, various types of activating agents (*e.g.*, gallium, copper, zinc, and platinum) have been added to zeolite. Several systematic studies have been described [4–11]. However, only a few researchers have studied *n*-hexane aromatization. Popova *et al.* reported the batch transformation of *n*-hexane over Cu/ZSM-5 with 82% conversion and 14% aromatic selectivity [12]. Bhattacharya *et al.* found that the aromatization of *n*-hexane over H-ZSM-5 zeolite in batch mode was enhanced by the promoters ZnO and Ga₂O₃, while Fe₂O₃ and Cr₂O₃ decreased its aromatization activity [13]. Bhattacharya *et al.* also reported that ZSM-5 gave the highest aromatization activity compared to those of ZSM-22 and EU-1 [14]. Moreover, Rojasova and co-workers studied the role of zinc in Zn/ZSM-5 zeolite in a batch aromatization of *n*-hexane, of which the conversion of 47.6% with 50.2% aromatic selectivity was obtained [15].

Surprisingly, although there have been several studies using Pd/ZSM-5 on alkanes combustion [16–20], none has reported on the ability of Pd/ZSM-5 toward the aromatization, and the present work is the first aromatization reaction upon Pd/ZSM-5.

Aromatization is of industrial interest since it could be employed for the conversion of petrochemical byproduct that contains alkane (*e.g.*, natural gasoline and light naphtha) into other useful products for other chemical industries. The natural gasoline is a natural gas byproduct, which contains mainly saturated aliphatic hydrocarbons, practically free of olefins and also some aromatics [21]. The present work is aimed at developing a continuous process for the production of benzene and naphthalene derivatives from natural gasoline using *n*-hexane as a model compound and Pd-loaded ZSM-5 as catalyst.

Objectives of this research

The objectives of this research are aimed at (a) preparing ZSM-5 catalysts with various concentrations of Pd-loaded for the production of aromatic hydrocarbons from *n*-hexane and natural gasoline; (b) determining both qualitative and quantitative analyses of the reaction products; and (c) optimization of reaction conditions in order to obtain desirable products.

Scope of this research

The scope of this research covers the preparation of Pd-loaded ZSM-5 catalysts (0, 0.2, 0.3, and 0.5 wt%). These catalysts were characterized by XRD and XRF techniques. Product distributions, when using *n*-hexane and natural gasoline as substrates, are qualitatively and quantitatively determined by GC and GC/MS techniques.

CHAPTER II

THEORY AND LITERATURE REVIEW

2.1 Catalysis

In the early years of the 19th century, when many important discoveries of chemistry and physics were being made, it was noticed that a number of chemical reactions were affected by trace amount of substances that were not consumed in the reaction. Berzelius introduced the term catalysis in the early of 1836 in order to explain various decomposition and transformation reactions [22,23]. He assumed that catalysts possess special powers that can influence the affinity of chemical substances [22,23].

The basic concept of a catalyst is that of a substance that in small amount causes a large change in reaction rate. More precise definitions of catalysis have been gradually presented since the understanding of catalysis phenomena has grown. Nevertheless, even today there is no universal agreement on catalyst definitions, the point of view varying depending upon the investigator. A definition, which was given in the term of physical chemistry law, that is still valid today was presented by Ostwald in 1895, stated that “catalyst is a substance that accelerating a chemical reaction without affecting the position of the equilibrium.” While it was formerly known that the catalyst remained unchanged in the course of the reaction, it is now known that the catalyst is involved in chemical bonding with the reactants during the catalytic process. Thus, catalysis is a cyclic process: the reactants are bound to one site of the catalyst, and the products are released from another, regenerating the initial site. In theory, an ideal catalyst would not be consumed, but this is not the case in practice. Owing to competing reactions, the catalyst undergoes chemical changes, and its activity becomes lower (catalyst deactivation). Catalysts also have another important property, apart from accelerating reaction; they can influence the selectivity of chemical reactions. This means that completely different products can be obtained from a given starting material by using different catalyst system. Industrially, this targeted reaction control is often even more important than the catalytic activity [22–26].

2.1.1 Catalysis activity [23,24,26]

The activity of a catalyst refers to the rate at which it causes the reaction to proceed to chemical equilibrium [24]. Generally, in kinetic treatment, the reaction rate is measured in a temperature and concentration ranges that will be present in the reactor. The reaction rate r is calculated as the rate of change of the amount of substance n_A of reactant A with time relative to the reaction volume or the mass of catalyst:

$$r = \frac{\text{converted amount of substance of a reactant}}{\text{volume or catalyst mass} \times \text{time}} \quad (\text{mol L}^{-1} \text{h}^{-1} \text{ or mol kg}^{-1} \text{h}^{-1}) \quad (1-2-1)$$

Kinetic activities are derived from the fundamental rate laws, for example, that for a simple irreversible reaction $A \rightarrow P$:

$$\frac{dn_A}{dt} = kV f(c_A) \quad (1-2-2)$$

The temperature dependence of rate constants is given by the Arrhenius equation:

$$k = k_0 e^{-(E_a/RT)} \quad (1-2-3)$$

E_a = activation energy of the reaction

k_0 = pre-exponential factor

R = gas constant

As Equations (1-2-2) and (1-2-3) show, there are three possibilities for expressing catalyst activity: reaction rate, rate constant k , and activation energy E_a [23].

Another measure of catalyst activity is the turnover number (TON) or turnover frequency, which is the number of molecules that react per site per unit time. As a basic measure of true catalytic activity, this is a useful concept, but it is limited by the difficulty of determining the true number of active sites. In general, it is easier to do this for metals than for non-metal catalysts since techniques such as selective chemisorption are available to measure the exposed surface area of metals. For acid catalysts, the measurement of site concentration by poisoning or adsorption of bases

may lead to erroneously high value since sites may be active for sorption but not for reaction. As with rates of reaction, the turnover number is a function of pressure, temperature, and composition of reactants [24].

Catalysts are often investigated in continuously operated test reactors, in which the conversions attained at constant space velocity are compared [23]. The liquid hourly space velocity (LHSV) is the volumetric flow rate V_0 relative to the reactor volume (unpacked) V :

$$\text{LHSV} = \frac{V_0}{V} \quad (\text{h}^{-1}) \quad (1-2-4)$$

The volumetric flow rate may be calculated at the inlet or reactor conditions, or at standard temperature and pressure (STP) and usually based on the volume of entering reactant. The reciprocal of this is *contact time* or *superficial contact time*, which has unit of time. In some cases the LHSV is given in term of volumetric feed rate of a liquid, even though it may be vaporized and mixed with other reactants before entering the catalyst bed.

If the volumetric flow rate and reactor volume in Equation (1-2-4) were replaced by mass flow rate and catalyst mass, respectively, it will give the weight hourly space velocity (WHSV) [23,24].

2.1.2 Catalysis selectivity [24]

The selectivity of the reaction usually defined as percentage of reactant that is converted to the desired product. The selectivity usually varies with pressure, temperature, reactant composition, and extent of conversion as well as nature of the catalyst.

Yield is an engineering or industrially used term which refers to the quantity of product formed per quantity of reactant consumed in overall reactor operation. Within this overall operation there may be recycle of various reactants, as after separation. Yield is frequently reported on a weight basis, so a yield exceeding 100 wt% may be obtained [24].

2.1.3 Catalysis deactivation

A catalyst may lose its activity or its selectivity for a wide variety of reasons. The four most common causes of catalyst deactivation are: [23,24]

1. Poisoning of the catalyst. Typical catalyst poisons are H₂S, Pb, Hg, and S.
2. Fouling
3. Reduction of active area by sintering or migration
4. Loss of active species *via* the gas phase

2.1.3.1 Catalyst poisoning

Catalyst poisoning is a chemical deactivation effect, which is happened by forming strong adsorptive bonds between the catalyst poisons and the active catalyst surfaces, thus blocking the active centers. Therefore, even very small amounts of catalyst poisons can influence the adsorption of reactants on the catalyst. The term catalyst poison is usually applied to foreign materials in the reaction system. If the substances that blocked the active centers are the reaction products that slowly diffuse away from the catalyst surface, these substances are referred as inhibitors.

Metal catalysts are highly sensitive to small amount of impurities in reaction medium. Catalytically active metals make their *d*-orbitals available for adsorption, and this is the key to understanding both their catalytic activity and their sensitivity to poisons. Particularly strong catalyst poisons are the ions of elements group 15 (P, As, Sb, and Bi) and 16 (O, S, Se, and Te). The poisoning activity depends on the presence of electron lone pairs, which have been shown to form bonds with transition metals on chemisorption. If these are involved in bonding to other elements, then the ions are nonpoisons. Catalyst poisoning can be reversible or irreversible, depending on the reaction conditions [23].

2.1.3.2 Fouling

Fouling is a physical blockage of the catalyst active sites, which might be caused by the deposition of fine powder or carbonaceous deposit (coke). In the case of fouling by carbonaceous deposit, the catalyst activity can be restored by burning to remove the coke from the catalyst surface [24].

2.1.3.3 Sintering [23,24]

Sintering is an irreversible physical process leading to a reduction of effective catalytic area. It may result from growing of metal crystallites on a support or decreasing of area of non-support catalyst. The rate of sintering increases with increasing temperature, decreasing crystallite size, and increasing contact between crystallite particles. Other factors are the amount and type of impurities on the crystallite surface and the support composition in supported catalysts.

2.1.3.4 Loss of catalyst species *via* the gas phase

High reaction temperatures in catalytic processes can lead to loss of active components by evaporation. This does occur with compounds that are known to be volatile, but also by reaction of metals to give volatile oxides, chlorides, or carbonyls [23,24].

2.2 Classification of catalyst

According to the state of aggregation that they incorporate, catalysts can be classified into two groups: heterogeneous catalyst and homogeneous catalyst (Figure 1-2-1).

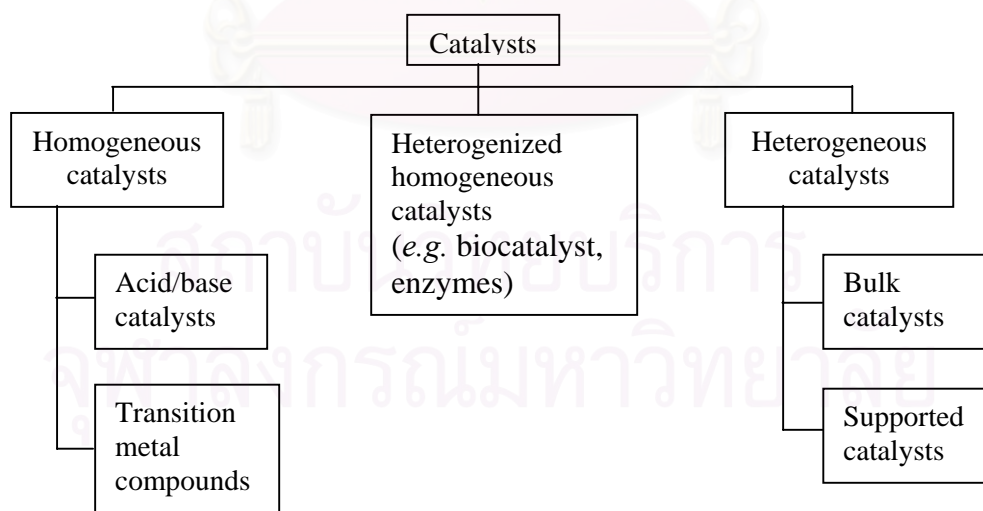


Figure 1-2-1: Classification of catalysts

By far the most important catalysts used are the heterogeneous catalysts [23]. Heterogeneous catalysis takes place between several phases. Generally, the catalyst is

a solid, and the reactants are gases or liquids. In supported catalysts the catalytically active substance is added to a support material that has a large surface area and that is usually porous.

2.2.1 Comparison of homogeneous catalysis and heterogeneous catalysis [22–25]

Generally, in the heterogeneous catalysis, phase boundaries are always present between the catalyst and the reactants, while in the homogeneous catalysis, catalyst, reactants, and products are in the same phase. Homogeneous catalysts have a higher degree of dispersion than heterogeneous catalysts since each individual atom can be catalytically active. In heterogeneous catalysts only the surface atoms are active. Due to high degree of dispersion, homogeneous catalysts exhibit a higher activity per unit mass of metal than heterogeneous catalysts. The major disadvantage of homogeneous transition metal catalysts is the difficulty of separating catalyst from the product. Heterogeneous catalysts are either automatically removed in the process (*e.g.*, gas phase reaction in fixed bed reactor), or they can be separated by simple method such as filtration or centrifugation. In case of homogeneous catalysts, more complicated process such as distillation, liquid-liquid extraction, and ion exchange must be often used. Table 1-2-1 summarizes the advantages and disadvantages of the two classes of catalysts.

Table 1-2-1: Comparison of homogeneous and heterogeneous catalysts [23]

	Homogeneous	Heterogeneous
<i>Effectivity</i>		
Active centers	all metal atoms	only surface atoms
Concentration	low	high
Selectivity	high	lower
Diffusion problems	practically absent	present (mass-transfer controlled reaction)
Reaction conditions	mild (50–200 °C)	severe (often > 250 °C)
Applicability	limited	wide
Activity loss	irreversible reaction with products; poisoning	sintering of the metal crystallites; poisoning
<i>Catalyst properties</i>		
Structure/ stoichiometry	defined	undefined
Modification possibilities	high	low
Thermal stability	low	high
Catalyst separation	sometimes laborious (distillation, extraction)	fixed bed: unnecessary suspension: filtering
Catalyst recycling	possible	easy
Cost of catalyst losses	high	low

2.3 Heterogeneous catalysis

2.3.1 Individual steps in heterogeneous catalysis [22–24]

Heterogeneously catalyzed reactions are composed of purely chemical and purely physical reaction steps. For the catalysis process to take place, the reactants must be transported to the catalyst surface. Thus, apart from the actual chemical reaction, diffusion, adsorption, and desorption processes are of importance for the progress of the overall reaction. The total process may be divided into the following seven steps, any one of which can be rate determining.

1. Diffusion of the reactants through the boundary layer to the catalyst surface
2. Diffusion of the reactants into the pores (pore diffusion)
3. Adsorption of reactants on the inner surface of the pores

4. Chemical reaction on the catalyst surface
5. Desorption of the products from the catalyst surface
6. Diffusion of the products out of the pores
7. Diffusion of the products away from the catalyst through the boundary layer and into the gas phase

Steps 1, 2, 6, and 7 involve no chemical change. Steps 1 and 2 are the physical processes whereby the reactant are brought through the gaseous or liquid phase surrounding the solid catalyst to the active sites on the catalyst's surface. This is a diffusion process and the phenomenon is called mass transport or mass transfer. Step 6 and 7 is the process for getting products away from the surface. When either of these is slower than the catalytic rate itself, the rate is determined by the rate of arrival of reactants (or removal of products), which is referred as diffusion limitation or mass-transport limitation. Diffusion limitation at the external surface of catalyst particles is recognized by the following characteristics.

1. The rate is proportional to catalyst weight (or to the concentration of active component) and raised to a power less than unity
2. The rate is increased by improving the movement of the gas or liquid with respect to the catalyst
3. The temperature coefficient and the apparent activation energy are low [22].

2.3.2 Promoters

Promoters are substances that they are not catalytically active, but increase the activity of the catalysts. The function of these substances, which are added in the catalyst in small amounts, has not been elucidated. There are four types of promoters: (a) structural promoters; (b) electronic promoters; (c) textural promoters; and (d) catalyst-poison-resistant promoters [23].

Structural promoters increase the selectivity by influencing the catalyst surface so that the number of possible reactions for the adsorbed molecules decreases and a favored reaction path dominates.

Electronic promoters influence the electronic character of the active phase by dispersing in the phase and therefore chemically binding with the adsorbate.

Textural promoters inhibit the growth of catalyst particles to form larger and less active structures during the reaction. They prevent loss of active surface by sintering, thereby increasing the thermal stability of the catalyst.

Catalyst-poison-resistant promoters protect the active phase against poisoning by impurities, either present in the reactant feed or formed during the reactions.

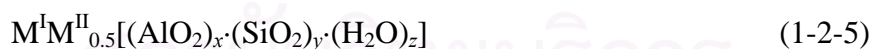
A catalyst may contain one active component and one or more promoters. Since the above four effects tend to overlap in practice, it is sometimes difficult to precisely define the function of a promoter [23].

2.4 Zeolites

2.4.1 Structure of zeolites [23–27]

Zeolites are water containing crystalline aluminosilicates of natural or synthetic origin with highly ordered structures. They consisted of SiO_4 and AlO_4^- tetrahedra, which are linked through common oxygen atoms to give a three-dimensional network through which long channel run. In the interior of these channels, which are characteristic of zeolite, are located water molecules and mobile alkali metal ions, which can be exchanged with other cations. These compensate for the excess negative charge in the anionic framework resulting from the aluminum content. The interior of the pore system, with its atomic scale dimensions, is the catalytically active surface of the zeolite. The inner pore structure depends on the composition, zeolite type, and the cations.

The general formula of zeolite is



Where M^{I} and M^{II} are alkali and alkali earth metals. The indices x and y denote the oxide variables, and z is the number of molecules of water of hydration. The composition is characterized by the Si/Al atomic ratio and the pore size of zeolites.

Zeolites are mainly distinguished according to the geometry of the cavities and channels formed by the rigid framework of SiO_4 and AlO_4^- tetrahedra. The tetrahedra are the smallest structure units into which zeolite can be divided. Linking these primary building units together leads to 16 possible secondary building blocks (polygons), the interconnection of which produces hollow three-dimensional structures.

The entrances to the cavities of the zeolites are formed by 6-, 8-, 10-, and 12-ring apertures (small, medium, and wide-pore zeolite). A series of zeolites is composed of polyhedra (sodalite or β -cage, Figure 1-2-2), composed of 4- and 6-rings, which can be connected in various manners to give the fundamental zeolite structures. The sodalite cage, which consists of 24 tetrahedra, is generally depicted schematically as a polyhedron, generated by connecting the center of neighboring tetrahedra with a line. Each vertex of this polyhedron represents a silicon or aluminum atom, and the midpoint of each edge, an oxygen atom.

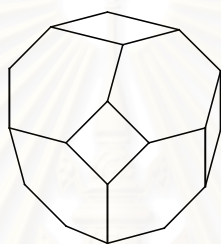


Figure 1-2-2: Structural unit of sodalite cage (β -cage)

Examples of medium-pore zeolites are the pentasils, which belong to the silicon-rich zeolites. Their polyhedra are composed of 5-rings as secondary building units. These so-called 5-1 units are structurally analogous to methylcyclopentane. Linking of the resulting chains give a two-dimensional pore system, one consisting of zig-zag channels of near circular cross-section and another of straight channels of elliptical shape. All the intersections in pentasil are of the same size [25]. The three-dimensional structure of pentasil is represented in Figure 1-2-3a. The 10-membered rings provided access to a network of intersecting pore within the crystal. The pore structure is depicted schematically in Figure 1-2-3b; there is a set of straight, parallel pores intersected by a set of perpendicular zig-zag pores. Many molecules are small enough to penetrate into this intracrystalline pore structure, where they may be catalytically converted [23,26]. An advantage of these zeolites is the uniformed channel structure, in contrast to zeolites A and Y, in which the pore windows provide access to larger cavities. A well-known representative of this class of zeolites is ZSM-5 (from Zeolite Socony Mobil no.5) [23,27].

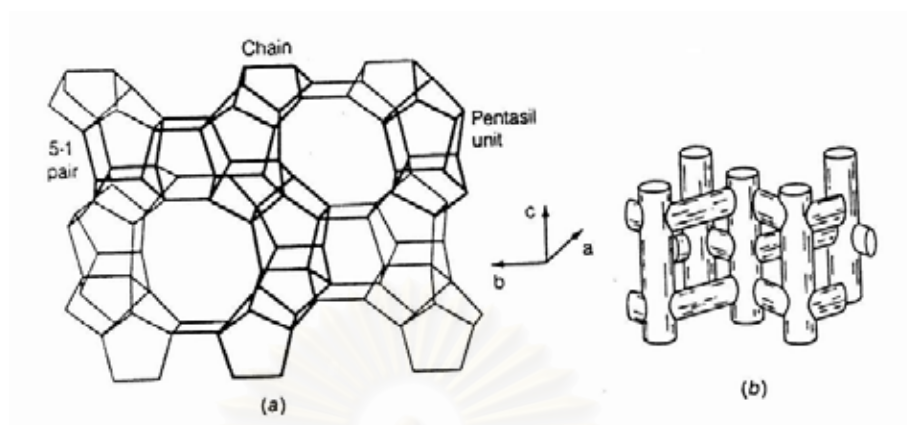


Figure 1-2-3: Three-dimensional structure of ZSM-5 (a) structure formed by stacking of sequences of layers (b) intracrystalline pore structure (After Gates [26]).

The aluminosilicates structure is ionic, incorporating Si^{4+} , Al^{3+} , and O^{2-} . When some of the Si^{4+} ions in the SiO_4 tetrahedra in this framework are replaced by Al^{3+} ions, as in the ZSM-5, an excess negative charge is generated. A compensating source of positive charge must be added, namely cation, in addition to the framework Si^{4+} and Al^{3+} . These nonframework cations play a central role in determining the catalytic nature of zeolites. The zeolites are ion exchanger. Bringing an aqueous salt solution in contact with the zeolite leads to incorporation of cations from the salt into the zeolite, replacing some of the nonframework cation initially present [25,26].

Table 1-2-2: Characteristics of important zeolites [23]

Type	Pore diameter (nm)	Pore aperture
Zeolite Y	0.74	12-ring
Pentasil zeolite	0.54×0.56 and 0.51×0.55	10-ring (ellipsoid)
Zeolite A	0.41	8-ring
Sodalite	0.26	4-ring

2.4.2 Catalytic properties of zeolites [23,26]

In 1962, zeolites were introduced by Mobil Oil Corporation as new cracking catalyst in refinery technology. They were characterized by higher activity and selectivity in cracking and hydrocracking. At the end of 1960s, the concept of shape-selective catalysis with zeolite was introduced to petrochemistry (Selectoforming process), and then zeolite becoming the importance topics in catalysis research and applied catalysis [23,26]. Their advantages over conventional catalysts can be summarized as follows:

1. Crystalline and precisely defined arrangement of SiO_4 and AlO_4^- tetrahedra resulted in good reproducibility in production.
2. Shape selectivity: only molecules that are smaller than the pore diameter of the zeolite can undergo the reaction.
3. Controlled incorporation of acid centers in the intracrystalline surface is possible during synthesis.
4. At above 300 °C, pentasil and zeolite Y have acidities comparable to mineral acid.
5. Catalytically active metal ions can be easily applied to the catalyst by ion exchange or impregnation.
6. Zeolite catalysts are thermally stable up to 600 °C, and can be regenerated by burning of carbon deposit [23].

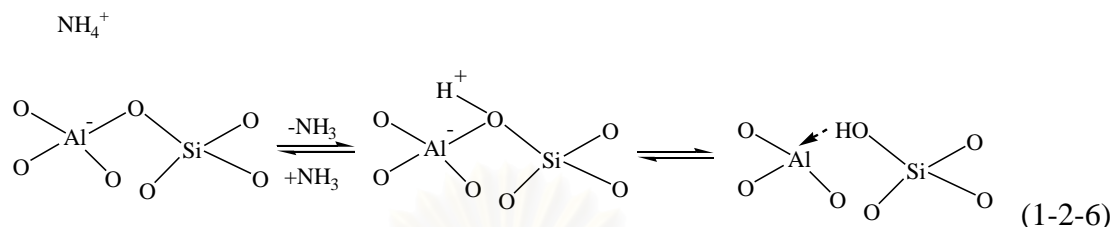
2.4.2.1 Shape selectivity

The shape selectivity of zeolites is based on the interaction of reactants with the well-defined pore system. A distinction is made between these factors, which can overlap: (a) reactant selectivity; (b) product selectivity; and (c) restricted transition state selectivity.

2.4.3 Acidity of zeolites [23,25–27]

Acid strength of zeolite can be varied by numerous preparation methods (ion exchange, partial dealumination, and substitution of the framework of Al and Si atoms). Direct replacement of the alkali metal ions with protons by treatment with mineral acids is only possible in exceptional cases (*e.g.*, mordenite and ZSM-5 zeolite). The best method is exchanging of the alkali metal ions by NH_4^+ ions,

followed by heating the resulting ammonium salts at 500 to 600 °C (deammonization; Equation 1-2-6)



Infrared investigations have shown that the protons are mainly bound as silanol groups but have a strongly acidic character due to strongly polarizing influence of the coordinative unsaturated ammonium center. Bronsted acid center are generally the catalytically active sites of the H-zeolites. Weak to moderate strong acid sites can be generated in zeolite by ion exchange with multivalent cations. Owing to the polarizing effect of the metal cations, water is dissociatively adsorbed, and the equilibrium of Equation 1-2-7 is established.



The following order of Bronsted acidity is given for cation-exchanged zeolite: H form \gg La form $>$ Mg form $>$ Ca form $>$ Sr form $>$ Ba form. The influence of the exchanged ions is considerable, as shown by the example of cumene dealkylation on faujasite (Table 1-2-3). Reasons for the large differences in reactivity are the different charges on the ions, and the decreasing ionic radii from Na^+ to H^+ and the associated polarizing power of the ions. The incorporation of transition metal ions into zeolites leads to interesting bi-functional catalysts in which metal and acid centers can act simultaneously.

Table 1-2-3: Effect of metal ion in faujasite on cumene dealkylation [23]

Cation	Relative activity
Na ⁺	1
Ba ²⁺	2.5
Sr ²⁺	20
Ca ²⁺	50
Mg ²⁺	100
Ni ²⁺	1100
La ³⁺	9000
H ⁺	8500
SiO ₂ /Al ₂ O ₃	1

Another major influence on the acidity of zeolites is the Si/Al ratio. The zeolite can be classified into three groups, according to the Si/Al ratio and the associated acid/base properties (Table 1-2-4). Since the ion exchange capacity corresponds to the Al³⁺ content of the zeolites, those with lower Si/Al ratios have higher concentrations of active centers.

สถาบันวิทยบริการ
จุฬาลงกรณ์มหาวิทยาลัย

Table 1-2-4: Classification of acidic zeolite according to Si/Al ratio [26]

Si/Al ratio	Zeolite	Acid/base properties
Low (1 to 1.5)	A, X	relatively low stability of lattice; low stability in acids; high stability in base; high concentration of acid groups of medium strength
Medium (2 to 5)	erionite, chabazite, chinoptilolite, mordenite, Y	
High (<i>ca.</i> 10 to ∞)	ZSM-5, dealuminated erionite, mordenite, Y	relatively high stability of lattice; high stability in acids; low stability in base; low concentration of acid groups of high strength

Zeolites with high concentrations of protons are hydrophilic and have high affinities for small molecules that can enter the pores. Zeolites with low H^+ concentrations, such as silicalite, are hydrophobic and can take up organic components from aqueous solution. The boundary lies at a Si/Al ratio of around 10. The stability of the crystal lattice also increases with increasing Si/Al ratio. The decomposition temperatures of zeolites are in the range of 700 to 1,300 °C. The highest proton donor strengths are exhibited by zeolites with the lowest concentration of AlO_4^- tetrahedra such as ZSM-5 and the ultrastable zeolite HY. These are superacids, which at high temperature (*ca.* 500 °C) can even protonate alkanes. It was found that the acid strength depends on the number of Al atoms that are adjacent to a silanol group. Since the Al distribution is non-uniform, a wide range of acid strengths results.

2.4.4 Metal-doped zeolites [23,25]

Zeolites are especially suitable as support materials for active components such as metals. Suitable metals are effective catalysts toward hydrogenations and oxidations, whereby the shape selectivity of the carrier is retained.

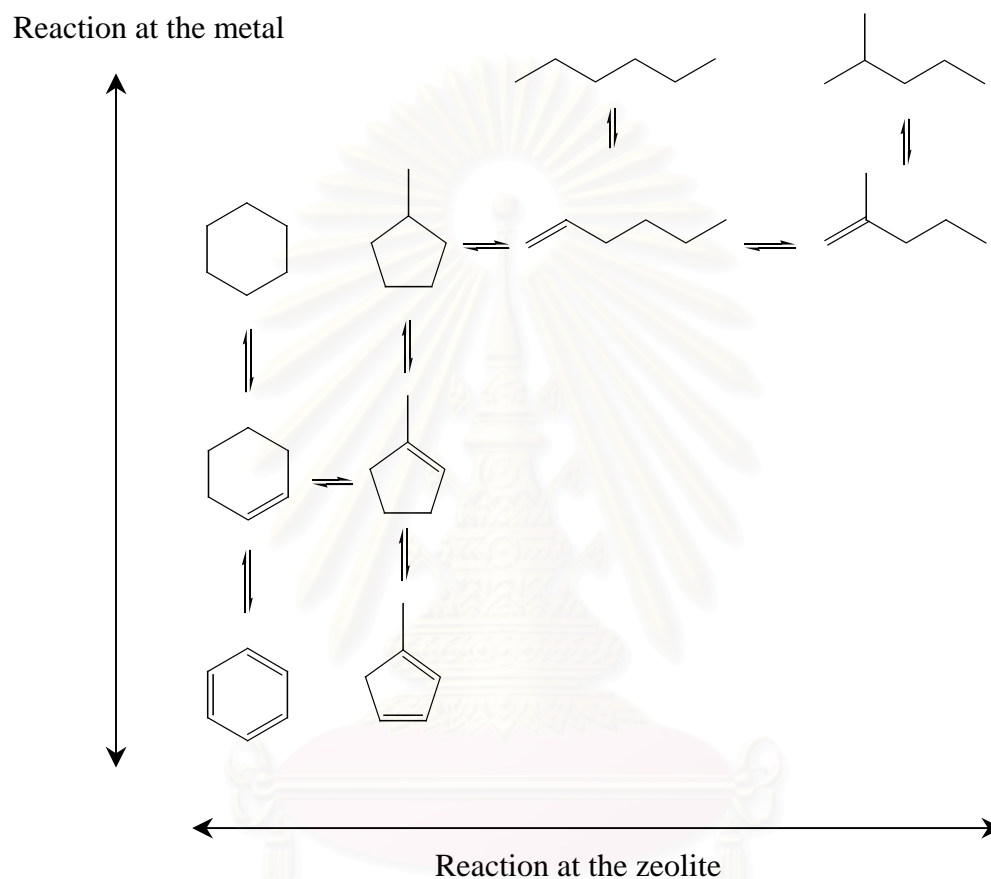


Figure 1-2-4: Bifunctionality of metal-doped zeolites: isomerization and hydrogenation

Important factors influencing the reactions of bifunctional catalysts are the location of the metal, the particle size, and the metal-support interaction. The bifunctionality of the metal-doped zeolite catalysts is explained as for the important example of isomerization and hydrogenation. The metal content facilitates the hydrogenation and dehydrogenation steps, while the acid catalyzed isomerization step takes place under the restricted conditions of the zeolite cavities (Figure 1-2-4) [23].

Bifunctional catalysts are used in many reactions, including hydrocracking, reforming, and dewaxing process [25]. They usually contain *ca.* 0.5% Pt, Pd, or Ni.

2.5 Literature review of *n*-hexane and natural gasoline aromatization over zeolite catalysts

In 1989, Kawata *et al.* [28] studied the batch aromatization of *n*-hexane over galloaluminosilicate and gallosilicate. They found that proton forms of galloaluminosilicate and gallosilicate exchanged with ammonium nitrate solution have much higher activity for the aromatization of *n*-hexane than Ga³⁺-exchanged HZSM-5 or Ga₂O₃-supported ZSM-5. They implied that large amounts of gallium species are uniformly introduced into zeolite crystalline of galloaluminosilicate and gallosilicate, which promote the dehydrogenation of *n*-hexane to *n*-hexene. On the other hand, a proton form of gallosilicate exchange with hydrochloric acid showed lower activity for the aromatization of *n*-hexane, but the activity of the proton form of galloaluminosilicate is increased by a small addition of Ga³⁺. They suggested that active gallium species over galloaluminosilicate and gallosilicate are not gallium species in the framework but those outside the framework.

Popova *et al.* [12] reported the batch transformation of *n*-hexane over ZSM-5 zeolite with various metals-loaded, which are 2.2% NaZSM-5, 1.0% CuHZSM-5, 1.75% Cu-0.5% NaZSM-5, and HZSM-5. The results are shown in Table 1-2-5.

Table 1-2-5: Transformation of *n*-hexane over zeolite catalysts at 380 °C

Quantity	Catalyst			
	2.2% NaHZSM-5	1.0% CuHZSM-5	1.75% Cu - 0.5% NaZSM-5	HZSM-5
Conversion, %	6	81	68	88
Cracking products, %	2.4	48	37	62
Aromatics, %	-	16.5	7.6	18.5

They also found that the degree of aromatization is related to carbonium ion formation and depends on the acid strength and copper content of the zeolite.

Alario and co-workers [29] investigated the aromatization of light naphtha, which composed of 90% C₅-alkane, 5.4% C₆-alkane, 3.7% C₅-cycloalkane, and 0.9% C₆-cycloalkane, using zeolite ZSM-5 that is modified by treatment with a fluorosilicate solution (*e.g.*, aqueous (NH₄)₂SiF₆) and ZSM-5 zeolites (Si/Al ratio = 27) doped with Ga. The results are presented in Table 1-2-6. From the results, they concluded that modification of ZSM-5 zeolite with both fluorosilicate solution and gallium significantly improved the aromatic products.

Table 1-2-6: Aromatization of light naphtha on zeolite catalysts at 480 °C and 2.5 bar

Catalyst	Conversion (wt%)	Selectivity (wt%)					aromatics
		methane	ethane + ethylene	propane + propylene	butane + butene	olefins + C ₅ + C ₆	
ZSM-5	93	30	26	14	18	1	11
NH ₄ ZSM-5	78	27	24	13	17	1	18
3.5% GaZSM-5	95	7	17	28	8	1	39
3.45% Ga- NH ₄ ZSM-5	86	6	16	28	7	1	42

Bhattacharya *et al.* [14] reported the batch aromatization of *n*-hexane by three-medium pore zeolites with different pore geometry, which are ZSM-5, ZSM-22, and EU-1 zeolites. The conversion of *n*-hexane over ZSM-5 is nearly 100% at all temperatures in the range of 450 to 540 °C. In the same range of temperatures, there is between 60 to 90% conversion in the case of ZSM-22 zeolite and between 43 to 51% in the case of EU-1 zeolite. The lower conversions recorded over ZSM-22 and EU-1 zeolites suggested that the reaction is probably constrained by diffusion limitations in the case of the above two zeolites that have small pore apertures (0.55 × 0.45 nm for ZSM-22 zeolite and 0.58 × 0.41 nm for EU-1 zeolite) than kinetic diameter of *n*-hexane (0.47 nm).

Smirniotis and co-workers [30] investigated the performance of the L, β, and USY zeolites supported platinum and of composites of Pt/BaKL with either Pt/β, or Pt/USY zeolite on the reforming reaction of *n*-hexane, methylcyclopentane, methylcyclohexane, and their mixtures. They found that the reactions of different mixtures of the above three hydrocarbons over the composite resulted in increased selectivities for C₇₊ aromatics compared to those calculated as molar averages by

multiplying the selectivities corresponding to the individually reacting feed hydrocarbons with their molar fractions in the feed mixture. They suggested that this behavior is attributed to the synergism caused by the components of the composites in combination with the components of the feed mixture.

Zheng *et al.* [31] studied the activities of zeolites K β and KL supported platinum as a bifunctional catalyst for the reforming of *n*-hexane. They found that due to the stronger acidity of zeolite β , Pt/K β exhibited more skeletal isomerization and cracking than does Pt/KL zeolite, while the latter shows superior aromatization activity (54% benzene compared to 8% benzene in the case of Pt/K β zeolite). They also reported that ion exchange of β zeolite with Cs⁺ could reduce the acidity and increase benzene selectivity as well as ion exchange with Ba²⁺ that could lead to better dispersion of platinum and so can improve the aromatization activity.

Yashima and co-workers [32] reported the isomerization of *n*-hexane over Pt-loaded H β , HZSM-5, and H-dealuminated mordenite at temperatures lower than 300 °C under atmospheric pressure. They found that Pt loaded H β showed the highest activity and selectivity of these three catalysts. The conversion of *n*-hexane was 76% and selectivities to dimethylbutanes, methylpentanes, and cracking products were 19.4, 76.2, and 4.4%, respectively, under the following conditions: reaction temperature, 275 °C; W/F, 5 g h mol⁻¹; molar ratio of hydrogen to *n*-hexane, 4. They also found that Pt/H β catalyst showed a good stability because H β has medium strength acid sites and three-dimensional large pores.

Bhattacharya *et al.* [13] studied the influence of promoters such as ZnO, Ga₂O₃, Fe₂O₃, and Cr₂O₃ on the aromatization of *n*-hexane over HZSM-5. They found that while ZnO and Ga₂O₃ increase aromatization, Fe₂O₃ and Cr₂O₃ decrease the aromatization. They suggested that the promoting action of both Ga- and Zn-oxides has been attributed to their ability to dehydrogenate alkanes and the production of allylic species. They also added that the addition of N₂ to the feed increases aromatization over HZSM-5, while H₂ decreases aromatization.

Chatterjee *et al.* [2] investigated the aromatization of *n*-hexane over medium pore zeolites *e.g.* ZSM-5, ZSM-22, and EU-1, using density functional theory (DFT). They found that aromatization was not always determined by the Bronsted acidity but also by the pore architecture and geometry of the different zeolites, which is determined by the change in electronic environment of the respective zeolite. They

also used DFT to observe the reactivity order (ZSM-5 > ZSM-22 > EU-1) as well as product selectivity order (ZSM-5 > EU-1 > ZSM-22) of the reaction. From the DFT results, they concluded that ZSM-5 was more suitable zeolite in the aromatization reaction than other medium pore zeolites.

Rojasová *et al.* [15] studied the role of zinc in Zn/ZSM-5 zeolite in a batch aromatization of *n*-hexane, of which the conversion of 47.6% with 50.2% aromatic selectivity was obtained. Moreover, they also studied the effect of incorporation of Zn into ZSM-5, which are ion exchange, mechanical mixing, and impregnation methods. They found that incorporation of Zn by ion exchange into cationic positions of NH₄-ZSM-5 zeolite causes acid site strength redistribution and generation of new relatively strong Lewis acid sites in zeolite, increasing the selectivity of *n*-hexane aromatization in comparison with the parent NH₄-ZSM-5 zeolite.

Ali and co-workers [33] reported the hydroconversion activities of 0.35 wt% of Pt/Al₂O₃ promoted by addition of a second metal (0.35 wt%) such as Ir, Rh, Re, or U, in the conversion of *n*-pentane and *n*-hexane at different temperatures of 300 to 500 °C, except for Rh catalyst (from 150 to 500 °C) in the presence of H₂ atmosphere, 0.049 mol/h. They also investigated the reaction by the addition of 3.0 wt% F into the mono- and bimetallic catalysts. The studies revealed that reaction temperature influenced the acidity and selectivities. Incorporation of second metal and fluorination improved the activity of Pt/Al₂O₃. They suggested that incorporation of 3.0 wt% F leads to the formation of newly acidic sites, crystallinity improvement, and creation of pore available for the reactant molecules. The orders of selectivities of fluorinated bimetallic catalysts were: PtRe (15.4 wt%) > PtU (9.6 wt%) > PtIr (4.7 wt%) > PtRh (0.2 wt%) for hydroisomerization; PtRh (54.6 wt%) > PtIr (30.0 wt%) > PtU (27.1 wt%) > PtRe (17.7 wt%) for hydrocracking; and PtRe (1.3 wt%) > PtU (1.2 wt%) > PtIr (0.9 wt%) > PtRh (0.07 wt%) for dehydrocyclization of *n*-pentane at 500 °C.

Essayem *et al.* [34] investigated the hydroisomerization of *n*-hexane using heteropolyacids (HPA) such as 12-tungstophosphoric acid, H₃PW₁₂O₄₀, and a series of its acid alkalis salts (*e.g.*, Cs, Ru, K, and ammonium salts) associated with silica-supported platinum as well as platinum-supported dealuminated mordenite as catalysts. They found that the protons in the HPA bifunctional catalysts are more efficient than those of zeolites such as mordenite probably because they were more

acidic and also because the reaction was less affected by diffusion since, on HPA material only, nonconstraint surface protons interfered in the reaction. During *n*-hexane conversion the selectivity toward isomerization is similar when the reaction is carried out over heteropolyacid catalysts and over H-mordenite. The studies revealed that the Pt-(NH₄)_{2.6}H_{0.4}PW₁₂O₄₀ gave the highest conversion (82.0%) with 87.6% isomerization activity at 225 °C. They also found that the isomer product distributions depended mainly on the conversion level at a given reaction temperature. The formation of dibranched alkanes, *i.e.*, dimethylbutanes, required to improve fuel octane number, apparently is not more effectively obtained over HPA than over H-mordenite. They suggested that the reason was that the formation of 2,2-dimethylbutane, which contained a quaternary carbon, is kinetically limited even over HPA. Thus, the low reaction rate for the conversion of 2,3-dimethylbutane into 2,2-dimethylbutane accounted for the limited amounts of dibranched isomers.

2.6 Practical applications

2.6.1 Cyclar process [35]

The Cyclar process converts liquefied petroleum gas (LPG) directly into a liquid aromatics product in a single operation, developed jointly by BP and UOP. LPG consists mainly of the propane and butane fraction recovered from gas and oil fields and petroleum and refining operations. The reaction is described as dehydrocycloisomerization, and is thermodynamically favored at temperatures above 425 °C. The dehydrogenation of light paraffins (propane and butanes) to olefins is the rate-determining step. Once formed, the highly active olefins oligomerized to form larger intermediate, which then rapidly cyclized to naphthenes. These reactions, dehydrogenation, oligomerization, and cyclization are all acid catalyzed. The shape selectivity of the zeolite component of the catalyst also promotes the cyclization reaction and limits the size of the rings formed. The major liquid products from the Cyclar process are benzene, toluene, xylenes, and heavier aromatics. In general, the aromatic yield increases with the carbon number of the feedstock. In a low pressure operation, the overall aromatic yield increases from 61 wt% of fresh feed with an all-propane feedstock, to 66% with an all-butane feed, with a corresponding decrease in fuel gas production. Butane feedstocks produce a product that is leaner in benzene

and richer in xylenes than that produced from propane. With either propane or butane feeds, the liquid product contains about 91% BTX and 9% heavier aromatics.

BP commissioned the first commercial Cyclar unit at its refinery in Grangemouth, Scotland in January 1990. This unit was designed to process propane and butane feedstock at either high or low pressure, over a wide range of operating conditions.

2.6.2 RZ–Platforming Process [36]

The RZ–Platforming process selectively reforms naphtha feed (C_6 and C_7 paraffins and naphthenes) to aromatics (BTX). Four major reactions occur in Platforming reactors to produce the desired products:

1. Dehydrocyclization
2. Isomerization of 5-membered to 6-membered rings
3. Dehydrogenation of 6-membered rings to aromatics
4. Hydrocracking of large hydrocarbons to smaller hydrocarbons

The RZ-100 catalyst offers constant aromatic selectivity, in the range of 80% or higher, even when processing the most difficult C_6 and C_7 paraffin feed components.

The first RZ-Platforming unit was brought on stream and has been operating continuously since August 1998. The RZ-100 catalyst system performance continues to meet all expectations of activity, selectivity, and stability [36].

2.6.3 Alpha process [37]

The alpha process converts olefin-rich hydrocarbons (C_4 or C_5 raffinates from ethylene plant) into aromatics (BTX) by using a zeolite-type catalyst. The catalyst developed is Zn-doped HZSM-5 zeolite, followed by hydrothermal treatment. The catalyst shows high aromatic selectivity (14% benzene, 44% toluene, 3% ethylbenzene, 26% xylenes, and 13% C_{9+} aromatics).

This process had been operating since July 1993, with capacity of 3,500 BPSD of feed, in Mizushima plant, Okayama, Japan [37].

2.6.4 Toray TAC9 Process [38]

The Toray TAC9 process is used to selectively convert C₉ and C₁₀ aromatics into mixed xylenes. The typical feedstock derived either from reformates or hydrotreated pyrolysis gasoline (an aromatic-rich by product from ethylene cracker).

The TAC9 process involves several types of reactions of C₉ and C₁₀ aromatics, which are disproportionation (rearrangement of alkyl groups within a molecule), transalkylation (transfers of groups across molecules), and dealkylation (complete or partial removal of an alkyl group). In the TAC9 process, the dealkylation of the alkyl groups occurs such that the methyl groups are retained. The highly active TAC9 catalyst converts almost all ethyl, propyl, and butyl groups to methyl groups and benzene by dealkylation. The methyl groups react *via* disproportionation and transalkylation. By dealkylation of ethyl groups, a methyl balance for xylene production is achieved. The optimal xylene yield is a function of both the methyl to phenyl ratio as well as the ratio of ethyl group to methyl group in the fresh feed. Higher ratio results in higher xylene yields.

As of mid-2002, two commercial units had been brought on-stream, with feeding rates of 210,000 MT/Y and 850,000 MT/Y. Both units had consistently performed to expectation since the initial commercialization in 1996 [38].

CHAPTER III

EXPERIMENTAL SECTION

3.1 Materials and general methods

Zeolite NaZSM-5 ($\text{SiO}_2/\text{Al}_2\text{O}_3 = 58$ and $d_p = 10\text{-}1000$ nm) was obtained from Nissan Girdler Co. Ltd., Japan. The structure of zeolite was confirmed by a JEOL (model JDX-8030) X-ray powder diffractometer. All reagents (*n*-hexane, PdCl_2 , AgNO_3 , and NH_4Cl_2) were of analytical grade from Fluka. Nitrogen and hydrogen (99.999% purity) was obtained from Praxair Ltd. The Pd and S contents in each reactant and catalyst, as well as the $\text{SiO}_2/\text{Al}_2\text{O}_3$ ratio, were determined using a Phillips (model PW-2400) X-ray fluorescence spectrometer. Natural gasoline was obtained from the PTT Public Co. Ltd., Thailand, and was analyzed and quantified in the same manner as that for reaction products by GC/MS. The reaction products were analyzed and quantified by two techniques: (A) a Hewlett-Packard (model 6890) gas chromatograph (GC) equipped with a HP-5 capillary column (30 m \times 0.32 mm i.d.) and flame ionization detector (FID); and (B) a Fisons Instruments (model 8060) gas chromatograph equipped with a HP-5 capillary column (30 m \times 0.32 mm i.d.) using a Fisons Instruments (model Trio 2000) mass spectrometer as a detector. All products were identified by comparison with their authentic compounds obtained from Fluka.

3.2 Aromatization reactor

The aromatization reactor (Figure 1-3-1) was constructed from a stainless steel tubing of 120 cm long (105 cm long catalyst bed), 0.62 cm i.d., and 0.68 cm o.d. bent into a spiral shape, and was heated in an old GC oven equipped with 3000W heating coil. The temperature of the column was controlled by a temperature-controlled unit. Each column was separately packed between two glass wool plugs with 8.0 g of ZSM-5 catalysts with various amounts of Pd. Nitrogen and hydrogen, supplied from cylinder, were mixed before entering the top of the column. Prior to each experiment, the catalyst was reduced *in situ* under constant flow of nitrogen and hydrogen mixed gas. Subsequently, both nitrogen and hydrogen streams were removed from the system, and the reactant was continuously introduced into the top of the column at various feeding rates using a Waters (model 510) HPLC pump. The reactor effluent

was collected in an acetone/dry ice cooling-unit, which composed of a condenser cooled with acetone/dry ice and a reservoir that was dipped in an acetone/dry ice bath (Figure 1-3-1).

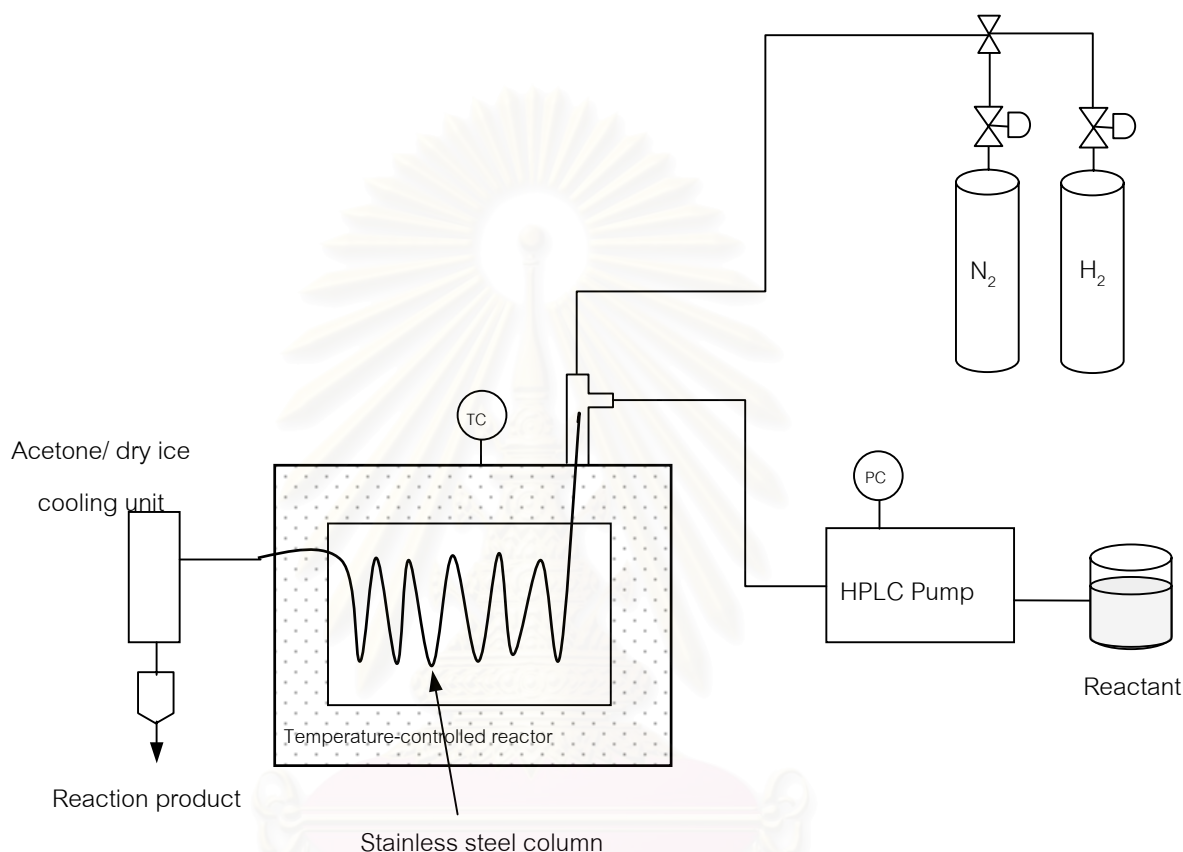


Figure 1-3-1. Reactor for continuous aromatization of *n*-hexane and natural gasoline

3.3 Aromatization procedure

All experiments were carried out in a home-built tubular reactor (Figure 1-3-1). Prior to each experiment, the catalyst was reduced *in situ* at 450 °C for 5 h under constant flow of nitrogen and hydrogen mixed gas. Subsequently, both nitrogen and hydrogen streams were removed from the system, and the reactant was continuously introduced into the top of the column at various feeding rates using a HPLC pump. The reactant volume that was fed through each column was kept constant at 48 ml in each experiment. The reactor effluent was collected in an acetone/dry ice cooling-unit and subsequently analyzed by GC and GC/MS.

3.4 Preparation of Pd/ZSM-5 catalyst

3.4.1 Preparation of 0.2%Pd/ZSM-5 catalyst

Pd/ZSM-5 catalysts were prepared by an ion-exchange technique. Aqueous solutions of palladium (II) chloride (0.0019 M, 500 ml) were vigorously stirred with 30 g of NaZSM-5 at 80 °C for 15 h. The cation-exchanged zeolite was filtered and washed with deionized water (*ca.* 1000 ml) to remove chloride ions until it tested negative with an aqueous solution of silver nitrate. Then, the zeolite catalyst was dried at 110 °C, calcined at 550 °C for 4 h, and stored as powdered form in a desiccator.

3.4.2 Preparation of 0, 0.3, and 0.5%Pd/ZSM-5 catalysts

The procedure of 3.3.1 was repeated except that aqueous solutions of palladium (II) chloride (0 M, 0.0028 M, or 0.0047 M) were used instead of an aqueous solution of palladium (II) chloride (0.0019 M).

3.5 Characterization of Pd/ZSM-5 catalyst

The Pd and S contents in each calcined Pd/ZSM-5 catalyst, as well as the SiO₂/Al₂O₃ ratio, were determined using an X-ray fluorescence spectrometer, while the structure of each calcined Pd/ZSM-5 catalysts was confirmed by an X-ray powder diffractometer.

3.6 Aromatization of *n*-hexane

3.6.1 Various effects on aromatization of *n*-hexane

3.6.1.1 Effect of Pd contents in ZSM-5 zeolite

The effects of Pd contents (0, 0.2, 0.3, and 0.5%) in ZSM-5 zeolite on both conversion and aromatic contents in reaction product of *n*-hexane were investigated at 400 °C reaction temperature and 0.4 ml/min *n*-hexane feeding rate. The Pd/ZSM-5 catalyst that gave the highest conversion and aromatic contents in reaction products was regarded as the optimum amount of Pd in ZSM-5 zeolite.

3.6.1.2 Effect of reactant feeding rate and reaction temperature

The effects of reactant feeding rate (0.4, 0.6, 0.8, and 1.0 ml/min) on both conversion and aromatic contents in reaction product of *n*-hexane over different

temperatures (300, 350, 400, and 450 °C) were studied using the optimum Pd/ZSM-5 catalyst from the Section 3.6.1.1.

3.6.2 Regeneration of spent catalyst

The catalyst was regenerated when its catalytic activity was reduced *ca.* 20%. Each spent catalyst was taken out of a tubular column and heated in a furnace at 650 °C for 10 h. After that, these regenerated catalysts were used for the determination of their S contents by an X-ray fluorescence spectrometer. Their structures were also confirmed using an X-ray powder diffractometer. Each regenerated catalyst was repacked again in a column and reduced *in situ* as mentioned in the Section 3.2, prior to each experiment.

3.6.3 Activity of regenerated catalyst

The activity of regenerated catalyst was studied, on both conversion and aromatic contents in reaction product of *n*-hexane, over different temperatures (300, 350, 400, and 450 °C) at 0.4 ml/min *n*-hexane feeding rate using the optimum Pd/ZSM-5 catalyst from the Section 3.6.1.1.

3.7 Aromatization of natural gasoline

Since the comparison of S content in fresh and regenerated catalyst of each reactant has to be made, aromatization of natural gasoline was carried out using a newly packed catalyst.

3.7.1 Various effects on aromatization of natural gasoline

3.7.1.1 Effect of Pd contents in ZSM-5 zeolite

The procedure of 3.6.1.1 was repeated except that natural gasoline was used instead of *n*-hexane.

3.7.1.2 Effect of reactant feeding rate and reaction temperature

The procedure of 3.6.1.2 was repeated except that natural gasoline was used instead of *n*-hexane.

3.7.2 Regeneration of spent catalyst

The catalyst was regenerated as described in the Section 3.6.2.

3.7.3 Activity of regenerated catalyst

The procedure of 3.6.3 was repeated except that natural gasoline was employed instead of *n*-hexane.

3.8 Characterization of products obtained from *n*-hexane and natural gasoline aromatization

The reaction products were analyzed and quantified by two techniques: (A) a Hewlett-Packard (model 6890) gas chromatograph equipped with a HP-5 capillary column (30 m × 0.32 mm i.d.) and flame ionization detector (FID); and (B) a Fisons Instruments (model 8060) gas chromatograph equipped with a HP-5 capillary column (30 m × 0.32 mm i.d.) using a Fisons Instruments (model Trio 2000) mass spectrometer as a detector.

The conditions for the characterization of products from *n*-hexane and natural gasoline aromatization are: H₂ carrier gas; 30 m × 0.32 mm i.d. fused silica column coated with a 0.25 μm film of HP-5; flame ionization detector or mass spectrometer detector; linear temperature program from 45 °C to 180 °C with heating rate of 5 °C/min).

3.9 Properties of *n*-hexane and natural gasoline

The S contents in *n*-hexane and natural gasoline were observed using an X-ray fluorescence spectrometer. Compositions of natural gasoline were analyzed and quantified as described in the Section 3.8.

CHAPTER IV

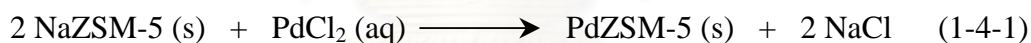
RESULTS AND DISCUSSION

4.1 Characterization of ZSM-5 zeolite

Zeolite ZSM-5 was characterized before using for the preparation of Pd/ZSM-5 catalysts by XRD and XRF techniques (XRD spectrum is shown in the Appendix 1-1A). The Si/Al ratio of 58 obtained from XRF techniques, showing that this zeolite is a high acidity zeolite.

4.2 Preparation of Pd/ZSM-5 catalyst by ion-exchange method

Pd/ZSM-5 catalysts were prepared using an ion-exchange technique. Fully hydrated NaZSM-5 zeolite, which was prepared by storing NaZSM-5 in saturated ammonium chloride (NH₄Cl₂) atmosphere for *ca.* 7 days, was ion-exchanged with aqueous solution of palladium (II) chloride. The ion-exchange reaction is shown in the Equation (1-4-1).



Preparation of 0.2% Pd/ZSM-5 catalyst was a model procedure to find the optimal ion-exchange time by vigorously stirring aqueous solutions of palladium (II) chloride (0.0013 M, 200 ml) with 8.0 g of NaZSM-5 at 80 °C for 9, 12, 15, and 18 h. Then, the cation-exchanged zeolite was filtered and washed with deionized water (*ca.* 1,000 ml) to remove chloride ions until it tested negative with an aqueous solution of silver nitrate. After that, this zeolite catalyst was dried at 110 °C, calcined at 550 °C for 4 h, and stored as powdered form in a desiccator. The concentrations of Pd in ZSM-5 zeolite were measured using XRF technique, and the results are shown in Table 1-4-1.

Table 1-4-1: Relationship between concentrations of Pd in ZSM-5 zeolite^a and various ion-exchange times

Ion-exchange time (h)	Concentration of Pd in ZSM-5 zeolite (wt%) ^b
9	0.09 ± 0.01
12	0.14 ± 0.00
15	0.17 ± 0.01
18	0.18 ± 0.01

^a Determined by X-ray fluorescence spectrometer

^b Average ± standard deviations, $n = 2$

From these data, ion-exchange time of 15 h was the optimal ion-exchange time for the preparation of Pd/ZSM-5 catalyst and was used for further Pd/ZSM-5 catalyst preparations.

4.2.1 Preparation of 0, 0.2, 0.3, and 0.5% Pd/ZSM-5 catalysts

Pd/ZSM-5 catalysts with various amounts of Pd (0, 0.2, 0.3, and 0.5%) were successfully prepared by ion-exchange techniques at 80 °C. After calcination at 550 °C, the SiO₂/Al₂O₃ ratios of all of catalysts, which were determined using an X-ray fluorescence spectrometer, were changed from 58 to 63 due to partial dealumination caused by high temperature. However, the structures of the calcined Pd/ZSM-5 catalysts, as revealed by X-ray powder diffractometer, were found to be the same as that of non-calcined ZSM-5 zeolite (XRD spectra are shown in the Appendices 1-1A and 1-2A). Moreover, the Pd contents of the exchanged catalyst, which were determined by an X-ray fluorescence spectrometer, were found close to the expected values as shown in Table 1-4-2.

Table 1-4-2: Comparison of expected values and experimental values^a of the Pd contents of the prepared catalysts

Catalyst	Expected value (wt%)	Experimental value (wt%) ^b
0% Pd/ZSM-5	0.00	0.00 ± 0.00
0.2% Pd/ZSM-5	0.20	0.17 ± 0.01
0.3% Pd/ZSM-5	0.30	0.27 ± 0.02
0.5% Pd/ZSM-5	0.50	0.46 ± 0.01

^a Determined by an X-ray fluorescence spectrometer

^b Average ± standard deviations, $n = 2$

4.3 Aromatization of *n*-hexane

4.3.1 Various effects on aromatization of *n*-hexane

4.3.1.1 Effect of Pd contents in ZSM-5 zeolite

The experiments were carried out in a home-built tubular reactor (Figure 1-3-1). The effects of Pd contents (0 to 0.5%) in ZSM-5 zeolite on both conversion and aromatic contents of *n*-hexane aromatization were investigated at 400 °C reaction temperature and 0.4 cm³/min *n*-hexane feeding rate. As seen in Figure 1-4-1, *n*-hexane conversion and aromatic contents in reaction product of all catalysts increased when Pd contents in ZSM-5 zeolite increased.

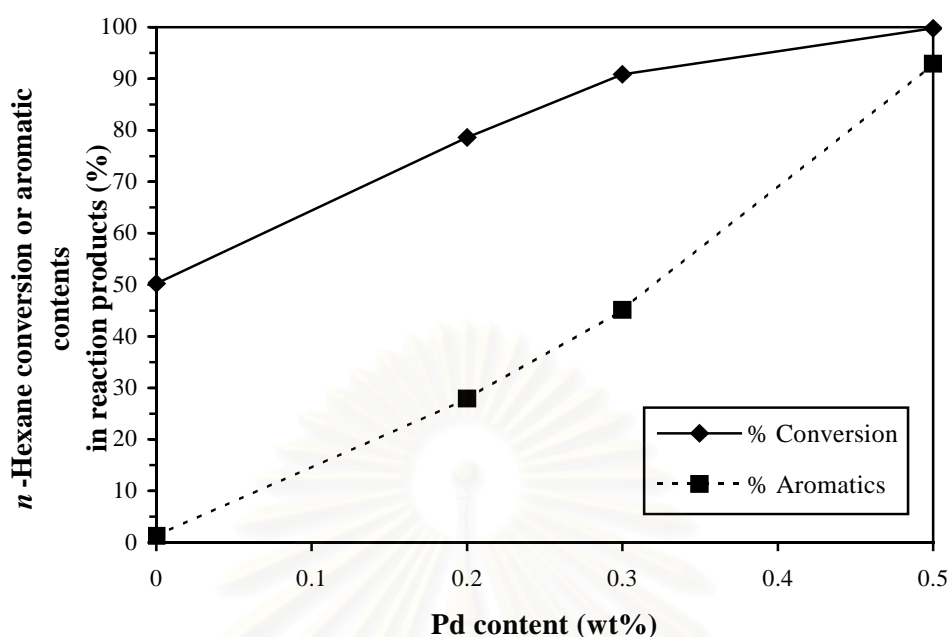


Figure 1-4-1: Effect of Pd contents in ZSM-5 zeolite on conversion and aromatic contents in reaction product of *n*-hexane aromatization. Conditions: reaction temperature, 400 °C; feeding rate, 0.4 cm³/min.

Although the *n*-hexane conversion at 0% Pd content in ZSM-5 zeolite was relatively high (50.2%), the aromatic contents in reaction product was considerably low (1.2%) (Figure 1-4-1). This might be because *n*-hexane was cracked and converted to other products, *e.g.* small hydrocarbon molecules, without oligomerization and aromatization. It can further be noticed that *n*-hexane conversion (99.7%) and aromatic contents in reaction product (92.3%) attained their corresponding maximum when using 0.5% Pd in ZSM-5 zeolite.

4.3.1.2 Effect of reactant feeding rate and reaction temperature

The effects of reactant feeding rate on both conversion and aromatic contents of *n*-hexane aromatization over different temperatures were studied (Figure 1-4-2).

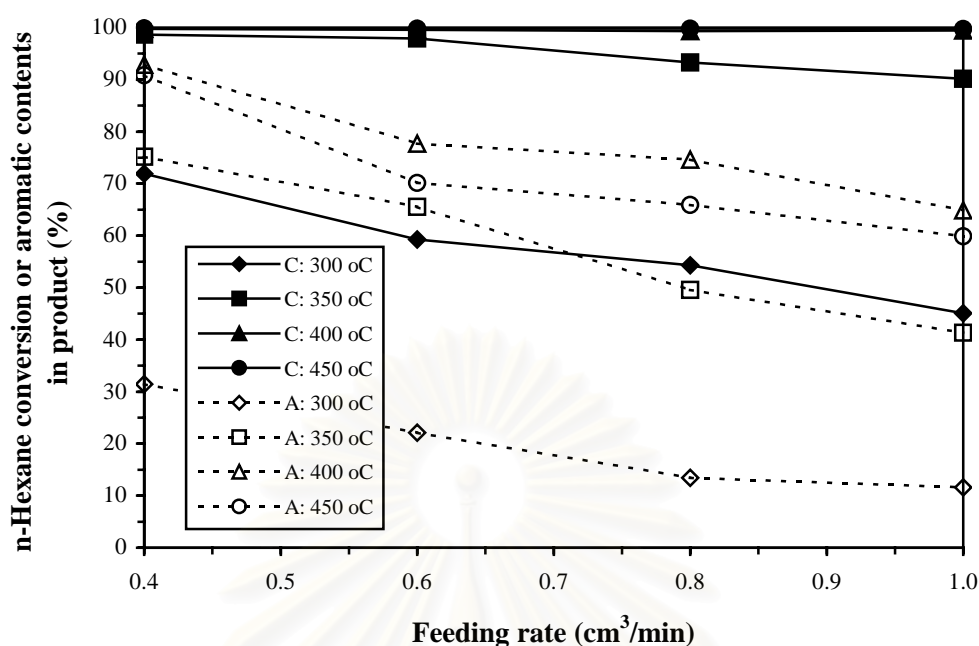


Figure 1-4-2: Effect of the feeding rate on *n*-hexane conversion and aromatic contents in reaction product over 0.5% Pd in ZSM-5 zeolite at different temperatures (C and A represent conversion and aromatic contents in reaction product, respectively).

It was found that when the reaction temperatures increased, both conversion and aromatic contents in the reaction products proportionally increased (Figure 1-4-2). However, the aromatic contents in the reaction product at 450 °C was lower than that at 400 °C (Figure 1-4-2), and this might be due to the enhanced degradation of aromatic products to small hydrocarbon molecules. Decreasing trends in their conversion and aromatic contents in the reaction products, at all reaction temperatures, were observed when the feeding rate increased (Figure 1-4-2). These results indicated that both conversion and aromatic contents in the reaction products were affected by the contact time between *n*-hexane and catalyst (Table 1-4-3).

Table 1-4-3: Contact time between reactants (*n*-hexane and natural gasoline) and catalyst at different reactant feeding rates

Reactant feeding rate (cm ³ /min)	Contact time ($\frac{V}{V_0}$, min)
0.4	79.25
0.6	52.83
0.8	39.63
1.0	31.70

The feeding rate of 0.4 cm³/min at the reaction temperature of 400 °C provided the highest *n*-hexane conversion (also highest contact time) and aromatic contents in the reaction products as compared to other conditions. For high contact time condition, *n*-hexane generally has more time to oligomerize on the acid active sites in the zeolite channels and undergo dehydrocyclization to aromatics *via* the Pd-function than that at low contact time [8,9].

4.3.1.3 Activity of regenerated catalyst

The activities of fresh and regenerated catalysts on *n*-hexane aromatization were also studied (Figure 1-4-3). The catalysts were regenerated when their activity was *ca.* 80% of fresh catalyst (after feeding 3,024 cm³ of *n*-hexane for 86 h). It was found that all catalysts showed similar increasing trends in their *n*-hexane conversion and aromatic contents when reaction temperature increased (Figure 1-4-3). Fresh catalyst generally provided higher *n*-hexane conversion and aromatic contents in reaction product than did regenerated catalysts (Figure 1-4-3). The margin 10% activity loss was observed between fresh and regenerated catalyst. The regenerated catalyst might have some carbon deposits that covered the catalyst surface, thus reducing the catalyst activity [24,39]. Considering the structures of the regenerated catalysts, as revealed by X-ray powder diffractometer, it was found to be the same as that of fresh catalyst (XRD spectra are shown in the Appendices 1-2A and 1-3A).

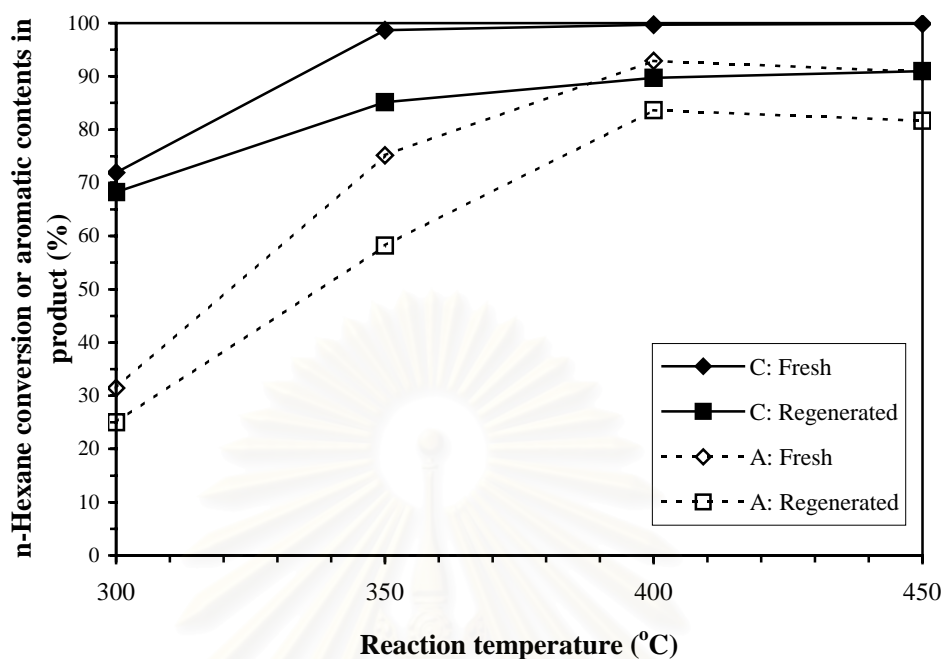


Figure 1-4-3: Comparison of activity between fresh and regenerated catalysts on *n*-hexane conversion and aromatic contents in reaction product at different temperatures. Conditions: feeding rate, 0.4 cm³/min; catalyst, 0.5% Pd in ZSM-5 zeolite (C and A represent conversion and aromatic contents in reaction product, respectively).

4.3.2 Aromatic contents in reaction product and product distributions

The aromatic contents in reaction product and product distributions of *n*-hexane were explored at the suitable conditions (reaction temperature, 400 °C; reactant feeding rate, 0.4 cm³/min; catalyst, 0.5% Pd in ZSM-5), and the results are shown in Table 1-4-4. GC and GC/MS analysis revealed that this continuous process for *n*-hexane aromatization yielded not only benzene and its derivatives but also naphthalene derivatives. Typical GC chromatogram of *n*-hexane aromatization is shown in the Appendix 1-4A. The product distributions were benzene (5.67%), toluene (23.63%), xylenes (24.97%), 4-ethyltoluene (3.50%), 1,3,5-trimethylbenzene (4.86%), 1-methylnaphthalene (4.33%), and 1,5-dimethylnaphthalene (3.57%). Among these aromatics, xylenes were obtained as the highest percentage (25.0%). When comparing among three isomers of xylene, the percentage of *p*-xylene was higher than that of *m*- and *o*-isomers (Table 1-4-4). This can be explained

theoretically by comparing pore aperture of ZSM-5 zeolite (0.54×0.56 nm and 0.51×0.55 nm) with kinetic molecular diameters of *m*-, *o*-, and *p*-isomers of xylene, which are 0.63, 0.64, and 0.57 nm, respectively [8]. On the basis of these data, only *p*-xylene possesses a certain size that could easily exit from the pore system. In addition, the slimmer shape of *p*-xylene molecule, which exhibits a rate of diffusion faster by a factor of 10^4 than the other two isomers, also explains the favor formation of *p*-xylene [23].

Table 1-4-4: Product distributions from continuous aromatization of *n*-hexane at the suitable conditions^a compared to the corresponding reactant compositions and commercial mixture of benzene, toluene, and xylene.

	<i>n</i> -Hexane		Commercial mixture of benzene, toluene, and xylene ^b
	Before aromatization ^b	After aromatization ^b	
Conversion (%)	–	99.73 ± 0.0070	–
Product distributions (%)			
Less than C ₆ hydrocarbons	2.19 ± 0.0446	6.83 ± 0.0084	7.03 ± 0.0017
Hexane	96.69 ± 0.0729	0.27 ± 0.0070	1.11 ± 0.0000
Total aromatics ^a	–	92.25 ± 0.0226	91.03 ± 0.0035
Benzene	–	5.67 ± 0.0057	6.50 ± 0.0004
Toluene	–	23.63 ± 0.0085	19.99 ± 0.0017
Xylenes	–	24.97 ± 0.1476	29.54 ± 0.0013
<i>m</i> -Xylene	–	2.17 ± 0.0082	5.19 ± 0.0000
<i>o</i> -Xylene	–	5.20 ± 0.0247	8.11 ± 0.0008
<i>p</i> -Xylene	–	17.59 ± 0.1312	16.24 ± 0.0003
4-Ethyltoluene	–	3.50 ± 0.0083	5.73 ± 0.0007
1,3,5-Trimethylbenzene	–	4.86 ± 0.0072	7.75 ± 0.0003
1-Methylnaphthalene	–	4.33 ± 0.0105	–
1,5-Dimethylnaphthalene	–	3.57 ± 0.0071	–

^a Conditions: catalyst, 0.5% Pd in ZSM-5; reaction temperature, 400 °C; feeding rate, 0.4 cm³/min

^b Average ± standard deviations, *n* = 2

On the basis of the products formed from *n*-hexane aromatization, the main reaction pathways converting *n*-hexane to aromatics may be explained as follows. Due to the bi-functional property of the Pd loaded ZSM-5, in the presence of metal and acidity, *n*-hexane is cracked to small hydrocarbon molecules and then oligomerized on the acid sites in the zeolite channels. The oligomerized products can undergo either cracking to light hydrocarbons (C₂–C₄) or dehydrocyclization to aromatics *via* the Pd-function [8,9]. At higher conversion levels (high temperature), naphthalene derivatives were formed because mononuclear aromatics might condense into polynuclear aromatics, especially naphthalene and its derivatives [8].

Under the suitable conditions (reaction temperature, 400 °C; reactant feeding rate, 0.4 cm³/min; catalyst, 0.5% Pd in ZSM-5), *n*-hexane aromatization gave higher conversion (99.7%) and aromatic contents in reaction product (92.3%) than those previously reported by Rojasova *et al.* [15], from which the conversion of 47.6% with 50.2% aromatic contents in reaction product was obtained in a batch aromatization of *n*-hexane using Zn/ZSM-5 zeolite as a catalyst. Previous works on the aromatization of alkanes were conducted in a batch system [4–15], and this present work is the first aromatization carried out using a continuous mode.

Concerning the catalyst performance (under the suitable conditions), we found that 2.28 g of the total products formed per g catalyst per h for the aromatization of *n*-hexane (or 455 g product formed per g Pd per h). This continuous aromatization process is expected to be employed for the conversion of petrochemical byproducts that contains alkane (*e.g.*, natural gasoline and light naphtha) into high-value-added products. The following experiments were performed using the eventual continuous system for the aromatization of natural gasoline, which is one of the major petrochemical byproduct from natural gas separation industry.

4.4 Aromatization of natural gasoline

4.4.1 Various effects on aromatization of natural gasoline

4.4.1.1 Effect of Pd contents in ZSM-5 zeolite

The aromatization of natural gasoline was conducted in the invented continuous system (Figure 1-3-1). The effects of Pd contents (0 to 0.5%) in ZSM-5 zeolite on both conversion and aromatic contents of natural gasoline aromatization

were investigated at 400 °C reaction temperature and 0.4 cm³/min natural gasoline feeding rate.

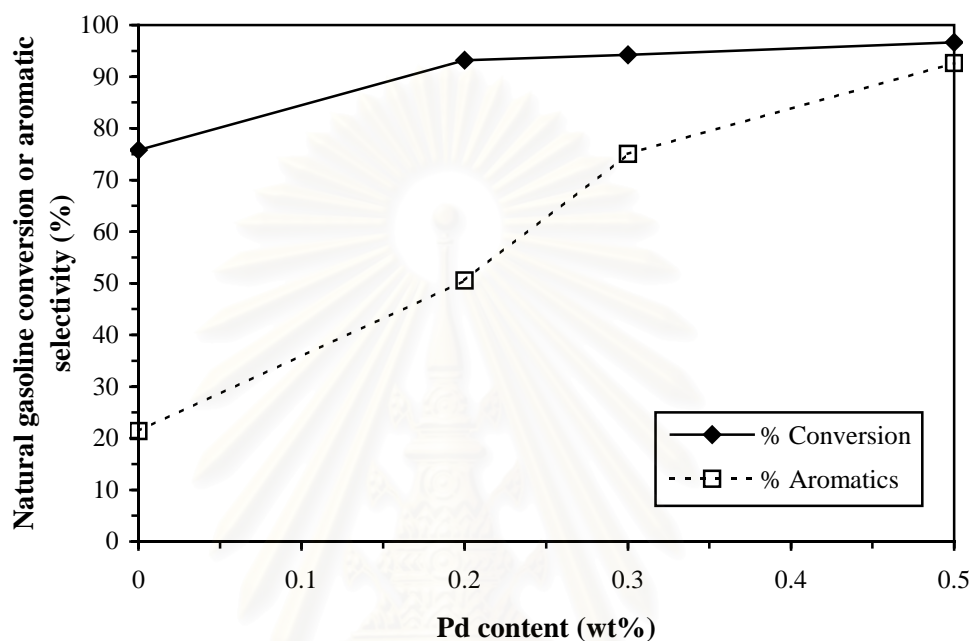


Figure 1-4-4: Effect of Pd contents in ZSM-5 zeolite on conversion and aromatic contents in reaction product of natural gasoline. Conditions: reaction temperature, 400 °C; feeding rate, 0.4 cm³/min.

Natural gasoline conversion and aromatic contents in reaction product of all catalysts increased when Pd contents in ZSM-5 zeolite increased (Figure 1-4-4). It was found that natural gasoline conversion (94.3%, calculation based on 21.57% of 2-methylbutane in natural gasoline) and aromatic contents in reaction products attained their corresponding maximum when using 0.5% Pd in ZSM-5 zeolite. It was also noticed that the effect of Pd contents in ZSM-5 zeolite on natural gasoline aromatization was similar to that of *n*-hexane aromatization.

4.4.1.2 Effect of reactant feeding rate and reaction temperature

The effects of natural gasoline feeding rate on both conversion and aromatic contents in reaction product over different temperatures were studied (Figure 1-4-5).

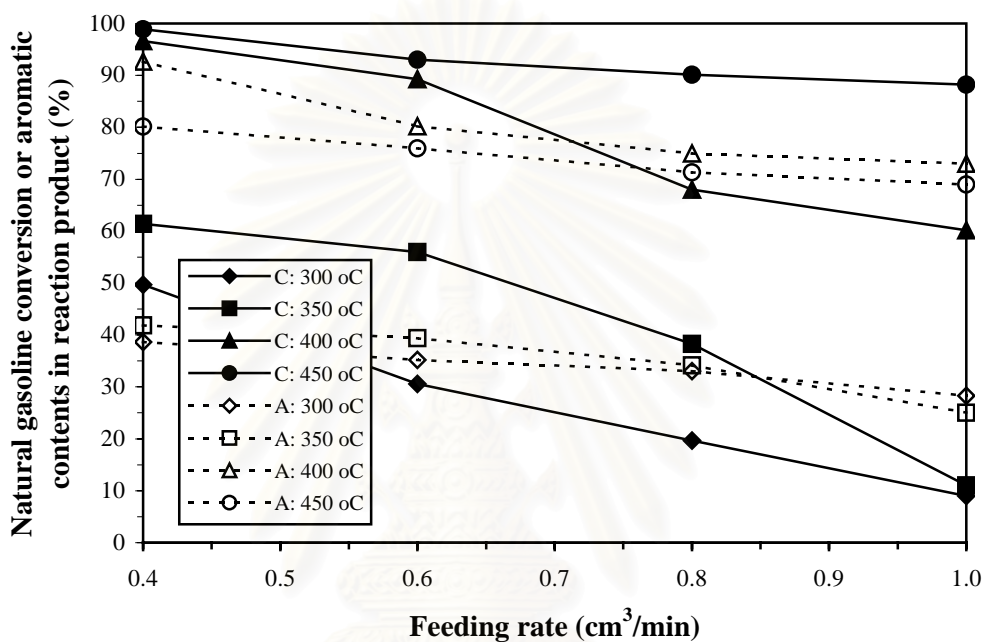


Figure 1-4-5: Effect of the feeding rate on natural gasoline conversion and aromatic contents in reaction product over 0.5% Pd in ZSM-5 zeolite at different temperatures (C and A represent conversion and aromatic contents in reaction product, respectively).

When the reaction temperature increased, both conversion and aromatic contents in reaction product proportionally increased (Figure 1-4-5). However, the aromatic contents in reaction product at 450 °C were lower than that at 400 °C (Figure 1-4-5). The feeding rate of 0.4 cm³/min at the reaction temperature of 400 °C provided the highest natural gasoline conversion. It was found that the effect of reaction temperature and reactant feeding rate on natural gasoline aromatization was also similar to that of *n*-hexane aromatization.

4.4.1.3 Activity of regenerated catalyst

The activities of fresh and regenerated catalysts on natural gasoline aromatization were studied (Figure 1-4-6). The catalysts were regenerated when their activity was *ca.* 80% of fresh catalyst (after feeding 2,160 cm³ of natural gasoline for 61 h). It was found that all catalysts showed similar increasing trends in their natural gasoline conversion and aromatic contents in reaction product (Figure 1-4-6). Fresh catalyst generally provided higher natural gasoline conversion and aromatic contents in reaction product than did regenerated catalysts (Figure 1-4-6). The margin 7% activity loss was observed between fresh and regenerated catalyst. Similarly to that of *n*-hexane, the regenerated catalyst might have some carbon deposits, thus reducing the catalyst activity [24,39].

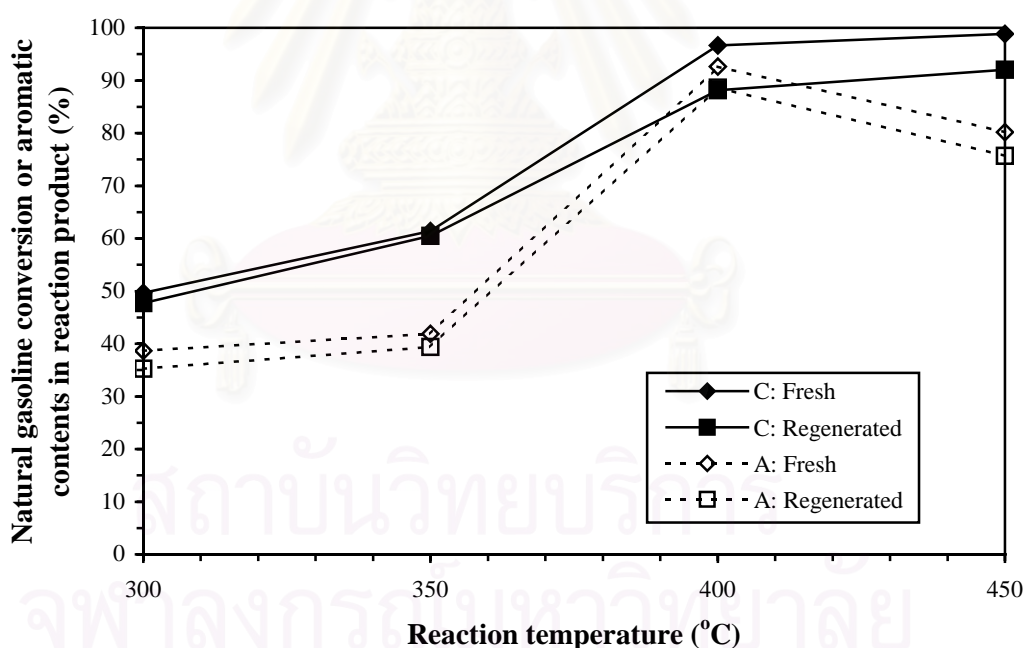


Figure 1-4-6: Comparison of activity between fresh and regenerated catalysts on natural gasoline conversion and aromatic contents in reaction product at different temperatures. Conditions: feeding rate, 0.4 cm³/min; catalyst, 0.5% Pd in ZSM-5 zeolite (C and A represent conversion and aromatic contents in reaction product, respectively).

Additionally, sulfur present in natural gasoline (0.0030 wt%, Table 1-4-5) could also deactivate the catalyst. It is known that sulfur poisoning in catalysts leads to the deactivation of catalyst performance [40]. In the suitable system, the amount (2,160 cm³) of natural gasoline (sulfur containing substrate) that caused 20% reduction of the catalyst activity was less than that (3,024 cm³) of *n*-hexane (AR grade reagent with a sulfur content less than 0.0020 wt%, Table 1-4-5), clearly demonstrating that the presence of sulfur had a negative effect to the catalytic performance.

Table 1-4-5: Sulfur contents in reactants (*n*-hexane and natural gasoline), fresh catalysts, and regenerated catalysts.

	Sulfur content (wt%) ^a
<i>n</i> -Hexane	0.0019 ± 0.0001
Natural gasoline	0.0030 ± 0.0003
Fresh catalyst before <i>n</i> -hexane aromatization	0.0180 ± 0.0028
Regenerated catalyst after <i>n</i> -hexane aromatization	0.0425 ± 0.0021
Fresh catalyst before natural gasoline aromatization	0.0180 ± 0.0028
Regenerated catalyst after natural gasoline aromatization	0.0625 ± 0.0035

^a Average ± standard deviations, *n* = 2

4.4.2 Aromatic contents in reaction product and product distributions

The aromatization of natural gasoline was conducted in the continuous system (Figure 1-3-1). It was found that the effects of Pd contents in ZSM-5 zeolite, reaction temperature and reactant feeding rate, and the activity of regenerated catalyst, on natural gasoline aromatization were similar to that of *n*-hexane aromatization. The suitable conditions for natural gasoline conversion (94.3%, calculation based on 21.57% of 2-methylbutane in natural gasoline, Figure 1-4-5) and aromatic contents in reaction product (92.6%, Figure 1-4-5) were at 400 °C reaction temperature (Figure 1-4-5) and 0.4 cm³/min natural gasoline feeding rate (Figure 1-4-5) with 0.5% Pd content in ZSM-5 catalyst (Figure 1-4-4)

Typical GC chromatogram of natural gasoline aromatization is shown in the Appendix 1-5A. GC and GC/MS analysis (Table 1-4-6) demonstrated that the present continuous aromatization of natural gasoline yielded benzene (8.08%), toluene (23.31%), xylenes (22.75%), 4-ethyltoluene (4.30%), 1,3,5-trimethylbenzene (3.65%), 1-methylnaphthalene (4.06%), and 1,5-dimethylnaphthalene (2.87%). However, similar to *n*-hexane aromatization, toluene, and xylenes were found to be the major percentage of products (23.31% and 22.75%, respectively) from the natural gasoline reaction.



สถาบันวิทยบริการ
จุฬาลงกรณ์มหาวิทยาลัย

Table 1-4-6: Product distributions from continuous aromatization of natural gasoline at the suitable conditions^a compared to the corresponding reactant compositions and commercial mixture of benzene, toluene, and xylene.

	Natural gasoline		Commercial mixture of benzene, toluene, and xylene ^b
	Before aromatization ^b	After aromatization ^b	
Conversion (%)	–	94.30 ± 0.0530	–
Product distributions (%)			
Less than C ₆ hydrocarbons	61.62 ± 0.0328 ^c	5.32 ± 0.0131	7.03 ± 0.0017
Hexane	6.54 ± 0.0047	0.30 ± 0.0044	1.11 ± 0.0000
Total aromatics	27.34 ± 0.0275	92.64 ± 0.0241	91.03 ± 0.0035
Benzene	8.24 ± 0.0018	8.08 ± 0.0113	6.50 ± 0.0004
Toluene	3.29 ± 0.0046	23.31 ± 0.0077	19.99 ± 0.0017
Xylenes	1.28 ± 0.0030	22.75 ± 0.0220	29.54 ± 0.0013
<i>m</i> -Xylene	–	3.31 ± 0.0026	5.19 ± 0.0000
<i>o</i> -Xylene	0.22 ± 0.0070	4.45 ± 0.0167	8.11 ± 0.0008
<i>p</i> -Xylene	1.06 ± 0.0039	14.99 ± 0.0079	16.24 ± 0.0003
4-Ethyltoluene	–	4.30 ± 0.0028	5.73 ± 0.0007
1,3,5-Trimethylbenzene	–	3.65 ± 0.0034	7.75 ± 0.0003
1-Methylnaphthalene	–	4.06 ± 0.0167	–
1,5-Dimethylnaphthalene	–	2.87 ± 0.0230	–

^a Conditions: catalyst, 0.5% Pd in ZSM-5; reaction temperature, 400 °C; feeding rate, 0.4 cm³/min

^b Average ± standard deviations, *n* = 2

^c Compositions of less than C₆ hydrocarbons in natural gasoline were 2-methylpropane (0.25%), *n*-butane (2.25%), 2,2-dimethylpropane (0.06%), 2-methylbutane (21.57%), *n*-pentane (20.07%), 2,2-dimethylbutane (0.82%), cyclopentane (1.50%), 2,3-dimethylbutane (1.99%), 2-methylpentane (8.64%), and 3-methylpentane (4.47%).

Concerning the catalyst performance (under the suitable conditions), we found that 2.23 g of the total products formed per g catalyst per h for the aromatization of natural gasoline (or 446 g product formed per g Pd per h). The above experiments

provided the evidence that this continuous aromatization process may be applied for the conversion of petroleum byproduct into high value-added products.



สถาบันวิทยบริการ
จุฬาลงกรณ์มหาวิทยาลัย

CHAPTER V

CONCLUSION

The model process for the production of aromatic hydrocarbons using *n*-hexane as a model substrate was successfully performed over Pd-loaded ZSM-5 zeolite in a continuous mode. The suitable conditions were at 0.5% Pd content in ZSM-5, 400 °C reaction temperature, and 0.4 cm³/min reactant feeding rate, providing *n*-hexane conversion and aromatic contents in reaction product at 99.7% and 92.3%, respectively. GC and GC/MS analysis revealed that this *n*-hexane aromatization preferably yielded benzene and naphthalene derivatives, including benzene (5.67%), toluene (23.63%), xylenes (24.97%), 4-ethyltoluene (3.50%), 1,3,5-trimethylbenzene (4.86%), 1-methylnaphthalene (4.33%), and 1,5-dimethylnaphthalene (3.57%).

Under the same reaction conditions, natural gasoline gave 94.3% conversion and 92.6% aromatic contents in reaction product, and the aromatization products were benzene (8.08%), toluene (23.31%), xylenes (22.75%), 4-ethyltoluene (4.30%), 1,3,5-trimethylbenzene (3.65%), 1-methylnaphthalene (4.06%), and 1,5-dimethylnaphthalene (2.87%).

Up to date, there have been only few applications in turning natural gasoline into other useful products, besides burnt out as fuel. The present work demonstrated that the continuous process for the aromatization of natural gasoline might be another option for the conversion of natural gasoline into high value-added products.

สถาบันวิทยบริการ
จุฬาลงกรณ์มหาวิทยาลัย



PART II

OXIDATION OF PHENOL ON FIXED BED OF ACTIVE CARBON

สถาบันวิทยบริการ
จุฬาลงกรณ์มหาวิทยาลัย

CHAPTER I

INTRODUCTION

The increasing release of concentrated toxic organic pollutants contained in many industrial end stream effluents has been the driving force for developing alternative effluent treatments prior to their discharge to conventional biofilters or sewage plants. Incineration though widely used in industry for simplicity may be a hazardous process depending on the nature of pollutants and is always expensive as far as organic pollution is not very concentrated to produce the energy for water vaporisation. A suitable solution to the destruction of rather dilute organic pollutants is catalytic wet air oxidation (CWAO) that provides milder operating conditions and more attractive process economics than wet air oxidation. It is noteworthy that catalysts with improved stability for CWAO have been recently developed based on either noble metals or mixed oxides.

On the other hand, activated carbon (AC) as catalyst is a promising low price alternative for the remediation of phenol and various substituted phenols due to its proven high adsorption capacity and oxidation activity at low oxygen pressures. By employing AC, unit operations of adsorption and chemical reaction are naturally combined in an adsorptive oxidation reactor (AD-OX process). Moreover, CWAO over AC becomes especially attractive when integrated with biological end-treatments. Such processes provide a superior cleaning effectiveness compared to single step oxidation and avoid the need of complete organic pollutant mineralisation, which is difficult to obtain with CWAO alone.

Given the range of liquid flow rates commonly to be treated, continuous reactor operation should be considered in industrial CWAO applications. Within the category of common gas-liquid-solid catalytic reactors, fixed bed reactors are more convenient than slurry or fluidised bed reactors to carry out CWAO studies, as they provide both higher catalyst loading and close to plug flow operation.

Three phase fixed bed catalytic reactors are most often operated with cocurrent gas and liquid flow. Downflow operation in trickle bed reactors is widely used in many industrial applications especially in petrochemistry but also in biotechnology. Upflow reactors or flooded beds are less frequently used, but they may have some

advantages concerning liquid distribution and thermal stability. These two flow modes have yet been compared at LGC Toulouse for selective hydrogenation, proving the flooded bed to perform better conversions and selectivities.

In the case of phenol oxidation trickle bed could have determining advantage due to its smaller liquid hold-up at low liquid flow rate as many aromatic pollutants show a high ability to undergo homogeneous condensation reactions in the liquid phase *via* oxidative coupling. These unwanted side reactions could lead to fast catalyst deactivation due to irreversible adsorption or deposition of the condensation products on AC particles.

The present work is aimed at developing and modelling a continuous process for the CWAO of phenol using AC as catalyst. Optimal operation conditions including temperature, pressure, reaction time, air flow rate, and upflow or downflow mode are to be found.

In order to involve complex heat and mass transfers coupling phenomena as in large industrial reactors, a three phase fixed bed of intermediate scale will be operated and modelled for subsequent scale up.

Objectives of this research

The objectives of this research are aimed at

- (a) thoroughly investigating the CWAO of phenol over AC in a pilot scale fixed bed reactor;
- (b) providing qualitative and quantitative analyses of the reaction products;
- (c) finding convenient reaction conditions in order to obtain the highest phenol degradation.
- (d) modelling the continuous reaction process at pellet and reactor scales, where hydrodynamics, heat and mass transfers interfere with reaction kinetics.

CHAPTER II

THEORY AND LITERATURE REVIEW

2.1 Wastewater treatment

Pollution control of aquatic environments is of primary concern, especially in regions where water is not easily available. New legislation is progressively imposing more stringent environmental constraints for the discharge of industrial aqueous effluents. Thus, wastewater reduction and treatment is increasingly gaining more attention. In the actuality, chemical and related industries generate large quantities of wastewater containing organic compounds, such as phenol and derivatives, which are poorly biodegradable or even toxic for the microorganisms [1].

Phenol and substituted phenols are commonly present in industrial waste streams especially in industrial wastewater from oil refineries, coal conversion plants, petrochemicals, polymeric resins, coal tar distillation, pharmaceuticals, *etc.* [2]. Phenol concentration in the range of 0.05 g/l causes a rapid decline of the active biomass due to the inhibition of reproduction of microorganism, and the concentration exceeding 1 g/l even leads to their total destruction [3]. Generally, the most common depolluting technology for wastewater is the conventional biological treatment [4]. However, direct biological treatment is not advisable for wastewater stream having phenol concentration more than 0.5 g/l [4]. Alternative methods have been developed for the remediation of these effluents; the most important are the adsorption on activated carbon, the thermal incineration, and the liquid phase chemical oxidation. Adsorption on activated carbon is very effective for a broad range of organic pollutants [4]. Nevertheless, it requires an additional step of regeneration of the adsorbent during which the pollutant is usually transferred to a vapor or an organic phase. In this step, pollution is generally concentrated but not converted to less hazardous materials [5]. Incineration is the other well-established technology for the treatment of concentrated and toxic organic waste streams. Organic pollutants are burnt at atmospheric pressure and high temperatures between 1,000 °C and 1,700 °C. Thus, incineration can offer almost complete pollutant destruction, although at very high energy costs, because an organic load above 25% is necessary to guarantee

autothermal oxidation. Furthermore, this technique has been accused for the emission of toxic byproducts such as dioxins and furans [4].

Wet Air liquid phase Oxidation process is known to have a great potential in advance wastewater treatment facilities by destroying the pollutant while being dissolved in the liquid phase [4,6]. Several emerging liquid phase oxidation methods can be distinguished in terms of the different oxidants, catalysts and operating conditions selected. However, for the non-catalytic process, the reaction conditions required to achieve oxidation are severe, typically being in the range of temperature of 200 to 300 °C and pressure of 70 to 130 atm [7]. Under such extreme conditions, the selection of material for construction becomes critical, as corrosion rates are rather high due to the presence of a variety of oxygenated compounds. Oxidation of dilute aqueous solutions of organic pollutants over a solid catalyst offers an alternative to non-catalytic wet air oxidation as means of purifying of wastewater [8]. In this process organics are oxidized to carbon dioxide and water at relatively mild temperatures and pressures: less than 200 °C and 100 bar [5].

The incorporation of a catalyst has also been considered in combination with all types of oxidants (air, oxygen, hydrogen peroxide, and ozone) aiming to reduce the operating temperature and pressure, and to treat pollutants that cannot be destroyed during non-catalytic liquid phase oxidation processes. Homogeneous catalysts, such as copper ions in solution, were very effective in oxidizing several organics when air was used as oxidant [9]. Nevertheless, the addition of a homogeneous catalyst has the inherent disadvantage of the posterior catalyst removal from the treated effluent, because the metal ions are pollutants themselves in the range of concentrations used. Heterogeneous catalysts, on the other hand, do not need any extra separation step and are thus more attractive. Solid catalysts, mostly noble metals and base metal oxides, have been tested in combination with all types of oxidants. Less frequently, active carbon (AC) also has been chosen as a catalyst without any additional active phase [1,10–13]. The incorporation of heterogeneous catalysts has exhibited promising results in laboratory tests, but industrial applications have been hindered because of the lack of stable catalytic performance over sufficiently long periods.

2.2 Wet air oxidation fundamentals

Wet Air Oxidation (WAO) process, first developed and applied as a commercial process by Zimmerman and Diddams [14,15], is an effective destruction method for the treatment of hazardous organic wastes, especially when these are too dilute to incinerate or too toxic to biotreat [16]. WAO is a process by which components are oxidized in a liquid phase by oxygen. The process takes place at elevated pressures, to enhance the solubility of oxygen in the aqueous solution and to keep water in the liquid phase, and at elevated temperatures to make possible a rapid reaction. In this process, the organic waste is oxidized to carbon dioxide, water, and intermediate oxidation products that are predominantly low molecular weight organic compounds including carboxylic acids, acetaldehydes, and alcohols. Although the degree of oxidation depends upon the process conditions, retention time, and feed composition, in most operations low molecular weight compounds will accumulate as they tend to be refractory to further oxidation [17]. An advantage of WAO is that the majority of contaminants remain in the aqueous phase. The final aqueous liquid effluent will contain a considerable quantity of low molecular weight organics, ammonia (from nitrogen-containing compounds), inorganic acids (from elemental sulphur or phosphorus), and inorganic salts (from elemental sulphur or phosphorus). This effluent is usually biologically treated, allowing the majority of organics and ammonia to be removed. WAO has successfully been used to treat a range of industrial wastewaters including pulp and paper mill black liquor wastes, spent caustic scrubbing liquids, and cyanide/nitrile bearing wastes such as acrylonitrile plant wastewater. Still, most of the installed wet air oxidation units are used for the treatment of sewage sludge. [18,19].

2.3 Catalytic Wet Air Oxidation catalysts

Although Catalytic Wet Air Oxidation (CWAO) processes have not been yet as widely implemented as WAO, they have received special research efforts to develop active and stable catalyst.

The heterogeneous catalysts that have been employed in CWAO can be divided into three major groups, *i.e.* supported noble metals, metal oxides, and active carbon.

2.3.1 Noble metals

The use of noble metals catalysts has been shown to enhance the reaction rate in wet air oxidation processes. The most frequent uses for noble metals are Pt and Ru, while Pd, Ir, and Rh have also been tested. Applications of noble metal catalysts in the CWAO are summarized in Table 2-2-1.

Table 2-2-1: The applications of noble metal catalysts in the CWAO

Noble metal	Support	Substrate	T (°C)	P _T (bar)	Reference
Pt	TiO ₂	phenol	150–205	45	[20]
Pt	γ-Al ₂ O ₃	phenol	155–200	20	[21]
Pt, Pd, Ru	C	phenol	120–160	50–80	[22]
Pt, Ag	MnO ₂ , CeO ₂	phenol	80–130	5 (P _{O2})	[23]
Ru	C	phenol, acrylic acid	160	20	[24]
Ru	TiO ₂	phenol	175–200	3.4–13.8	[25]
Ru	CeO ₂	phenol	200	10	[26]
Pt-Ru	C	phenol	35–60	-	[27]
Pt	C	<i>p</i> -chlorophenol	170	26 (P _{O2})	[28]
Pt	C	low MW carboxylic acid	200	6.9 (P _{O2})	[29]
Ru, Ir, Pd, Ag	CeO ₂ , TiO ₂ , ZrO ₂	acetic acid	200	20	[30]
Ru	TiO ₂	carboxylic acid	150–200	50	[31]
Pt	γ-Al ₂ O ₃ , resin	carboxylic acid	80	1 (P _{O2})	[32]

From Table 2-2-1, numerous noble metal catalysts are available for the CWAO, however the optimum metal depends on the pollutant that is considered. In the case of acetic acid oxidation, Barbier *et al.* [30] reported that the catalytic activity decreases in the order Ru > Ir > Pd, while for the oxidation of *p*-chlorophenol, Qin *et al.* [28] found out that catalytic activity decreases in a reverse order Pt > Pd > Ru. The noble metal support also influences significantly on the catalyst performance.

Metal oxides, *e.g.* alumina, ceria, titania, and zirconia, as well as active carbon or high specific area graphite, have been mainly studied [4].

2.3.2 Metal oxides

Pure or mixed metal oxides also provided high efficiency to catalyze wet air oxidation processes.

The catalytic activity of metal oxides during phenol oxidation showed the following typical order: $\text{CuO} > \text{CoO} > \text{Cr}_2\text{O}_3 > \text{NiO} > \text{MnO}_2 > \text{Fe}_2\text{O}_3 > \text{YO}_2 > \text{Cd}_2\text{O}_3 > \text{ZnO} > \text{TiO}_2 > \text{Bi}_2\text{O}_3$ [33,34].

Copper oxide, alone or combined with other oxides, has thus received special attention in the CWAO of aqueous effluents oxidation [35–39]. A commercial Harshaw Cu-0803 T1/8 catalyst, comprising 10% copper oxide supported over $\gamma\text{-Al}_2\text{O}_3$, was successfully investigated for phenol oxidation [35–37]. Baldi *et al.* [39] tested a commercial CuO/ZnO catalyst to oxidize formic acid.

Mixtures of metal oxides often exhibited greater activity than the single oxide. Pintar and Levec [40] reported that CuO/ZnO/ $\gamma\text{-Al}_2\text{O}_3$ catalyst (42/47/10 wt%) and CuO-ZnO-CoO catalyst (9.3/6.9/1.4 wt%) supported on steam-treated porous cement are more effective for phenol oxidation and more stable in a hot oxidizing phenolic aqueous solution than a catalyst containing 10% CuO on $\gamma\text{-Al}_2\text{O}_3$ used in earlier works [35]. Kochetkova *et al.* [41] also observed that a mixture of CuO-CoO-TiO₂/Al₂O₃ oxides on a cement carrier provided more activity and stability, in the oxidation of phenol in aqueous solutions below 200 °C, than supported CuO/ $\gamma\text{-Al}_2\text{O}_3$. Other metal mixed oxide catalysts, not based on copper, have also been successfully tested to oxidize organic compounds, like manganese-ceria mixed oxides [42].

2.3.3 Active carbon

Active Carbon (AC) has most often been used as a support for active metal dedicated to CWAO. It is well known that AC alone can perform as a true catalyst for several reactions [13,43]. However, the potential of AC, in the absence of an active metal, as direct catalytic material for CWAO has only been recently proved for the destruction of phenol and other bio-toxic compounds [10,43,44]. It is noticeable that AC can perform better activity than other supported catalysts based on transition

metals in the oxidation of phenol [10]. This better performance could be due to the phenol adsorption capacity of the AC that may enhance the oxidation environment conditions. Nevertheless, the performance of different ACs can be significantly different [44], which strongly suggests that not only adsorption but also other specific characteristics of the ACs affect their behaviors in the CWAO. In all the above studies using AC [10,43,44], the only compound tested was phenol and less attention was devoted to other organic compounds.

The underlying mechanisms that are responsible for the catalytic activity of AC in CWAO are far from being well understood. The most important conclusion is that the phenol oxidation over AC seems to proceed through the formation of a carbonaceous layer on the AC surface. Indeed, it has been reported that during the CWAO of phenol over powdered AC in a semi batch slurry reactor it was impossible to balance the total carbon mass over the liquid and gas phase: only a certain quantity of the destroyed phenol was found as intermediate products in the liquid phase, or end product carbon dioxide [1]. Related trickle bed reactor studies using AC at 140°C and oxygen partial pressure ranging from 0.1 to 0.9 MPa showed an initial increase of the AC weight of 20% at 0.9 MPa. Then, the AC weight (as well as the phenol conversion) continuously decreased to result in a loss of 33% after 10 days [44]. In the same run, a final reduction of the initial AC surface area of about 63% occurred, most probably due to blockage of micropores by some organic deposit.

A possible explanation of these results can be deduced from related studies. Active carbon is known to catalyze other reactions, like the oxidative dehydrogenation of ethylbenzene [45–47]. For these reactions, the AC surface functional groups oxidize the substrate and are consequently reoxidized by oxygen in a redox cycle, in which the functional groups present on the AC surface participate. In the gas phase oxydehydrogenation of ethylbenzene over AC, Pereira *et al.* [45–47] observed conversion and AC weight evolution in three-day long runs that are similar to the trends observed by Fortuny *et al.* [44] for the CWAO of phenol. The former authors reported the initial formation of coke deposit in the AC surface and found out by measurements of the total and micropore surface area that the formed coke layer completely blocked the micropores of AC. An elemental analysis of their carbons samples indicated a temporal change in its composition, *i.e.* a decrease of carbon content with a corresponding increase of oxygen and hydrogen at higher run times.

Due to this composition change of the coke layer, the rate of gasification progressively became dominant, as the new oxygen containing surface groups formed with run time were shown by TPO analysis to be only effective in the coke gasification but not in its formation. Milder conditions of oxygen pressure and temperature delayed, but not avoided, both the consumption of AC and the shift of active surface groups to groups not available for the organic redox cycle. In the case of the phenol oxidation, the application of milder conditions (lower oxygen pressure) also had a positive effect on AC weight, as shown in Table 2-2-2, although in this case the activity towards phenol oxidation remained practically constant over 10 days.

Table 2-2-2: Influence of the oxygen partial pressure on the carbon consumption [44].

P _{O2} (bar)	1	2	4	9
Weight consumption (%) ^a	-18	-3	16	33

^aWith respect to the initially active carbon loaded.

Two additional trickle bed reactor runs of phenol oxidation were conducted at 0.9 MPa using either air with a phenol free feed or pure nitrogen with a phenol feed. Without phenol fed to the reactor, the combustion rate of AC is greatly enhanced, leading to its total consumption after nine-day running. In the absence of oxygen, the phenol conversion dropped rapidly to zero after the adsorption step and no intermediates were found in the reactor effluent. Apparently, the oxygen containing surface groups of the AC alone are not capable of oxidizing the adsorbed phenol in significant quantities. Given that there are similarities between the findings of the work of Pereira *et al.* [45–47] and Fortuny [44], the assumption of the formation of a coke-like layer and its participation in the liquid phase oxidation of phenol seems to be reasonable. According to the work on the oxidative dehydrogenation of ethylbenzene, a redox cycle can be figured out to take place on the formed coke layer. However, differences certainly will arise compared to the oxidative dehydrogenation of ethylbenzene, because the oxidation of phenol is carried out in the liquid phase and seems to follow a much more complex mechanisms. For instance, the rate of combustion of the AC is greatly enhanced in the liquid phase and the adsorption of water on the AC surface also should play an important role in the coke formation during the CWAO of phenol.

2.4 Industrial application of Wet Air Oxidation

Some industrial applications, as summarized by Luck [48] and Kolaczowski *et al.* [49], are given in Table 2-2-3. The major differences between each process are the reactor type used and the incorporation, or not, of a catalyst.

Table 2-2-3: Industrial processes of wet air oxidation

Process	Waste type	No. Plants	Reactor Type	T (°C)	P (MPa)	Catalyst
<i>1) Non-catalytic system</i>						
Zimpro	sewage sludge,	200	bubble column	150–250	2–12	none
	spent AC	20		200–250	2–12	
	regeneration,					
	industrial	50				
Wetox	N/A ^a	N/A	stirred tanks	200–250	4	none
Vertech	sewage sludge	1	deep shaft	< 280	8.5–11	none
Kenox	N/A	N/A	recirculation	< 240	4.5	none
			reactors			
Oxyget	N/A	N/A	tubular jet	< 300	N/A	none
<i>2) Catalytic system</i>						
<i>2a) Homogeneous catalyst</i>						
Bayer	industrial	>1	bubble column	< 200	5–20	Fe ²⁺
Loprox ^b						
<i>2b) Heterogeneous catalyst</i>						
NS-LC	N/A	N/A	monolith	220	4	Pt–Pd/ TiO ₂ –ZrO ₂
Osaka Gas	coal gasifier,	N/A	slurry bubble	250	7	ZrO ₂ or TiO ₂
	coke oven,		column			with noble
	cyanide,					or basic
	sewage sludge					metals

^a Not available

^b This process uses organic quinone substances to generate hydrogen peroxide.

For the heterogeneous CWAO process, in Japan, two CWAO technologies have been developed in the late eighty's by Nippon Shokubai (NS-LC process) and Osaka Gas. Both processes rely on heterogeneous catalysts based on precious metals

deposited on titania or titania-zirconia carriers. Compared to standard wet oxidation, these processes are able to oxidize two refractory compounds, both acetic acid and ammonia, thus allowing direct discharge of treated water or reuse as industrial water [48].

2.4.1 NS-LC process

The NS-LC process involves a Pt-Pd/TiO₂-ZrO₂ honeycomb catalyst. Two-phase flow in vertical monoliths gives in a broad range of gas-liquid velocities a very beneficial flow pattern, the slug flow (segmented gas-liquid flow). Since each liquid plug is sandwiched between two gas plugs, a recirculation pattern is developed within each liquid plug, which significantly improves mass transfer and prevents solids deposition. In addition, a thin liquid film is formed between the gas and the channel wall, which allows high mass transfer rates while keeping the catalyst continuously wetted. Typical operating conditions of the NS-LC process are at temperature of 220 °C, pressure of 4 MPa, and space velocity of 2 h⁻¹. In these conditions the oxidation of compounds such as phenol, formaldehyde, acetic acid, glucose, *etc.* reaches or exceeds 99%. In the absence of catalyst the removal efficiencies would be limited to 5–50% [48,49].

2.4.2 Osaka Gas process

The Osaka Gas CWO process is based on a mixture of precious and base metals (such as iron, cobalt, nickel, ruthenium, palladium, platinum, copper, and gold) on titania or titania-zirconia carriers (honeycomb or spheres). The operating conditions including temperature, pressure, and initial pH vary depending on the composition of the waste and required destruction efficiency, with the catalyst retaining activity for a long service life. For example, in the treatment of gas liquor wastewater from coke ovens over 11,000 h of continuous operation was obtained at 250 °C and 6.86 MPa, with no change in catalytic activity. After a residence time of 24 min the waste was decomposed from an initial chemical oxygen demand (COD) of 5870 g/l to a value of less than 10 mg/l. Further, the process can be used to destroy a variety of wastewaters and sludge including sewage sludge, ammonium nitrate wastewater, domestic wastes, and pharmaceutical waste. In addition, catalysts used for the treatment of various nitrogen containing compounds (*e.g.* ammonia,

ammonium salts and nitrates) will achieve a virtually complete conversion of nitrogen content to nitrogen gas [48,49].

Given the range of liquid flow rates commonly to be treated, continuous reactor operation should be considered in industrial CWAO applications. Within the category of common gas-liquid-solid catalytic reactors, Fixed Bed Reactors have been preferred over slurry or fluidised bed reactors to carry out recent CWAO studies [1,10,11,40,44].

2.5 Three phase fixed-bed reactors

2.5.1 Introduction

In this type of reactor, the two fluid phases move over a stationary bed of catalyst particles. The various modes of operation of fixed bed reactors are (a) cocurrent downflow of both gas and liquid, (b) cocurrent upflow of both gas and liquid, and (c) downflow of liquid and countercurrent upflow of gas. These operations are schematically shown in Figure 2-2-1. The reactor, in which liquid and gas flow downward (Figure 2-2-1a), is referred to as a trickle bed reactor [50]. On the other hand, a reactor with cocurrent upflow of gas and liquid (Figure 2-2-1c) is generally referred to as a packed bubble-bed reactor [51]. The upflow configuration is used sparingly in industrial practice where trickle bed reactor is prevailed [52], because of its relative lower pressure drop and the absence of flooding [53].

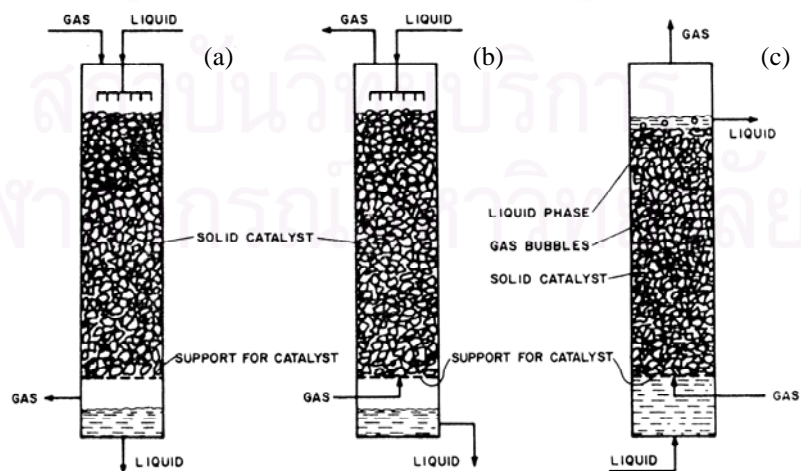


Figure 2-2-1: Schematic diagrams of three-phase packed-bed reactors

(After Ramachandran and Chaudhari [54])

Among the three-phase gas-liquid-solid reaction systems encountered in industrial practice, trickle bed reactors (TBRs) are the most widely used. They are employed in petroleum, petrochemicals and chemical industries, in waste treatment, and in biochemical and electrochemical processing, as well as other applications. Table 2-2-4 lists some of the processes which are carried out in this reactor.

Table 2-2-4 Some examples of reactions carried out in trickle bed reactors

-
1. Hydrocracking for production of high-quality middle distillate fuels [55]
 2. Sweetening of diesel, kerosene, jet fuels, and heating oils [55]
 3. Hydrogenation: of glucose to sorbitol [56], butadiene to butene [57], from benzene to cyclohexane [58], and α -methylstyrene to cumene [59]
 4. Oxidation: of formic acid [60], acetic acid [61], and ethanol [62]
-

A comparison between the cocurrent upflow and the cocurrent downflow reactor is shown in Table 2-2-5. This comparison shows that the upflow reactor gives higher mixing (both radial and axial), higher gas-liquid mass-transfer coefficients, higher liquid holdup, better liquid distribution, better heat transfer between liquid and solid and to reactor wall, less solids plugging, and, sometimes better aging of the catalyst than the downflow reactor under equivalent flow conditions. However, it is also reported to give higher pressure drop, poorer conversion (due to axial mixing), more homogeneous reactions (higher liquid-to-solid ratio), larger catalyst attrition (due to lower mechanical stability of the bed), and more intraparticle diffusional effects than downflow operation (due to full internal wetting; nevertheless full internal wetting is the most common situation in both reactors due to capillarity).

Partial external wetting may occur in downflow mode, especially at low liquid flow rate. It may have very important positive effect when the reaction process is limited by mass transfer of the gaseous reagent due to fast direct gas particle transfer. On the contrary when the main mass transfer limitation concerns the liquid reagent, partial wetting will have negative effects due to less solid liquid area.

Table 2-2-5: Upflow versus downflow cocurrent fixed bed reactors according to [63]

Upflow versus downflow cocurrent fixed bed reactors

1. Larger pressure drop in an upflow reactor
 2. Better mixing in an upflow reactor. This may give better heat transfer, but larger axial mixing would give poorer conversion in an upflow reactor.
 3. At low flow rates upflow behaves like a bubble column, *i.e.*, gas as a dispersed phase, liquid as a continuous phase. In downflow trickle bed operation, gas is a continuous phase and liquid flows as a film.
 4. High pressure drop in an upflow reactor would cause significant drop in partial pressure of the reactant across the length of the reactor.
 5. Under similar flow conditions, a higher gas-liquid mass-transfer coefficient is obtained in an upflow operation than in downflow operation.
 6. High liquid holdup and liquid-to-solid ratio in an upflow reactor.
 7. At low liquid flow rate, upflow will provide better liquid distribution of liquid, and, in many cases, better performance of the reactor than the downflow reactor under similar operating conditions.
 8. If the reaction is rapid and highly exothermic, heat transfer between liquid and solid is more effective in an upflow reactor.
 9. In an upflow reactor, the catalyst must be kept in place by suitable mechanical methods; otherwise the bed will be fluidized. In a downflow reactor, the catalyst is held in place tightly by the flow.
 10. In an upflow reactor, the catalyst pores are more likely to be filled completely with liquid than in a downflow reactor. The catalyst effectiveness factor is lower when the catalyst pores are completely filled with liquid compared to the case when they are only partially filled with liquid.
 11. Better sweeping of the catalyst by liquid in an upflow reactor may sometimes give better aging of the catalyst. If the solid reactant were used (*e.g.*, coal liquefaction), an upflow would therefore cause less solid plugging problems than in the downflow operation.
 12. In an upflow reactor, flooding may be a problem.
-

2.5.2 Hydrodynamics of cocurrent gas-liquid fixed bed reactor

2.5.2.1 Flow regimes

2.5.2.1.1 Flow regimes of cocurrent downflow fixed bed reactor

For cocurrent gas-liquid downflow over a packed bed, various flow regimes such as trickle-flow (gas continuous), pulse flow, spray flow, and bubble flow (liquid continuous), can be obtained, depending upon the gas and liquid flow rates, the nature and size of packing, the properties of the liquid and gas. Hernandez [57] classified flow regimes of cocurrent downflow fixed bed reactor into two main categories:

a) The poor interaction regime

This regime, which is also referred to the *gas continuous flow regime* or *trickle flow regime*, is obtained for the low gas and liquid flow rates. The liquid flows over the packing in the shape of films, rivulets, and drops, while the continuous gas phase flows in the center core of the catalyst bed [63,64]. In this regime, the flow in one phase is not significantly affected by the flow in the other phase. The catalyst can be partially externally wetted at low liquid velocities leading to hot spot problem, which is resulted from bad heat evacuation from exothermic reaction. When the liquid flow rate is increased, the catalyst will become completely externally wetted with the liquid film.

b) The high interaction regime

This flow regime, in which significant interaction between gas and liquid exists, is composed of many types of flow. For the non-foaming systems, the flow regimes can be classified into three categories:

- *pulse flow* occurs at high gas and liquid flow rates. The characteristics of this flow is the formation of the gas-rich region and liquid-rich region, which tend to propagate down the catalyst bed as pulses or waves with a frequency that depends on the liquid flow rate;

- *spray flow* occurs at very high gas flow with relatively low liquid flow rate. In this flow regime, the gas phase is continuous, with part of the liquid being carried through the column suspended as a heavy mist in the gas stream;

- *bubble flow* occurs at very high liquid flow rate and low gas flow rate. The liquid becomes the continuous phase and gas flows as a dispersed phase in the form of bubbles; but if the gas flow rate is increased, the bubbles may coalesce.

In practice, industrial processes are carried out predominantly in the gas continuous flow regime, and also, in recent years, in the lower range of flow rates which correspond to the pulsing flow region [65]. Among many flow-pattern diagrams, which were established for the representation of different flow regimes, the diagram from Charpentier and Favier [66] is generally recommended (Figure 2-2-2).

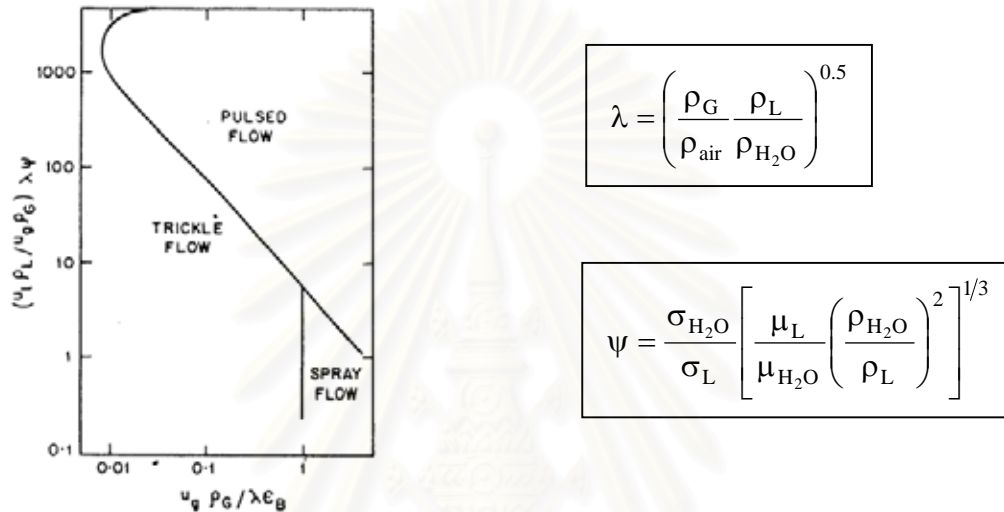


Figure 2-2-2: Flow regime boundaries of non-foaming liquid for cocurrent gas-liquid downflow fixed-bed reactor. (After Charpentier and Favier [66])

Larachi *et al.* [67] proposed a modification of flow regime boundaries of Charpentier to account for an influence of the operating pressure. They introduced the correction coefficient, Φ , which included the effect of gas density (the properties of reference fluid, which are water and air, are estimated at 293 K and 1 bar). The transition between trickle regime and pulsed regime is given by the following equation:

$$\frac{L\lambda\psi\Phi}{G} = \left(\frac{G}{\lambda}\right)^{-1.25} \quad \text{with} \quad \Phi = \frac{1}{4.76 + 0.5 \frac{\rho_G}{\rho_{\text{air}}}}$$

However, the effect of pressure (or of gas density) can be neglected as long as the gas density is lower than 2.3 kg/m³ [68].

2.5.2.1.2 Flow regimes of cocurrent upflow fixed bed reactor

The flow regimes for cocurrent upflow through a packed column can be classified in three major categories, namely:

a) Spray flow

The spray flow occurs at high gas flow rate with relatively low liquid flow rate and represents a situation where the gas is the continuous phase and the liquid is the dispersed phase.

b) Bubble flow

The bubble flow regime occurs at low gas flow rate. It is usually characterized by a continuous liquid phase containing small spherical bubbles, but elongated bubbles can be observed at medium gas flow rates.

c) Slug flow

The slug flow (or pulsed flow) is obtained at high gas flow rate and moderate to high liquid flow rate. The slug flow characteristics are alternate portions of more or less dense phases passing through the column. At very high gas flow rate, the zones merge and tend to become gas-continuous.

Among many flow-pattern diagrams which were proposed to represent flow regimes in cocurrent upflow reactor, the diagram of Turpin and Huntington [69] is often recommended, although established for air-water system (Figure 2-2-3). On this figure was superposed the flow map of Charpentier for downflow mode.

For high interaction regimes, hydrodynamics are mainly governed by inertia (gravity and flow direction do not play an important role), thus the hydrodynamic characteristics of the two flow modes become comparable [70].

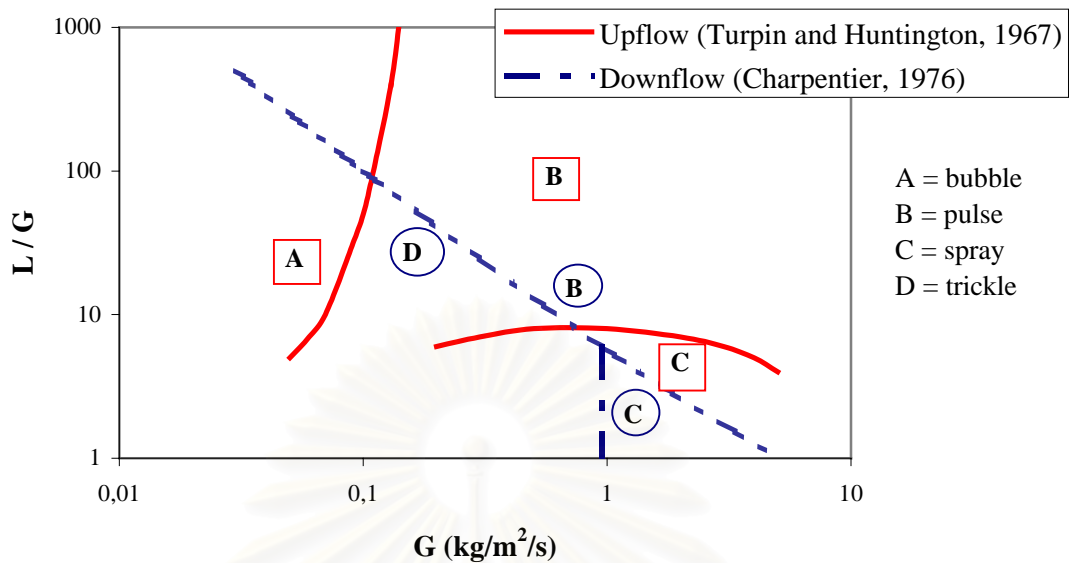


Figure 2-2-3: Flow regime boundaries (air-water system) for cocurrent upflow and downflow fixed-bed reactor ([70]).

2.5.2.2 Pressure drop

The pressure drop is one of the main factors controlling the reactor design because it is directly related to the energy required to move the fluids through the bed and thus to the sizing of equipment for pumping and compression.

According to Larachi [71], the major physical resistances during the time that gas and liquid flow through the porous catalyst are due to (a) inertia force; (b) frictional force; (c) static or dynamic capillary force which becomes an important factor if the liquid is foaming or when the size of catalyst particles is small enough; and (d) gravity force. The importance of these forces depends on the flow regime in the reactor. Thus, in the high interaction regime, the flowing resistance is mainly controlled by the gas flow through the reactor; while in the poor interaction regime (trickle flow in cocurrent downflow fixed bed reactor), the frictional force, capillary force, and gravity force are the parameters that controlled the flowing resistance.

The total pressure drop is composed of both static component (gravitational term) and dynamic component (provoked by the two-phase flow through the catalyst packing). Table 2-1A (in the Appendix) proposes some correlations for estimating the

pressure drop in both the cocurrent downflow (references [69,72–75]) and upflow fixed bed reactors (references [69,71,76]).

In general, two different approaches are proposed to correlate the two-phase pressure drop in cocurrent gas-liquid fixed bed reactor. The first approach follows the method of Lockhart-Martinelli who defines two-phase pressure drop using single-phase pressure drops of each fluid, determined at the same flow rate as that in two-phase flow [77]. Generally, the single-phase pressure drops can be calculated by the Ergun equation. The second approach regroups empirical correlations based on operating conditions, fluid and bed characteristics, and their application domain is therefore limited [69–71].

Literature reports the following conclusions concerning the influence of the operating parameters on two-phase pressure drop:

(a) liquid and gas flow rates

Two-phase pressure drop is an increasing function of both gas and liquid flow rates, the latter having the largest effect [71,76].

(b) liquid properties

Physico-chemical properties of the liquid phase (*e.g.* viscosity, surface tension, foaming or non-foaming behavior) influences two-phase pressure drop. For example, an increase of liquid viscosity can provoke a significant pressure drop in the reactor [71,77].

(c) catalyst size and reactor diameter

Pressure drop is a decreasing function of particle size, while the influence of the column diameter is found negligible when $D_C/d_p > 18$ [76].

(d) operating pressure and gas properties

At constant gas and liquid mass flow rates, an increase of operating pressure results in higher gas density and thus lower gas superficial velocity and inertia, leading to a pressure drop decrease. On the contrary, when superficial velocity is kept constant, rising the reactor pressure will increase gas mass flow rate and thus pressure drop [71].

When the pressures of gases of different molecular weights are set to have equal densities at constant liquid throughputs, they bring about identical pressure drops [68].

Larachi [71] also studied in both two flow directions the effect of gas viscosity on the pressure drop, and found that the gas viscosity did not affect the pressure drop.

(e) flow direction

The comparison between downward and upward flow showed that, for the same operating conditions, upflow fixed bed reactor always gives higher pressure drop [78].

However, for high liquid and gas flow rates, the contribution of static component tends to be negligible, and the total pressure drops in upflow and downflow reactor become comparable [78]. Moreover, Yang *et al.* [79] found also an hydrodynamic similarity between both modes of operation in high interaction regime, so that the correlation of Ellman *et al.* [73], originally developed for trickle beds, could satisfactorily fit their pressure drop results in upflow mode for non-foaming liquids.

2.5.2.3 Liquid holdup

Liquid saturation (or holdup) plays a fundamental role in hydrodynamics as well as in mass and heat transfers, in both downflow and upflow cocurrent fixed-bed reactors. From the hydrodynamic viewpoint, it is affected strongly by the flow regime occurring in the reactor. Liquid saturation also affects both wetting efficiency and mass transfer: high liquid saturations are needed for the processes in which reaction occurs exclusively on the wetted catalyst. However, a low value is desirable if both gas-solid and liquid-solid reactions can occur [63,80]. Furthermore, numerous reactions are exothermic, for which the knowledge of liquid saturation becomes necessary to prevent hot spots and thermal runaway [80].

The total liquid holdup, ε_L , is the total volume of liquid held in the reactor bed per unit bed volume. An alternative definition, sometimes referred to as the liquid saturation, is the total volume of liquid held in the reactor bed per unit void volume, β_L . These two definitions are related as follows: $\varepsilon_L = \beta_L \varepsilon$ (where ε is the bed void fraction) [81].

For a bed of porous particles the total liquid holdup may be divided into the internal or intraparticle holdup ($\varepsilon_{L,int}$ or $\varepsilon_{L,int}$) and the external or interparticle holdup ($\varepsilon_{L,ext}$ or $\varepsilon_{L,ext}$). The latter can be divided into a dynamic holdup ($\varepsilon_{L,dyn}$) and a static

holdup ($\varepsilon_{L,sta}$). The dynamic holdup can be taken as that volume of liquid in the reactor which is continually being renewed, whereas the static holdup is defined as the amount of liquid at the contact points between particles and between particles and reactor wall, that remains in the bed after the liquid inlet is shut off and the column is allowed to drain [82].

$$\varepsilon_{L,tot} = \varepsilon_{L,int} + \varepsilon_{L,ext} = \varepsilon_{L,int} + \varepsilon_{L,dyn} + \varepsilon_{L,sta}$$

Table 2-2A (in Appendix) proposes some correlations for calculation of liquid holdup or liquid saturation in fixed bed reactors (references [69,72,81–86]).

The static liquid holdup is the result of the balance between capillary and gravity forces and can be related to the Eötvös number: $Eö = \frac{\rho_L g d_p^2}{\sigma_L}$ [74].

According to numerous studies on different operating parameters related to liquid holdup, we can summarize some influences on total or dynamic liquid holdup in cocurrent downflow and upflow fixed bed reactors as follows:

(a) liquid and gas velocities

Total liquid holdup is an increasing function of liquid superficial velocity and a decreasing function of gas velocity in both two flow directions. In upflow, Larachi [71] and Yang [77] confirmed that the effect of gas velocity is more important than liquid velocity, while in downflow liquid holdup is largely influenced by liquid flow rate [71]. Similarly, in downward flow, the dynamic fraction of the liquid $\phi = \varepsilon_{L,dyn} / \varepsilon_{L,tot}$ increases when increasing liquid velocity, while this fraction is much less dependent of the liquid velocity in upflow mode [87].

(b) particle size and reactor diameter

According to Gutsche [88] and Goto *et al.* [89], a larger particle diameter would result in a higher liquid holdup in upflow mode, while the column diameter does not influence this parameter [77].

(c) liquid properties

Liquid holdup is generally slightly increased when increasing the liquid viscosity in both flow directions [71,81]. However, Yang [77] did not observe any significant effect of this parameter on liquid saturation for cocurrent upflow (the more viscous liquid they studied was a 4 mPa.s liquid).

Foaming liquids lead to lower liquid holdups than non-foaming ones [77]. In general, in upflow reactor, liquid holdup is slightly improved by increasing liquid velocity, but Yang *et al.* [77] reported the opposite effect for foaming liquids.

(d) operating pressure and gas properties

Liquid holdup was found to be a function of operating pressure [74,75,80,81, 84,85,90,91]. Larachi [71] and Larachi *et al.* [80] reported that, for given gas and liquid mass flow rates, an increase of total pressure increases liquid retention. This can be explained by the fact that the same gas mass flow rate would occupy less space under elevated pressure. However liquid retention is pressure-independent for very low gas velocity in trickle beds ($u_G \leq 1$ cm/s) [80].

Gas viscosity appears to have little effect on liquid holdup [81].

(e) flow direction

Total liquid saturation obtained in upflow is always larger than that measured under the same conditions in downflow regardless of the operating pressure [85]. At high gas superficial velocities ($u_G > 0.1$ m/s), the authors observed that liquid holdup becomes independent of the flow direction. Such an asymptotic behavior was pointed out by Yang *et al.* [79] who showed the hydrodynamic equivalence between the high interaction regimes observed for both flow modes.

2.5.2.4 Axial dispersion in the gas and liquid phases

The design of trickle bed reactors is usually based on the assumption of plug flow, that is, all reactants reside in the reactor for the same time, as determined by the flow rate and bed volume. However, different phenomena can result in deviations from the ideal plug flow (*e.g.* non-uniformity of the velocity profiles, flow turbulence, wall effect), and this is usually treated as axial dispersion [92]. Many theoretical models concerning these deviations were proposed in the literature for the explanation of axial dispersion [57,63]. The axial dispersion plug flow model is the simplest and the most popular one among the proposed models [57,93]. The axial flux describing the axial dispersion plug flow model is:

$$F = u \times C - D_{zs} \frac{\partial C}{\partial z}$$

where u is the superficial velocity of the fluid and D_{zs} the axial dispersion coefficient based on superficial velocity.

Generally, a dimensionless number is defined to characterize the extent of axial dispersion, either based on the particle size (Bodenstein number, B_o , for correlations), or the reactor length (Peclet number, Pe_m , for reactor performance calculations):

$$B_o = \frac{ud_p}{D_{zs}} \quad ; \quad Pe_m = \frac{uL_R}{D_{zs}}$$

Although axial dispersion can occur in both gas and liquid phases, gas-phase dispersion is not ordinary of concern in cocurrent gas-liquid fixed-bed reactor, where gas plug flow may be assumed, because axial profiles of concentration in the gas phase are usually much flatter than those in the liquid phase [92].

The liquid axial dispersion coefficient increases with an increase of the liquid flow rate. In the case of downflow reactor, gas flow rate has nearly no influence on the liquid axial dispersion. Conversely, in upflow mode, D_{zs} depends also on the gas flow rate [63,94].

2.5.2.5 Catalyst wetting

As mentioned in Table 2-2-5, partial wetting of the catalyst may occur in down flow and its effects are positive if the overall reaction rate is controlled by mass transfer of the gaseous reactant and negative in other cases. The catalyst wetting efficiency depends upon the liquid holdup as well as proper distribution of liquid. Generally, in commercial trickle bed reactors, all the catalyst particles are completely wetted by the liquid, while, in the lab-scale reactors, liquid velocities are low and the liquid flows downwards in form of rivulets, which tend to maintain their position with time. Some particles are covered with a trickling liquid film while others, although internally wet, are without a liquid film on the surface. This type of flow nonuniformity causes an ineffective wetting of the particles [63]. In general, catalyst wetting can be classified into two types:

(a) internal wetting or pore filling, (*i.e.* the liquid volume inside the catalyst pores). It defines the amount of internal (active) surface potentially available for the reaction. As catalyst pellets are almost always porous, internal wetting is in most cases eventually total, due to capillary effects;

(b) external effective wetting, (*i.e.* the amount of external area of the catalyst effectively contacted by the flowing liquid). Unlike internal wetting, the external catalyst wetting efficiency increases with the liquid velocity and is unity only at high liquid velocities [63,95].

Depending on the flow pattern of the flowing liquid in the trickle flow regime (in downflow reactor), the catalyst can be partially externally wetted at low liquid velocities or completely externally wetted at higher liquid velocities, as illustrated in Figure 2-2-4.

Recent work at LGC Toulouse proves the nature of the liquid-solid interface to have more effect on the wetting efficiency than the liquid flow rate on a monolayer of beads: at high contact angle (close to 90°), corresponding to poor solid-liquid affinity, the wetting efficiency is much less than at low contact angle even at much higher liquid flow rate.

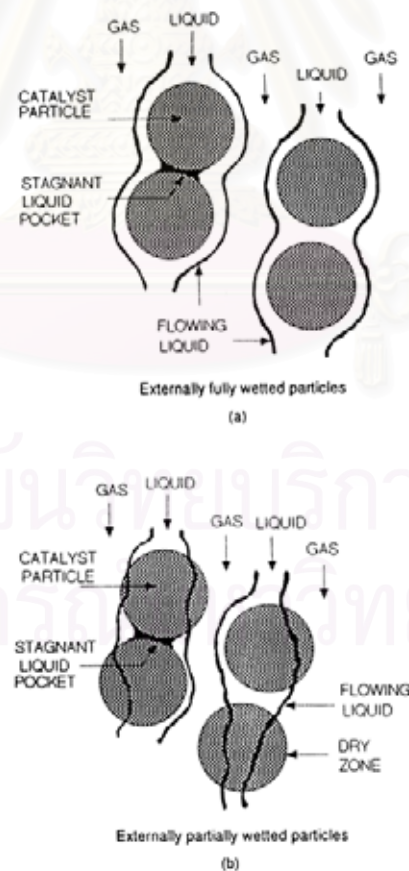


Figure 2-2-4: Flow patterns in trickle flow regime for externally completely and partially wetted particles. (After Al-Dahhan and Dudukovic [64])

2.5.3 Mass transfer

In gas-liquid-solid catalytic reaction, there are many different mass transfer steps between phases. Consider a reaction with two reactants (one gas, A, and one liquid, B) that generated a nonvolatile product, and a fully externally wetted catalyst, the total process may be divided into the following steps:

1. Transport of reactant A within the gas phase.
2. Mass transfer of reactant A from the bulk gas phase to the gas-liquid interface.
3. Mass transfer of gas reactant A from the gas-liquid interface to the bulk liquid phase.
4. Transport of reactants A and B within the bulk liquid phase.
5. Mass transfer of reactants A and B in the liquid film to the external surface of the catalyst particles.
6. Intraparticle diffusion of reactants A and B into the catalyst pores.
7. Adsorption of reactants A and/or B on the catalyst active sites.
8. Reaction on the catalyst.
9. Desorption of product from the catalyst.
10. Intraparticle diffusion of product in the catalyst pores.
11. Mass transfer of the product in the liquid film from the catalyst surface.
12. Transport of the product within the bulk liquid.

When reactant in the gas phase is highly soluble in the liquid phase, the gas-side film resistance at the gas-liquid interface is negligible comparing to the liquid-side film resistance. When all mass transfer resistances have to be considered, the typical concentration profiles of the gaseous reactant A and liquid reactant B are shown in Figure 2-2-5.

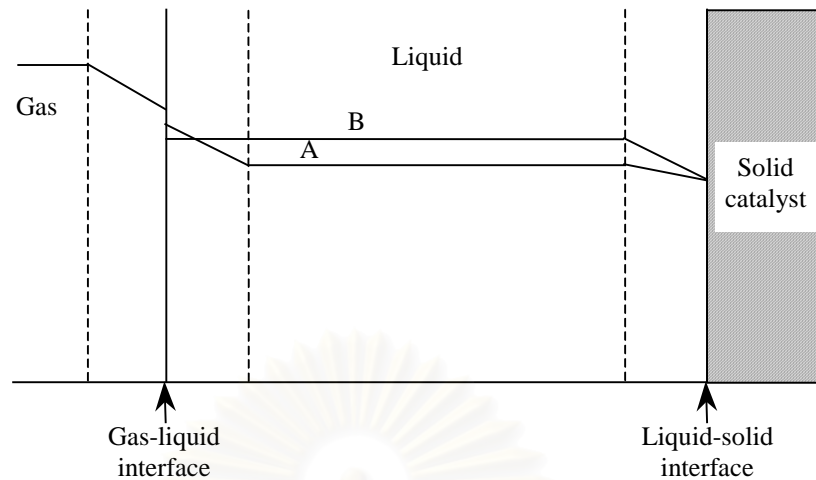


Figure 2-2-5: Concentration profiles for the gaseous reactant A and liquid reactant B.

2.5.3.1 Gas-liquid mass transfer

Generally the molar flux of gas reactant A at the gas-liquid interface can be written as:

$$N_{GL} = K_L a (C_L^* - C_L) = k_L a (C_L^i - C_L) = k_G a (C_G - C_G^i)$$

With a = gas-liquid interfacial area

C_G^i, C_L^i = respectively gas-side and liquid-side concentrations of reactant A at gas-liquid interface

C_L = concentration of reactant A dissolved in the liquid

C_G = concentration of reactant A within the gas phase

C_L^* = saturation concentration of reactant A in the bulk liquid

k_G, k_L = respectively gas-side and liquid-side mass transfer coefficients at the gas-liquid interface

$k_L a$ = volumetric liquid-side mass transfer coefficient

K_L = overall gas-liquid mass transfer coefficient

According to the two-film concept, with assumption of thermodynamic equilibrium at the gas-liquid interface, the overall gas-liquid mass transfer coefficient is related to the liquid-side and gas-side coefficients as follows:

$$\frac{1}{K_L a} = \frac{1}{H_e \times k_G a} + \frac{1}{k_L a}$$

(H_e = Henry constant of gas reactant defined as the ratio C_G^i/C_L^i). For the case of the pure or sparingly soluble gases, $K_L a$ is not much different from $k_L a$.

Gas-liquid mass transfer depends mainly on liquid and gas flow rates, catalyst characteristics, and liquid properties. It may be obtained by absorption measurements with or without chemical reaction.

Many correlations were established for the cocurrent gas-liquid fixed-bed reactors. Table 2-3A (in the Appendix) lists the most representative ones (references [78,96–106]).

The following conclusions emerge from a literature survey on gas-liquid mass transfer in fixed bed reactors:

In downflow mode, $k_L a$ and a decrease when decreasing gas and liquid throughputs, increasing particle size or decreasing liquid viscosity [97,102,103].

In upflow mode, same trends are observed, excepting that $k_L a$ seems to slightly decrease when increasing liquid viscosity [106].

Regarding the pressure effect, it was observed in trickle beds that, at constant gas and liquid mass flow rates, $k_L a$ and a decrease when gas density is increased. For gas superficial velocities about 10 mm/s, neither $k_L a$ nor a depends on gas density and can be estimated at atmospheric pressure. Above this limit, when gas superficial velocity is kept constant, $k_L a$ and a are improved by increasing gas density [106].

Gas-liquid mass transfer is also influenced by a flow direction; it is generally reported that the upflow mode results in larger $k_L a$ [78,98]. In low interaction regime, $k_L a$ was found to be greatly affected by gas flow rate in upflow mode, while in downflow mode $k_L a$ depended mainly on liquid velocity [98].

2.5.3.2 Liquid-solid mass transfer

The general expression for the reactant molar flux at the liquid-solid interface is written as:

$$N_{LS} = k_{LS} a_{LS} (C_L - C_S)$$

Where k_{LS} = liquid-solid mass transfer coefficient
 a_{LS} = liquid-solid interfacial area per unit reactor volume
 C_L = reactant concentration within the liquid phase
 C_S = reactant concentration at the catalyst surface

Liquid-solid mass transfer depends also mainly on liquid and gas flow rates, particle characteristics, and liquid properties.

In downflow mode, $k_{LS}a_{LS}$ is a decreasing function of the particle size [107,108] and an increasing function of the liquid flow rate. Concerning the gas flow rate, its effect is small in the poor interaction regime, but it greatly improves liquid-solid mass transfer in the pulse regime [97,107].

In upflow mode, $k_{LS}a_{LS}$ is an increasing function of the gas flow rate, even at low flow rates [108]. At same gas and liquid velocities, upflow mode leads to higher liquid-solid mass transfer than downflow mode [98,108].

2.5.4 Heat transfer

Trickle bed reactors are usually considered as adiabatic reactors with a flat radial temperature profile in their main applications of hydrotreatment. In large industrial units, however, considerable radial temperature gradient can exist, especially when heat losses are significant or when large reaction heat fluxes are produced in other applications. Many papers on fixed bed reactors have been published, but very few dealt with heat transfer phenomena.

Models proposed in literature consist of:

- (a) one-parameter model (an effective radial thermal conductivity of the bed, Λ_r)
- (b) two-parameter model (Λ_r and a wall heat transfer coefficient, h_w)

It is generally assumed that there is not any significant temperature difference between the phases (homogeneous model) and the heat axial dispersion is negligible.

Lamine *et al.* [109] studied heat transfer in upflow fixed bed reactor. They reported that for small particles ($d_p = 2$ mm), heat transfer was well described by the one-parameter model, while in the case of large particles ($d_p = 6$ mm), the wall heat transfer resistance became important and should be included.

Λ_r and h_w are increasing functions of the liquid flow rate, but the effect of the gas flow rate is more complex and depends also on the flow regime [109–111].

Studies on the effect of the flow direction reported that heat transfer is generally improved in upflow mode [109,112]. Nakamura *et al.* [112] obtained for the upward flow radial thermal conductivity and wall heat transfer coefficient values up to four times larger than for the downward flow.

2.5.5 Application of fixed bed reactors to the CWO of phenol

Literature provides successful examples of CWO of phenol in continuous fixed bed reactors, most often trickle bed reactors. Some of the most relevant studies are summarized below.

The Tarragona group (Fortuny *et al.* [10,37,113], Eftaxias [4], and Eugenia Suarez-Ojeda *et al.* [13]) published about ten articles on this topic.

Fortuny *et al.* [10,37,113] compared different types of catalyst in a lab-scale trickle bed reactor (20 cm long and 1.1 cm i.d.) to evaluate the catalyst activity and stability, and found that a commercial supported copper oxide (Harshaw Cu0803 T1/8) and a wood-based active carbon (Merck AC) were suitable for the continuous treatment of phenolic wastewater under mild conditions of air pressure (< 5 MPa) and temperature (< 160 °C). However, the Cu0803 underwent a rapid deactivation by losing the active species as a consequence of its poor stability in the hot acidic aqueous medium. Thus, after a short induction period (24 h), the highest phenol conversion was of 78% ($P_T = 4.7$ MPa ($P_{O_2} = 0.9$ MPa), $T = 140$ °C, and $WHSV = 2.4$ h⁻¹), and then it fell sharply to stabilize at a remaining phenol conversion of 30% after 240 working hours. The AC catalyst gave higher phenol conversion despite working at much higher liquid WHSV (8.2 h⁻¹), but it also presented a progressive fall in phenol conversion. Thus, the phenol conversion went from an initial 100% to final 48% in 240 h tests. It was observed that 33% (in weight) of initial AC was consumed by combustion during the runs and that AC surface area was nearly divided by 3, which, besides some decrease of catalytic efficiency, explained the loss of activity observed. However, this carbon loss was found to be faster in absence of phenol, suggesting phenol and carbon oxidation to be competitive reactions. Both catalytic substances showed similar selectivity to carbon dioxide, about 70%, even AC yielding higher phenol conversion than Cu0803. The selectivity to harmful partial oxidation

products was lower for AC, approximately 5%, than for Cu0803, around 12%, thus indicating the beneficial effect of the AC on the product yield. Lowering the oxygen partial pressure from 9 bar to 2 bar allowed to highly reduce the AC combustion, while maintaining acceptable phenol conversion. The authors also reported that the physical properties and the source of the active carbon could be hardly related to the phenol conversion, suggesting that the catalytic performance of the active carbon was rather related to the chemical surface characteristics, in particular, to the number and type of oxygen-containing groups.

Eftaxias [4] used also both copper oxide and AC catalysts in same lab-scale reactor and found that the mechanism over AC differed from that over the CuO catalyst, proceeding *via* two distinct routes: one in agreement with classical pathway to give benzoquinone then lower molecular-weight compounds intermediates to final carbon dioxide and water, the other conducting to the formation of 4-hydroxybenzoic acid which was not detected in the previous works. As found previously, AC exhibited both stable and higher activity compared to copper oxide catalyst. In trickling flow, almost complete phenol conversion (> 99%) along with a COD reduction of 85% were obtained at low space times (0.4 h), 160 °C and low oxygen partial pressures ranging from 0.1 to 0.2 MPa. At low conversion of phenol, mineralisation of reacted phenol to CO₂ and H₂O was almost complete, while the difference between phenol and COD conversion became larger as the phenol conversion increased. The main intermediates detected were 4-hydroxybenzoic acid, benzoquinone, maleic acid, formic acid, and acetic acid as well as traces of hydroquinone and oxalic acid. Also, downflow mode of gas-liquid resulted in considerably higher conversions than upflow mode for all operating conditions tested due to the positive effect of partial catalyst wetting and gaseous oxygen being the limiting reactant. The experiments in the small TBR were shown to be kinetically controlled by the typical diagnostic criteria and served thus to assess the reaction kinetics of phenol and intermediate oxidation by non-linear regression.

A recent experimental study [13] indicated that CWAO over AC trickle bed reactor was also active for different toxic pollutants, such as *o*-cresol, 2-chlorophenol, and dodecylbenzene sulfonate, giving conversions between 30 and 55% at 140 °C, 13.1 bar total pressure, and 8.2 h⁻¹ WHSV. The selectivity to the production of carbon dioxide was very high with total organic carbon abatement between 15 and 50%.

Tukac *et al.* [114,115] studied the impact of partial wetting on CWO of phenol in trickle bed reactor by using two different catalyst beds: a bed of randomly filled catalyst, and a catalyst bed diluted with fine inert particles (to avoid liquid maldistribution and improve catalyst wetting). In steady state operation mode, with temperature range of 125 to 170°C and total pressure of 1 to 7 MPa, they found that at low residence time values the highest conversion was obtained from the undiluted catalyst bed. The authors explained this result by the enhanced oxygen transfer from gas phase to catalyst surface on the dry zones existing in the undiluted bed. They also found that periodic ON-OFF modulation operated on the undiluted bed could significantly improve phenol conversion in comparison to that measured in the steady state operation at the same mean feed rate.

Singh *et al.* [116] performed CWO of phenol over CuO/Al₂O₃ catalyst in a 2.54 cm diameter trickle bed reactor with a bed length of 60 cm. They obtained higher phenol conversions with computer designed shape pellets compared to extrudates due to the reduction of wall effects. Phenol conversion was affected by the liquid and gas flow rates (respectively in the range of 0.6 to 1.2 l/h and 0.03 to 0.07 kg/m²/s). Phenol destruction decreased with the increasing of liquid flow rate, while gas flow rate had however a marginal effect. Phenol conversion increased when temperature and reactor pressure increased. However, the temperature having more significant effect on the conversion. An axial dispersion model assuming full catalyst wetting explained their experimental results with a deviation of ± 15%.

สถาบันวิทยบริการ
จุฬาลงกรณ์มหาวิทยาลัย

CHAPTER III

EXPERIMENTAL SECTION: MATERIALS AND METHOD

3.1 Materials

Analytical grade phenol was obtained from Scharlau and used without further purification. Phenol solutions (53 mmole/l or 5 g/l) were prepared in bidistilled water and used as feed solution. High purity synthetic air, oxygen, and nitrogen were obtained from Linde Gas. Activated carbon (AC) was supplied by Merck (Reference No. 2514) in the form of 1.5 mm pellets. This AC is obtained from wood and has low ash content (3.75%). Prior to use, the AC was sieved to obtain the 1.25–1.60 mm fraction, which was selected as catalyst throughout this experiment without further treatment. Other properties of the AC are reported in Table 2-3-1.

Table 2-3-1: Physical properties of Merck activated carbon 2514

Sieved particles size (mm)	1.25–1.6
Volume weighted mean diameter, D[4,3] (mm)	1.025
Carbon density (g/l)	2000
Apparent density (g/l)	935
Pore volume (cm ³ /g)	0.57
BET specific surface area (m ² /g)	975
Average pore diameter (nm)	2.3

3.2 Characterization of products

The reaction products were analyzed and quantified by a Thermofinnigan HPLC equipment using a ProntoSIL C₁₈ reversed phase column and a UV detector. The products were identified by comparison with pure compounds purchased from Aldrich. The chemical oxygen demand (COD) of reaction products was recorded using a Hach spectrophotometer operating at 620 nm.

3.2.1 HPLC analysis

The reaction products were analyzed by two methods: (a) fast analysis method (lasting less than 10 minutes) for the analysis of phenol concentration in the reaction products until the steady state was reached (only phenol peak was well separated from the others); and (b) full analysis method for the analysis of intermediate concentrations.

Both methods were analyzed using the Thermofinnigan HPLC system equipped with a degas unit (model SCM1000), an isocratic pump (model P1000XR), an autosampler (model AS1000), a ProntoSIL C₁₈ reversed phase column (250 mm × 4 mm × 5 μm), and a UV detector operating at the absorbance of 254 nm for fast analysis and 210 nm for full analysis. Prior to injection into the analytical HPLC column, the collected reaction samples were diluted with bidistilled water in order not to overload the column. In the case of fast analysis sample preparation, 0.15 g of reaction solution was weighed into 2 ml vial and made up the volume with bidistilled water to obtain the final solution at 1.0 g. In the case of sample preparation for full analysis, 0.7 g of reaction solution was diluted with bidistilled water to 1.0 g of the final solution.

The conditions of fast analysis for the determination of phenol concentration before reaching the steady state were as follows. Isocratic mobile phase was a mixture of solutions A and B (70:30, v/v). Solution A was ultra pure water adjusted pH with H₃PO₄ to pH 2.5, while solution B was acidified acetonitrile. The column was thermostated at 30 °C and a total flow rate of 1 ml/min was employed. UV detector was set at 254 nm. A sample volume of 10 μl was injected for each analysis.

Prior to each oxidation experiment the phenol calibration curve was checked to correct deviations in peak area, which could be caused by small changes in column performance.

For the full analysis, longer analysis and mobile phase gradients had to be operated to separate intermediate reaction products: 0–3 minutes isocratic of 100% of solution A; 3–16 minutes linear mobile phase gradient from 100% of solution A to a mixture of solutions A and B (60:40, v/v); and 16–25 minutes isocratic of a mixture of solutions A and B (60:40, v/v). UV detector was set at 210 nm. Total flow rate,

column temperature, and sample volume were similar to the values described previously.

The intermediates in the reaction products were identified by comparison with their corresponding pure commercial samples. Then, the calibration curves for each intermediate detected were established in the concentration ranges that they were found in the reaction products.

3.2.2 Determination of chemical oxygen demand (COD) of reaction products

The COD of reaction solution was measured by the reactor digestion method (Hach method 8000). The mg/l COD results were defined as the mg of O₂ consumed per liter of sample solution under the conditions described in this procedure. In this method, the sample was heated for 2 h with a strong oxidizing agent, potassium dichromate. Oxidizable organic compounds reduced the dichromate ion (Cr₂O₇²⁻) to green chromic ion (Cr³⁺). The amount of Cr³⁺ produced was subsequently determined colorimetrically using a UV spectrophotometer operating at 620 nm and expressed as COD. The COD reagent also contained silver and mercury ions. Silver acted as a catalyst, and mercury was used to form complex with the chloride interferences.

Prior to use, each reaction solution was diluted by weighing 1.66 g of sample, and then made up to 25.0 g with bidistilled water to obtain solutions with the COD ranges of 0–1500 mg/l. The COD reactor was turned on and preheated at 150 °C. 2 ml of diluted solution (or bidistilled water for blank preparation) was precisely pipetted into the COD digestion reagent tube. The closed tube was inverted gently several times to mix the contents, and placed in the preheated COD reactor to be heated for 2 h at 150 °C. The tubes were then cooled down to room temperature and carefully cleaned with a paper towel before analysis. The blank was first placed into the spectrophotometer to set the zero.

The accuracy of the method was checked by analyzing standard phenol solutions at respectively 1 g/l, 3 g/l, and 5 g/l, for which expected COD were obtained within ± 5%.

3.3 Catalytic reactors

The fixed bed reactor, originally developed by Stüber [117] for the study of hydrogenation selectivity of cyclododecatriene in cocurrent upflow fixed bed reactor, was adapted to study the continuous oxidation of phenol in both upflow and downflow of gas and liquid. This fixed bed reactor was composed of two distinct parts: the main circuit of reaction (air or oxygen and phenol solution) and the temperature-controlling circuit of the reactor (controlled by the circulation of thermal oil).

In parallel to the continuous CWAO of phenol, the evaluation of the reaction kinetics was performed in a stirred semi-batch autoclave.

3.3.1 Autoclave reactor

3.3.1.1 Description

For the determination of kinetic parameters, batch phenol oxidation was performed in a 300 ml-stirred autoclave (Parr Instruments) using uncrushed 1.5 mm AC pellets to minimize fast and continuous catalyst deactivation as reported with powder in previous studies [1].

The Hastelloy C-276 reactor was equipped with a gas inducing turbine with variable stirring speed up to 2000 rpm. The equipment was provided with automatic temperature control and pressure recording system. The temperature of the liquid in the reactor could be maintained within 1 K, by means of a PID regulator controlling the heating power of the annular furnace and the opening time of an electro-valve allowing cold water to enter the serpentine coil.

The AC pellets were placed in an annular fixed basket around the turbine in order to prevent catalyst attrition.

The gas outlet was equipped with a mass-flow controller to ensure a continuous renewing of the reactor gas phase, and a condenser to prevent the vaporizations of solvent and light products.

A schematic diagram of the apparatus is shown Figure 2-3-1.

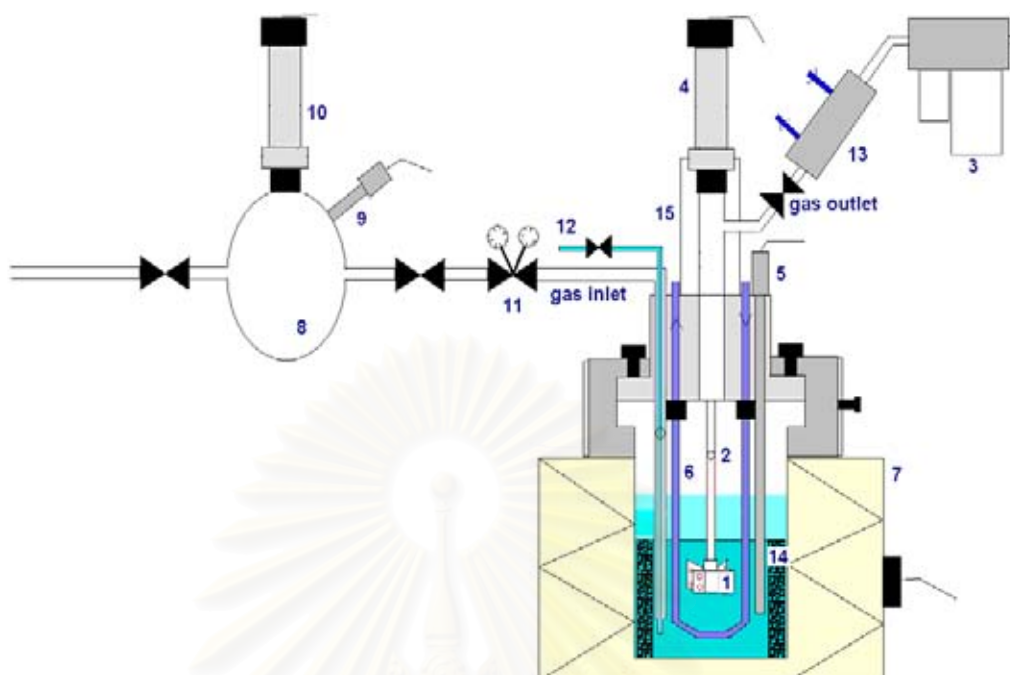


Figure 2-3-1: Schematic diagram of an autoclave reactor

1 gas inducing turbine, 2 hollow tube, 3 gas mass-flow controller, 4 pressure transducer, 5 Pt-100 probe, 6 cooling serpentine coil, 7 furnace, 8 gas reservoir, 9 Pt-100 probe, 10 pressure transducer, 11 pressure regulation valve, 12 liquid sampling valve, 13 condenser, 14 catalyst basket, 15 magnetic drive

3.3.1.2 Operating the reactor

Kinetic experiments of phenol oxidation were carried out batchwise for the liquid and continuous for air at a flow rate of 60 NI/h to ensure a constant oxygen partial pressure (a calculation from initial reaction rate gave an O_2 consumption of 0.22 NI/h for the reference conditions: $T = 150^\circ\text{C}$, $P_{O_2} = 3.3$ bar). The reactor was loaded with 9 g of AC pellets disposed in the fixed basket and 200 ml of 2.5 to 5 g/l phenol solution. To pre-saturate the catalyst, the reactor was pressurized with nitrogen and heated under mild stirring to the desired reaction temperature. After 2.5 h, when adsorption equilibrium was reached, a liquid sample was taken to measure the initial phenol concentration. Then, the stirring was turned off and nitrogen was carefully purged and replaced by fresh air. Once the required air pressure was reached again, vigorous stirring was switched on to start the reaction. The stirrer speed had been set at 800 rpm such as to avoid on one hand catalyst attrition and on the other hand

eventual external mass transfer limitations. During the course of reaction, liquid samples were periodically taken, filtered, and immediately analyzed by the HPLC to get the evolution of phenol concentration.

The same AC sample was used for the entire series of 15 experiments. Activity tests were regularly performed to ensure that only experimental results at the same catalytic activity were used for the kinetic modelling.

Physical damage of the catalyst due to attrition was not detected. The withdrawn liquid samples had been found all free from suspended fine solids, and a granulometry analysis of the used AC showed that the particle size had not changed after reaction experiments.

3.3.2 Fixed bed reactor

3.3.2.1 Description

3.3.2.1.1 Principal circuit of reaction

The schematic diagram for an experimental set-up of the fixed bed reactor is presented in Figure 2-3-2. The reactor unit consisted of a jacketed packed-bed stainless steel column (1) with an inner diameter of 2.5 cm and a bed height of 120 cm. The column was filled with 326 g of activated carbon (1.25–1.60 mm sieved fraction). A flexible grid was put at the top of the reactor to prevent fluidization of particles during the upflow mode operation.

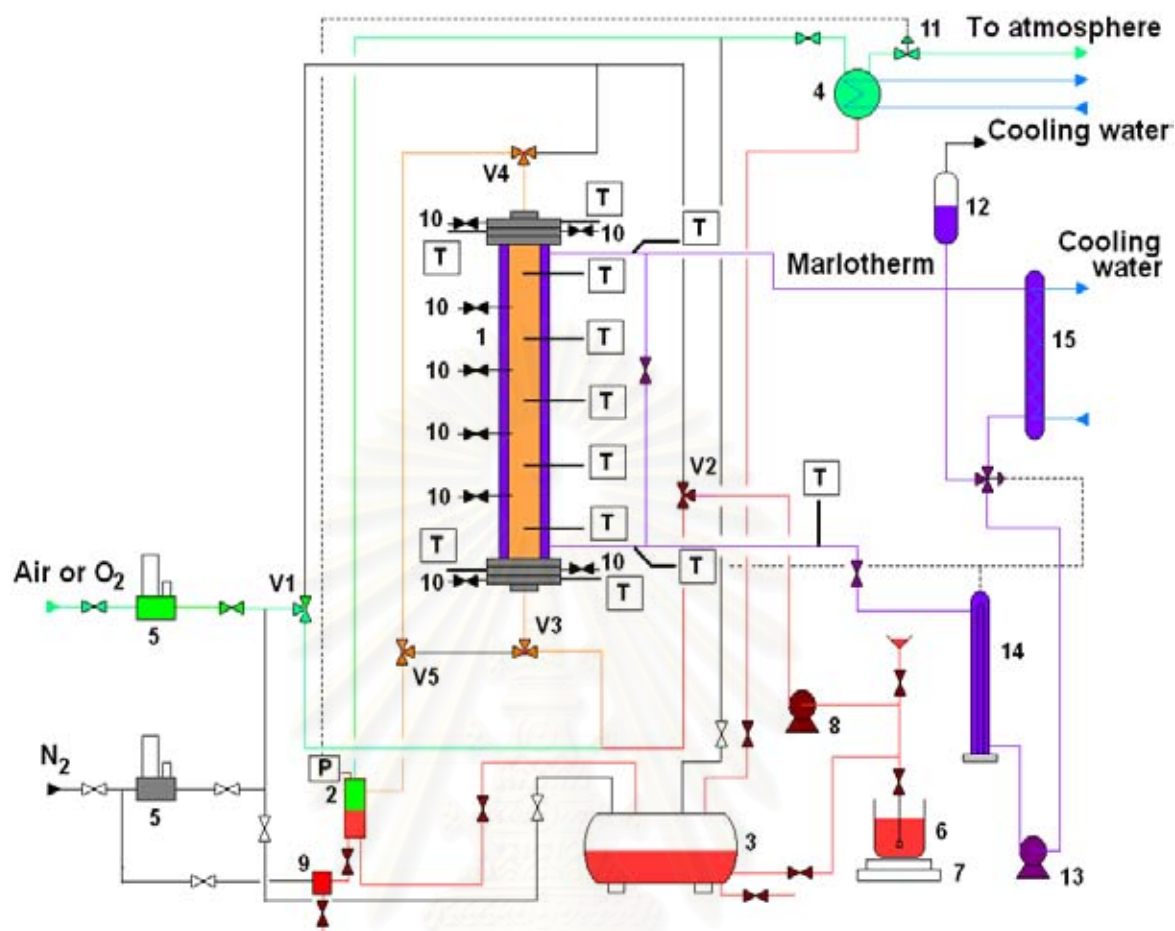


Figure 2-3-2: Schematic diagram of cocurrent gas-liquid fixed bed reactor

1 jacketed packed bed column, 2 gas-liquid separator, 3 liquid storage tank, 4 condenser, 5 gas mass-flow controllers, 6 feed tank, 7 balance, 8 dosing pump, 9 sampling device, 10 liquid sample valves, 11 pneumatic valve, 12 expansion vase, 13 gear pump, 14 heater, 15 cooling exchanger, V1-V5 three-way valves for up- or downflow mode

The liquid was fed to the column by a dosing pump (8). The liquid flow rate was controlled by adjusting the graduating valve (and/or motor frequency) of the calibrated pump. This flow rate was also checked by measurement of the mass of the feeding tank that was placed on a balance (0–16 kg). The liquid was mixed with synthetic air or a mixture of O₂ and N₂ before entering the catalyst bed. The mass flow rate of each gas was controlled by a Brooks mass flow controller (0–500 Nl/h) (5).

The fluid circulation mode (upflow or downflow) was controlled by five valves located along this circuit. Eight liquid sampling valves (**10**) and nine temperature sensors were located along the reactor length in order to measure the axial concentration and temperature profiles under non-isothermal conditions and wall-to-bed heat transfer in both modes of operation. One of these sensors was made of three thermocouples to monitor radial temperature gradients. Other sensors were of the type Pt100-resistance thermometers. Temperatures were monitored using a data acquisition system implemented in a microcomputer. Additionally, there was a sampling device (**9**) connected directly to the bottom of the gas-liquid separator to collect liquid only, and to the N₂ line for drying.

Soon after the two-phase mixture was running off the column, it was directly separated in a stainless-steel gas-liquid separator (**2**) equipped with a pressure transducer for controlling the pressure of the system (West PID regulator). After gas-liquid separation, the liquid was kept in an 8 l stainless-steel receiver (**3**), while the gas went through a condenser (**4**) to recover light organic compounds and was eventually diluted with N₂, in order to obtain a N₂:O₂ ratio close to air, before releasing to the atmosphere.

3.3.2.1.2 Temperature control circuit

Temperature control in the reactor was achieved by the fast circulation of a heating oil, Marlotherm S (whose properties are shown in Appendix 2-4A), in the jacket of the reactor. This oil was circulated at a nearly constant temperature in a closed loop system by a gear pump (**13**) ($P_{\max} = 0.5$ MPa, maximum flow rate = 2.5 m³/h).

The temperature controlling circuit of the Marlotherm was composed of:

- 1) Three heat resistances of 2 kW (**14**)
- 2) A stainless-steel multiple tube exchanger (**15**), with refrigerated water flowing countercurrent to the oil in order to cool it
- 3) A three-way valve, which distributed the oil flow to the cooling exchanger (**15**), and/or to a simple tube
- 4) A PID regulator (Eurotherm 818) self-adjustable and self-adapting, that continuously commanded, according to the difference between set-point

and actual oil temperature measured at the jacket inlet, the heating power as well as at the opening position of the three-way valve.

3.3.2.1.3 Data acquisition

Rough data signals of temperatures, pressure, gas flow rates, and mass of the feeding tank were sent to an interface and acquisition card (Analog Device RTI 820), connected to a microcomputer (Pentium III 550 MHz). A data acquisition software (DASYLab 7) allowed both visualising on the PC screen and recording time-evolutions of the measured variables.

3.3.2.2 Procedure for operating continuous oxidation reactor

3.3.2.2.1 Catalyst packing

The loading of catalyst was carried out by a slow introduction of the particles into the column, followed by a vibration at the wall of the reactor, in order to get a uniform distribution of the catalyst particles.

After packing, the reactor was checked for leaks by pressurizing the system with nitrogen or air up to working pressure.

3.3.2.2.2 Operating the reactor

The start up of oxidation experiment series consisted in saturating the AC bed with the 5 g/l phenol solution (operating either at reaction temperature and under pressure with cocurrent nitrogen flow, or at room temperature and atmospheric pressure with no gas flow). During transient adsorption, samples were regularly withdrawn at the reactor outlet and analyzed by the HPLC to monitor the experimental breakthrough.

Typical operation of continuous CWAO (either in upflow or downflow mode) proceeded then as follows.

First, the reactor unit was pressurized to reach the selected pressure with synthetic air or adjusted O₂/N₂ mixture (setting gas flow rate(s) on Brooks control unit and pressure on West regulator). After the pressure was stabilized, the reactor was fed with phenol solution, liquid flow rate having been adjusted by tuning the graduating valve (and/or adjusting motor frequency) of the dosing pump. In the same

time, the Marlotherm oil was circulated in the reactor jacket and heated to desired temperature. The data acquisition on the computer was started in order to record the evolutions of the measured variables.

The liquid flow rate was also re-checked for each experimental run by measuring in 30 minutes intervals the mass of the feeding tank, which was placed on a balance. Four liquid samples were taken hourly at different positions of the system, including the feeding tank, the reactor inlet and outlet, and after the separator. Two extra samples were also collected each 30 minutes from the outlet of the reactor and from the separator. After the steady state was reached, samples were collected additionally from each sampling valve along the reactor (four positions), to obtain the axial concentration profiles of reaction products.

3.3.2.2.3 Reactor shutdown

When the steady state was reached and all of the samples were collected, the experiment was stopped by setting the oil temperature to 20 °C, turning off the liquid feeding pump and gas-flow meters, as well as the data acquisition on the computer.

When the reactor was cooled down to around 40 °C, the pump for Marlotherm was turned off. Then, the pressure was gradually reduced to 1 atm.

After completion of each experiment, the liquid storage tank was emptied by passing N₂ directly through the tank until all liquid was completely removed.

CHAPTER IV

RESULTS AND DISCUSSION: EXPERIMENTAL AND MODELLING

This chapter gathers experimental results concerning phenol adsorption on a fixed bed of active carbon, batch kinetics of phenol oxidation performed in an autoclave reactor, and more importantly all the data of continuous three phase fixed bed operation obtained at various conditions of pressure, temperature, and gas and liquid flow rates. A systematic comparison of upflow mode (flooded bed) and downflow mode (trickle bed) is presented.

The discussion of results also contains an attempt to modelling of: unsteady adsorption with breakthrough curves, kinetic parameter optimisation including pore diffusion, and complete three phase catalytic reaction in fixed bed reactor accounting for transport phenomena, typical hydrodynamics with stagnant liquid zones and partly wetted catalyst, and even mass transfer limited vaporisation of water during non-isothermal reactor operation.

4.1 Phenol adsorption on active carbon

Before starting oxidation experiments, the bed of active carbon (AC, whose properties was shown in Tables 2-3-1 and 2-4-3) was first saturated using the same feed solution (5 g/l of phenol) and the evolution of the outlet phenol concentration during this adsorption step was monitored to get the typical breakthrough curve corresponding to the first step of the adsorption-oxidation (AD-OX) process.

In previous studies [5,10,13], the adsorption isotherms for the same Merck AC obtained in stirred batch vessels were found to be best-fitted by a Freundlich-type model:

$$q_e = a [\text{Ph}]_{\text{eq}}^n \quad (2-4-1)$$

where q_e is the amount of phenol adsorbed per unit weight of activated carbon and $[\text{Ph}]_{\text{eq}}$ is the remaining phenol equilibrium concentration in the liquid phase.

The corresponding Freundlich parameters optimised from these studies at room temperature are reported in Table 2-4-1.

The parameters (and the corresponding adsorption capacities) differ quite appreciably, might be due to some variations of BET surface between carbon lots and

also different operating conditions. The experiments of Polaert *et al.* [5] were carried out under nitrogen atmosphere, while the isotherms of Suarez-Ojeda *et al.* [13] and Fortuny *et al.* [10] were obtained in oxic conditions, *i.e.* the solution was always in contact with air, allowing some degree of oxidative coupling to take place as the result of the presence of dissolved oxygen.

Table 2-4-1: Parameters of the Freundlich equation and adsorption capacity at 5 g/l phenol solution from Fortuny *et al.* [10], Polaert *et al.* [5], and Suarez-Ojeda *et al.* [13]

	q_e^* (mol/g AC)	a (mol ⁽¹⁻ⁿ⁾ /g _{AC} × 1 ⁿ)	n
Fortuny <i>et al.</i> (1998) T = 20 °C, air	4.2×10^{-3}	9.07×10^{-3}	0.265
Polaert <i>et al.</i> (2002) T = 25 °C, N ₂	3.2×10^{-3}	5.75×10^{-3}	0.199
Suarez-Ojeda <i>et al.</i> (2005) T = 20 °C, air	4.3×10^{-3}	1.00×10^{-2}	0.29

* for [Ph]_{eq} = 5 g/l

In this study, the adsorption experiment was carried out in a fixed bed reactor with upflow of liquid (no gas flow) (Figure 2-3-2) under the following conditions: atmospheric pressure, wall temperature 25 °C, liquid flow rate 5.0 kg/h, and feed concentration of phenol 5 g/l.

The corresponding breakthrough curve is presented in Figure 2-4-1.

This transient fixed-bed adsorption was modelled by a classical chromatographic model developed by Félis [118] and modified by Polaert: axial dispersion was modelled by series of perfectly mixed tanks and the model also included transient adsorption/diffusion inside the pellets, as well as the external liquid to solid mass transfer limitation. The effective diffusivity of phenol was predicted using Wilke-Chang correlation [119] and assuming a tortuosity factor of 3. Liquid-solid mass transfer coefficient was calculated from Ranz and Levenspiel correlation [120]. Number of series tanks (N_{cell}) was estimated from Villermaux [121], leading to $N_{\text{cell}} = 299$.

The experimental breakthrough was much less stiff than the modelled one, especially at the end when exit concentration tends to the inlet concentration as complete bed saturation is achieving. This asymmetrical experimental behaviour could be simulated by using a much larger value of the “n” parameter than proposed previously ($n = 0.6\text{--}0.7$); nevertheless such high “n” isotherm curves are not at all in agreement with all previous works. Other possible explanations are deviation from plug flow due to imperfect filling of the AC bed, much slower adsorption-diffusion phenomena in AC porous particles, or lower external liquid to solid mass transfer coefficient due to gas stagnant pockets.

Here, “n” was set to values reported previously (0.2 and 0.3, respectively), while only the value of “a” was freely set to be optimised from the experimental breakthrough curve using a Gauss-Newton method (Figure 2-4-1).

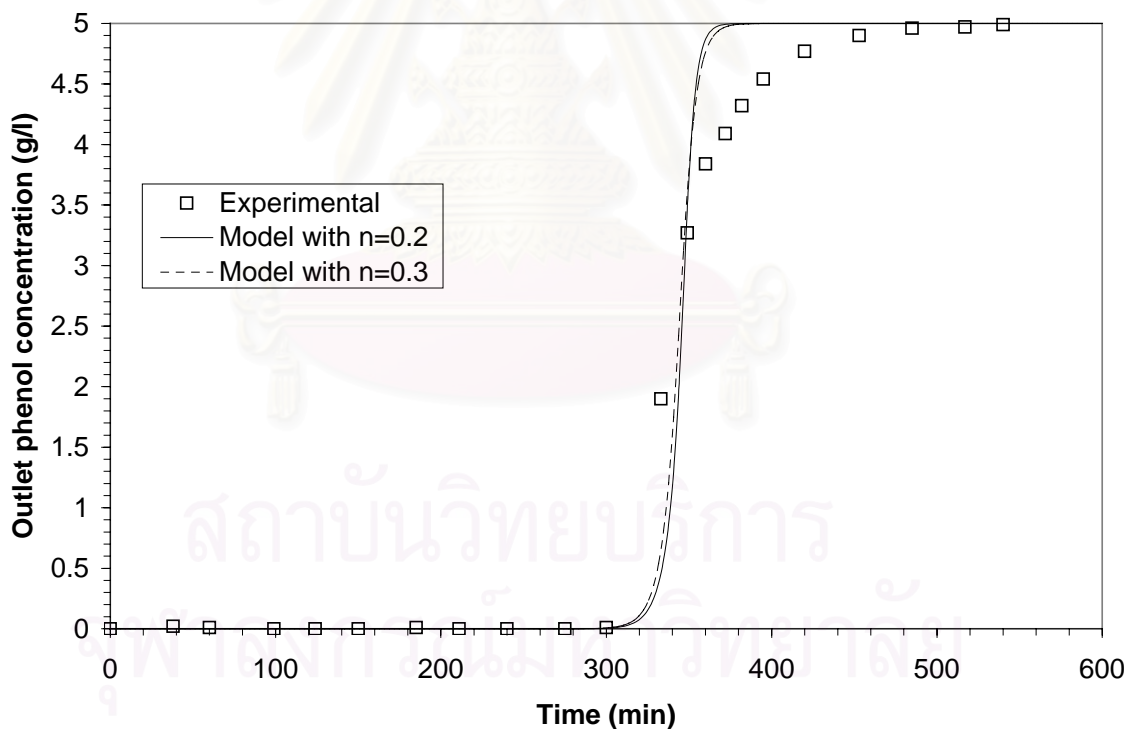


Figure 2-4-1: Experimental and modelled breakthrough curves. $T = 25\text{ }^{\circ}\text{C}$, $F_L = 5.0$ kg/h, $W_{\text{cat}} = 326$ g, $d_p = 1.25\text{--}1.60$ mm, and upflow operation.

The identifications led to the parameters reported in Table 2-4-2, with corresponding isotherms presented in Figure 2-4-2.

Table 2-4-2: Optimised values of Freundlich “a” parameter from experimental breakthrough curve.

a (mol ⁽¹⁻ⁿ⁾ /g _{AC} × l ⁿ)	n (fixed)	criteria*
8.26×10^{-3}	0.2	4.73
1.10×10^{-2}	0.3	4.03

$$* \sum (C_{\text{exp},i} - C_{\text{mod},i})^2$$

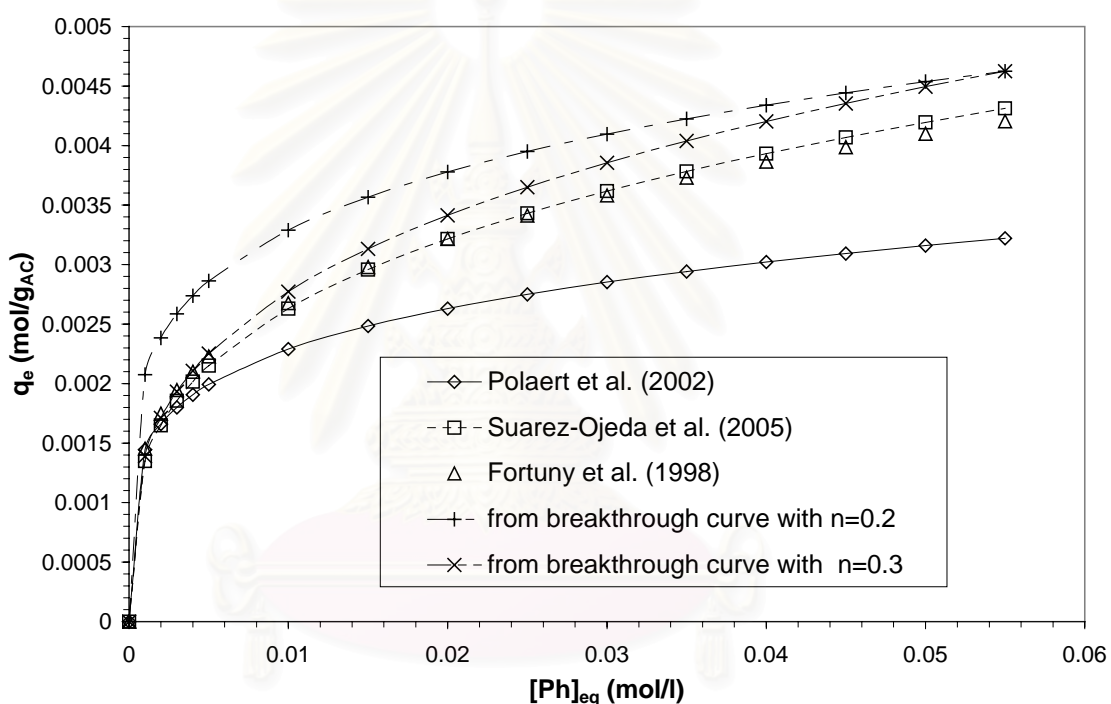


Figure 2-4-2: Adsorption isotherms of phenol on Merck AC at room temperature.

While the optimised isotherms were quite sensible to the value given to n (0.2 or 0.3), it did not much change the modelled breakthrough curve, which was above all sensible to the adsorption capacity at feed concentration.

Finally, the best agreement was found with $n = 0.3$ and experimental isotherms obtained under oxidic conditions in batch stirred reactor.

4.2 Kinetic study on catalytic wet air phenol oxidation on active carbon

To provide a sound interpretation of the data obtained in the pilot plant fixed bed reactor, a kinetic model for the main reaction is needed. It is derived in the first part by batch experiments in autoclave, using the same active carbon particles.

4.2.1 Evaluation of kinetic parameters

4.2.1.1 Interpretation of experimental results

As mentioned before, determination of kinetic parameters in batch reactor was performed using the same uncrushed 1.25–1.6 mm AC pellets as in the fixed bed reactor.

Experimental procedure was explained in Section 3.3.1.2, showing two distinct steps: adsorption step (around 2.5 h) under nitrogen to saturate the AC at reaction temperature, followed by oxidation step (5 to 7 h) where nitrogen was replaced by continuously renewed air.

Operation conditions are reported in Table 2-4-3:

Table 2-4-3: Operating conditions of the kinetic study in batch reactor

Size of sieved particles (mm)	1.25–1.6
Volume weighted diameter of particles, $D[4,3]$ (mm)	1.025
Catalyst load, W_{cat} (g)	9.0
Reactor volume (ml)	300
Liquid volume, V_L (ml)	200
Phenol inlet concentration, $[\text{Ph}]$ (g/l)	2.5–5
Oxygen partial pressure, P_{O_2} (bar)	1.2–3.7
Total operating pressure, P_T (bar)	10.5–20.5
Temperature ($^{\circ}\text{C}$)	130–160
Stirring speed, ω (rpm)	800
F_{air} (NI/h)	60

The same AC sample was used for the entire series of 15 experiments. Two problems had to be solved to allow for a significant estimation of kinetic parameters.

First, a fast deactivation occurred during the first runs as shown in Figure 2-4-3, however, after a steep decrease during the first three experiments, the time-concentration profiles in the liquid phase were found to be very similar. Only experiments at similar AC activity were thus considered to estimate kinetic parameters. Second, the active carbon being a very efficient adsorbent, during a batch oxidation of phenol, due to fast adsorption desorption processes driven by liquid-solid equilibrium and phenol oxidation, phenol concentration is decreasing in both liquid and solid phases. Then, calculations of the reaction rate should account for the total phenol disappearance. Nevertheless, it was observed a severe decay of the adsorption capacity of the AC particles after a few runs so that the amount of phenol re-adsorbed during the first hours under nitrogen became much lower than the value predicted using isotherms with fresh AC [5]. This evolution was explained by a large decrease of the BET surface area, due to the deposition of polymeric compounds, as reported by Suarez-Ojeda *et al.* [13] and also found during the fixed bed experiments (Section 4.2.2.3).

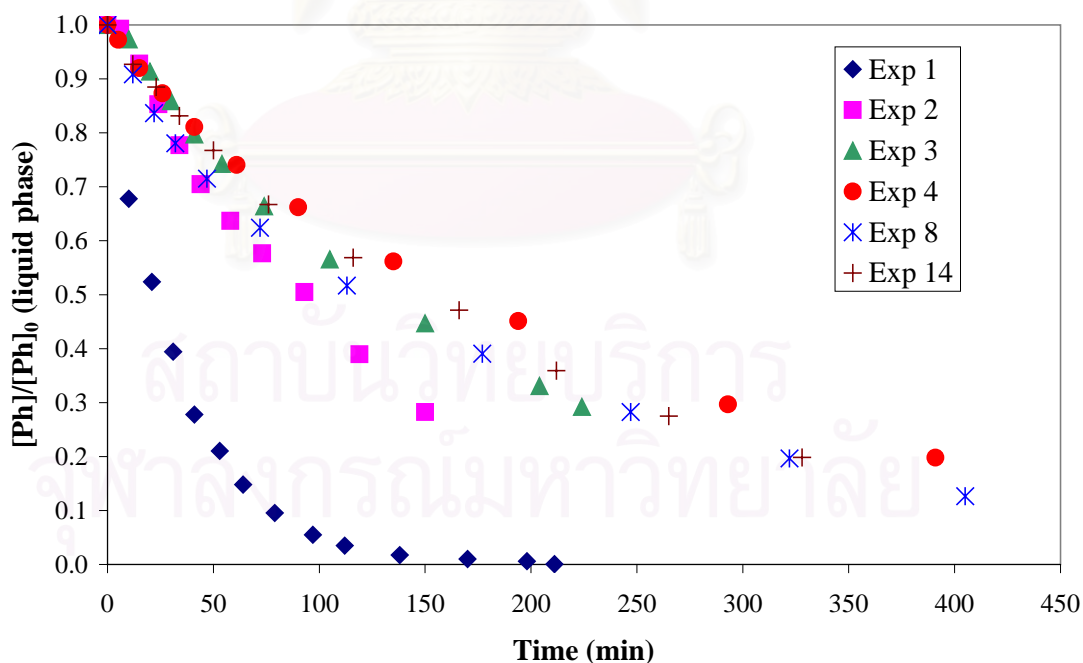


Figure 2-4-3: Time-evolution of phenol concentration in the liquid phase (normalized by initial phenol concentration). $T = 150\text{ }^{\circ}\text{C}$, $P_{\text{O}_2} = 3.3\text{ bar}$, $W_{\text{cat}} = 9\text{ g}$, $V_{\text{L0}} = 200\text{ ml}$, and $\omega = 800\text{ rpm}$.

The rough amounts of phenol consumed in the liquid phase by the reaction and re-adsorbed during the first hours under nitrogen are reported in Table 2-4-4.

Table 2-4-4: Amounts of phenol consumed and re-adsorbed during the experimental series

Exp. No.	P _{O2} (bar)	T (°C)	W _{Phenol} (re)adsorbed after 2.5 h under nitrogen (g) ^(*)	$\tau_{\text{oxidation}}$ (min)	[Ph] ₀ (g/l) ^(***)	[Ph] _f (g/l)	W _{Phenol} consumed in the liquid phase (g) ^(*)
1 ^(**)	3.3	150	1.27	211	2.78	2×10^{-3}	0.55
2 ^(**)	3.3	150	0.65	150	3.79	1.07	0.54
3 ^(**)	3.3	150	0.12	224	2.94	0.86	0.42
4 ^(**)	3.3	150	0.15	391	3.79	0.75	0.61
5	3.5	140	0.20	363	4.03	1.38	0.53
6	3.7	130	0.10	414	3.74	1.78	0.39
7	3.0	160	0.018	353	3.45	0.12	0.67
8	3.3	150	0.22	405	4.58	0.58	0.80
9	1.3	150	0.083	335	4.86	2.00	0.57
10	2.3	150	3.6×10^{-3}	384	3.24	0.60	0.53
11	3.4	140	0.13	364	4.50	1.17	0.61
12	3.4	130	0.058	411	3.97	1.96	0.40
13				Not usable			
14	3.3	150	0	328	2.54	0.5	0.41
15	1.8	150	0.13	387	4.38	1.42	0.59

^(*) calculation based on constant $V_L = 200$ ml

^(**) not used for kinetics evaluation

^(***) after adsorption step

A calculation for experiment no. 7 corresponding to the highest phenol conversion in the liquid phase showed that an evaluation of kinetics based on the evolution of phenol concentration in the liquid phase only (neglecting the disappearance of adsorbed phenol) would lead to an underestimation of phenol consumption of around 30% (0.22/0.67). Most often this ratio remained under 15%. As the determination of new adsorption parameters at each experiment would be a delicate task, it was decided to estimate the kinetic parameters based on the liquid phase only. Moreover, the error committed mainly affected the phenol degradation rates measured at the end of experiments (corresponding to very low phenol concentrations in the liquid phase and thus steeper part of the isotherm) and for which associated reaction volume was overestimated in the model: a mean constant value

was indeed implemented (around 175 ml), while due to sampling and vaporisation (even limited by the condenser), the solution volume was decreased up to 55 ml between the beginning and the end of each run. These two errors are then balancing at least partly.

A first order towards phenol was then found by plotting the logarithm of phenol concentration (in the liquid phase) as a function of time (not shown here).

Finally, the calculation of the Weisz modulus ϕ' :

$$\phi' = \frac{\rho_p R_{O_2}^{app}}{D_{O_2}^{eff} C_{L,O_2}^*} \left(\frac{d_p}{6} \right)^2 \quad (2-4-2)$$

at initial time (oxygen being the limiting reactant) led to: $0.45 < \phi' < 1.5$ (based on complete phenol oxidation to H_2O and CO_2), indicating that the reaction within the pores of the 1.5 mm pellets occurred in the intermediate diffusion regime, however close to kinetic control.

4.2.1.2 Modelling of batch reaction and evaluation of intrinsic kinetic parameters

In agreement with previous kinetic studies [4,44], a simple power law was convenient to accurately describe the phenol oxidation over AC assuming a first order of phenol (as seen previously), while the oxygen order had to be determined by the optimisation algorithm. The following rate equation for phenol destruction was thus used:

$$R_{phenol} = -k_0 \exp\left(\frac{-E}{RT}\right) C_{Ph} x_{O_2}^\alpha \quad (2-4-3)$$

Based on the Weisz modulus values, the intrinsic kinetics of phenol destruction was optimised from the autoclave experiments using a batch reactor model that accounted for transient diffusion of both oxygen and phenol inside the catalyst pores [122].

In the model, spherical geometry was assumed with $D[4,3] = 1$ mm as reference diameter, and a tortuosity value of 3 to determine the effective diffusivities of oxygen and phenol.

Other assumptions were:

- variations of phenol amount adsorbed on AC were neglected (as previously discussed),

- complete mineralisation of reacted phenol to CO₂ and H₂O was assumed, so that $R_{O_2} = 7 \times R_{\text{phenol}}$,
- external mass-transfer limitation was negligible (intense mechanical stirring),
- pellets were assumed to be isothermal, and
- liquid volume variations were neglected (a mean value was implemented).

In these conditions the mass balances led to the following classical equation:

$$\varepsilon_p \frac{\partial C_j}{\partial t} = D_j^{\text{eff}} \left(\frac{\partial^2 C_j}{\partial r^2} + \frac{2}{r} \frac{\partial C_j}{\partial r} \right) + \rho_p R_j \quad (2-4-4)$$

with boundary conditions:

$$\bullet \forall t, r = 0 \quad \frac{\partial C_j}{\partial r} = 0 \quad (\text{condition for symmetry}) \quad (2-4-5)$$

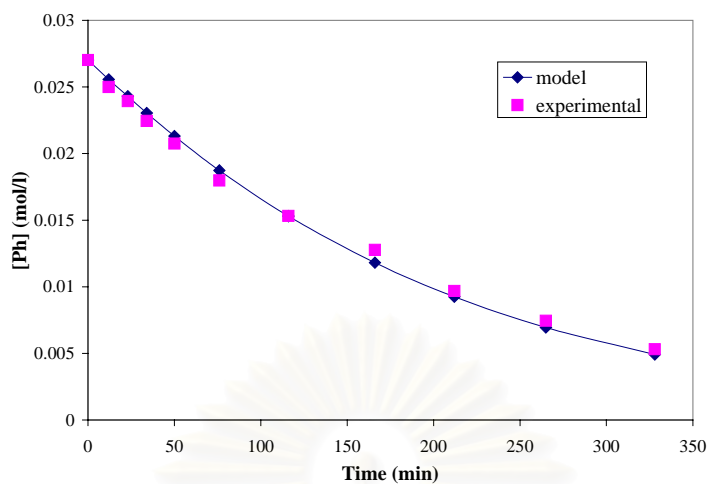
$$\bullet \forall t, r = r_p \quad C_j = C_{L,j} \quad (\text{negligible external mass-transfer resistance})$$

$$\text{and } V_L \frac{dC_{L,j}}{dt} = - \frac{D_j^{\text{eff}} \times W_{\text{cat}}}{\rho_p} \times \frac{6}{d_p} \times \frac{\partial C_j}{\partial r} \Big|_{r=r_p} \quad \text{for phenol} \quad (2-4-6)$$

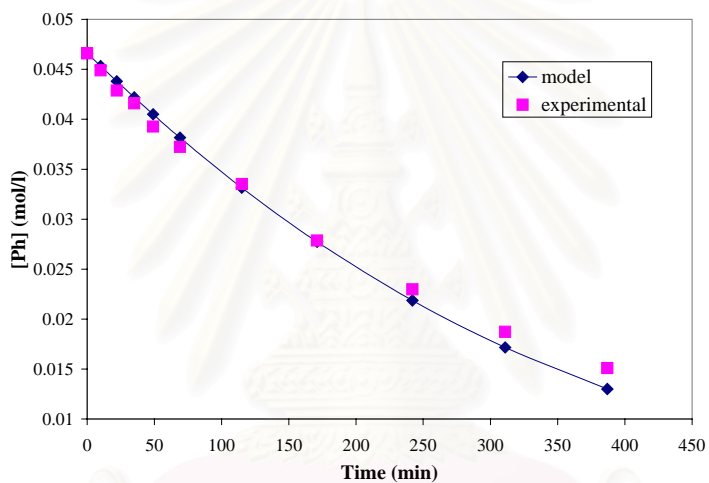
The LHS term of Equation 2-4-4 (negligible regarding the ratio of catalyst to liquid volume) was kept for numerical reasons.

The proposed model led to a partial differential equations system (PDE). It was solved by the method of lines: spatial derivatives were discretized using central difference formulas (50 spatial divisions) and the resultant ODE system was solved by the software package DISCO [123,124], using the Gear method [125].

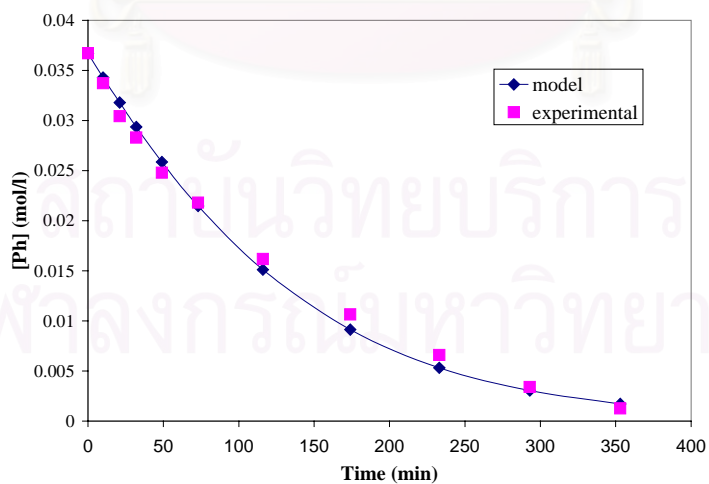
A Gauss-Newton method was used to optimise, from the time-evolution of phenol concentration in the liquid phase, the oxygen order at 140 °C, 1.2 to 3.7 bar of oxygen partial pressure, and the rate constants at different temperatures (see Figures 2-4-4a, b, and c).



(a)



(b)



(c)

Figure 2-4-4: Experimental and calculated time-concentration profiles in the liquid phase ($W_{\text{cat}} = 9$ g, stirrer speed of 800 rpm): (a) $P_{\text{O}_2} = 3.3$ bar, $T = 150$ °C; (b) $P_{\text{O}_2} = 1.8$ bar, $T = 150$ °C; (c) $P_{\text{O}_2} = 3.0$ bar, $T = 160$ °C

A 0.5 oxygen order was found to match the experimental phenol concentrations and the rate constants optimised at 130, 140, 150, and 160 °C are reported in Table 2-4-5. The corresponding Arrhenius plot (Figure 2-4-5) gave a slope and ordinate of $-8,895.7 \text{ K}^{-1}$ and 12.834, respectively, resulting in an activation energy and pre-exponential factor for phenol oxidation of 74 kJ/mol and $3.75 \times 10^5 \text{ m}^3 \text{ s}^{-1} \text{ kg}^{-1}$, respectively. Finally the reaction rate was

$$R_{phenol} = -3.75 \times 10^5 \exp\left(\frac{-74000}{RT}\right) C_{Ph} x_{O_2}^{0.5} \quad (2-4-3')$$

Table 2-4-5: Intrinsic rate constants at different temperatures from batch phenol destruction experiments with: $W_{cat} = 9 \text{ g}$, stirrer speed of 800 rpm.

Temperature (K)	k ($\text{m}^3 \text{ s}^{-1} \text{ kg}_{cat}^{-1}$)
403.15	1.00×10^{-4}
413.15	1.63×10^{-4}
423.15	2.71×10^{-4}
433.15	4.62×10^{-4}

สถาบันวิทยบริการ
จุฬาลงกรณ์มหาวิทยาลัย

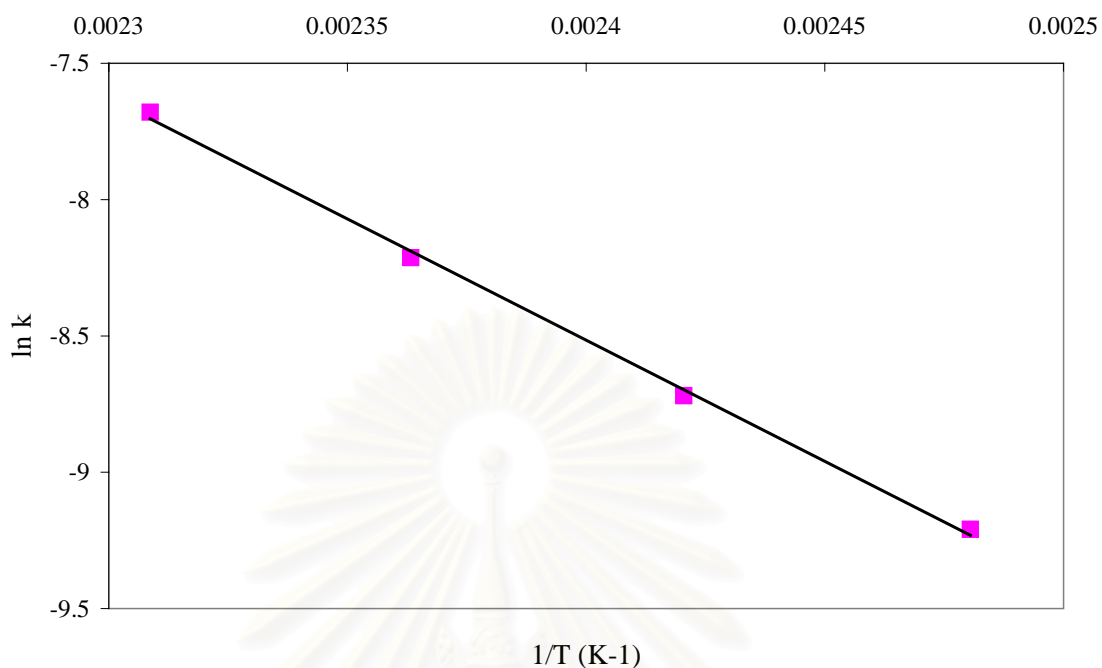


Figure 2-4-5: Arrhenius plot of intrinsic kinetics obtained in batch reactor.

4.2.2 Continuous oxidation in fixed bed reactor

The continuous oxidation experiments were carried out in a jacketed fixed bed reactor (Figure 2-3-2) in both upflow and downflow cocurrent modes, in order to compare the results between these two flow modes.

4.2.2.1 Operating conditions and flow regimes

The AC bed dimensions and operating conditions for phenol oxidation study are summarized in Table 2-4-6.

These investigated conditions were calculated as to give water vaporisation rate below 30%, and gaseous oxygen flow rate well above stoichiometry.

Table 2-4-6: AC bed dimensions and operating conditions for phenol oxidation in fixed bed reactor

Reactor diameter (mm)	25.4
Reactor height (m)	1.2
Size of sieved particles (mm)	1.25–1.6
Volume weighted diameter of particles, $D_{[4,3]}$ (mm)	1.025
Catalyst load, W_{cat} (g)	326
Phenol inlet concentration, [Ph] (g/l)	5
Oxygen partial pressure, P_{O_2} (bar) (equilibrium pressure at reactor outlet)	0.5–2.0
Total operating pressure, P_T (bar)	7.0–11.2
Oil temperature, T_{oil} (°C)	120–160
Liquid flow rate, F_L (kg/h)	0.5–3.5
Space time, τ (h)	0.095–0.65
Liquid superficial velocity (inlet), $u_{L,inlet}$ (mm/s)	0.3–2
Gas flow rate, F_G (NL/h)	50–200
Gas superficial velocity (inlet), $u_{G,inlet}$ (mm/s)	5–25

To define the flow regimes of each condition used in this experiment, liquid mass superficial flow rate (L) and gas mass superficial flow rate (G) for each condition are calculated accordingly to the Equations 2-4-7 and 2-4-8.

$$L = \frac{\dot{m}_L}{\pi \times \frac{D_c^2}{4}} \quad (2-4-7)$$

$$G = \frac{F_{G,NTP} \times \rho_{G,NTP}}{\pi \times \frac{D_c^2}{4}} \quad (2-4-8)$$

(NTP = Normal conditions of Temperature and Pressure)

The ratio of liquid mass superficial flow rate to gas mass superficial flow rate (L/G) was plotted as a function of gas mass superficial flow rate (G) and compared with the flow map obtained from Turpin and Huntington [69] (for upflow mode) and from Charpentier [66] (for downflow mode) as displayed in Figure 2-4-6.

For the conditions used in the cocurrent upflow and cocurrent downflow modes ($F_L = 0.5$ to 3.5 kg/h and $F_G = 50$ to 200 NI/h), the upflow mode was operated either in bubble flow regime or transition to pulsed flow regime, while the downflow mode was clearly operated in trickle flow (Figure 2-4-6).

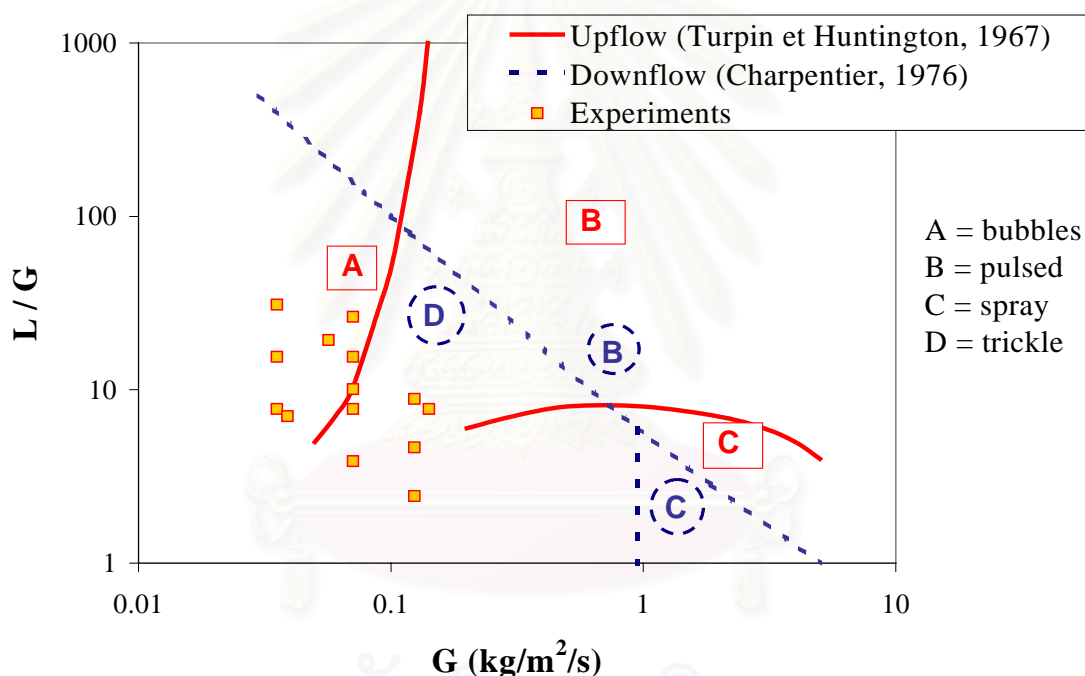


Figure 2-4-6: Location of our experimental conditions in the flow map of three phase fixed bed reactors for air-water system (cocurrent upflow: Turpin and Huntington [69]) cocurrent downflow: Charpentier [66]).

4.2.2.2 Transient profiles

Steady state conditions of reaction were verified through regular sampling as shown in Figure 2-4-7. The figure illustrates typical time-concentration profiles obtained from upflow and downflow at a given set of operating conditions. Transient

lengths to reach steady state mainly depend on the liquid flow rate selected as well as the operating conditions of the previous run, leading to different preliminary adsorption times.

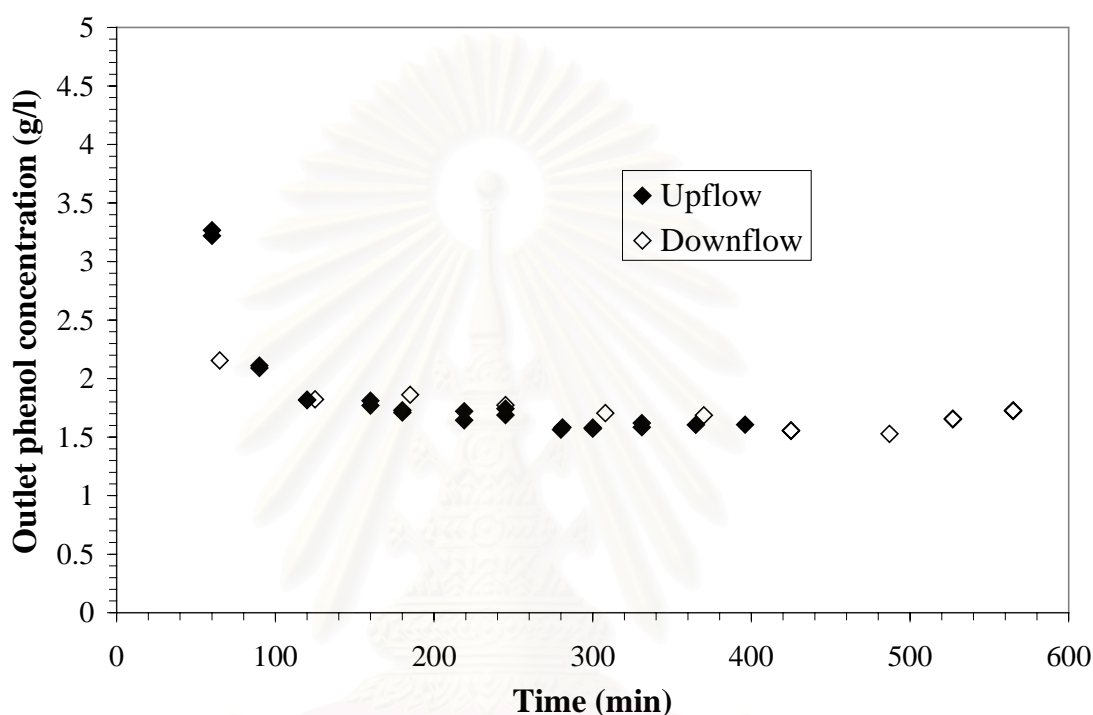


Figure 2-4-7: Transient phenol concentration profiles for cocurrent upflow and downflow fixed bed reactors. Conditions: oxygen partial pressure 1.2 bar, oil temperature 160 °C, gas flow rate 175 NI/h, and liquid flow rate 0.55 kg/h.

4.2.2.3 Activity of catalyst

Catalyst activity had been regularly checked at the following standard conditions: heating-oil temperature of 140 °C, liquid flow rate of 1 kg/h, gas flow rate of 100 NI/h, and oxygen partial pressure of 1.2 bar. After more than 300 working hours corresponding to 5 g of phenol treated per g of AC, no deactivation was observed when operating the reactor at 120 and 140 °C. However, the catalyst activity

was reduced by 20% after only a few runs (30 h) at the highest reaction temperature of 160 °C.

The analysis of samples of aged AC from different parts of the bed showed that during experimental series the AC surface area dramatically dropped to 35–70 m²/g, and pore volume to less than 0.15 cm³/g. These large variations seemed to occur very soon and have more effects on the adsorption performance than on catalytic activity.

Thermogravimetric analysis (TGA) of fresh and aged ACs (see Appendix 2-5A) showed different behaviour of the two carbons: for the fresh one, weight loss was very small (less than 3%) up to 700 °C when combustion started to occur, while for the aged one, significant weight loss started at lower temperatures (around 200 °C), showing that some low volatile and/or uneasily accessible compounds might be deposited on the AC.

4.2.2.4 Influence of operating parameters on phenol conversion

In the experimental series, the four main operating parameters (T_{oil} , P_{O_2} , u_L , and u_G) and flow direction have been investigated varying adequately the standard conditions (see Table 2-4-6).

4.2.2.4.1 Effect of temperature

The effects of oil temperature (120 to 160 °C) on phenol conversion over different space times (τ) (0.095 to 0.65 h) were investigated at constant gas inlet velocity of 1.1 to 1.2×10^{-2} m/s. The total pressure was changed accordingly to the temperatures in order to keep constant partial oxygen pressure at around 1.2 bar (based on thermodynamic equilibrium).

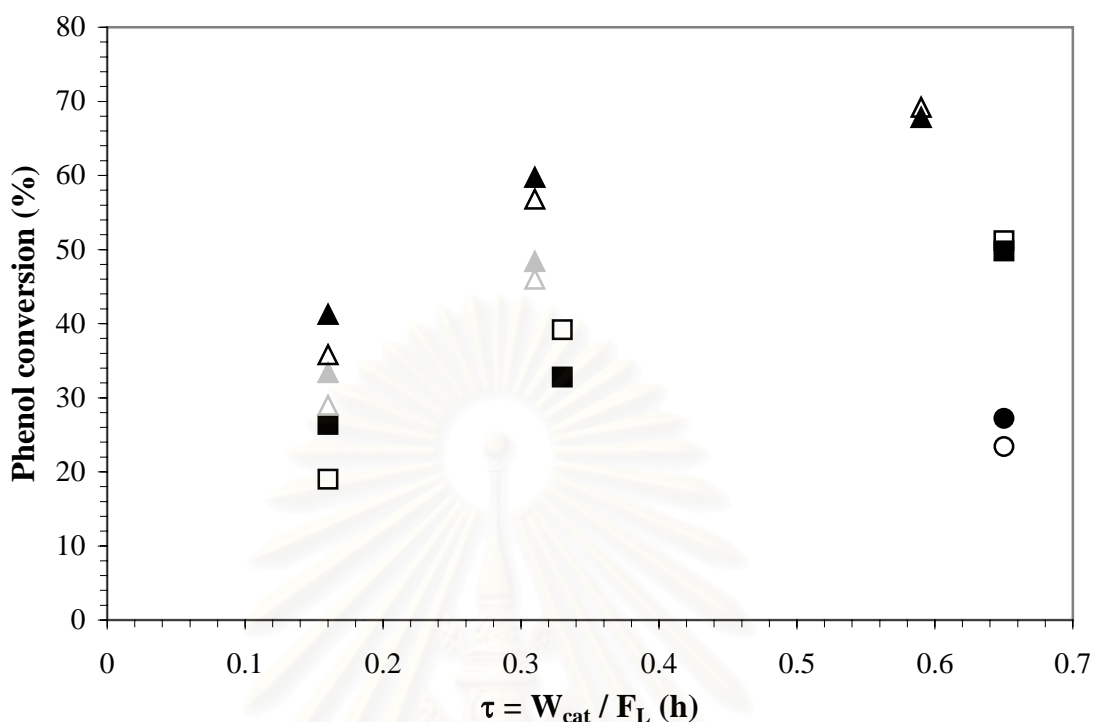


Figure 2-4-8: Phenol conversion versus the liquid contact time for downflow (open symbols) and upflow (filled symbols) at different oil temperatures: (O) 120 °C, (□) 140 °C, (△) 160 °C; $u_{G,inlet} = 1.1-1.2 \times 10^{-2}$ m/s, $P_{O_2} = 1.12-1.2$ bar. Grey symbols show experimental results without correction by catalyst deactivation.

The phenol conversion was significantly increased when the oil temperature increased. For instance, same phenol conversion was roughly obtained at $\tau = 0.16$ h, $T_{oil} = 160$ °C and at $\tau = 0.33$ h, 140 °C (*i.e.* at about half liquid flow rate) indicating that the overall reaction rate approximately doubled within 20 °C. Such temperature effect suggested that phenol destruction in the pilot fixed bed reactor might be only marginally limited by external mass transfers, which are not much influenced by temperature. At given temperature, pressure and gas velocity, the phenol conversion was increased with the increase of space time (or decrease in liquid flow rate).

When comparing phenol conversions obtained in same conditions from the upflow and downflow experiments (Figures 2-4-8 to 2-4-10), they were found to be quite similar in the investigated range of liquid space time, oil temperature, oxygen

partial pressure, and gas velocity. This result was confirmed by the standard deviation between upflow and downflow that was calculated to about 12% without any clear correlation to the four operating parameters.

4.2.2.4.2 Effect of oxygen partial pressure

The effects of oxygen partial pressure (0.5, 1.2, and 2.0 bar) on phenol conversion at various space times (τ) (0.095 to 0.65 h) were studied at 140 °C and gas inlet velocity of 1.1 to 1.2×10^{-2} m/s. The gas composition (O_2 to N_2 ratio) was changed accordingly to the oxygen partial pressure.

As shown in Figure 2-4-9, the phenol conversions were noticeably increased in both flow modes when the oxygen partial pressure increased (from 0.5 bar to 1.2 bar) in rough agreement with kinetics. However, at oxygen partial pressure of 2.0 bar, the oxygen partial pressure seemed to have less effect on phenol conversion. This might be due to the catalyst deactivation; the four experiments at low space time were conducted at the end of the experimental set (and after the experiments at 160 °C), therefore the catalyst was yet partly deactivated.

Corrected values taking roughly into account this catalyst deactivation (see Section 4.2.2.3) showed more expected trends.

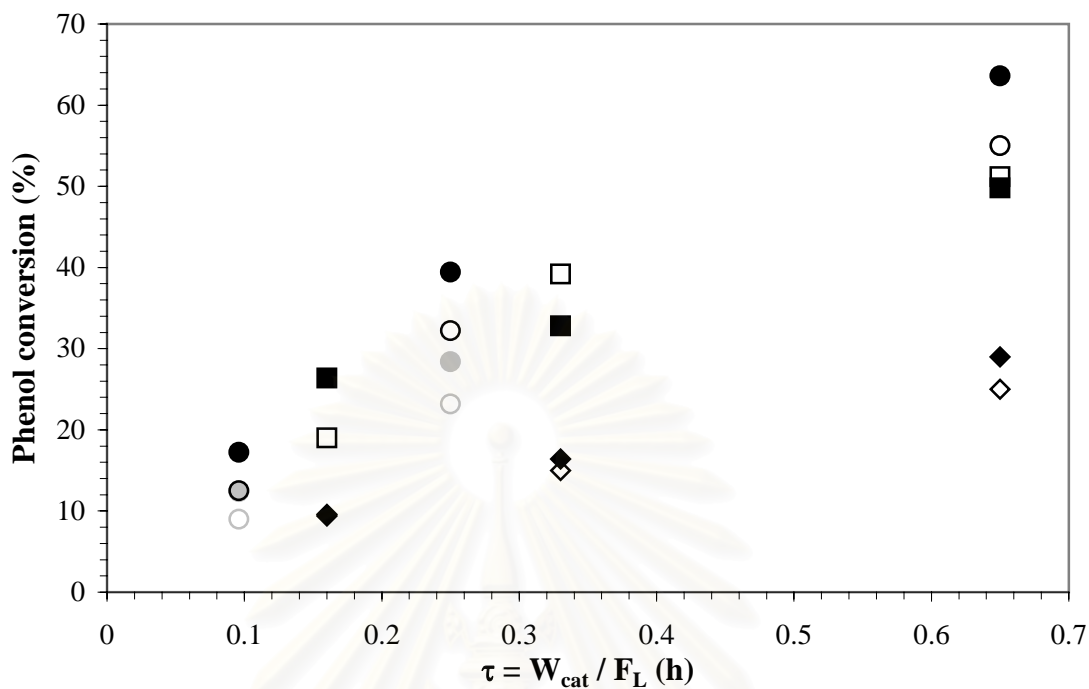


Figure 2-4-9: Phenol conversion versus the liquid contact time for downflow (open symbols) and upflow (filled symbols) at different oxygen partial pressures: (\diamond) 0.5 bar, (\square) 1.2 bar, (O) 2 bar; $u_{G,inlet} = 1.1\text{--}1.2 \times 10^{-2}$ m/s, $T_w = 140$ °C. Grey symbols show experimental results without correction by catalyst deactivation.

4.2.2.4.3 Effect of gas inlet velocity

The effects of gas velocity ($u_{G,inlet}$) (0.53×10^{-2} , 1.1×10^{-2} , and 2.1×10^{-2} m/s) on phenol conversion over different liquid flow rates (1.0 and 2.0 l/h) and different oxygen partial pressures (0.5 and 1.2 bar) were studied at temperature of 140 °C. The results are reported in Figure 2-4-10.

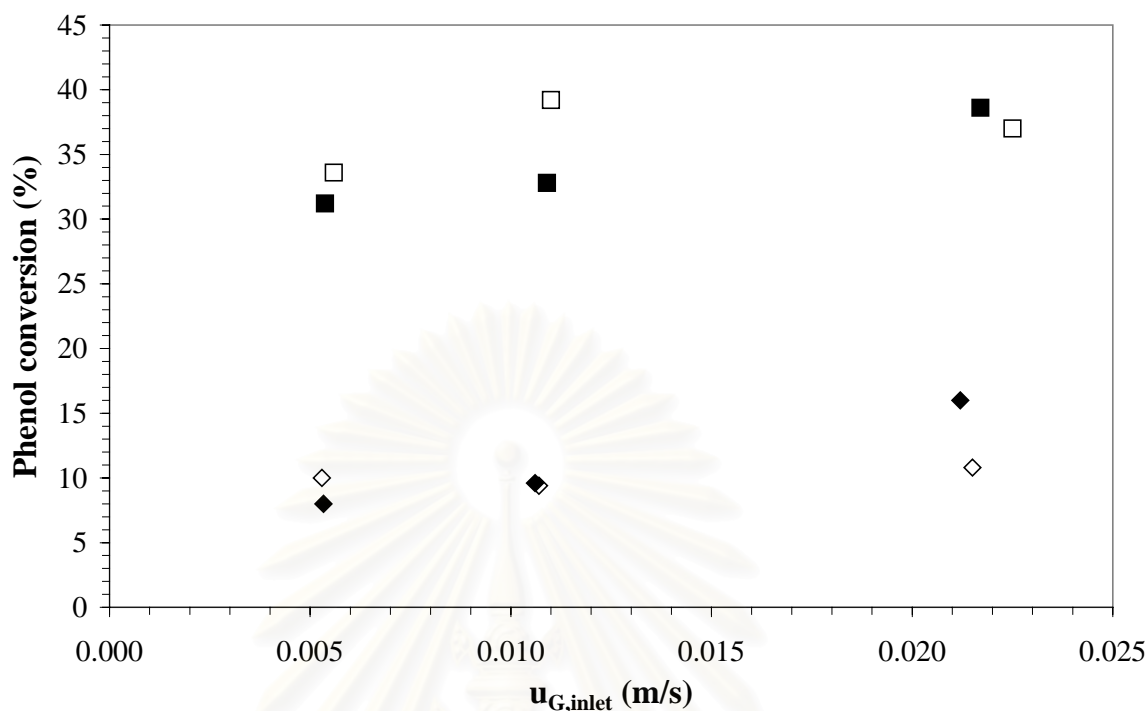


Figure 2-4-10: Phenol conversion versus gas velocity for downflow (open symbols) and upflow (filled symbols) at different operating conditions ($T_w = 140$ °C): (◇) $P_{O_2} = 0.5$ bar and $F_L = 2$ l/h, (□) $P_{O_2} = 1.2$ bar and $F_L = 1$ l/h.

The phenol conversion appeared to be slightly sensitive to gas inlet velocity in upflow mode, while almost no effect was found in downflow system. Other operating conditions being fixed, phenol conversions obtained from upflow experiments were improved when the gas inlet velocities increased, while in downflow mode phenol conversions were relatively similar whatever the gas inlet velocities (above stoichiometric value). This may be due to an increase of the external mass transfer coefficients in upflow mode, while in downflow operation they were known to depend mostly on the liquid velocity.

For the upflow experiment, when the gas inlet velocity increased, the number of bubbles of nearly same size (rising at higher or same velocity) increased and the flow transition from bubble to pulse flow regime could also occur (*cf.* Figure 2-4-6), enhancing thus oxygen transfer to the liquid phase (larger interfacial area and regime transition) and from the liquid phase to the catalyst surface (increased frequency of bubbles over the catalyst) [126].

In contrast, in the downflow experiments, the two-phase flow is completely segregated at the moderate gas and liquid velocities operated, with no significant interaction between the gas and the liquid flowing in the interparticle space. Therefore the increase in gas velocity did not significantly improve gas-liquid and liquid-solid mass transfer coefficients. Moreover a fraction of the external particle surface was covered by an extremely thin liquid layer or directly exposed to the gas phase, this partial wetting having a quite huge influence on external mass transfer and being only affected by liquid velocity.

However, vaporisation of the solvent having to be accounted for, the scenario was even more complex, as an increase of gas flow rate enhanced water vaporisation, which increased phenol concentration in the remaining liquid. Surprisingly, this last effect was not experimentally noticeable and will be discussed in more details in the modelling section.

Shortly, the poor effect of gas flow rate in the two modes could be explained either by marginal effect of external mass transfer in quasi-kinetic control or by its balanced influences on mass transfer and on vaporisation.

Based upon the experiments mentioned above, it was concluded that the phenol destruction was significantly improved with the increase of operating temperature, oxygen partial pressure and liquid space time, and that the flow mode did not much affect the phenol destruction in this pilot reactor. The highest phenol conversion (69%) was obtained under the following conditions: 160 °C, 1.2 bar of oxygen partial pressure, 0.59 h of space time, and 175 NI/h of gas flow rate. However, under this high temperature condition the catalyst deactivation was much higher than that observed in the 140 °C experiments (the highest phenol conversion obtained from 140 °C experiments was 51%, at oxygen partial pressure of 1.2 bar, and 0.65 h space time).

4.2.2.5 Characterisation of reaction products

4.2.2.5.1 Main intermediates

Before the steady state was reached, the collected reaction samples were analysed by means of HPLC analysis (using fast analysis method which was previously described in the Section 3.2.1) to obtain the transient phenol concentration

profiles for each experiment. After the steady state was attained, reaction samples were also analysed to evaluate the concentration of intermediate compounds (using full analysis method as previously described in the Section 3.2.1). The intermediates in the reaction products were identified by comparison with pure commercial samples. HPLC analysis revealed that phenol oxidation process (in both two flow modes) yielded numerous intermediates (about 20 compounds). Among them, only twelve compounds could be successfully identified, including oxalic acid, formic acid, malonic acid, acetic acid, maleic acid (*cis*-2-butenedioic acid), fumaric acid (*trans*-2-butenedioic acid), hydroquinone (benzene-1,4-diol), 1,4-benzoquinone, catechol (benzene-1,2-diol), 4-hydroxybenzoic acid, and 2-hydroxybenzoic acid. According to Devlin and Harris [127] and Eftaxias [4] other compounds were searched: propanoic acid, muconic acids (*trans,trans*- and *cis,cis*-), succinic acid, acrylic acid, pyrogallol, phloroglucinol, glyoxal, and glyoxylic acid, but they were either not found or present in trace amounts in the reaction products.

Typical HPLC chromatograms of (a-b) fast analysis of phenol standard and reaction sample, (c) full analysis of standard solution including some of the principle intermediates, and (d) full analysis of phenol oxidation product are presented in the Appendix 2-6A to 2-9A.

The concentration profiles of six principal intermediates (formic acid, acetic acid, malonic acid, oxalic acid, 1,4-benzoquinone, and 4-hydroxybenzoic acid) obtained from phenol oxidation in both two flow modes are shown in Figures 2-4-11 to 2-4-16. It should be noted that the concentrations of other identified intermediates were lower than 0.5 mmol/l, therefore their concentration profiles are not shown here.

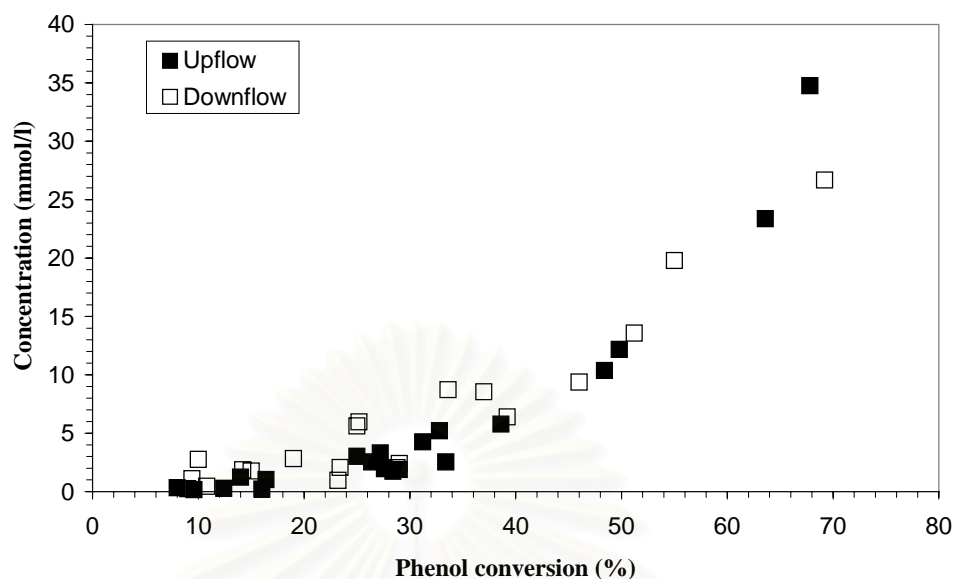


Figure 2-4-11: Formic acid concentration profile after phenol conversion in both upflow and downflow fixed bed reactors. Inlet phenol concentration 53 mmol/l, temperature 140 to 160 °C, oxygen partial pressure 0.5 to 2.0 bar, liquid flow rate 0.5 to 3.5 kg/h, and gas flow rate 50 to 200 NI/h.

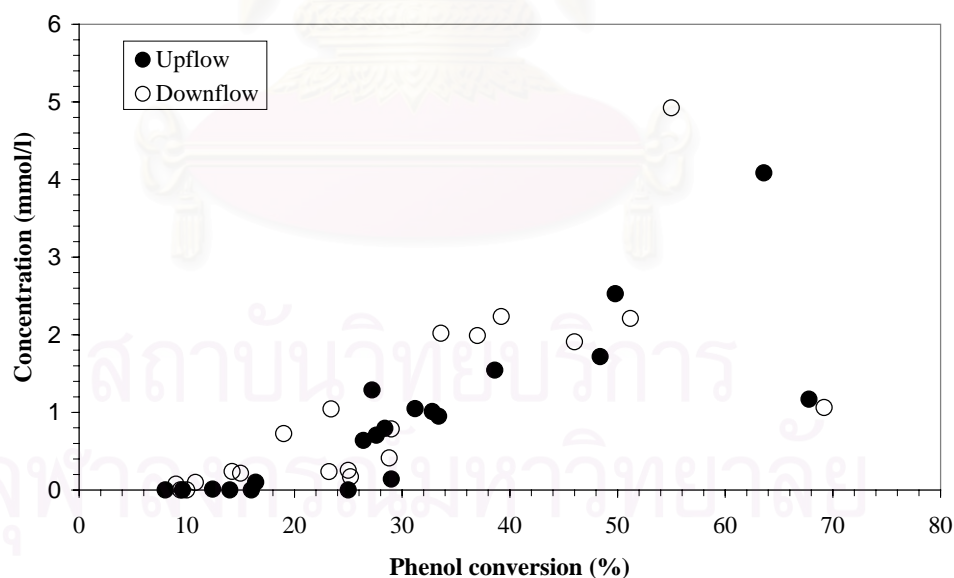


Figure 2-4-12: Acetic acid concentration profile after phenol conversion in both upflow and downflow fixed bed reactors. Inlet phenol concentration 53 mmol/l, temperature 140 to 160 °C, oxygen partial pressure 0.5 to 2.0 bar, liquid flow rate 0.5 to 3.5 kg/h, and gas flow rate 50 to 200 NI/h.

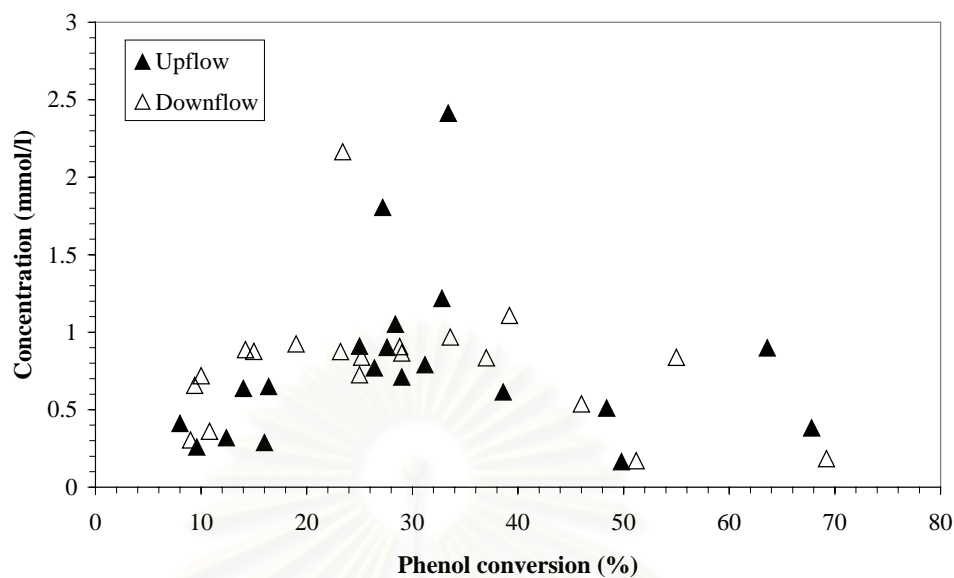


Figure 2-4-13: Malonic acid concentration profile after phenol conversion in both upflow and downflow fixed bed reactors. Inlet phenol concentration 53 mmol/l, temperature 140 to 160 °C, oxygen partial pressure 0.5 to 2.0 bar, liquid flow rate 0.5 to 3.5 kg/h, and gas flow rate 50 to 200 NI/h.

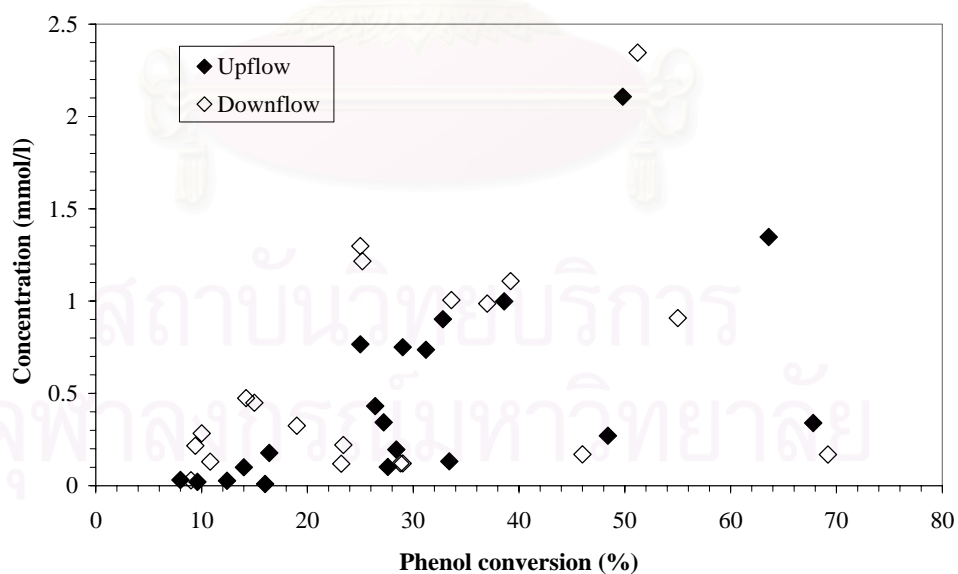


Figure 2-4-14: Oxalic acid concentration profile after phenol conversion in both upflow and downflow fixed bed reactors. Inlet phenol concentration 53 mmol/l, temperature 140 to 160 °C, oxygen partial pressure 0.5 to 2.0 bar, liquid flow rate 0.5 to 3.5 kg/h, and gas flow rate 50 to 200 NI/h.

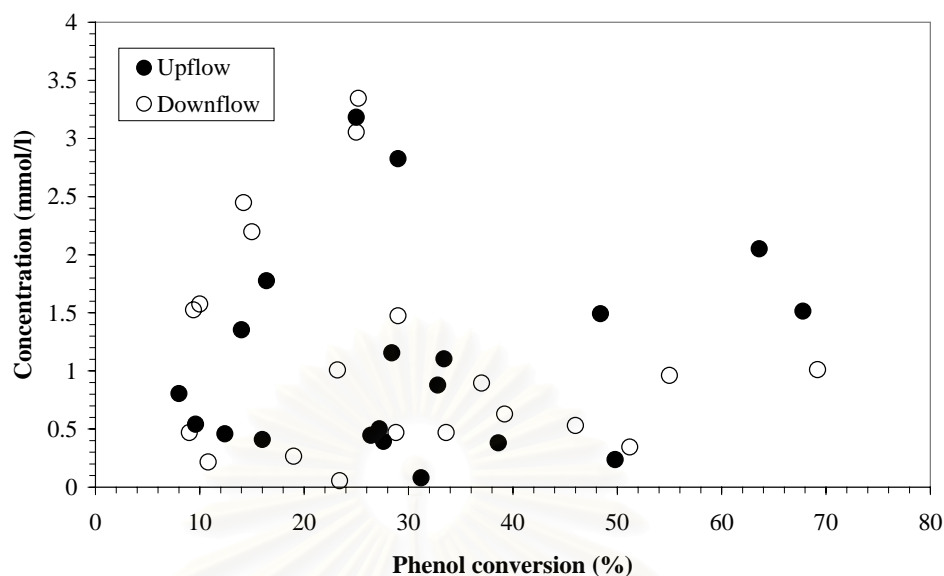


Figure 2-4-15: 1,4-Benzoquinone concentration profile after phenol conversion in both upflow and downflow fixed bed reactors. Inlet phenol concentration 53 mmol/l, temperature 140 to 160 °C, oxygen partial pressure 0.5 to 2.0 bar, liquid flow rate 0.5 to 3.5 kg/h, and gas flow rate 50 to 200 NI/h.

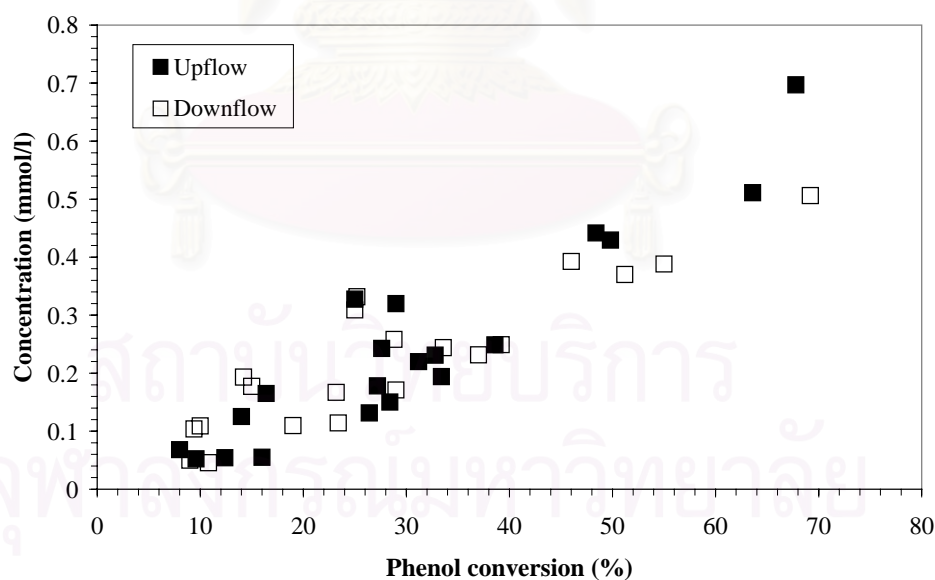


Figure 2-4-16: 4-Hydroxybenzoic acid concentration profile after phenol conversion in both upflow and downflow fixed bed reactors. Inlet phenol concentration 53 mmol/l, temperature 140 to 160°C, oxygen partial pressure 0.5 to 2.0 bar, liquid flow rate 0.5 to 3.5 kg/h, and gas flow rates 50 to 200 NI/h.

Formic and acetic acids were the major intermediates detected in the reaction products (Figures 2-4-11 to 2-4-16). Formic acid concentration in reaction products was found up to 35 mmol/l (Figure 2-4-11), while acetic acid concentration in reaction products was found up to 5 mmol/l. Indeed it was often reported [4,13,38,127] that the major intermediates from the WAO of phenol (both non-catalytic and catalytic reactions) were the highly oxidized and highly stable final organic products, which were formic acid, acetic acid, and oxalic acid. According to Figures 2-4-11 to 2-4-16, it was found that formic acid, acetic acid, and 4-hydroxybenzoic acid concentrations were clearly increased when phenol conversion increased, while other major intermediates had no clear correlation to phenol conversion. Therefore, it is no doubt that at high phenol conversion observed in this present study, higher amounts of formic acid and acetic acid were obtained, because these acids are the final organic compounds derived from oxidative process. However, formic and acetic acids are regarded as non-hazardous chemicals, since these acids can be utilized as carbon source by microorganism (*Pseudomonas* sp., *Alcaligene* sp., and cocci sp.) [128–130]. When comparing the identified intermediates obtained from this study with other studies on catalytic aqueous phenol oxidation similar intermediate distributions were obtained.

Ohta *et al.* [36] reported the formation of catechol, hydroquinone, maleic acid, and oxalic acid as the intermediates from CWAO of phenol using copper oxide as catalyst. With similar system to that of Ohta *et al.* [36], Fortuny *et al.* [38] found additional intermediates including benzoquinone, malonic acid, acetic acid, and formic acid. Pintar and Levec [131] also reported the formation of acetic acid, in considerable quantities, as a final organic product, while benzoquinone and dihydric phenols were present in small quantities. Moreover, Pintar and Levec [131] reported that neither maleic nor oxalic acids was found in the reaction products obtained from the CWAO of phenol using ZnO, CuO, and γ -Al₂O₃ as catalysts.

Eftaxias [4] investigating CWAO of phenol on active carbon (Merck) found additional two compounds: 4-hydroxybenzoic acid and 2-hydroxybenzoic acid which could only appear *via* carbon coupling. These acids were also found in our reaction media suggesting that phenoxide ions (generated from phenol) could undergo electrophilic aromatic substitution with generated CO₂. The reaction mechanisms to form these two acids are shown in the Appendix 2-10A.

4.2.2.5.2 Determination of chemical oxygen demand

As previously mentioned, there were about twenty intermediates found as the result of phenol oxidation, while only twelve could successfully be identified. Therefore, chemical oxygen demand (COD), an alternative measurement for organic contents, was employed in order to evaluate organic materials in the reaction products. The comparison of measured COD values and HPLC-based COD values is presented in Figure 2-4-17.

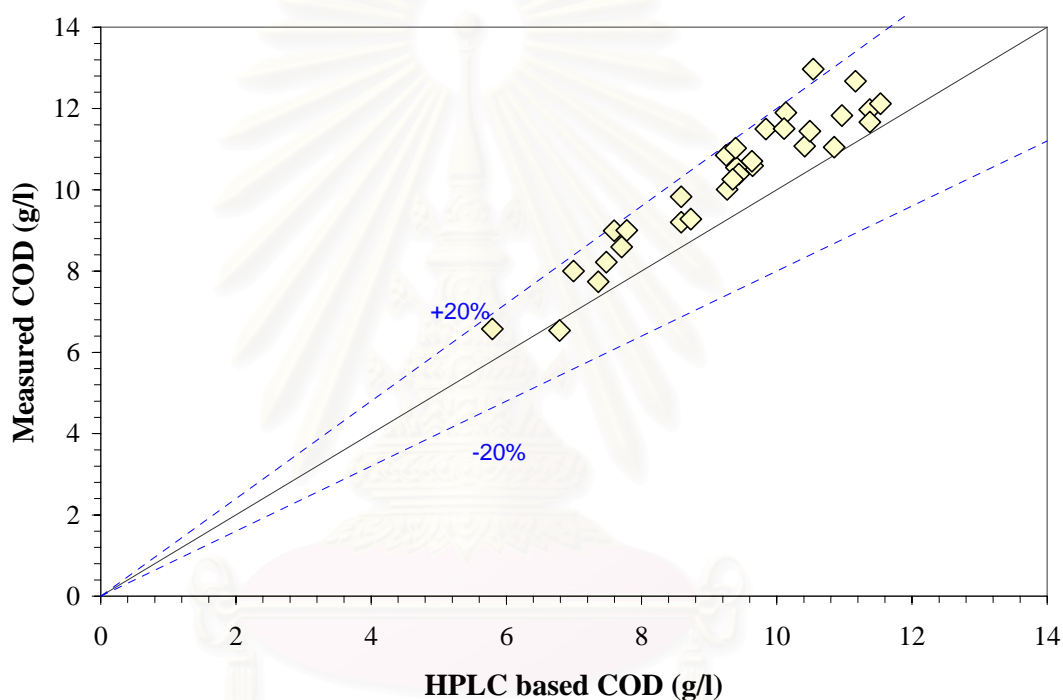


Figure 2-4-17: Comparison of measured COD values and HPLC-based COD values in both upflow and downflow fixed bed reactors. Inlet phenol concentration 53 mmol/l, temperature 140 to 160°C, oxygen partial pressure 0.5 to 2.0 bar, liquid flow rate 0.5 to 3.5 kg/h, and gas flow rate 50 to 200 NI/h.

As seen in Figure 2-4-17, HPLC-based COD values were systematically lower than that of measured COD values. This may be due to the reason that HPLC-based COD values were calculated based only on the identified intermediates, while there were some unidentified compounds that were not taken into account, therefore HPLC-based COD values were underestimated. It should be noted however that nearly all the

data points were in + 0–20% error ranges, so that it could be concluded that main reaction intermediates were actually detected.

4.2.2.5.3 Proposed mechanism for oxidative destruction of phenol over activated carbon in fixed bed reactor

Wet air oxidation (both catalytic and non-catalytic) of phenol seems to result in a similar intermediate distribution. Most intermediates detected in this study, as well as in other previous works [4,36,38,131], were already described by Devlin and Harris [127], for the non-catalytic WAO of phenol at elevated temperature and pressure (Figure 2-4-18a).

Due to some differences in intermediates and especially the above mentioned production of 4-hydroxybenzoic acid and 2-hydroxybenzoic acid (salicylic acid), this reaction scheme was simplified and modified according to Figure 2-4-18b.

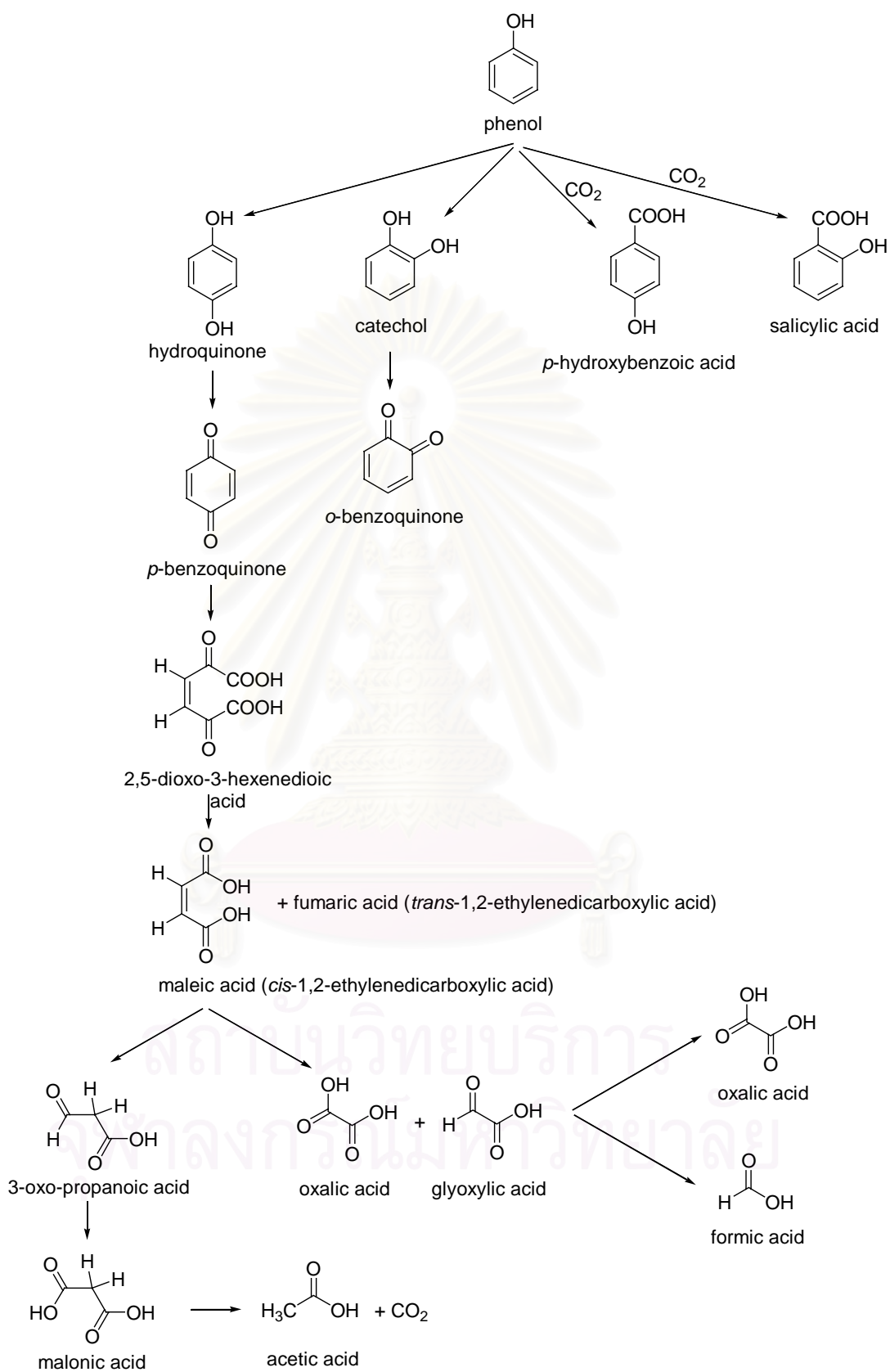


Figure 2-4-18a: Mechanism for phenol WAO according to Devlin and Harris [127].

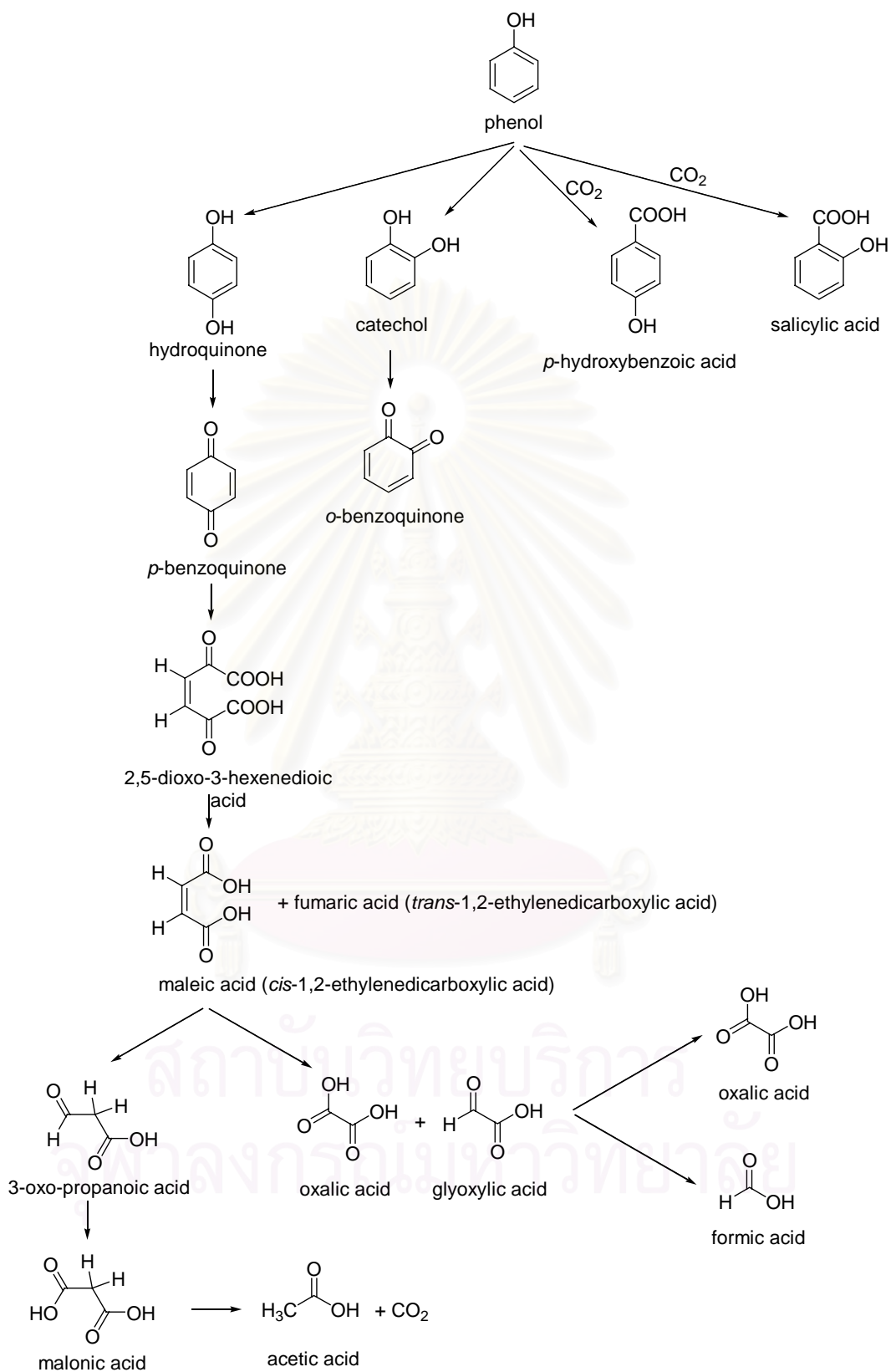


Figure 2-4-18b: Proposed reaction pathway for phenol CWAO based on the identified intermediates in the reaction products.

The reaction mechanisms are also proposed based on the identified intermediates. Details are presented in the Appendix 2-10A.

4.2.2.6 Axial temperature and concentration profiles

The pilot plant reactor is provided with 7 thermocouples and 5 liquid sampling valves axially dispatched. Axial temperature profiles are required to know whether the reactor is isothermal *i.e.* quickly at the oil temperature and without hot spot. Axial concentration profiles may be helpful when analysing reactor performance and reactor models.

4.2.2.6.1 Axial temperature profiles

Axial temperature profiles in upflow and downflow cocurrent fixed bed reactors were investigated for each experimental condition, and similar trends of temperature profile were observed. Typical axial temperature profiles in both upflow and downflow modes are presented in Figure 2-4-19. Experimental conditions were: oxygen partial pressure 1.2 bar, oil temperature 140 °C, gas inlet velocity 1.1×10^{-2} m/s (gas flow rate 100 NI/h), and liquid flow rate 1 kg/h.

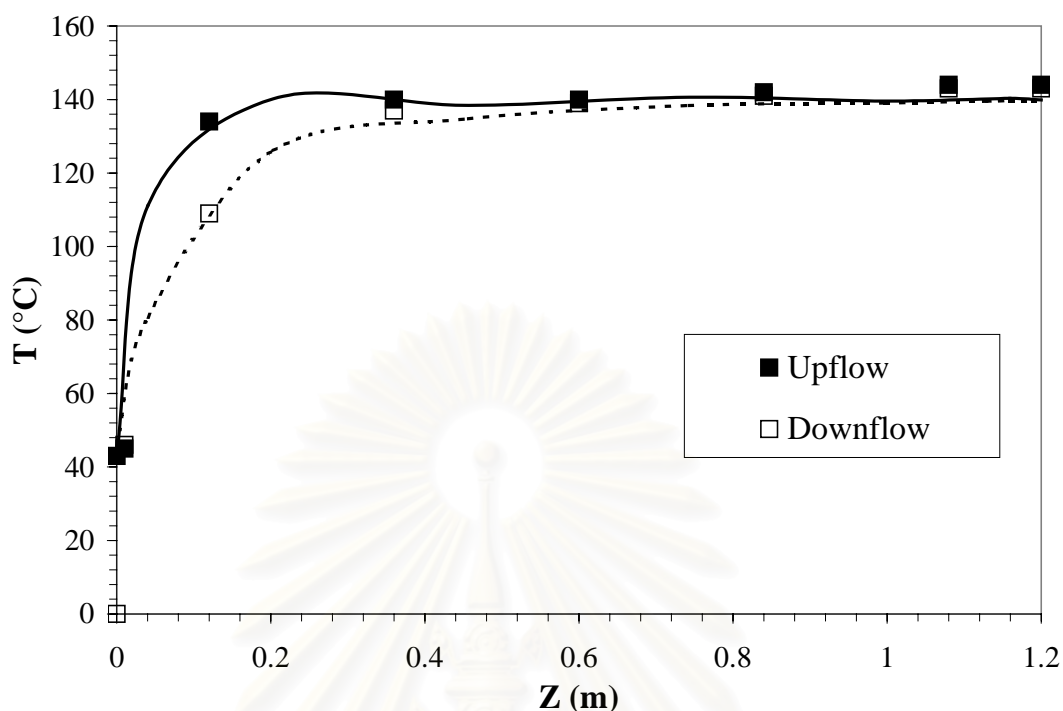


Figure 2-4-19: Axial temperature profiles for $P_{O_2} = 1.2$ bar, $T_{oil} = 140^\circ\text{C}$, $u_{G,inlet} = 1.1 \times 10^{-2}$ m/s (FG = 100 NI/h), and $F_L = 1$ kg/h in cocurrent upflow and downflow fixed bed reactors. Symbols show experimental results, lines show simulation

As seen in Figure 2-4-19, the upflow mode provided steeper temperature profiles due to higher wall-to-bed heat transfer coefficient (continuous liquid phase in upflow mode). However, in the downflow mode, the reactor temperature was found to be nearly the same as the wall temperature at only 30 cm of the catalytic fixed bed, suggesting that the reactor temperature rapidly reaches the wall temperature. Thus, as a first approximation the reactor can be considered to operate quasi isothermally even in a downflow mode.

4.2.2.6.2 Axial concentration profiles

Axial concentration profiles of phenol and identified intermediates in upflow and downflow cocurrent fixed bed reactors were investigated in all experimental conditions. It was found that similar trends of concentration profiles were observed for all conditions explored. Typical axial concentration profiles of phenol and intermediates in both upflow and downflow modes are displayed in Figures 2-4-20

and 2-4-21, respectively. Experimental conditions were as follows: oxygen partial pressure of 2.0 bar, oil temperature of 140 °C, gas inlet velocity of 1.1×10^{-2} m/s (gas flow rate of 100 NI/h), and liquid flow rate of 0.5 kg/h.

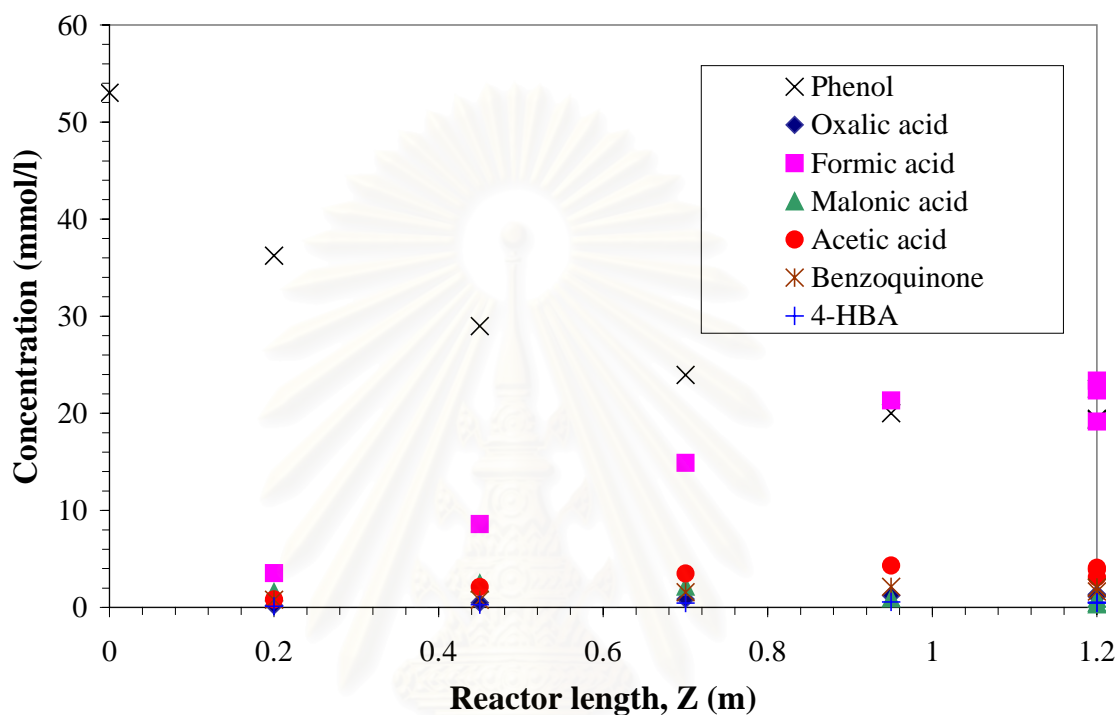


Figure 2-4-20: Axial concentration profiles for $P_{O_2} = 2.0$ bar, $T_{oil} = 140$ °C, $u_{G,inlet} = 1.1 \times 10^{-2}$ m/s ($F_G = 100$ NI/h), and $F_L = 0.5$ kg/h in cocurrent upflow fixed bed reactor.

สถาบันวิทยบริการ
จุฬาลงกรณ์มหาวิทยาลัย

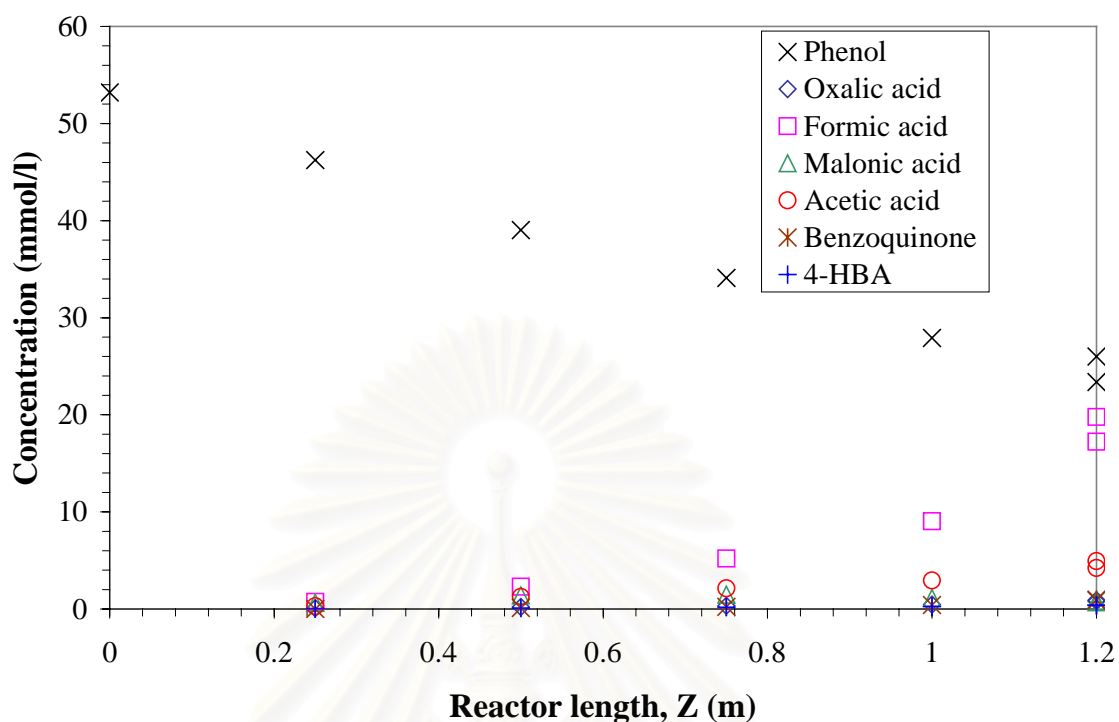


Figure 2-4-21: Axial concentration profiles for $P_{O_2} = 2.0$ bar, $T_w = 140$ °C, $u_{G,inlet} = 1.1 \times 10^{-2}$ m/s ($F_G = 100$ NI/h), and $F_L = 0.5$ kg/h in cocurrent downflow fixed bed reactor.

As shown in Figures 2-4-20 and 2-4-21, concentrations of acetic acid and moreover formic acid continually increased along the reactor, as phenol concentration decreased. As mentioned before, concentrations of other intermediate compounds were quite low.

Axial concentration profile of phenol seemed to be first steeper in upflow mode than downflow mode and then flatter, which could be due to the presence of higher axial dispersion in the upflow reactor leading to a larger Danckwerts concentration jump at the reactor inlet or to faster temperature increase. This will be analysed in more details in the modelling section.

4.2.2.7 Considerations on scale-up of phenol oxidation over AC

In a previous study (Eftaxias, [4]), continuous CWAO of phenol over AC was investigated in an isothermal laboratory trickle bed reactor ($D = 1.1$ cm and

$L = 20$ cm) filled with 7 g of Merck AC ($d_p = 0.5$ mm). The experiments in the small TBR were shown to be kinetically controlled by using the typical diagnostic criteria.

The reactor performance is illustrated in Figure 2-4-22 for 0.2 MPa of oxygen partial pressure and different temperatures.

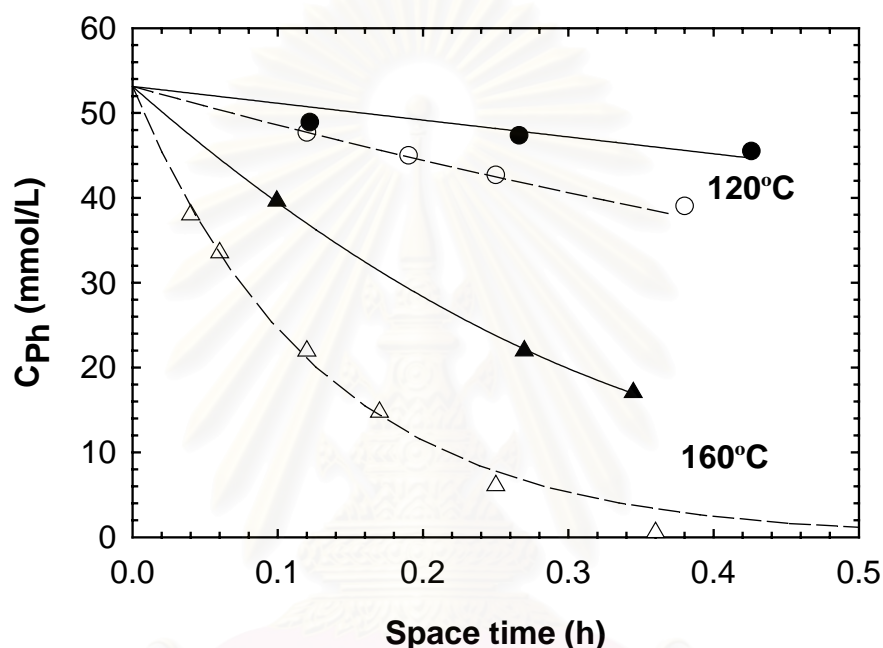


Figure 2-4-22: Phenol concentration for downflow (open symbols) and upflow (filled symbols) oxidation over active carbon at 0.2 MPa of O_2 ; lines indicate trends.

Operating this small-scale reactor (SSR) with much lower liquid and gas velocities (0.04–0.5 mm/s and 3.3–7.4 mm/s, respectively) than in the pilot fixed-bed reactor, downflow mode of gas-liquid resulted there in considerably higher conversion than upflow mode for all operating conditions tested. Eftaxias [4] explained this important difference by the positive effect of very low catalyst wetting

efficiencies in downflow, while the fully wetted upflow mode was affected by gas-liquid mass transfer limitations due to low gas velocity and some axial dispersion due to the low liquid velocity.

When comparing principle intermediate compounds found in both reactors (laboratory and pilot), phenol oxidation in the small-scale reactor yielded much less amounts of malonic acid and oxalic acid (traces), but provided much more amounts of maleic acid (1.7 mmol/l in SSR and < 0.3 mmol/l in pilot reactor).

Regarding the contents of main intermediates, formation of formic acid in the pilot FBR was found twice higher than that in the SSR, while acetic acid content in the pilot FBR was only one-fourth of that found in the SSR. However, concentrations of remaining aromatic compounds remain similarly low in both the small and pilot FBRs.

On the whole, it can be concluded that the scale-up of phenol CWAO over AC based on mere liquid space-time analogy would lead to erroneous reactor design, which clearly highlights the need for developing detailed reactor models to predict the reactor performance on different reactor length scales.

4.3 Modelling of continuous CWO

It was shown in Section 4.2.2.7 that a liquid space-time analogy based scale-up of results obtained at a smaller scale (with much lower liquid and gas velocities) would have failed to correctly predict our pilot reactor performance, demonstrating the need for a reactor model including thorough description of hydrodynamics and heat and mass transfers phenomena.

4.3.1 Fixed bed model and numerical solution

4.3.1.1 Model equations

The non-isothermal model used was based on the previous work of Eftaxias *et al.* [4,132] and focused on gas-liquid-solid packed-bed reactors incorporating the complex oxidation of phenol over an AC catalyst. The main model variables were the axial liquid phase temperature and the axial liquid phase concentrations of dissolved oxygen and organic compounds, in particular the conversion of the phenol reactant. The model reflected the complex interplay of reaction kinetics, gas-liquid hydrodynamics and heat and mass transfers on both the pellet and reactor length scale. For downflow mode, partial wetting and splitting of the total liquid hold-up into stagnant and dynamic parts were considered to establish weighted effectiveness factors that address both the gas limiting and liquid limiting reactant situation. Furthermore, to simulate non-isothermal reactor operation, two limiting cases of water vaporisation were described, *i.e.* either instantaneous vapour-liquid equilibrium or progressive axial saturation of the gas phase with water. On the whole, the model accounted for:

- Static and dynamic liquid portions
- Constant partial catalyst wetting in trickle flow regime throughout the reactor
- Axial dispersion in the dynamic liquid phase
- Pore diffusion and gas-liquid and liquid-solid mass transfer
- Axial concentration and temperature gradients without radial gradients ($D_R/d_p=25$)
- Heat transfer between catalytic fixed bed and reactor wall (constant wall temperature)
- Instantaneous water vapour-liquid equilibrium or mass transfer limited axial saturation of gas phase with water

The following assumption were made in the model development:

- Stable catalyst activity
- Complete internally wetted catalyst pores
- No temperature gradient between gas liquid and catalyst
- Negligible pressure drop, *i.e.* the total pressure is constant
- Ideal gas phase behaviour
- Non-volatile organic reactants

For simulations presented in following sections, only complete mineralisation of reacted phenol to H₂O and CO₂ was considered, as intermediates represented in most cases less than 20% of total COD and do not significantly increase at high phenol conversion.

Pellet scale model

To describe the simultaneous diffusion–reaction of reactants and products within the liquid filled catalyst pores, the following mass balance equations were solved numerically, assuming spherical symmetry of pellets:

$$\frac{1}{r^2} \frac{d}{dr} \left(r^2 D_j^{\text{eff}} \frac{dC_j}{dr} \right) + \rho_p R_j = 0 \quad (2-4-9)$$

with boundary conditions at $r = 0$:

$$\left. \frac{dC_j}{dr} \right|_{r=0} = 0 \quad (2-4-10)$$

and $r = r_p$:

$$C_j \Big|_{r=r_p} = C_{S,j} \quad (2-4-11)$$

$$D_j^{\text{eff}} \left. \frac{dC_j}{dr} \right|_{r=r_p} = k_{LS,j}^{\text{dyn}} f_{\text{dyn}} (C_{L,j}^{\text{dyn}} - C_{S,j}) + k_{LS,j}^{\text{sta}} f_{\text{sta}} (C_{L,j}^{\text{sta}} - C_{S,j}) + \left[k_{GS} (1-f) (C_{G,O_2} - HC_{S,O_2}) \right]_{\text{only for } O_2} \quad (2-4-12)$$

Note that the last RHS-term of Equation (2-4-12) was necessary only for oxygen in the downflow mode. Equation (2-4-12) accounted thus for the effect of stagnant liquid pockets and partial wetting without the need of assuming limiting reactants. By superimposing the diffusive fluxes coming from the wetted and dry areas of the pellet, this definition gave a better flexibility for systems that lied between the asymptotic cases of mainly gas-limited or liquid-limited reactions. However, this approach considered a uniform concentration of reactants on the catalyst surface (required by the use of a one dimensional-diffusion model) assuming infinite radial diffusion. The boundary condition at the pellet surface as listed above in the Equation (2-4-12) was based on the reactant concentration j in the liquid bulk or gas bulk phases, which had to be calculated by the reactor scale model. To link the fluid and surface concentration of each compound j , a weighted effectiveness factor that accounted for the fluid-solid mass transfer resistance was defined for each of the fraction of the pellet surface in contact with the liquid or gas phases:

$$\begin{aligned}\eta_j^{\text{dyn}} &= \frac{3k_{\text{LS},j}^{\text{dyn}} f_{\text{dyn}} (C_{\text{S},j} - C_{\text{L},j}^{\text{dyn}})}{r_p \rho_p R_{\text{S},j}} \\ \eta_j^{\text{sta}} &= \frac{3k_{\text{LS},j}^{\text{sta}} f_{\text{sta}} (C_{\text{S},j} - C_{\text{L},j}^{\text{sta}})}{r_p \rho_p R_{\text{S},j}} \\ \eta_{\text{O}_2}^{\text{gas}} &= \frac{3k_{\text{GS}} (1-f)(HC_{\text{S},\text{O}_2} - C_{\text{G},\text{O}_2})}{r_p \rho_p R_{\text{S},\text{O}_2}}\end{aligned}\quad (2-4-13)$$

Reactor scale model

Axial dispersion in the liquid phase can alter the reactor performance and the one-dimensional Piston Dispersion Exchange (PDE) model was used to calculate the bulk liquid concentrations of reactants and products. The gas phase was assumed to be in plug flow, since the Peclet number is usually several orders of magnitude higher than that of the liquid phase. As catalyst wetting might not be as complete as in the trickle bed regime, the following equation resulted for the oxygen gas phase concentration:

$$\frac{d(u_G C_{G,O_2})}{dz} + k_L a \left(\frac{C_{G,O_2}}{H} - C_{L,O_2}^{dyn} \right) - \eta_{O_2}^{gas} \rho_b R_{S,O_2} = 0 \quad (2-4-14)$$

The dynamic liquid concentrations were given by the following mass balance equation, which includes axial dispersion:

$$-D^{ad} \varepsilon_{L,dyn} \frac{d^2 C_{L,j}^{dyn}}{dz^2} + \frac{d(u_L C_{L,j}^{dyn})}{dz} + (ka)_{LL,j} (C_{L,j}^{dyn} - C_{L,j}^{sta}) - \eta_j^{dyn} \rho_b R_{S,j} - \left[k_L a \left(\frac{C_{G,O_2}}{H} - C_{L,O_2}^{dyn} \right) \right]_{\text{only for } O_2} = 0 \quad (2-4-15)$$

Note that the last LHS-term of Equation (2-4-15) was only necessary for the balance over the dissolved oxygen reactant.

For the stagnant liquid pockets that might exist on the reactor length scale, the convection term dropped out and algebraic equations could be developed to describe the stagnant liquid concentrations:

$$(ka)_{LL,j} (C_{L,j}^{dyn} - C_{L,j}^{sta}) + \eta_j^{sta} \rho_b R_{S,j} = 0 \quad (2-4-16)$$

Finally, based on the approach of Van Gelder *et al.* [133], the energy balance for the pseudo-homogeneous gas-liquid fluid incorporating water evaporation and bed to wall heat transfer gave:

$$(u_L \rho_L c_{pL} + u_G \rho_G c_{pG}) \frac{dT}{dz} + \frac{\varphi}{A} \Delta H^v - \rho_b \sum r_i^{app} (-\Delta H_i) + \frac{h_w A}{V_R} (T - T_w) = 0 \quad (2-4-17)$$

The apparent rate of the i^{th} reaction (r_i^{app}) was calculated from the stoichiometry and the compound overall reaction rates ($\eta_j R_j$). Here as mentioned before only one reaction of complete oxidation was considered. Thermal fluid was circulated at a high volumetric flow rate through a thermally isolated double jacket to maintain the reactor wall temperature constant. This allowed dropping out the differential heat balance over the thermal fluid

The water evaporation rate (φ) per unit reactor length was determined assuming that the gas stream reached either instantaneously liquid-vapour equilibrium or was progressively saturated while flowing through the catalytic fixed bed.

Denoting the total molar gas flow rate by $\dot{n}_{G,T}$ and the water vapour molar flow rate by \dot{n}_{G,H_2O} , instantaneous saturation of the gas stream with water vapour resulted in the following equality:

$$\frac{\dot{n}_{G,H_2O}}{\dot{n}_{G,T}} = \frac{P_{H_2O}^v(T)}{P_T} \quad (2-4-18)$$

If the mass transfer of water from the liquid to the gas phase were not fast enough, the gas phase would become progressively saturated along the axial reactor coordinate, leading to:

$$\frac{1}{A} \frac{d\dot{n}_{G,H_2O}}{dz} + k_G a \left(C_{G,H_2O} - \frac{P_{H_2O}^v(T)}{RT} \right) = 0 \quad (2-4-19)$$

$$C_{G,H_2O} = \frac{\dot{n}_{G,H_2O}}{\dot{n}_{G,T}} \frac{P_T}{RT} \quad (2-4-20)$$

The total system pressure, P_T , being only marginally affected by the pressure drop throughout the bed under the giving operating conditions was considered constant in the model.

Assuming that the cold gas entered already saturated in the reactor, then it followed:

$$\dot{n}_{G,H_2O} = \left(\dot{n}_{G,H_2O} \right)_{inlet} + \int_0^z \varphi(z) dz \quad (2-4-21)$$

$$\dot{n}_{G,T} = \left(\dot{n}_{G,T} \right)_{inlet} + \int_0^z \varphi(z) dz \quad (2-4-22)$$

The fluid temperature and the total molar gas and liquid flow rates underwent changes along the fixed bed reactor length and the gas and liquid superficial velocities

had to be adjusted accordingly. For the gas phase, the axial variation of the superficial velocity was calculated assuming ideal gas behaviour:

$$u_G = \frac{\dot{V}}{A} = \frac{\dot{n}_{G,T} R T}{P_T A} \quad (2-4-23)$$

which led by differentiation to:

$$\frac{du_G}{dz} = \frac{R T}{P_T A} \varphi + \frac{\dot{n}_{G,T} R}{P_T A} \frac{dT}{dz} \quad (2-4-24)$$

For the dynamic liquid phase, the change in superficial velocity was calculated respectively, using the liquid density of pure water:

$$\frac{du_L}{dz} = \frac{d}{dz} \left(\frac{\dot{m}_L}{A \rho_L} \right) = \frac{\dot{m}_L}{A} \frac{d}{dT} \left(\frac{1}{\rho_L} \right) \frac{dT}{dz} + \frac{1}{A \rho_L} \frac{d\dot{m}_L}{dz} \quad (2-4-25)$$

The boundary conditions for the reactor scale model were the following.

At the reactor entrance ($z = 0$):

$$C_{G,O_2} = \left(C_{G,O_2} \right)_{inlet} \quad (2-4-26)$$

$$u_L \left(C_{L,j}^{dyn} \right)_{inlet} = u_L C_{L,j}^{dyn} \Big|_{z=0^+} - \varepsilon_{L,dyn} D^{ad} \frac{\partial C_{L,j}^{dyn}}{\partial z} \quad (2-4-27)$$

$$T = T_{inlet} \quad (2-4-28)$$

At the reactor outlet ($z = L_R$):

$$\frac{\partial C_{L,j}^{dyn}}{\partial z} = 0 \quad (2-4-29)$$

4.3.1.2 Numerical solution

The pellet and reactor scale models led to a set of algebraic-differential equations that involved non-linear reaction rate expressions. To solve these model equations with boundary constraints, the robust numerical method of orthogonal collocation on finite elements was used [134]. In brief, the unknowns $y_i(x)$ in each finite element were written as an expansion of orthogonal polynomials $y_k(x)$ (Legendre polynomials with degree 6):

$$y_i(x) = \sum_{k=1}^{N_c} \alpha_{ik} y_k(x) \quad (2-4-30)$$

The coefficients α_{ik} were determined so as to nullify the values of the PDE $L[y_i(x), y_i'(x), y_i''(x)]$ at prescribed points, the resulting set of algebraic equations being solved by the Newton method. Boundary conditions of each finite element, apart from that applied in the first and the last ones, was simply the continuity function, *i.e.* $y_i(x) = y_{i+1}(x)$ and $y_i'(x) = y_{i+1}'(x)$. In most cases, 8 collocation points were necessary to obtain readily model convergence both for reactor and pellet length scales with only one finite element.

The numerical solution of the whole equation system was done by performing a sequential approach. In a first step, the PDE reactor scale model was solved with the given reactor inlet values and estimated of the effectiveness factors to predict the spatial temperature and concentrations, *i.e.* dynamic liquid and surface concentrations, at each reactor collocation point. Once these profiles were known, the boundary conditions of the pellet scale model could be determined and the diffusion equations were subsequently solved to calculate the concentrations inside the pellet at each pellet collocation point. Then, the local concentrations of the PDE model were updated with the newly obtained surface concentrations. This procedure was repeated until convergence had been achieved, *i.e.* when the latest concentrations calculated with the PDE model matched within a given error tolerance the ones used in the previous iteration.

4.3.2 Evaluation of physicochemical properties and fixed bed parameters

4.3.2.1 Physicochemical and thermodynamic properties

Pure water and air or gas mixtures properties were considered for the bulk liquid and gas phases. Water and gas heat capacities, heat of evaporation, heat of phenol combustion, water vapour pressure, water density as well as phenol diffusion coefficients were obtained from data or methods included in Reid *et al.* [119]. Dissolved oxygen diffusion coefficient and Henry constants for oxygen solubility in water are taken from Diaz *et al.* [135] and Himmelblau [136], respectively. Table 2-4-7 gives the values of these parameters calculated for the three selected temperatures.

Table 2-4-7: Values of physical properties in the range of operating conditions

Property	120 °C	140 °C	160 °C
$\rho_{\text{H}_2\text{O}}$ (kg/m ³)	943	926	908
$\mu_{\text{H}_2\text{O}}$ (Pa s)*10 ⁴	2.34	1.93	1.75
$\sigma_{\text{H}_2\text{O}}$ (N/m)*10 ²	5.69	5.38	5.08
$P^{\text{v}}_{\text{H}_2\text{O}}$ (MPa)	0.199	0.362	0.619
c_{pL} (kJ/kg/K)	4.24	4.28	4.34
c_{pG} (kJ/kg/K)	1.05	1.05	1.05
ΔH^{v} (kJ/mol)	40.2	39.13	38
ΔH^{r} (kJ/mol) ⁽¹⁾	3000	3000	3000
D_{O_2} (m ² /s)*10 ⁻⁸	1.72	2.35	3.12
D_{Phenol} (m ² /s)*10 ⁻⁸ ⁽²⁾	0.528	0.671	0.779
H (MPa)*10 ⁻³	6.83	6.25	5.53

⁽¹⁾ Heat of phenol combustion to form CO₂ and H₂O

⁽²⁾ from Wilke-Chang (1955) in [119]

4.3.2.2 Hydrodynamic, mass, and heat transfers parameters

The quality of prediction of the packed-bed model depends primarily on the accuracy of the involved model parameters that are used to describe the complex interaction of reaction kinetics, hydrodynamics, and heat and mass transfers. The determination of these parameters is very important and needs to be carefully addressed. Therefore, the recommended literature correlations were examined for each specific parameter to select the appropriate values.

Hydrodynamic and transport key parameters strongly depend on the nature of contacting the gas-liquid flow through the catalytic fixed bed. For cocurrent two-phase upflow and bubble flow regime, the liquid phase is a continuous phase and the packed-bed column operates with high liquid hold-ups and fully wetted pellets. External mass transfer and axial dispersion are thus gaining importance for reactor performance. When the packed-bed is operated in a trickle downflow regime, the gas phase becomes the continuous phase and partial wetting of pellets may occur. In this

situation, external mass transfer and axial dispersion are less influent, whereas the pellet wetting efficiency is thought to be crucial for the reactor conversion.

The accurate estimation of all these parameters is a very critical task as it largely determines the accuracy of reactor modelling. Various correlations exist for the main model parameters, although a dramatic prediction spreading up to two orders of magnitude could result from their applications, as in the case of the volumetric mass transfer coefficient. A large difference is also found for the liquid axial dispersion coefficient in upflow operation. Moreover, for the most refined trickle bed model, some model parameters could hardly be estimated due to the lack of specific correlations. Table 2-4-8 lists both the literature correlations selected for the two distinct gas-liquid flow modes and a set of values of key model parameters calculated at typical operating conditions.

Table 2-4-8: Parameter values and correlations used in up- and downflow reactor models of pilot plant at: $T = 140\text{ }^{\circ}\text{C}$, $P_T = 6\text{ bar}$, $F_G = 100\text{ NI/h}$, and $F_L = 0.5\text{ l/h}$.

Parameter	Downflow operation mode		Upflow operation mode	
D^{ad} , m^2/s	2.2×10^{-5}	Michell & Furzer [137]	6.4×10^{-5}	*
D^{eff} (Ph/O ₂), m^2/s	$1.2/4.2 \times 10^{-9}$	**	$1.2/4.2 \times 10^{-9}$	**
k_{GS} , m/s	3.8×10^{-2}	Dwivedi <i>et al.</i> [138]	----	----
k_{LS}^{dyn} (Ph/O ₂), m/s	$1.4/3.1 \times 10^{-4}$	Tan & Smith [139]	$3.2/7.3 \times 10^{-4}$	Specchia <i>et al.</i> [108]
k_{LS}^{sta} (Ph/O ₂), m/s	$0.9/2.1 \times 10^{-6}$	Iliuta <i>et al.</i> [140]	$0.9/2.1 \times 10^{-6}$	Iliuta <i>et al.</i> [140]
$(ka)_{LL}$, s^{-1}	1.0×10^{-2}	Hochmann-Effron [141]	1.0×10^{-2}	Hochmann-Effron [141]
k_{La} , s^{-1}	8.1×10^{-2}	Morsi [103]	1.3×10^{-1}	Saada [105]
$\epsilon_{L,dyn}$	0.10	Ellman <i>et al.</i> [81]	0.22	Yang <i>et al.</i> [86]
$\epsilon_{L,sta}$	0.05	Saez <i>et al.</i> [142]	0.05	Saez <i>et al.</i> [142]
f	0.68 (or 1)	El-Hisnawi <i>et al.</i> [143]	1.0	----
h_w ($\text{W}/\text{m}^2/\text{K}$)	1.1×10^2	***	5.1×10^2	Sokolov-Yablokova [144]

* Axial dispersion estimated from Stüber [117] (correlation derived from Syaiful [145])

** Calculated assuming tortuosity factor = 3

*** Estimated from axial temperature profiles (correlation of Mariani *et al.* [146] is used to describe h_w evolution with operating conditions)

The static, f_{sta} , and dynamic, f_{dyn} , components of the wetting efficiency, f , were obtained from the approximation of Rajashekharam *et al.* [147]:

$$\frac{f_{sta}}{f_{dyn}} = \frac{\varepsilon_{L,sta}}{\varepsilon_{L,dyn}} \quad (2-4-31)$$

4.3.3 Prediction of pilot plant reactor performance

Pilot reactor data were thoroughly analysed with the detailed PDE model developed in Section 4.3.1.1.

In the case of phenol CWAO, heat transfer and axial temperature profiles could be analysed separately due to relatively high heat transfer (small tube diameter), very low heat production by reaction (diluted phenol), and moderate heat consumption for water vaporisation.

4.3.3.1 Axial temperature profiles

As shown in Figure 2-4-19 (Section 4.2.2.6.1) the predicted temperatures fit well with the experimental temperature profiles when using the correlation of Sokolov and Yablokova [144] for the upflow operation and a modified correlation of Mariani *et al.* [146] (divided by 2) for the downflow operation. These correlations resulted in a much larger wall-to-bed heat transfer coefficient for upflow than downflow modes (*cf.* Table 2-4-8).

4.3.3.2 Outlet phenol conversions and axial concentration profiles

4.3.3.2.1 Upflow mode

The situation of gas-liquid upflow operation being less complex was first examined. The sensibility of the reactor performance to oxygen mass transfer and to water vaporisation was not straightforward. In the non-isothermal reactor zone (first 20 to 30 cm of the fixed bed) the water vapour pressure increased exponentially and the induced water vaporisation reduced gradually the oxygen partial pressure in the gas phase and at the same time increased the phenol concentration in the remaining liquid. As yet mentioned the effect of vaporisation is rarely accounted for in modelling and therefore two vaporisation rates were implemented and compared: either instantaneous vapour-liquid equilibrium, *i.e.* infinitely fast vaporisation, or

mass transfer limited vaporisation, involving the gas side volumetric mass transfer coefficient (k_{Ga}). This parameter is not well known neither for upflow nor downflow operations where it was supposed to be at least equal to the liquid side mass transfer coefficient [148].

4.3.3.2.1.1 Outlet phenol conversions

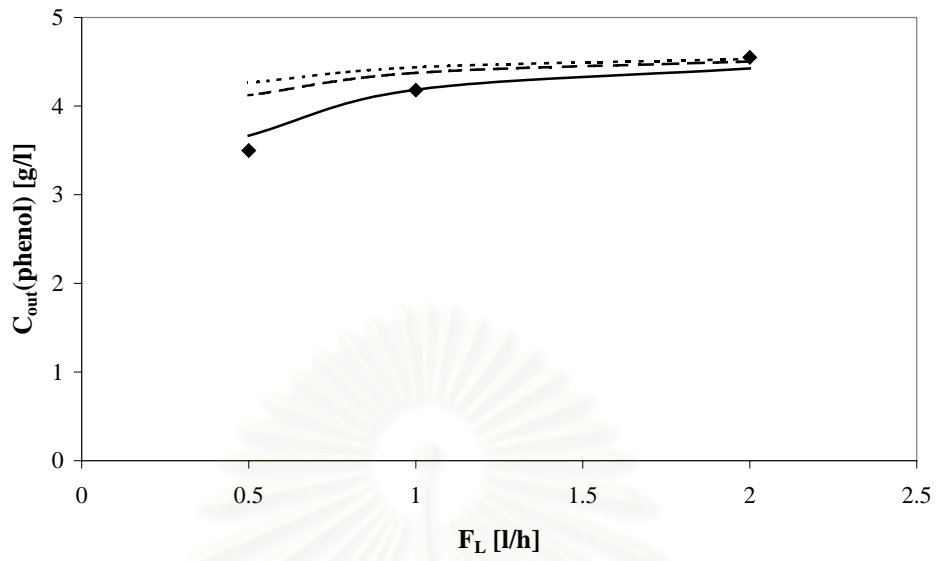
To assess the influence of water vaporisation on reactor performance a set of simulations with $k_{Ga} = k_{La}$, $k_{Ga} = 5 \times k_{La}$ and $k_{Ga} = \text{infinite}$ (equilibrium) was carried out. Saada correlation [105] was used to calculate k_{La} (then k_{La} values obtained were also multiplied or divided by 5). The results of the sensitivity study are summarised in Table 2-4-9 for the reference conditions of $T_{oil} = 140 \text{ }^\circ\text{C}$, $F_G = 100 \text{ NI/h}$ and $P_{O_2} = 1.2 \text{ bar}$. A lower liquid flow rate of $F_L = 0.5 \text{ l/h}$ was however selected to achieve a larger phenol conversion. Also, the effect of axial dispersion in the liquid phase was tested.

Table 2-4-9: Influence of k_{La} , k_{Ga} , and D^{ad} on upflow model conversion: comparison with reference case and experimental conversion at $T_{oil} = 140 \text{ }^\circ\text{C}$, $F_L = 0.5 \text{ l/h}$, $F_G = 100 \text{ NI/h}$, and $P_{O_2} = 1.2 \text{ bar}$.

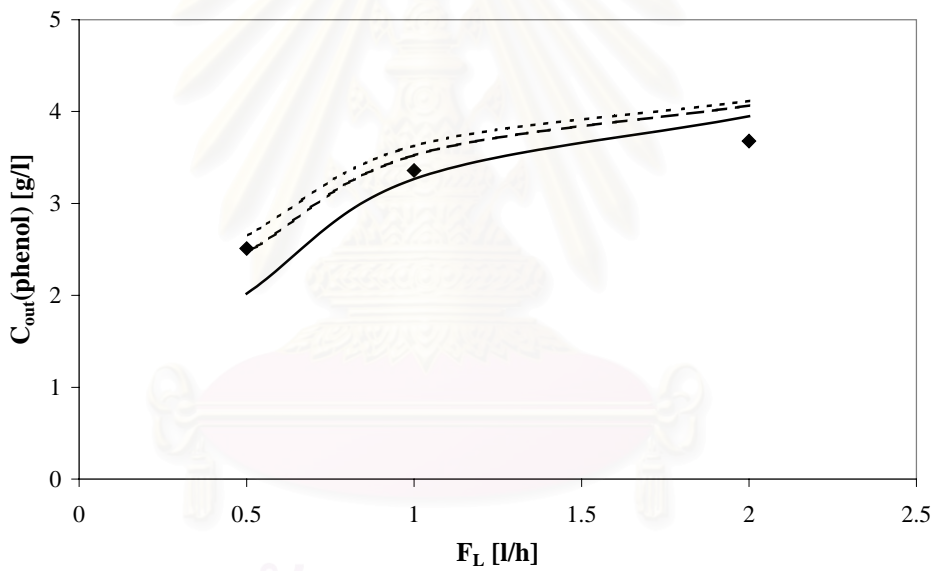
$k_{La}/k_{La(Saada)}$	k_{Ga}/k_{La}	$D^{ad}/D^{ad}_{(Stüber)}$	$\Delta X_{rel} (\%)$ (compared to case of line 1)	$\Delta X_{rel} (\%)$ (compared to experiments)
1	infinite	1	0	-5.5
1	5	1	7.7	1.8
1	1	1	26.7	19.7
0.2	infinite	1	-84.3	-85.2
0.2	5	1	-56.2	-58.7
0.2	1	1	-15.5	-20.1
5	infinite	1	30.1	23
5	5	1	31.4	24.2
5	1	1	35.3	27.8
1	infinite	4.2	-4	-9.3
5	1	4.2	26.9	19.8

In the studied range of relevant values of the axial dispersion coefficient, only a limited change of phenol conversion (always less than 7%) was observed in the simulation runs. Thus, it could be concluded that axial dispersion effects on phenol conversion remain moderate under the given operating conditions. Simulation results were first compared with the simulated reference case (k_{La} from Saada [105], equilibrium and dispersion from Stüber [117]) then to the experimental conversion (as show in the last column of Table 2-4-9). With respect to the gas-liquid mass transfer, at high k_{La} values (5 times higher), the vaporisation rate had nearly no influence (conversion increases slowly from 30.1 to 35.3%) and the experimental outlet conversion was overestimated from 23 to 27.8%. The situation became very different at low k_{La} values ($0.2 \times k_{La}$ from Saada) that could generate very large underestimation of conversion up to -85% depending on the vaporisation rate. Experimental data and simulations suggested thus that the gas-liquid mass transfer was only moderately limiting the reactor conversion. The Saada correlation giving the best agreement with experimental data will be further used in the model predictions.

Figures 2-4-23a, b, c, and d present profiles of experimental exit concentration and corresponding simulations for upflow operation. It was seen that the best agreement with experimental data was found with $k_G/k_L = 5$. Nevertheless in the range of conditions studied in this work it appeared that the rate of water evaporation did not significantly change the outlet concentration and vapour-liquid equilibrium could be assumed for simplicity.

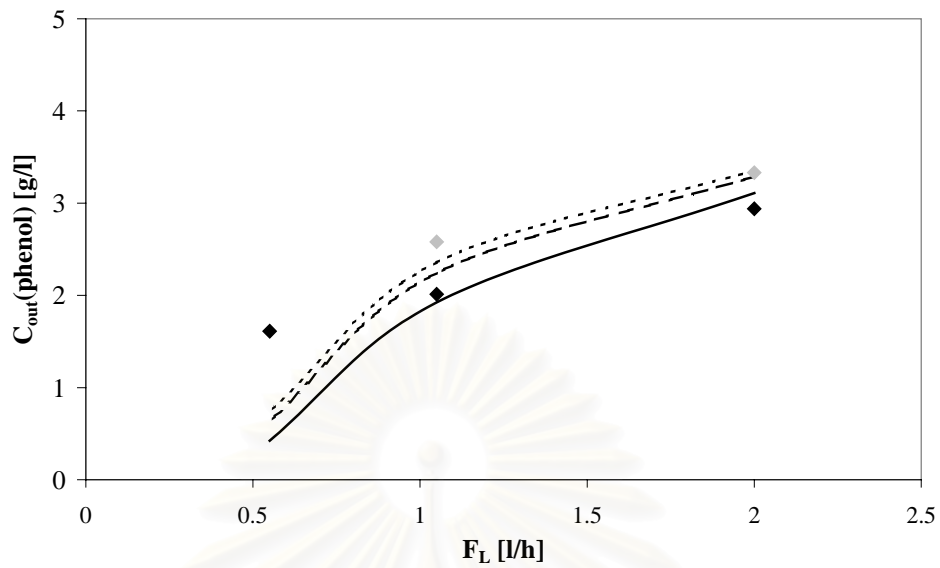


(a)

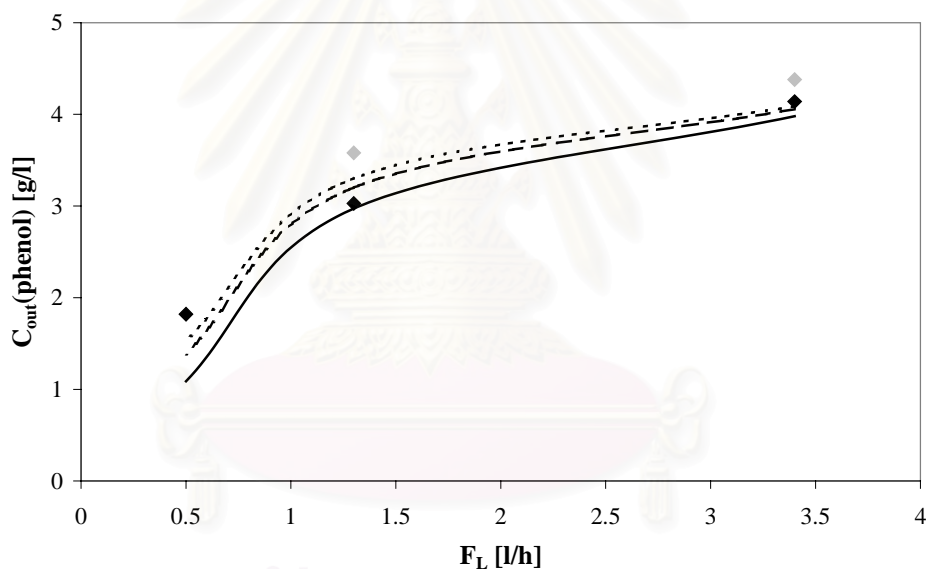


(b)

สถาบันวิทยบริการ
จุฬาลงกรณ์มหาวิทยาลัย



(c)



(d)

Figure 2-4-23: Outlet phenol concentrations: experimental (\diamond) and corresponding simulations for fully wetted catalyst ($D^{ad} = D^{ad}_{(St\ddot{u}ber)}$): $k_{Ga} = k_{La}$ (solid line), $k_{Ga} = 5 \times k_{La}$ (long dotted line), and instantaneous liquid-vapour equilibrium (short dotted line).

(a) $P_{O_2}=0.5$ bar, $T_w=140^\circ\text{C}$, $F_G=100$ NI/h; (b) $P_{O_2}=1.2$ bar, $T_w=140^\circ\text{C}$, $F_G=100$ NI/h;

(c) $P_{O_2}=1.2$ bar, $T_w=160^\circ\text{C}$, $F_G=175$ NI/h; (d) $P_{O_2}=2$ bar, $T_w=140^\circ\text{C}$, $F_G=100$ NI/h.

Grey symbols show experimental results without correction of catalyst deactivation.

However, the slightly positive effect of gas velocity found in the experiments could not be proved by the model. The best prediction from the model ($k_{Ga} = k_{La}$) gave nearly no influence of gas velocity, or an increase of outlet phenol concentration due to higher water vaporization flux.

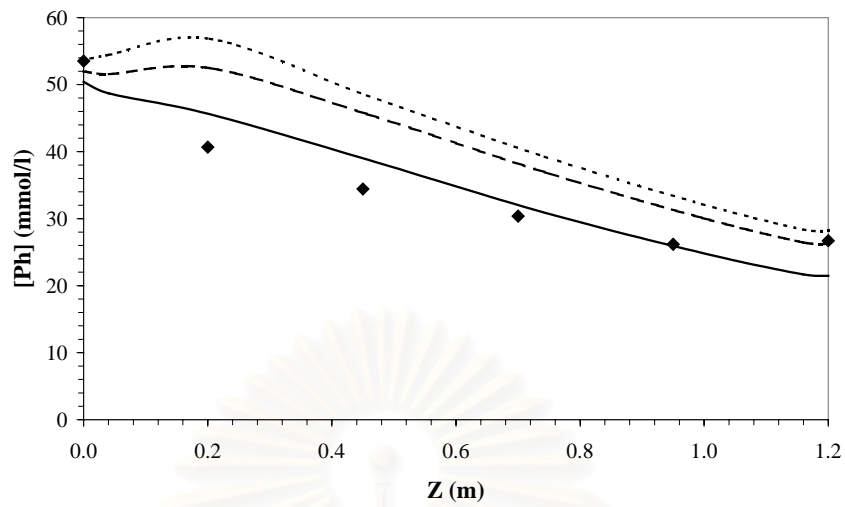
4.3.3.2.1.2 Axial concentration profiles

Figures 2-4-24 and 2-4-25 show how axial dispersion and water vaporisation could affect axial concentration profiles. Some other simulations are reported in the Appendices 2-11A to 2-13A.

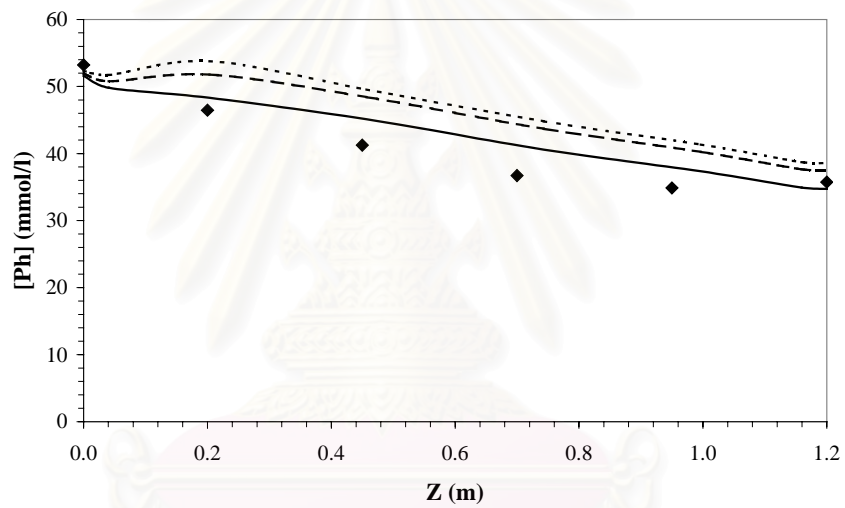
At low liquid flow rate and low axial dispersion (Figures 2-4-24a and b), instantaneous vaporisation condition would lead to an increase of phenol concentration up to 20 cm after the reactor inlet, when liquid temperature reached wall temperature.

For higher axial dispersion (Figure 2-4-25 and Appendix 2-11A for the case of $D^{ad} = 16.7 \times D^{ad}(\text{Stüber})$), this maximum would tend to vanish and a large concentration jump before and after the bed would be observed, while afterwards the concentration profile would be flatter.

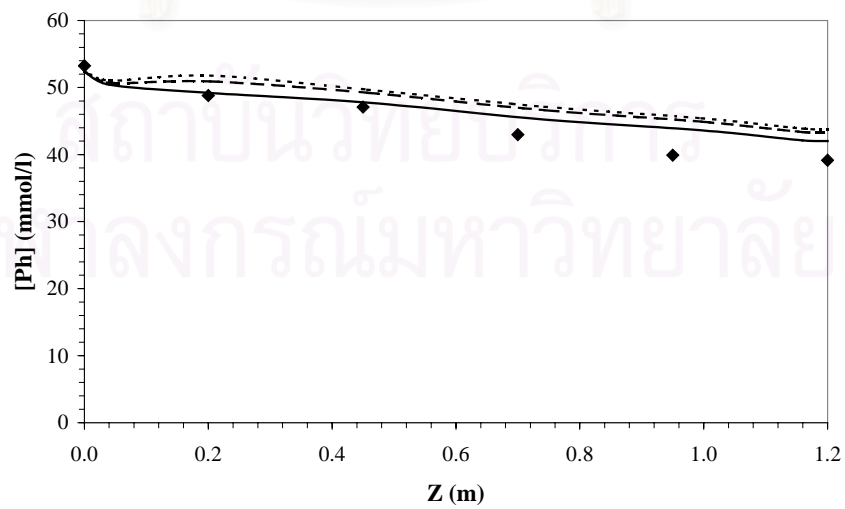
On the one hand no concentration maximum was observed experimentally on the concentration profiles which were best fitted when assuming a large axial dispersion coefficient, but on the other hand when a few samplings were performed from both side of the distributor and they did not show significant concentration shift. Therefore some complementary experiments would be required to quantify axial dispersion (by tracer technique) and to understand vaporisation conditions by comparing concentration profiles when operating isothermally with a gas flow which already saturated with water or a dry gas.



(a)



(b)

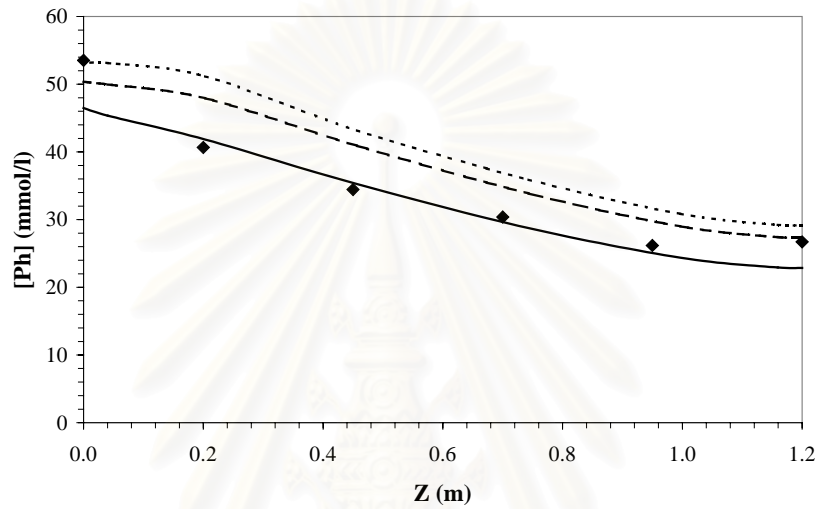


(c)

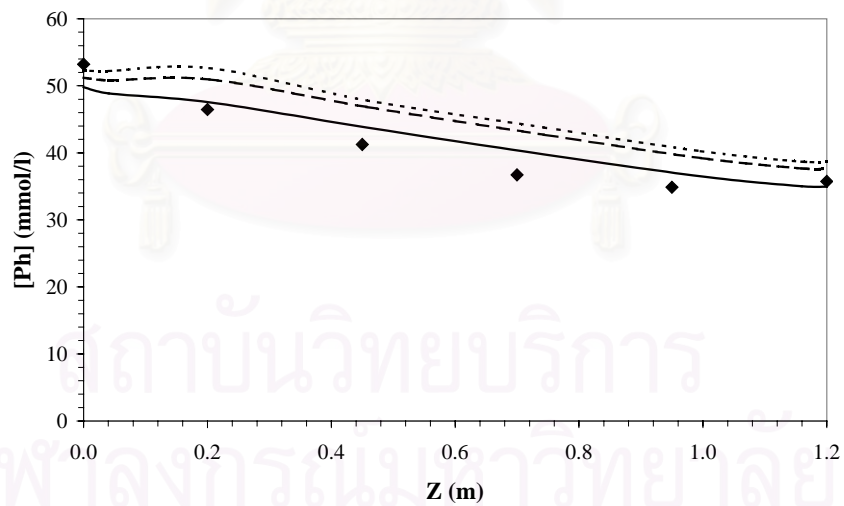
Figure 2-4-24: Axial phenol concentration profiles: experimental (\diamond) and corresponding simulations for fully wetted catalyst: $k_{Ga} = k_{La}$ (solid line), $k_{Ga} =$

$5 \times k_L a$ (long dotted line), and instantaneous liquid-vapour equilibrium (short dotted line). $D^{ad} = D^{ad}_{(Stüber)}$; $P_{O_2} = 0.5$ bar, $T_w = 140^\circ\text{C}$, $F_G = 100$ NI/h

(a) $F_L = 0.5$ l/h; (b) $F_L = 1$ l/h; (c) $F_L = 2$ l/h.



(a)



(b)

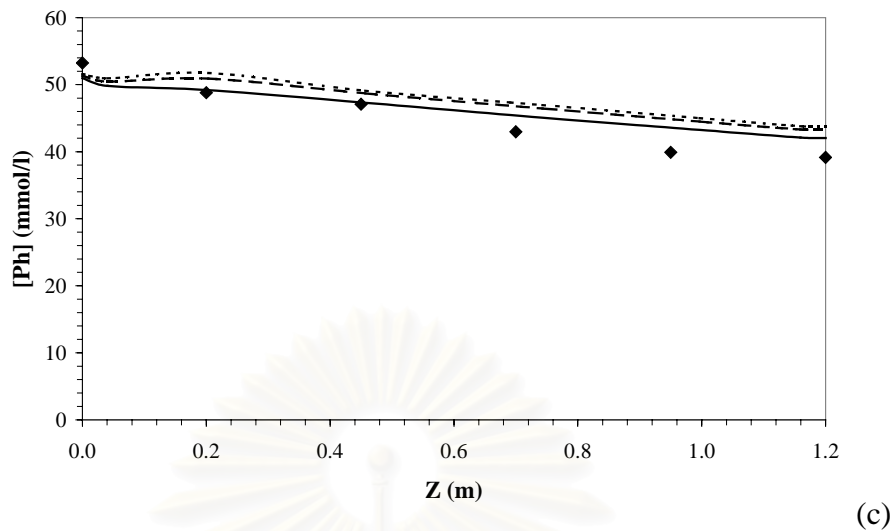


Figure 2-4-25: Axial phenol concentration profiles: experimental (\diamond) and corresponding simulations for fully wetted catalyst: $k_{Ga} = k_{La}$ (solid line), $k_{Ga} = 5 \times k_{La}$ (long dotted line), and instantaneous liquid-vapour equilibrium (short dotted line). $D^{ad} = 4.2 \times D^{ad}_{(Stüber)}$; $P_{O_2} = 0.5$ bar, $T_w = 140^\circ\text{C}$, $F_G = 100$ NI/h
 (a) $F_L = 0.5$ l/h; (b) $F_L = 1$ l/h; (c) $F_L = 2$ l/h.

4.3.3.2.2 Downflow mode

Simulation of the trickle bed reactor was even more complex involving partial catalyst wetting, which was found to have a strong impact on reactor performance as shown in Table 2-4-10.

As soon as full wetting was not assumed ($f < 1$), fast mass transfer of oxygen from the gas phase to the dry zone vanished any oxygen mass transfer limitation. This dramatic overestimation of the model was due to the assumption of uniform concentration at the catalyst surface whatever wet or dry. Indeed, there is no simple way to account for multidirectional pore diffusion resulting from non-uniform oxygen transfer to the catalyst surface. The use of different overall effectiveness factor for each zone could have been a solution, but would have been very difficult to implement as limitations due to both the liquid and dissolved gaseous reactant. As a consequence there was no sensitivity to the value of the external wetting efficiency, the only important hypothesis was either fully or partially wetted conditions.

Table 2-4-10: Influence of particle wetting efficiency on the simulated outlet phenol concentration in downflow mode: $P_{O_2} = 1.2$ bar, $T_w = 140$ °C, $F_G = 100$ NI/h, $F_L = 0.5$ l/h, Case: k_{Ga} infinite.

f	1	0.9999	0.9	0.68*
$C_{Ph,out}$ [g/l]	3.22	2.18	2.02	2.02

* calculated from El-Hisnawi correlation [143]

The volumetric mass-transfer coefficient remained the one key model parameter. The correlation of Morsi [103] giving a lower value than that for upflow mode in similar operating conditions [78,98] was selected.

4.3.3.2.2.1 Outlet phenol conversions

In Figures 2-4-26 and 2-4-27, experimental downflow data were thus compared to the two models of either full or partial catalyst wetting. In general, the experimental data lied mostly in between the two simulations, oxygen mass transfer being too fast with any partial wetting and too slow at full wetting.

These simulations results indicated that the opposite roles of oxygen mass transfer and water vaporisation were not simply balanced and might have different importance depending on the reaction and hydrodynamic conditions. This question is not often addressed in modelling of FBR involving oxidation in the liquid phase, though it corresponds to typical industrial condition for CWAO and thus should deserve further research work.

สถาบันวิทยบริการ
จุฬาลงกรณ์มหาวิทยาลัย

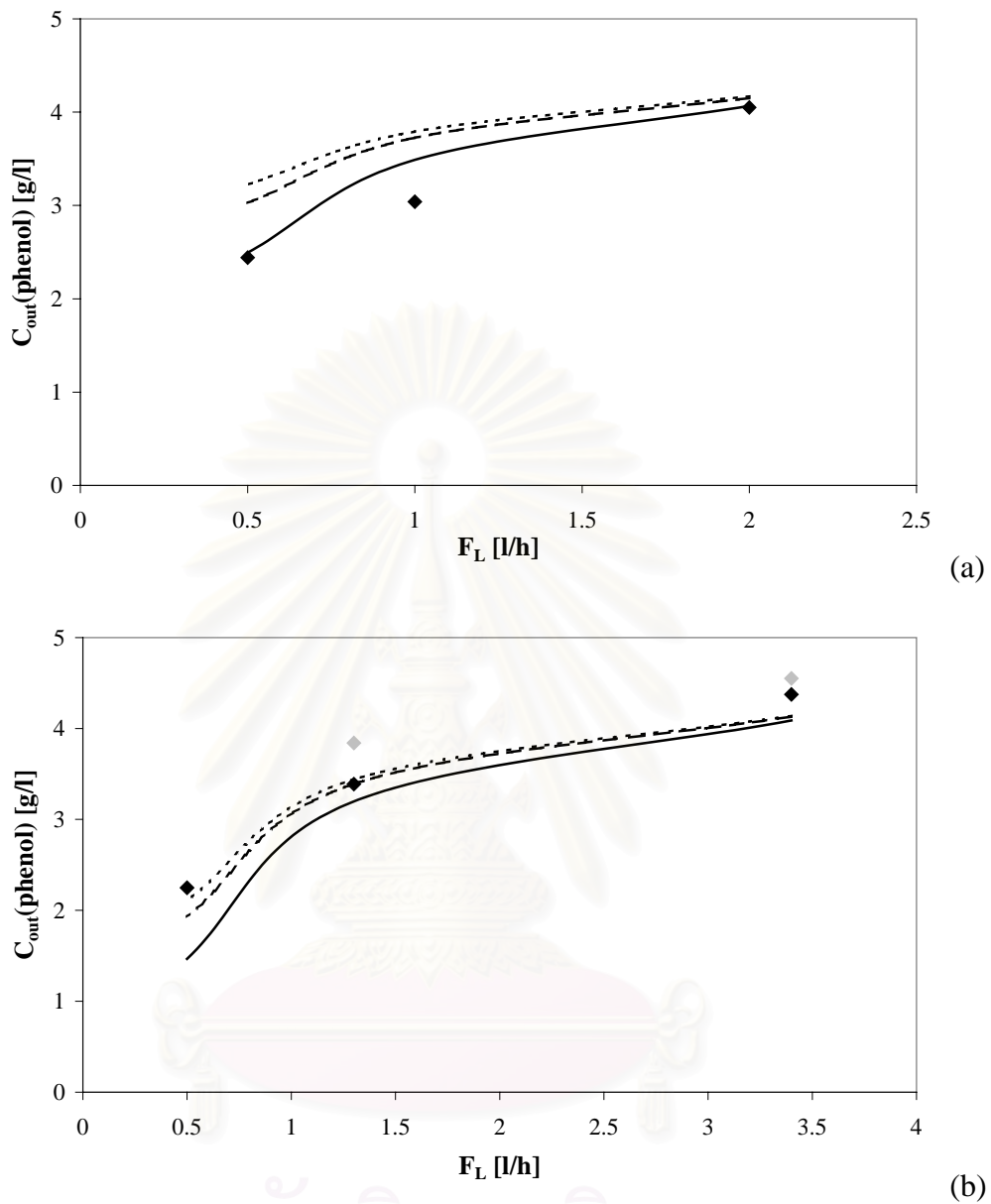
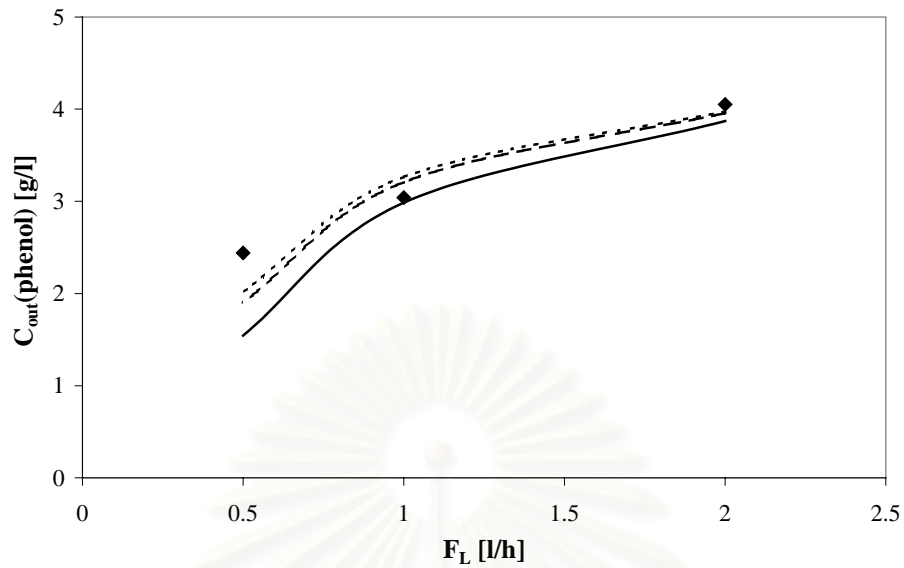
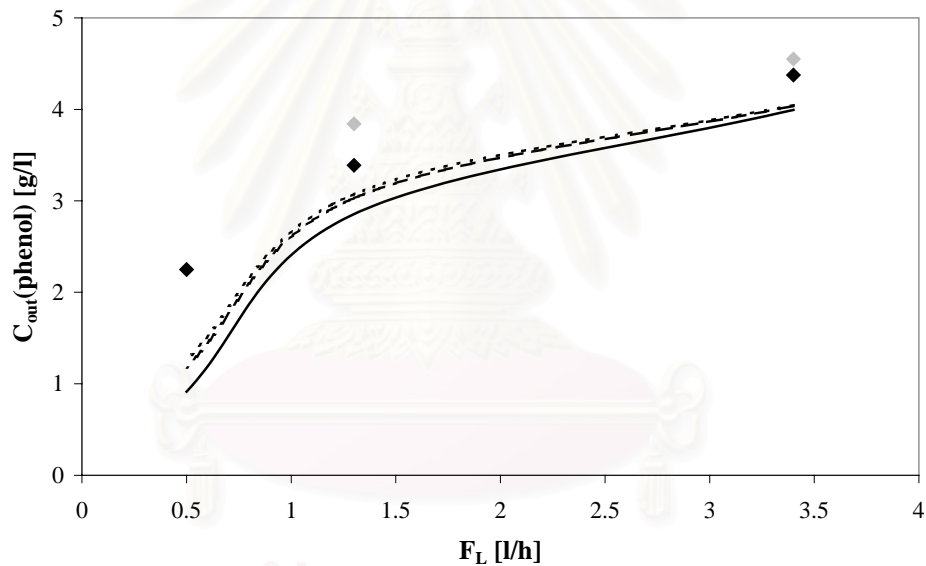


Figure 2-4-26: Outlet phenol concentrations: experimental (\diamond) and corresponding simulations for fully wetted catalyst: $k_{Ga} = k_{La}$ (solid line), $k_{Ga} = 5 \times k_{La}$ (long dotted line), and instantaneous liquid-vapour equilibrium (short dotted line).

(a) $P_{O_2} = 1.2$ bar, $T_w = 140$ °C, $F_G = 100$ NI/h; (b) $P_{O_2} = 2$ bar, $T_w = 140$ °C, $F_G = 100$ NI/h. Grey symbols show experimental results without correction by catalyst deactivation.



(a)



(b)

Figure 2-4-27: Outlet phenol concentrations: experimental (\diamond) and corresponding simulations for partially wetted catalyst: $k_{GA} = k_{La}$ (solid line), $k_{GA} = 5 \times k_{La}$ (long dotted line), and instantaneous liquid-vapour equilibrium (short dotted line).

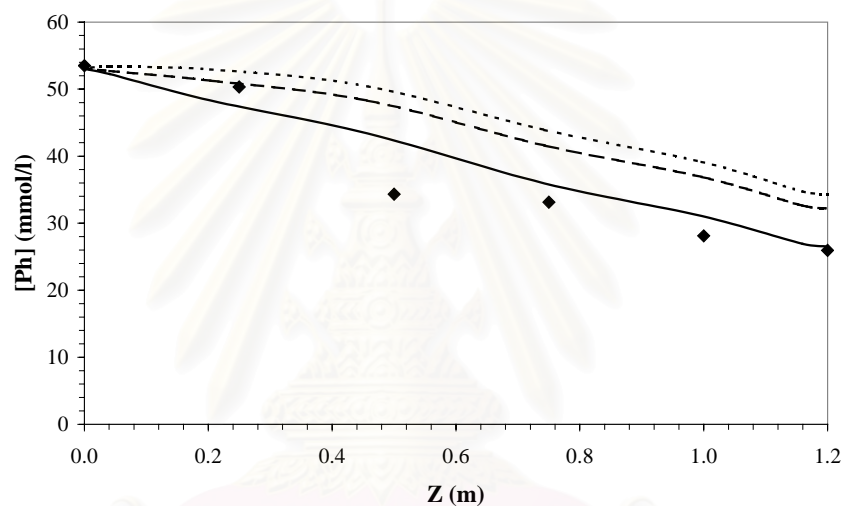
(a) $P_{O_2} = 1.2$ bar, $T_w = 140$ °C, $F_G = 100$ NI/h; (b) $P_{O_2} = 2$ bar, $T_w = 140$ °C, $F_G = 100$ NI/h. Grey symbols show experimental results without correction by catalyst deactivation.

4.3.3.2.2 Axial concentration profiles

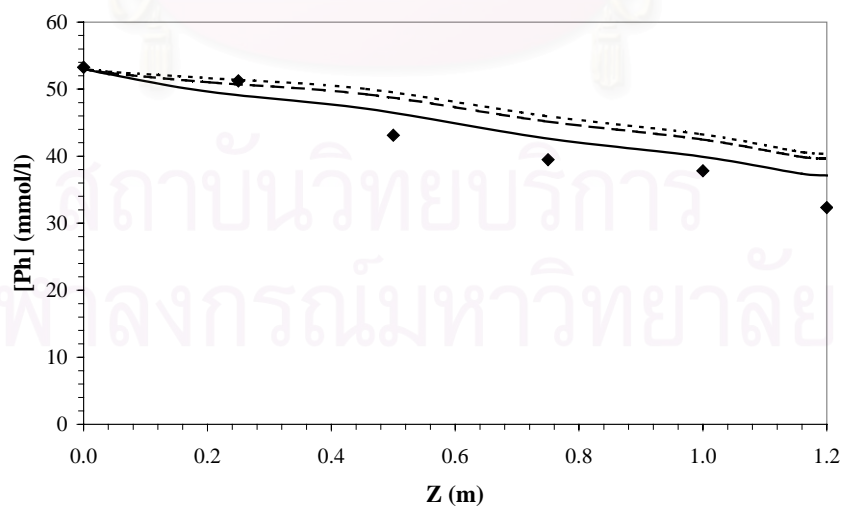
Figures 2-4-28 and 2-4-29 compare the simulated axial concentration profiles respectively for fully and partially wetted catalyst to the experimental ones.

For the same operating conditions, simulated profiles did not show any maximum concentration as seen previously in the upflow mode, due to a lower wall to bed heat transfer coefficient, leading to a slower vaporization along the bed.

As seen previously, the experimental data lied mostly in between the two simulated cases.



(a)



(b)

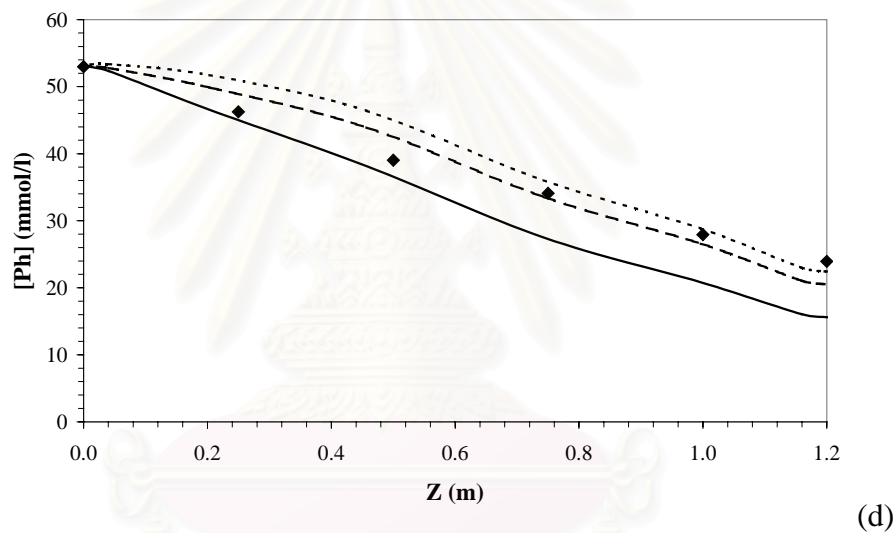
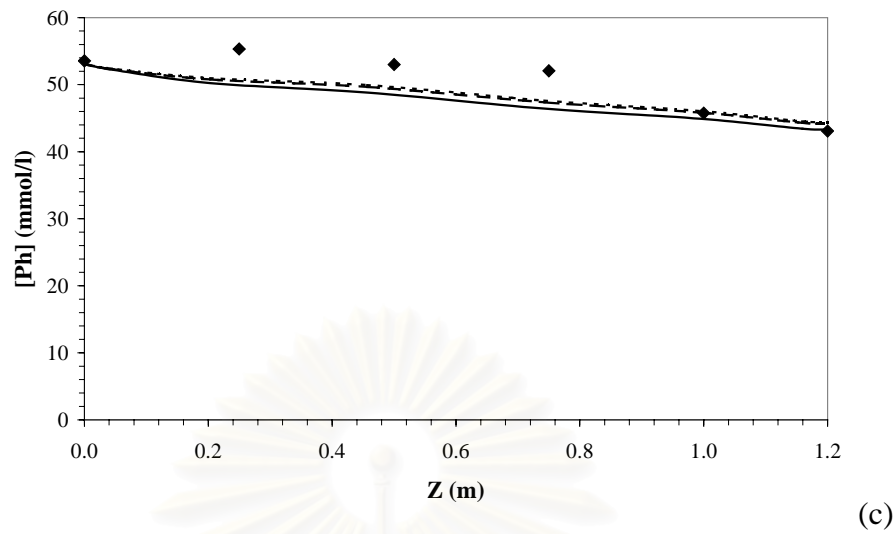


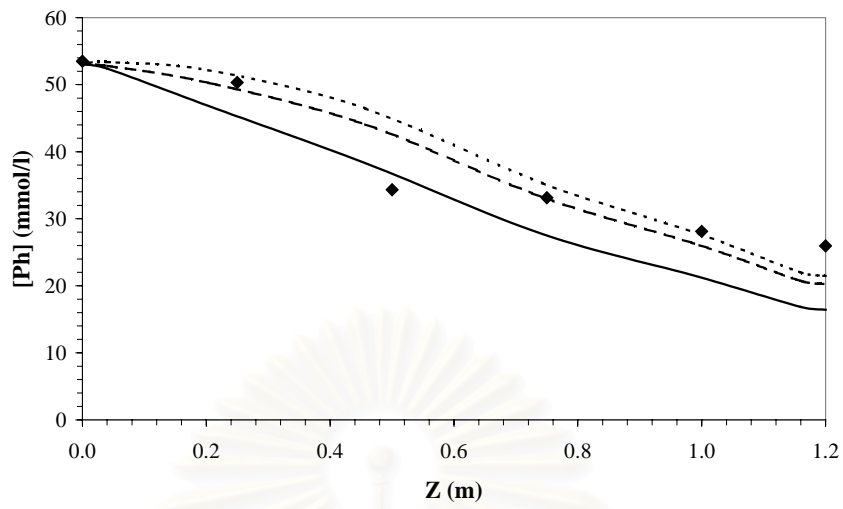
Figure 2-4-28: Axial phenol concentration profiles: experimental (\diamond) and corresponding simulations for fully wetted catalyst: $k_{Ga} = k_{La}$ (solid line), $k_{Ga} = 5 \times k_{La}$ (long dotted line), and instantaneous liquid-vapour equilibrium (short dotted line).

(a) $P_{O_2} = 1.2$ bar, $T_w = 140$ °C, $F_G = 100$ NI/h; $F_L = 0.5$ l/h;

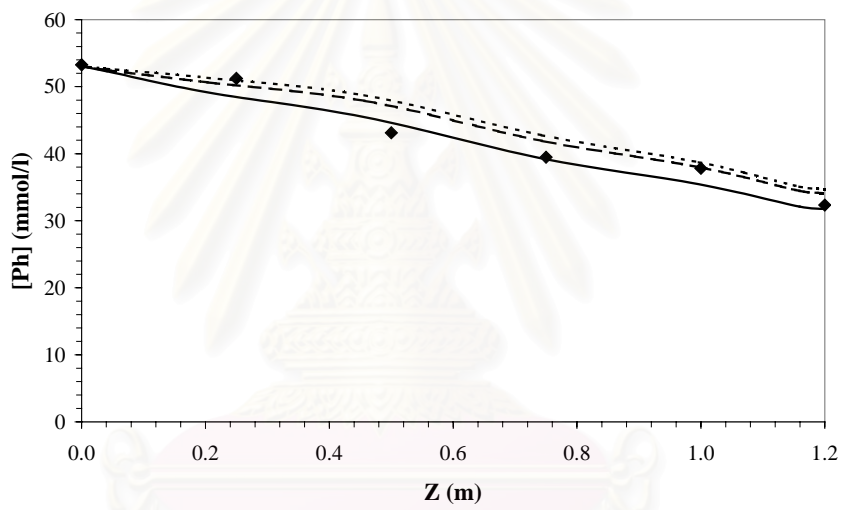
(b) $P_{O_2} = 1.2$ bar, $T_w = 140$ °C, $F_G = 100$ NI/h; $F_L = 1$ l/h;

(c) $P_{O_2} = 1.2$ bar, $T_w = 140$ °C, $F_G = 100$ NI/h; $F_L = 2$ l/h;

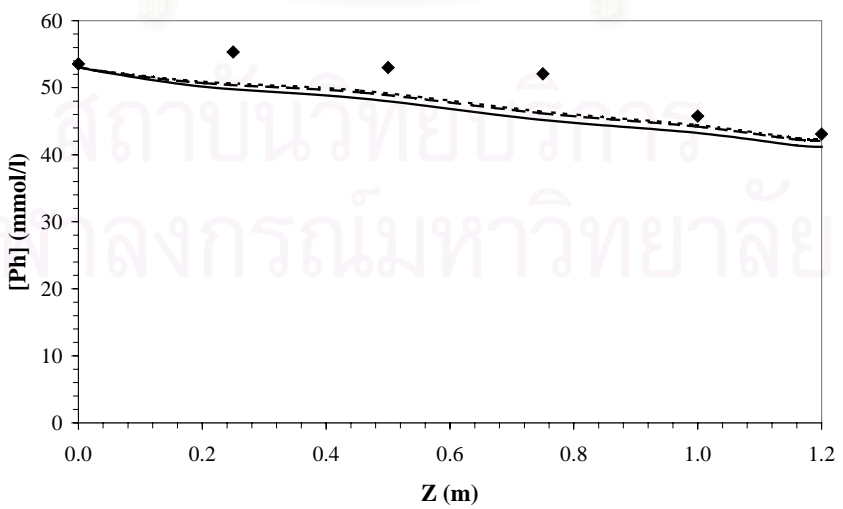
(d) $P_{O_2} = 2$ bar, $T_w = 140$ °C, $F_G = 100$ NI/h; $F_L = 0.5$ l/h.



(a)



(b)



(c)

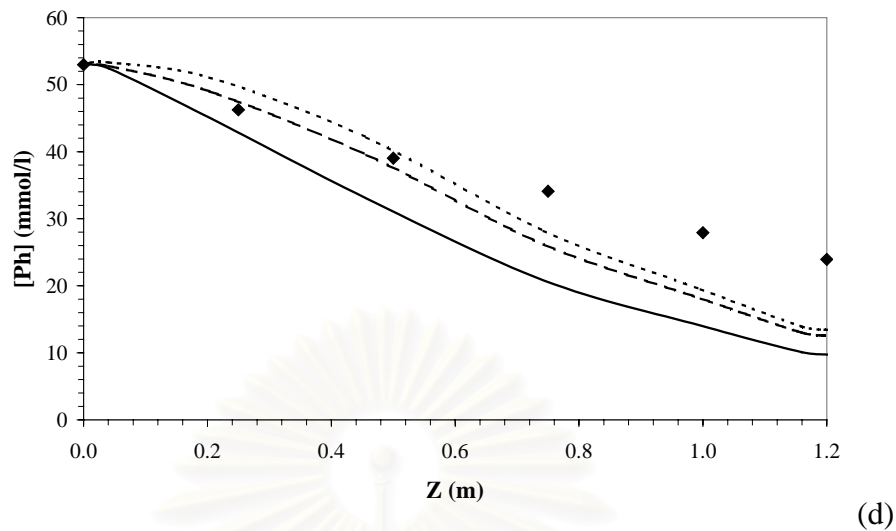


Figure 2-4-29: Axial phenol concentration profiles: experimental (\diamond) and corresponding simulations for partially wetted catalyst: $k_{Ga} = k_{La}$ (solid line), $k_{Ga} = 5 \times k_{La}$ (long dotted line), and instantaneous liquid-vapour equilibrium (short dotted line).

- (a) $P_{O_2} = 1.2$ bar, $T_w = 140$ °C, $F_G = 100$ NI/h; $F_L = 0.5$ l/h;
- (b) $P_{O_2} = 1.2$ bar, $T_w = 140$ °C, $F_G = 100$ NI/h; $F_L = 1$ l/h;
- (c) $P_{O_2} = 1.2$ bar, $T_w = 140$ °C, $F_G = 100$ NI/h; $F_L = 2$ l/h;
- (d) $P_{O_2} = 2$ bar, $T_w = 140$ °C, $F_G = 100$ NI/h; $F_L = 0.5$ l/h.

This comparison showed that the large uncertainties of using a refined model involving many parameters were not easily available or estimated through widely spread correlations. It is clear that the partial wetting effect is not well accounted for with too much increase of oxygen transfer as far as wetting is not fully achieved.

As a general trend, upflow mode was better simulated despite an overestimated effect of vaporization, which would theoretically involve some maximum phenol concentration that never found experimentally. On the other hand experimental downflow profiles generally lay in between simulations with fully and partly wetted catalyst, which did not exhibit a clear maximum phenol concentration.

4.4 Conclusion

This work on aqueous phenol treatment on active carbon may be divided into three parts:

First, a breakthrough curve for phenol adsorption on active carbon at room temperature has been obtained with the pilot FBR showing the high adsorption potential of active carbon. A model accounting for flow characteristics, adsorption isotherm, diffusion inside the active carbon pores, and mass transfer around active carbon particles, gave satisfactory predictions for the concentration take off but not for the end of the process, the arrival to the final plateau being much stiffer than experimentally.

Second, a kinetic analysis of phenol degradation based on phenol concentration profiles in batch autoclave phenol oxidation over the same active carbon pellets showed a rapid decrease of AC activity that stabilised after 3 to 4 runs despite a consecutive strong reduction of adsorption capacity.

The concentration profiles were used in a kinetic parameter optimisation including both diffusion of phenol and dissolved oxygen in AC pores. A rather usual first order was found for phenol while oxygen order 0.5 would suggest a dissociation process if it was confirmed on a much wider oxygen pressure range.

Third, and most important part, continuous wet catalytic air oxidation of phenol solutions was performed in the three phase fixed bed reactor of active carbon being operated successively in upflow and downflow modes.

A stable regime was achieved after a few hours and complete HPLC analysis was then performed at each operation condition. Many intermediate products of phenol partial oxidation were identified, both aromatics and carboxylic acids and a rather complex reaction scheme was proposed including carbon coupling to produce 2- and 4-hydroxybenzoic acids. In order to manage this complex chemical process, a simplified vision was proposed through global COD measurements, proving complete oxidation to carbon dioxide and water to be the main reaction.

AC stability was verified by repeating test reaction conditions at regular intervals during the complete work. No sensible deactivation was observed after 300 oxidation hours at any condition at 120 and 140 °C while a 20% reduction of catalytic activity occurred at 160 °C.

Four main operating parameters have been varied independently: temperature of the thermal oil in the jacket, oxygen partial pressure through the total pressure and the inlet gas composition, and liquid and gas flow rates. The three first variables were proved to highly influence the reactor performance as they are directly connected to the reaction kinetics. Conversely gas flow rate, which was always stoichiometric excess, had only secondary effect especially in the downflow mode. This behaviour suggests that particle kinetics controlled the process with no severe gas-liquid mass transfer limitation.

In order to better understand the results a complete reactor model was carried out based on Eftaxias [4,132]. This model accounts for axial dispersion, heat transfer at the reactor wall, liquid-gas and liquid-particle mass transfers, pore diffusion of both dissolved oxygen and phenol, AC partial wetting, and stagnant liquid zones. In our work due to large temperature variations connected with cold liquid and gas feeds, an important water vaporisation flux had to be included in the model. This was achieved by two ways, comparing instantaneous vaporisation (governed by heat transfer at the wall) and mass transfer limited vaporisation.

Another problem related to the model is the extreme influence given to partial wetting which cannot correspond to physical trends: as soon as wetting is not fully achieved, direct gas-solid oxygen transfer is so intense that external mass transfer limitation vanished. In fact, experimental data appear to range in between partly and fully wetted models. Here the question is how to proceed to avoid complete resolution of two-dimensional diffusion in partly externally wetted porous particles while keeping sound physics?

CHAPTER V

CONCLUSION

Catalytic oxidation of phenol solution was performed in a three phase fixed bed reactor of active carbon being operated both in upflow and downflow modes.

Prior to this investigation a breakthrough curve for phenol adsorption on active carbon was compared to a model accounting for flow characteristics, adsorption isotherm, diffusion inside the active carbon pores, mass transfer around active carbon particles, and predicting a much stiffer arrival to the final plateau than measured. Though some explanations have been proposed, this asymmetrical experimental breakthrough curve should deserve more attention in future adsorption works.

In oxidation operation, a large set of steady state data was collected by varying separately temperature, oxygen partial pressure, liquid space time, and gas velocity. In the selected range of these operation parameters, the reactor performance appeared mainly controlled by the reaction parameters (*i.e.* temperature, oxygen pressure, and liquid space time) and marginally by oxygen mass transfer to the liquid phase, mainly connected to gas and liquid flow rates. Probably for this reason no clear effect of upflow or downflow modes was observed as for a CWAO of phenol in a smaller TBR. Nevertheless a complete model was set up accounting for all usual mass and heat transfers phenomena in trickle or flooded beds. In addition, water vaporisation in the non-isothermal process had important effects and was also included in the model either with equilibrium assumption or using a mass transfer limited flux.

Such a complex model needs a lot of parameters to be established by specific literature correlations. This work clearly faced the lack of reliable data and correlations for many parameters as important as the gas-liquid volumetric mass transfer k_{La} , which could differ by two orders of magnitude depending on several correlations. The situation is even worse for mass transfer limited vaporisation, for which the gas side coefficient is not available at all. Additional work is required on this interesting phenomenon, which typically corresponds to industrial application of CWAO and is not enough addressed in open literature.

Besides this specific work on vaporisation in trickle bed and flooded bed, tracer analysis for RID study would be a relatively easy and fruitful task as

simulations showed it could partly explain the difference of concentration profiles in upflow and downflow modes.

The kinetic study performed in autoclave reactor pointed out fast stabilisation of AC catalytic activity after a few runs where significant deactivation was observed. Simultaneously, active carbon underwent a severe drop of its adsorption capacity.

These two concomitant steep variations of activity and adsorption would deserve additional work. Samples of fresh and aged ACs had been taken and analysed by BET showing a dramatic decrease of the surface area. In addition, TGA proved significant amounts of oxidisable compounds to be fixed on the aged AC. TPO and TPD had also been performed but results are still not available. If the quality of AC was proved to change depending on oxidation conditions, it would open a new field of investigations to find the best operation for a longer use of AC. Up to now, no such conclusion should be derived as very long range experiments have not yet been performed and only temperature seems to affect catalyst stability. These very long experiments correspond to a research and development programme starting soon and connected with the validation and development of the AD-OX process.

From a technical and industrial point of view the CWAO process for phenol aqueous solutions to be treated on active carbon at mild temperature and pressure appears rather promising as no deactivation was found for a significant oxidation time (300 h) in various conditions except high temperature (more than 140 °C). Aromatics were mainly degraded to aliphatic compounds that are easily oxidised later in usual biological wastewater treatment processes.

As many industrial phenolic wastewaters are less concentrated than that used in this work (5 g/l) a new AD-OX process is being developed at LGC Toulouse using both qualities of strong semi-continuous adsorption at room temperature and batch regenerative oxidation of adsorbed pollutants at mild temperature and pressure with only a small fraction of water to be heated. The complete modelling of three phase continuous reactor has been validated in this work. It will constitute a strong basis for AD-OX simulation but will need improvements on partial wetting and some modification to account for the batch process. Here again the feasibility of such process depends on long range stability of AC performances both for adsorption and oxidation.

REFERENCES

PART I

1. Wiseman, P. **Petrochemicals**. 1st ed. Chichester: Ellis Horwood, 1986, pp. 101-140.
2. Chatterjee, A.; Bhattacharya, D.; Chatterjee, M.; Iwasaki, T. Suitability of using ZSM-5 over other medium pore zeolites for *n*-hexane aromatization – a density functional study. **Microporous and Mesoporous Material**, 32 (1999): 189-198.
3. Chen, N. Y.; Township, H.; County, M.; Lucki, S. J.; Garwood, R.; Garwood, W. E.; Haddonfield, N. J. Dewaxing of oils by shape selective cracking and hydrocracking over zeolite ZSM-5 and ZSM-8. **U.S. Patent 3,700,585** (1972).
4. Chu, P. Aromatization of ethane. **U.S. Patent 4,120,910** (1978).
5. Mole, T.; Anderson, J. R.; Creer, G. The reaction of propane over ZSM-5-H and ZSM-5-Zn zeolite catalysts. **Applied Catalysis**, 17 (1985): 141-154.
6. Price, G. L.; Kanazirev, V. The oxidation state of Ga in Ga/ZSM-5 light paraffin aromatization catalysts. **Journal of Molecular Catalysis**, 66 (1991): 115-120.
7. Liu, W. Q.; Zhao, L.; Sun, G. D.; Min, E. Z. Saturation of aromatics and aromatization of C₃ and C₄ hydrocarbons over metal loaded pillared clay catalysts. **Catalysis Today**, 51 (1999): 135-140.
8. Dehertog, W. J. H.; Fromen, G. F. A catalytic route for aromatics production from LPG. **Applied Catalysis A: General**, 189 (1999): 63-75.
9. Komatsu, T.; Mesuda, M.; Yashima, T. Aromatization of butane on Pt-Ge intermetallic compounds supported on HZSM-5. **Applied Catalysis A: General**, 194-195 (2000): 333-339.
10. Choudhary, V. R.; Devadas, P.; Banerjee, S.; Kinage, A. K. Aromatization of diluted ethylene over Ga-modified ZSM-5 type zeolite catalysts. **Microporous and Mesoporous Materials**, 47 (2001): 253-267.
11. Choudhary, V. R.; Devadas, P.; Banerjee, S. Aromatization of propene and *n*-butene over H-gallosilicic acid (ZSM-5 type) zeolite. **Applied Catalysis A: General**, 231 (2002): 243-251.

12. Popova, Z.; Aristorova, K.; Dimitrov, C. Aromatization of C₂-C₆ aliphatic hydrocarbons on copper-containing ZSM-5 zeolite. **Collection of Czechoslovak Chemical Communications**, 57 (1992): 2553-2560.
13. Bhattacharya, D.; Sivasanker, S. Aromatization of *n*-hexane over H-ZSM-5: influence of promoters and added gases. **Applied Catalysis A: General**, 141 (1996): 105-115.
14. Bhattacharya, D.; Sivasanker, S. A comparison of aromatization activities of the medium pore zeolites, ZSM-5, ZSM-22, and EU-1. **Journal of Catalysis**, 153 (1995): 353-355.
15. Rojasová, E.; Smiešková, A.; Hudec, P.; Židec, Z. Role of zinc in Zn-loaded ZSM-5 zeolites in the aromatization of *n*-hexane. **Collection of Czechoslovak Chemical Communications**, 64 (1999): 168-176.
16. Thomson, R. T.; Wolf E. E. Hydrocarbon synthesis over palladium/ZSM-5 bifunctional catalysts. **Applied Catalysis**, 41 (1988): 65-80.
17. Resasco, D. E.; Loughran, C. J. Conversion of nitric oxide and methane over Pd/ZSM-5 catalysts in the absence of oxygen. **Applied Catalysis B: Environmental**, 5 (1995): 351-365.
18. Neyestanaki, A. K.; Kumar, N.; Lindfos, L. E. Catalytic combustion of propane and natural gas over Cu and Pd modified ZSM zeolite catalysts. **Applied Catalysis B: Environmental**, 7 (1995): 95-111.
19. Niwa, M.; Maeda, H.; Reddy, K. R.; Kinoshita, Y.; Muto, K.; Katada, N.; Kamai S. Activity of palladium loaded on zeolites in the combustion of methane. **Applied Catalysis A: General**, 163 (1997): 59-69.
20. Shi, C. K.; Yang, L. F.; He, X. E.; Cai, J. X. Enhanced activity and stability of Zr-promoted Pd/ZSM-5 catalyst for low-temperature methane combustion. **Chemical Communications**, 18 (2002): 2006-2007.
21. Olah, G. A.; Molnar, A. **Hydrocarbon chemistry**. 1st ed. New York: John Wiley & Sons, 1995, pp. 48-49.
22. Bond, G.C. **Heterogeneous catalysis: principles and applications**. 2nd ed. New York: Oxford University Press, 1987, pp. 2-11.
23. Hagen, J. **Industrial catalysis**. 1st ed. Weinheim: Wiley-VCH, 1999, pp. 1-14, 83-248, and 327-344.

24. Satterfield, C. N. **Heterogeneous catalysis in practice**. 1st ed. New York: McGraw-Hill, 1980, pp. 1-24, 42-179, and 235-279.
25. Dyer, A. **An introduction to zeolite molecular sieves**. 1st ed. New York: John-Wiley & Sons, 1988, pp. 1-37 and 87-134.
26. Gates, B. C. **Catalytic chemistry**. 1st ed. New York: John-Wiley & Sons, 1992, pp. 254-301.
27. Breck, D. W. **Zeolite molecular sieves**. 2nd ed. Malabar: Krieger Publishing, 1984, pp. 1-185.
28. Kanai, J.; Kawata, N. Aromatization of *n*-hexane over galloaluminosilicate and gallosilicate. **Applied Catalysis**, 55 (1989): 115-122.
29. Alario, F.; Benazzi, E.; Deves, J. M.; Joly, J. F. ZSM-5 Catalyseur composite et son utilisation en aromatization d'hydrocarbures C₂-C₁₂. **European Patent 0612564A** (1994).
30. Smirniotis, P. G.; Ruckenstein, E. Increased aromatization in the reforming of mixtures of *n*-hexane, methylcyclopentane and methylcyclohexane over composites of Pt/BaKL zeolite with Pt/ β or Pt/USY zeolites. **Applied Catalysis A: General** 123 (1995): 59-88.
31. Zheng, J.; Dong, J. L.; Xu, Q. H.; Liu, Y.; Yan, A. Z. Comparison between β and L zeolites supported platinum for *n*-hexane aromatization. **Applied Catalysis A: General**, 126 (1995): 141-152.
32. Yashima, T.; Wang, Z. B.; Kamo, A.; Yoneda, T.; Komatsu, T. Isomerization of *n*-hexane over platinum loaded zeolite catalysts. **Catalysis Today**, 29 (1996): 279-283.
33. Ali, A. G. A.; Ali, L. I.; Aboul-Fotouh, S. M.; Aboul-Gheit, A. K. Hydroisomerization, hydrocracking and dehydrocyclization of *n*-pentane and *n*-hexane using mono- and bimetallic catalysts promoted with fluorine. **Applied Catalysis A: General**, 215 (2001): 161-173.
34. Essayem, N.; Taârit, Y. B.; Gayraud, P. Y.; Sapaly, G.; Naccache, C. Heteropolyacid catalysts for hydroisomerization of *n*-hexane: effects of alkali salt modification. **Journal of Catalysis**, 204 (2001): 157-162.
35. UOP LLC. **Cyclar process**. Des Plaines: UOP. 2001.
36. UOP LLC. **RZ-Platforming process**. Des Plaines: UOP. 1999.

37. Nagamori, Y.; Kawase M. Converting light hydrocarbons containing olefins to aromatics (Alpha process). **Microporous and Mesoporous Materials**, 21 (1998): 439-445.
38. UOP LLC. **Toray TAC9 process**. Des Plaines: UOP. 2002.
39. Leach, B. E. **Applied Industrial Catalysis** 1st ed. New York: Academic Press, 1983, pp. 107-110, and 133-134.
40. Derouane, E. G.; Lemos, F.; Corma, A.; Ribeiro, F. R. **Combinatorial Catalysis and High Throughput Catalyst Design and Testing** 1st ed. Dordrecht: Kluwer, 2000, pp. 145-150.

PART II

1. Stüber, F.; Polaert, I.; Delmas, H.; Font, J.; Fortuny, A.; Fabregat, A. Catalytic wet air oxidation of phenol using active carbon: performance of discontinuous and continuous reactors. **Journal of Chemical Technology and Biotechnology**, 76 (2001): 743-751.
2. Khalid, M.; Joly, G.; Renaud, A.; Magnoux, P. Removal of phenol from water by adsorption using zeolites. **Industrial and Engineering Chemistry Research**, 43 (2004): 5275-5280.
3. Authenrieth, R. L.; Bonner, J. S.; Akgerman, A.; Okaygun, M.; McCreaney, E. M. Biodegradation of phenolic wastes. **Journal of Hazardous Material**, 28 (1991): 29-53.
4. Eftaxias, A. **Catalytic wet air oxidation of phenol in a trickle bed reactor: Kinetics and reactor modelling**. Ph.D. Thesis, Departament d'Enginyeria Química, Universitat Rovira i Virgili, 2002.
5. Polaert, I.; Wilhelm, A. M.; Delmas, H. Phenol wastewater treatment by two-step adsorption-oxidation process on activated carbon. **Chemical Engineering Science**, 57 (2002): 1585-1590.
6. Mishra, V. S.; Mahajani, V. V.; Joshi, J. B. Wet air oxidation. **Industrial and Engineering Chemistry Research**, 34 (1995): 2-48.
7. Singh, A.; Pant, K. K.; Nigam, K. D. P. Catalytic wet oxidation of phenol in a trickle bed reactor. **Chemical Engineering Journal**, 103 (2004): 51-57.

8. Pintar, A.; Levec, J. Catalytic oxidation of aqueous solutions of organics. An effective method for removal of toxic pollutants from wastewaters. **Catalysis Today**, 24 (1995): 51-58.
9. Imamura, S. Catalytic and noncatalytic wet oxidation. **Industrial and Engineering Chemistry Research**, 38 (1999): 1743-1753.
10. Fortuny, A.; Font, J.; Fabregat, A. Wet air oxidation of phenol using active carbon as catalyst. **Applied Catalysis B: Environmental**, 19 (1998): 165-173.
11. Tukac, V.; Hanika, J. Catalytic wet oxidation of substituted phenols in the trickle bed reactor. **Journal of Chemical Technology and Biotechnology**, 71 (1998): 262-266.
12. Nunoura, T.; Lee, G. H.; Matsumura, Y.; Yamamoto, K. Modeling of supercritical water oxidation of phenol catalyzed by activated carbon. **Chemical Engineering Science**, 57 (2002): 3061-3071.
13. Suarez-Ojeda, E.; M.; Stüber, F.; Fortuny, A.; Fabregat, A.; Carrera, J.; Font, J. Catalytic wet air oxidation of substituted phenols using activated carbon as catalyst. **Applied Catalysis B: Environmental**, 58 (2005): 107-116.
14. Zimmerman, F. J. New waste disposal process. **Chemical Engineering**, 1 (1958): 117-120.
15. Zimmerman, F. J.; Diddams, D. G. The Zimmerman process and its application to the pulp and paper industry. **Tappi**, 43 (1960): 710.
16. Baillod, C. R.; Lamporter, R. A.; Barna, B. A. Wet oxidation for industrial waste treatment. **Chemical Engineering Progress**, 3 (1985): 52-55.
17. Portela Miguelez, J. R.; Lopez Bernal, J.; Nebot Sanz, E.; Martinez de la Ossa, E. Kinetics of wet air oxidation of phenol. **Chemical Engineering Journal**, 67 (1997): 115-121.
18. Copa, W. M.; Gitchel, W. B. **Wet oxidation, standard handbook of hazardous waste treatment and disposal**. 1st ed. New York: McGraw-Hill, 1988.
19. Heimbuch, J. A.; Wilhelmi, A. R. Wet air oxidation - a treatment means for aqueous hazardous waste streams. **Journal of Hazardous Materials**, 12 (1985): 187-200.
20. Maugans, C. B.; Akgerman, A. Catalytic wet oxidation of phenol in a trickle bed reactor over a Pt/TiO₂ catalyst. **Water Research**, 37 (2003): 319-328.

21. Kim, S. K.; Ihm, S. K. Effect of Ce addition and Pt precursor on the activity of Pt/Al₂O₃ catalysts for wet oxidation of phenol. **Industrial and Engineering Chemistry Research**, 41 (2002): 1967-1972.
22. Trawczynski, J. Noble metals supported on carbon black composites as catalysts for the wet-air oxidation of phenol. **Carbon**, 41 (2003): 1515-1523.
23. Hamoudi, S.; Sayari, A.; Belkacemi, K.; Bonneviot, L.; Larachi, F. Catalytic wet oxidation of phenol over Pt_xAg_{1-x}MnO₂/CeO₂ catalysts. **Catalysis Today**, 62 (2000): 379-388.
24. Oliviero, L.; Barbier Jr., J.; Duprez, D. Guerrero-Ruiz, A.; Bachiller-Baeza, B. Rodriguez-Ramos, I. Catalytic wet air oxidation of phenol and acrylic acid over Ru/C and Ru-CeO₂/C catalysts. **Applied Catalysis B: Environmental**, 25 (2000): 267-275.
25. Vaidya, P. D.; Mahajani, V. V. Insight into heterogeneous catalytic wet oxidation of phenol over a Ru/TiO₂ catalyst. **Chemical Engineering Journal**, 87 (2002): 403-416.
26. Imamura, S.; Fukuda, I.; Ishida, S. Wet oxidation catalyzed by ruthenium supported on cerium (IV) oxides. **Industrial and Engineering Chemistry Research**, 27 (1988): 718-721.
27. Atwater, J. E.; Akse, J. R.; Mckinnis, J. A.; Thompson, J. O. Low temperature aqueous phase catalytic oxidation of phenol. **Chemosphere**, 34 (1997): 203-212.
28. Qin, J.; Zhang, Q.; Chuang, K. T. Catalytic wet oxidation of *p*-chlorophenol over supported noble metal catalysts. **Applied Catalysis B: Environmental**, 29 (2001): 115-123.
29. Gomes, H. T.; Figueiredo, J. L.; Faria, J. L. Catalytic wet air oxidation of low molecular weight carboxylic acid using a carbon supported platinum catalyst. **Applied Catalysis B: Environmental**, 27 (2000): L217-L223.
30. Barbier, Jr., J.; Delanoe, F.; Jabouille, F.; Duprez, D.; Blanchard, G.; Isnard, P. Total oxidation of acetic acid in aqueous solutions over noble metal catalysts. **Journal of Catalysis**, 177 (1998): 378-388.
31. Beziat, J. C.; Besson, M.; Gallezot, P.; Durecu, S. Catalytic wet air oxidation on Ru/TiO₂ catalyst in trickle-bed reactor. **Industrial and Engineering Chemistry Research**, 38 (1999): 1310-1315.

32. Lee, D. K.; Kim, D. S. Catalytic wet air oxidation of carboxylic acids at atmospheric pressure. **Catalysis Today**, 63 (2000): 249-255.
33. Kochetkova, R. P.; Babikov, A. F.; Shiplevskaya, L. I.; Shiverskaya, I. P.; Eppel, S. A.; Smidt, F. K. Liquid-phase oxidation of phenol. **Khim. Tekhnol. Topl. Masel**, 4 (1992): 31; **Chem. Abstr.**, 117, 156952 (1992).
34. Matatov-Meytal, Y. I.; Sheintuch, M. Catalytic abatement of water pollutants. **Industrial and Engineering Chemistry Research**, 37 (1998): 309-326.
35. Sadana, A.; Katzer, J. R. Catalytic oxidation of phenol in aqueous solution over copper oxide. **Industrial and Engineering Chemistry Fundamental**, 13 (1974): 127-134.
36. Ohta, H.; Goto, S.; Teshima, H. Liquid phase oxidation of phenol in a rotating catalytic basket reactor. **Industrial and Engineering Chemistry Fundamental**, 19 (1980): 180-185.
37. Fortuny, A.; Ferrer, C.; Bengoa, C.; Font, J.; Fabregat, A. Catalytic removal of phenol from aqueous phase using oxygen or air as oxidant. **Catalysis Today**, 24 (1995): 79-83.
38. Fortuny, A.; Bengoa, C.; Font, J., Castells, F.; Fabregat A. Water pollution abatement by catalytic wet air oxidation in a trickle-bed reactor. **Catalysis Today**, 53 (1999): 107-114.
39. Baldi, G.; Goto, S.; Chow, C. K.; Smith, J. M. Catalytic oxidation of formic acid in water. Intraparticle diffusion in liquid-filled pores. **Industrial and Engineering Chemistry Process Design and Development**, 13 (1974): 447-452.
40. Pintar, A.; Levec, J. Catalytic liquid-phase oxidation of phenol aqueous solutions. a kinetic investigation. **Industrial and Engineering Chemistry Research**, 33 (1994): 3070-3077.
41. Kochetkova, R. P.; Shiverskaya, I. P.; Kochetkov, A. Y.; Panfilova, I. V.; Kovalenko, N. A.; Eppel, S. A.; Minchenko, V. A.; Babikov, A. F. Technological parameters of liquid-phase oxidation of wastewater phenols. **Koks Khim.**, 9 (1992): 44; **Chem. Abstr.**, 119, 55256 (1993).
42. Hamoudi, S.; Larachi, F.; Sayari, A. Wet oxidation of phenolic solutions over heterogeneous catalysts: degradation profile and catalyst behavior. **Journal of Catalysis**, 177 (1998): 247-258.

43. Tukac, V.; Hanika, J. Catalytic effect of active carbon black Chezacarb in wet oxidation of phenol. **Collection of Czechoslovak Chemical Communications**, 61 (1996): 1010-1017.
44. Fortuny, A.; Miró, C.; Font, J.; Fabregat, A. Three-phase reactors for environmental remediation catalytic wet oxidation of phenol using active carbon. **Catalysis Today**, 48 (1999): 323-328.
45. Pereira, M. F. R.; Orfao, J. J. M.; Figueiredo, J. L. Oxidative dehydrogenation of ethylbenzene on activated carbon catalysts: 2. Kinetic modeling. **Applied Catalysis A: General**, 196 (2000): 43-54.
46. Pereira, M. F. R.; Orfao, J. J. M.; Figueiredo, J. L. Oxidative dehydrogenation of ethylbenzene on activated carbon catalysts: 3. Catalyst deactivation. **Applied Catalysis A: General**, 218 (2001): 307-318.
47. Pereira, M. F. R.; Orfao, J. J. M.; Figueiredo, J. L. Oxidative dehydrogenation of ethylbenzene on activated carbon catalysts: I. Influence of chemical groups. **Applied Catalysis A: General**, 184 (1999): 153-160.
48. Luck, F. A review of industrial catalytic wet air oxidation processes. **Catalysis Today**, 27 (1996): 195-202.
49. Kolaczowski, S. T.; Plucinski, P.; Beltran, F. J.; Rivas, F. J.; McLurgh, D. B. Wet air oxidation: a review of process technologies and aspects in reactor design. **Chemical Engineering Journal**, 73 (1999): 143-160.
50. Satterfield, C. N. Trickle-bed reactor. **AIChE Journal**, 21 (1975): 209-215.
51. Hofmann, H. Multiphase catalytic packed-bed reactors. **Catalysis Reviews-Science and Engineering**, 17 (1978): 71-80.
52. Al-Dahhan, M. H.; Larachi, F.; Dudukovic, M.; Laurent, A. High-pressure trickle-bed reactors: a review. **Industrial and Engineering Chemistry Research**, 36 (1997): 3292-3314.
53. Ng, K. M.; Chu, C. F. Trickle-bed reactors. **Chemical Engineering Progress**, 11 (1987): 55-63.
54. Ramachandran, P. A.; Chaudhari, R. V. **Three-phase catalytic reactors**. 1st ed. London: Gordon and Breach, 1983.
55. Meyers, R. A. **Handbook of petroleum refining processes**. 2nd ed. New York: McGraw-Hill, 1996.

56. Diakov, V.; Varma, A. Glucose hydrogenation in a membrane trickle-bed reactor. **AIChE Journal**, 49 (2003): 2933-2936.
57. Hernandez, V. **Les réacteurs à lit fixed avec écoulement de gaz et de liquide. Comparaison sur le plan théorique et expérimental de la performance du réacteur dans différents sens d'écoulement.** Thèse de doctorat, Spécialité Génie des Procédés, Institut National Polytechnique de Lorraine, 1993.
58. Sharma, S. D.; Gadgil, K.; Sarkar, M. K. Estimation of kinetic parameters of benzene hydrogenation in trickle bed reactor. **Chemical Engineering Technology**, 16 (1993): 347-359.
59. Satterfield, C. N.; Pelossof, A. A.; Sherwood, T. K. Mass transfer limitations in trickle-bed reactor. **AIChE Journal**, 15 (1969): 226-234.
60. Goto, S.; Smith, J. M. Trickle-bed reactor performance - Part II Reaction studies. **AIChE Journal**, 21 (1975): 714-720.
61. Levec, J.; Smith, J. M. Oxidation of acetic acid solutions in a trickle-bed reactor. **AIChE Journal**, 22 (1976): 59-68.
62. Goto S.; Mobuchi, K. Oxidation of ethanol in gas-liquid upflow and downflow reactor. **Canadian Journal of Chemical Engineering**, 62 (1984): 865-892.
63. Shah, Y. T. **Gas-Liquid-Solid Reactor Design.** 1st ed. New York: McGraw-Hill, 1979.
64. Al-Dahhan, M. H.; Dudukovic, M. P. Catalyst wetting efficiency in trickle-bed reactor at high pressure. **Chemical Engineering Science**, 50 (1995): 2377-2389.
65. Burghardt, A.; Bartelmus, G.; Jaroszynski, M.; Kolodziej, A. Hydrodynamics and mass transfer in a three-phase fixed bed reactor with cocurrent gas-liquid downflow. **The Chemical Engineering Journal**, 58 (1995): 83-99.
66. Charpentier, J. C.; Favier, M. Some liquid holdup experimental data in trickle-bed reactors for foaming and nonfoaming hydrocarbons. **AIChE Journal**, 21 (1975): 1213-1218.
67. Larachi, F.; Laurent, A.; Wild, G.; Midoux, N. Effet de la pression sur la transition ruisselant-pulsé dans les réacteur catalytiques à lit fixed arrosé. **Canadian Journal of Chemical Engineering**, 71 (1993): 319-321.

68. Al-Dahhan, M. H.; Larachi, F.; Dudukovic, M. P.; Laurent, A. High pressure trickle-bed reactor: a review. **Industrial and Engineering Chemistry Research**, 36 (1997): 3292-3314.
69. Turpin, J. L.; Huntington, R. L. Prediction of pressure drop for two-phase, two-component concurrent flow in packed beds. **AIChE Journal**, 13 (1967): 1196-1202.
70. Julcour, C. **Réacteur catalytiques à lit fixe et co-courant ascendant: modélisation dynamique, sélectivité et comparaison avec le co-courant descendant**. Thèse de doctorat, Spécialité Génie des Procédés, Institut National Polytechnique de Toulouse, 1999.
71. Larachi, F. **Les réacteurs triphasiques à lit fixe à cocourant vers le bas et vers le haut de gaz et de liquide. Etude de l'influence de la pression sur l'hydrodynamique et le transfert de matière gaz-liquide**. Thèse de doctorat, Spécialité Génie des Procédés, Institut National Polytechnique de Lorraine, 1991.
72. Specchia, V.; Baldi, G. Pressure drop and liquid holdup for two phase concurrent flow in packed beds. **Chemical Engineering Science**, 32 (1977): 515-523.
73. Ellman, M. J.; Midoux, N.; Laurent, A.; Charpentier, J. C. A new improved pressure drop correlation for trickle-bed reactor. **Chemical Engineering Science**, 43 (1988): 2201-2206.
74. Wammes, W. J. A.; Westerterp, K. R. Hydrodynamics in a pressurized cocurrent gas liquid trickle-bed reactor. **Chemical Engineering Technology**, 14 (1991): 406-413.
75. Larachi, F.; Laurent, A.; Midoux, N.; Wild, G. Experimental study of a trickle-bed reactor operating at high pressure: two-phase pressure drop and liquid saturation. **Chemical Engineering Science**, 46 (1991): 1233-1246.
76. Yang, X. L.; Euzen, J. P.; Wild, G. Etude de la perte de pression dans les réacteurs à lit fixe avec écoulement à cocourant ascendant de gaz et de liquide. **Entropie**, 159 (1990): 35-44.
77. Yang, X. **Etudes hydrodynamiques des réacteurs à lit fixe écoulement cocourant ascendant de gaz et de liquide**. Thèse de doctorat, Université de Paris VI, 1989.

78. Specchia, V.; Sicardi, S.; Gianetto, A. Absorption in packed towers with concurrent upward flow. **AIChE Journal**, 20 (1974): 646-652.
79. Yang, X.; Wild, G.; Euzen, J. P. A comparison of the hydrodynamics of packed-bed reactors with cocurrent upflow and downflow of gas and liquid. **Chemical Engineering Science**, 47 (1992): 1323-1325.
80. Larachi, F.; Laurent, A.; Midoux, N.; Wild, G. Liquid saturation data in trickle beds operating under elevated pressure. **AIChE Journal**, 37 (1991): 1109-1112.
81. Ellman, M. J.; Midoux, N.; Wild, G.; Laurent, A.; Charpentier, J. C. A new, improved liquid hold-up correlation for trickle-bed reactors. **Chemical Engineering Science**, 45 (1990): 1677-1684.
82. Steigel, G. J.; Shah, Y. T. Backmixing and liquid holdup in a gas-liquid cocurrent upflow packed column. **Industrial and Engineering Chemistry Process Design and Development**, 16 (1977): 37-43.
83. Fukushima, S.; Kusaka, K. Interfacial area and boundary of hydrodynamic flow region in packed column with cocurrent downward flow. **Journal of Chemical Engineering of Japan**, 10 (1977): 461-467.
84. Wammes, W. J. A.; Mechielson, S. J.; Westerterp, K. R. The influence of pressure on the liquid hold-up in a cocurrent gas-liquid trickle-bed reactor operating at low gas velocities. **Chemical Engineering Science**, 46 (1991): 409-417.
85. Larachi, F.; Laurent, A.; Wild, G.; Midoux, N. Some experimental liquid saturation results in fixed-bed reactors operated under elevated pressure in cocurrent upflow and downflow of the gas and the liquid. **Industrial and Engineering Chemistry Research**, 30 (1991): 2404-2410.
86. Yang, X. L.; Euzen, J. P.; Wild, G. Etude de la rétention liquide dans les réacteurs à lit fixe avec écoulement ascendant de gaz et de liquide. **Entropie**, 150 (1989): 17-28.
87. Iliuta, I.; Thyrion, F. C.; Bolle, L.; Giot, M. Comparison of hydrodynamic parameters for countercurrent and cocurrent flow through packed beds. **Chemical Engineering Technology**, 20 (1997): 171-181.
88. Gutsche, S. **Transfert de chaleur dans un réacteur à lit fixe à cocurrent ascendant de gaz et de liquide**. Thèse de doctorat, Spécialité Génie des Procédés, Institut National Polytechnique de Lorraine, 1990.

89. Goto, S.; Saikawa, K.; Gaspillo, P. D. Mass transfer and holdup in gas-liquid in gas-liquid cocurrent upflow and downflow reactors. **Canadian Journal of Chemical Engineering**, 69 (1991): 1344-1347.
90. Wammes, W. J. A.; Mechielson, S. J.; Westerterp, K. R. The transition between trickle flow in a cocurrent gas-liquid trickle-bed reactor at elevated pressure. **Chemical Engineering Science**, 45 (1990): 3149-3158.
91. Wammes, W. J. A.; Middelkamp, W. J.; Huisman, W. J.; deBass C. M., Westerterp, K. R. Hydrodynamics in a cocurrent gas-liquid trickle bed at elevated pressure. **AIChE Journal**, 37, 12 (1991): 1849-1862.
92. Goto, S.; Levec, J.; Smith, J. M. Trickle-bed oxidation reactors. **Catalysis Reviews Science and Engineering**, 15 (1977): 187-247.
93. Thanos, A. M.; Galtier, P. A.; Papayannakos, N. G. Liquid flow non-idealities and hold-up in a pilot scale packed bed reactor with cocurrent gas-liquid upflow. **Chemical Engineering Science**, 51 (1996): 2709-2714.
94. Cassanello, M.; Martinez, O.; Cukierman, A. Effect of liquid axial dispersion on the behaviour of fixed bed three phase reactor. **Chemical Engineering Science**, 47 (1992): 3331-3338.
95. Al-Dahhan, M. H.; Dudukovic, M. P. Catalyst wetting efficiency in trickle-bed reactors at high pressure. **Chemical Engineering Science**, 50 (1995): 2377-2389.
96. Reiss, L. P. Cocurrent gas-liquid contacting in packed columns. **Industrial and Engineering Chemistry Process Design and Development**, 6 (1967): 486-499.
97. Hirose, T; Toda, M.; Sato, Y. Liquid phase mass transfer in packed bed reactor with cocurrent gas-liquid downflow. **Journal of Chemical Engineering of Japan**, 7 (1974): 187-192.
98. Goto, S.; Levec, J.; Smith, J. M. Mass transfer in packed beds with a two phase flow. **Industrial and Engineering Chemistry Process Design and Development**, 14 (1975): 473-478.
99. Charpentier, J. C. Recent progress in two phase gas-liquid mass transfer in packed beds. **Chemical Engineering Journal**, 11 (1976): 161-181.
100. Fukushima, S.; Kusaka, K. Liquid-phase volumetric and mass-transfer coefficient, and boundary of hydrodynamic flow region in packed column with cocurrent

- downward flow. **Journal of Chemical Engineering of Japan**, 10 (1977): 468-474.
101. Turek, F.; Lange, R. Mass transfer in trickle-bed reactors at low Reynolds number. **Chemical Engineering Science**, 36 (1981): 569-579.
102. Midoux, N.; Morsi, B. I.; Purwasasmita, M.; Laurent, A.; Charpentier, J. C. Interfacial area and liquid side mass transfer coefficient in trickle bed reactors operating with organic liquids. **Chemical Engineering Science**, 39 (1984): 781-794.
103. Morsi B.I. Mass transfer coefficients in a trickle-bed reactor with high and low viscosity organic solutions. **Chemical Engineering Journal**, 41 (1989): 41-48.
104. Larachi, F.; Cassanello, M.; Laurent, A. Gas-liquid interfacial mass transfer in trickle-bed reactors at elevated pressure. **Industrial and Engineering Chemistry Research**, 37 (1998): 718-733.
105. Saada, M.Y. Assessment of interfacial area in co-current two-phase flow in packed beds. **Chimie et industrie, Génie chimique**, 105, 20 (1972): 1415-1422.
106. Lara Marquez, A.; Larachi, F.; Wild, G.; Laurent, A. Mass transfer characteristics of fixed beds with cocurrent upflow and downflow. A special reference to the effect of pressure. **Chemical Engineering Science**, 47 (1992): 3485-3492.
107. Satterfield, C. N.; Van Eak, M. W.; Bliss, G. S. Liquid-solid mass transfer in packed beds with downward concurrent gas-liquid flow. **AIChE Journal**, 24 (1978): 709-718.
108. Specchia, V.; Baldi, G.; Gianetto, A. Solid-liquid mass transfer in concurrent two-phase flow through packed beds. **Industrial and Engineering Chemistry Process Design and Development**, 17 (1978): 362-367.
109. Lamine, A. S.; Gerth, L.; Le Gall, H.; Wild, G. Heat transfer in a packed bed reactor with cocurrent downflow of a gas and a liquid. **Chemical Engineering Science**, 51 (1996): 3813-3827.
110. Specchia, V.; Baldi, G. Heat transfer in trickle-bed reactors. **Chemical Engineering Communications**, 3 (1979): 483-499.

111. Lamine, A. S.; Colli Serrano, M. T.; Wild, G. Hydrodynamics and heat transfer in a packed bed reactor with a cocurrent upflow. **Chemical Engineering Science**, 47 (1992): 3493-3500.
112. Nakamura, M.; Tanahashi, T.; Takada, D.; Ohsasa, K.; Sugiyama, S. Heat transfer in a packed bed with a gas liquid cocurrent upflow. **Kagaku Kogaku Ronbunshu**, 7 (1981): 71-76.
113. Fortuny, A.; Miró, C.; Font, J.; Fabregat, A. Three-phase reactors for environmental remediation: catalytic wet oxidation of phenol using active carbon. **Catalysis Today**, 48 (1999): 323-328.
114. Tukač, V.; Hanika, J.; Chyba, V. Periodic state of wet oxidation in trickle-bed reactor. **Catalysis Today**, 79-80 (2003): 427-431.
115. Tukač, V.; Vokál, J.; Hanika, J. Mass transfer-limited wet oxidation of phenol. **Journal of Chemical Technology and Biotechnology**, 76 (2001): 516-510.
116. Singh, A.; Pant, K. K.; Nigam K. D. P. Catalytic wet oxidation of phenol in a trickle bed reactor. **Chemical Engineering Journal**, 103 (2004): 51-57.
117. Stüber, F. **Sélectivité en réacteur catalytique triphasique : analyse expérimentale et théorique d'hydrogénations consécutives en lit fixe catalytique à co-courant ascendant de gaz et de liquide**. Ph.D. Thesis, INP Toulouse, France (1995).
118. Félis, V. **Dépollution d'effluents aqueux contenant des composés aromatiques chlorés par hydrogénation catalytique**. Ph.D. Thesis, Université Claude Bernard – Lyon I, 1998.
119. Reid R. C.; Prausnitz J. M.; Pauling B. E. **The properties of gases and liquids**. McGraw-Hill, New York (1987).
120. Kunii D.; Levenspiel O. **Fluidization engineering**. Wiley (1969).
121. Villermaux, J. Génie de la réaction chimique: conception et fonctionnement des réacteurs. Technique et documentation (Lavoisier 1982).
122. Julcour, C.; Le Lann, J. M.; Wilhelm, A. M.; Delmas, H. Dynamics of internal diffusion during the hydrogenation of 1,5,9-cyclododecatriene on Pd/Al₂O₃. **Catalysis Today**, 48 (1999): 147-159.
123. Sargousse, A.; Le Lann, J. M.; Joulia, X.; Jourda, L. DISCo: Un nouvel environnement de simulation orienté – objet. **MOSIM'99** (6-8 octobre 1999, Annecy): 61-66 (SCS International).

124. Le Lann, J. M. Internal Report, User Manual (1996).
125. Hindmarsh, A.C. LSODE and LSODI, two initial value ordinary differential equation solvers. **ACM SIGNUM Newsletter**, 15, 4 (1980): 10-11.
126. Stüber, F.; Wilhelm, A. M.; Delmas, H. Modeling of a three phase catalytic upflow reactor: a significant chemical determination of liquid-solid and gas-liquid mass transfer coefficients. **Chemical Engineering Science**, 51, 10 (1996): 2161-2167.
127. Devlin, H. R.; Harris, I. J. Mechanism of the oxidation of aqueous phenol with dissolved oxygen. **Industrial and Engineering Chemistry Fundamental**, 23 (1984): 387-392.
128. Constantin, H.; Fick, M. Influence of C-sources on the denitrification rate of a high-nitrate concentrated industrial wastewater. **Water Research**, 31 (1997): 583-589.
129. Morimoto, T.; Tashiro, F.; Nagashima, H.; Nishizawa, K.; Nagata, F.; Yokogawa, Y.; Suzuki, T. Production of poly- β -hydroxybutyric acid by microorganisms accumulated from river water using a two-stage perfusion culture system. **Journal of Bioscience and Bioengineering**, 89 (2000): 97-99.
130. Kragelund, L.; Nybroe, O. Competition between *Pseudomonas fluorescens* Ag1 and *Alcaligenes eutrophus* JMP134 (pJP4) during colonization of barley roots. **FEMS Microbiology Ecology**, 20 (1996): 41-51.
131. Pintar, A.; Levec, J. Catalytic oxidation of organics in aqueous solution: I. kinetic of phenol oxidation. **Journal of Catalysis**, 135 (1992): 345-357.
132. Eftaxias, A.; Larachi, F.; Stüber, F. Modelling of trickle bed reactors for the catalytic wet air oxidation of phenol. **Canadian Journal of Chemical Engineering**, 81 (2003): 784-794.
133. Van Gelder K.B.; Borman P.C.; Weenink R.E.; Westerterp, K.R. Three-phase packed bed reactor with an evaporating solvent – II. Modelling of the reactor. **Chemical Engineering Science**, 45, 10 (1990): 3171-3192.
134. Finlayson, B. A. **Nonlinear analysis in chemical engineering**. McGraw-Hill, New York (1980).
135. Diaz, M.; Vega, A.; Coca J. Correlation for the estimation of gas-liquid diffusivity. **Chemical Engineering Communications**, 52 (1987): 271-281.

136. Himmelblau D. M. Solubilities of inert gases in water: 0 °C to near the critical point of water. **Journal Chemical and Engineering Data**, 5 (1960): 10-15.
137. Michell, R. W.; Furzer I. A. Mixing in trickle flow through packed beds. **Chemical Engineering Journal**, 4 (1972): 53-63.
138. Dwivedi, P. N.; Upadhyay S. N. Particle-fluid mass transfer in fixed and fluidized beds. **Industrial & Engineering Chemistry Process Design and Development**, 16 (1977): 157-165.
139. Tan C. S.; Smith J. M. A dynamic method for liquid-particle mass transfer in trickle beds. **AIChE Journal**, 28 (1982): 190-195.
140. Iliuta, I.; Larachi, F.; Grandjean, B. P. A. Residence time, mass transfer, and back-mixing of the liquid in trickle flow reactors containing porous particles. **Chemical Engineering Science**, 54 (1999): 4099-4109.
141. Hochman, J. M.; Effron E. Two-phase cocurrent downflow in packed beds. **Industrial and Engineering Chemistry Fundamentals**, 8 (1969): 63-71.
142. Saez, A.E.; Carbonell, R.G. Hydrodynamic parameters for gas-liquid cocurrent flow in packed beds. **AIChE Journal**, 31 (1985): 52-61.
143. El-Hisnawi, A.A.; Dudukovic, M.P.; Mills P.L. Trickle - bed reactors: dynamic tracer tests, reaction studies, and modeling of reactor performance. **ACS Symposium Series**, 196 (1982): 421-440.
144. Sokolov, V. N.; Yablokova, M. A. Thermal conductivity of a stationary granular bed with upward gas-liquid flow. **Journal of Applied Chemistry USSR**, 56 (1983): 551-553.
145. Syaiful. **Réacteurs polyphasiques à co-courant ascendant : influence de la viscosité sur les rétentions, dispersions axiales et transfert gaz – liquide**. Ph.D. thesis, INP Toulouse, France (1992).
146. Mariani, N. J.; Martinez, O. M.; Barreto G. F. Evaluation of heat transfer parameters in packed beds with cocurrent downflow of liquid and gas. **Chemical Engineering Science**. 56 (2001): 5995-6001.
147. Rajashekharan, R.; Jaganathan, R.; Chaudhari V. A Trickle bed reactor model for hydrogenation of 2,4-dinitrotoluene: experimental verification. **Chemical Engineering Science**, 53 (1998): 787-805.
148. Gianetto, A.; Silveston, P. L. **Multiphase Chemical Reactors: Theory, Design, Scale-Up**. Hardcover (1986).

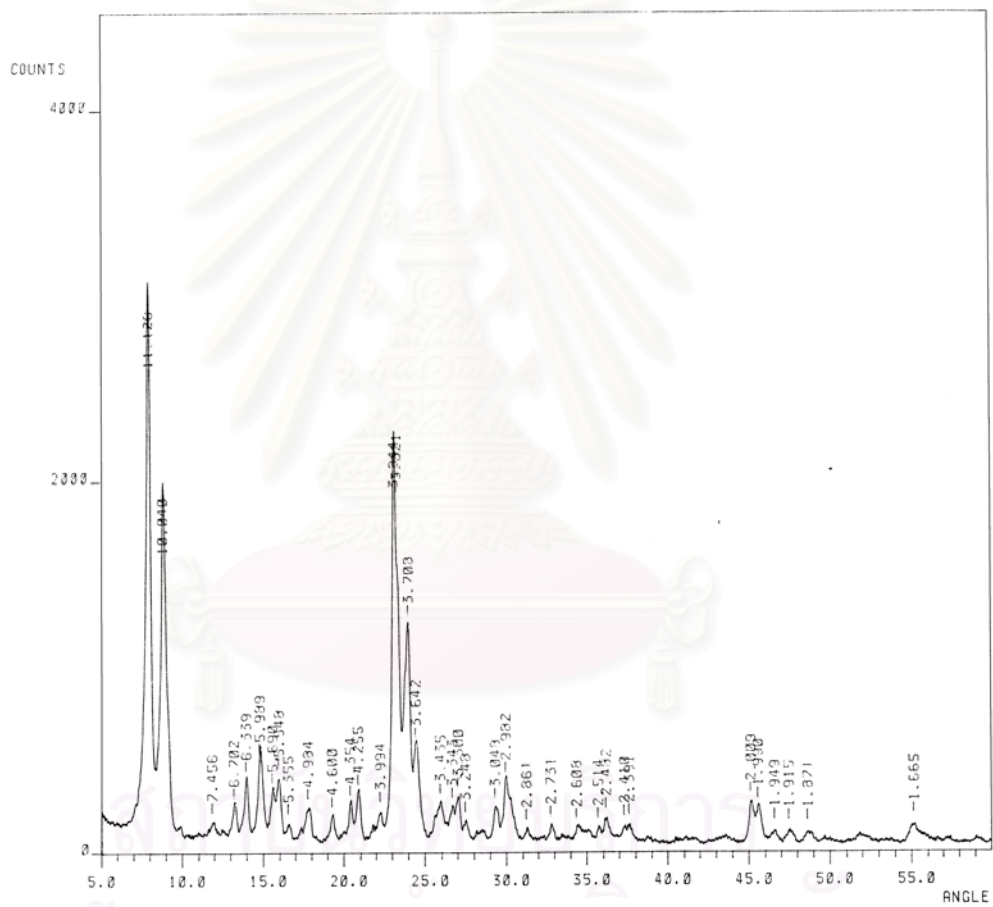


APPENDICES

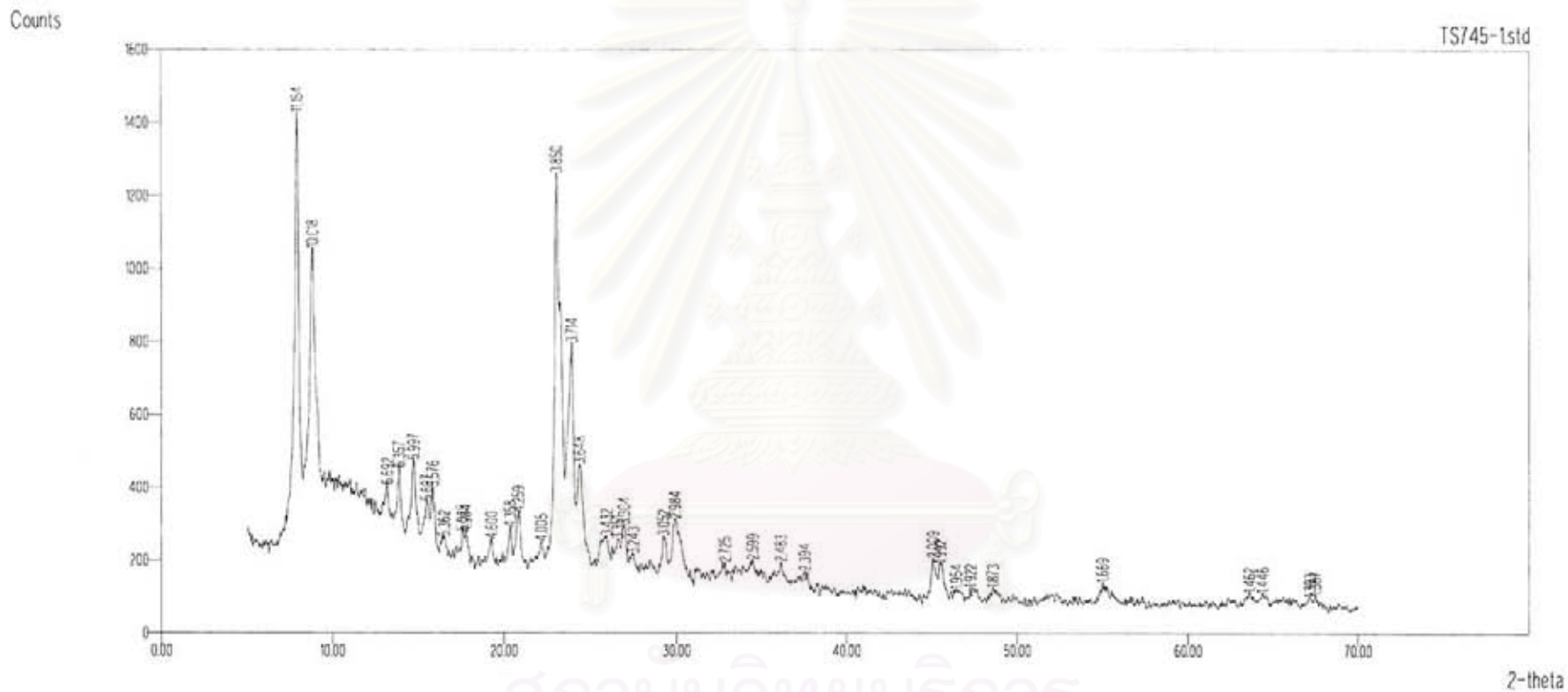
สถาบันวิทยบริการ
จุฬาลงกรณ์มหาวิทยาลัย

Appendix 1-1A: XRD spectrum of zeolite ZSM-5

This spectrum was recorded on a JEOL X-ray powder diffractometer (model JDX-8030).

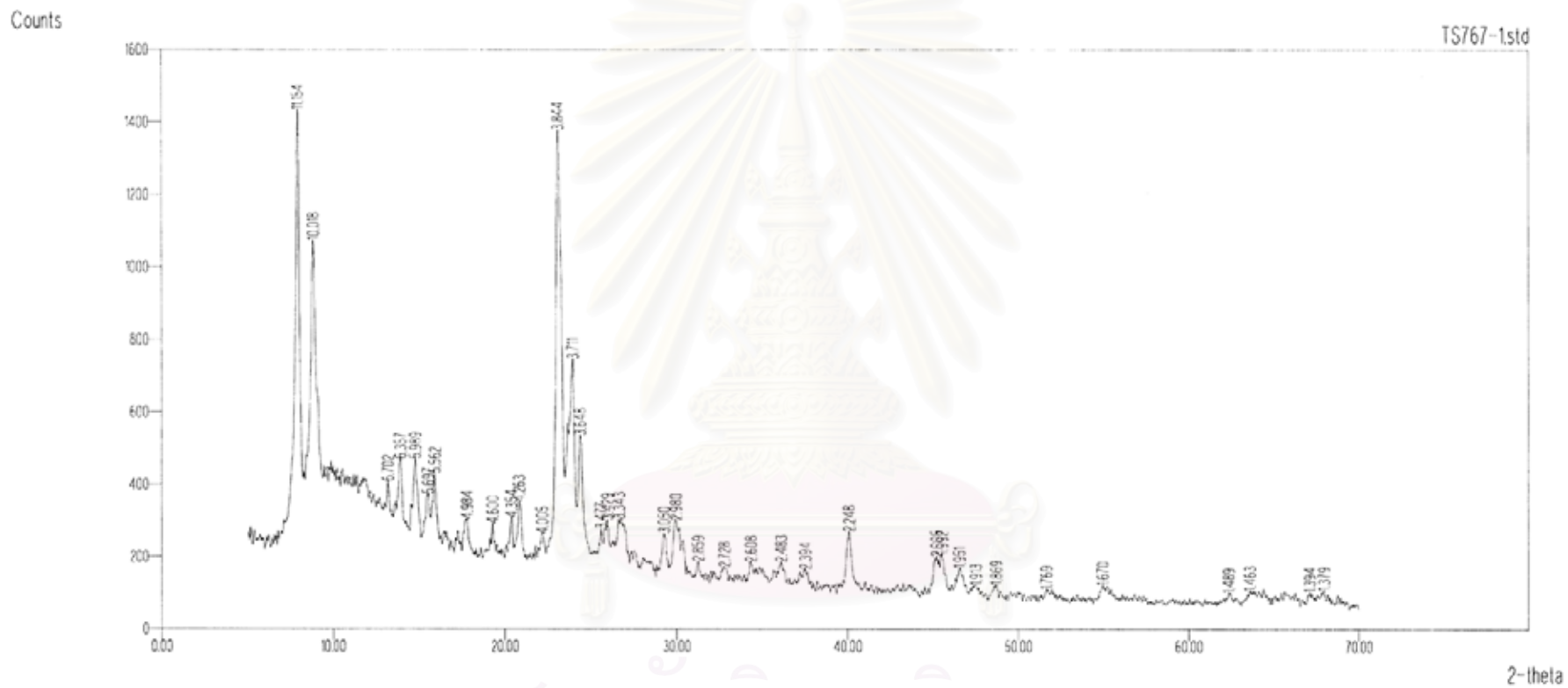


จุฬาลงกรณ์มหาวิทยาลัย



Appendix 1-2A: XRD spectrum of fresh Pd/ZSM-5 catalyst

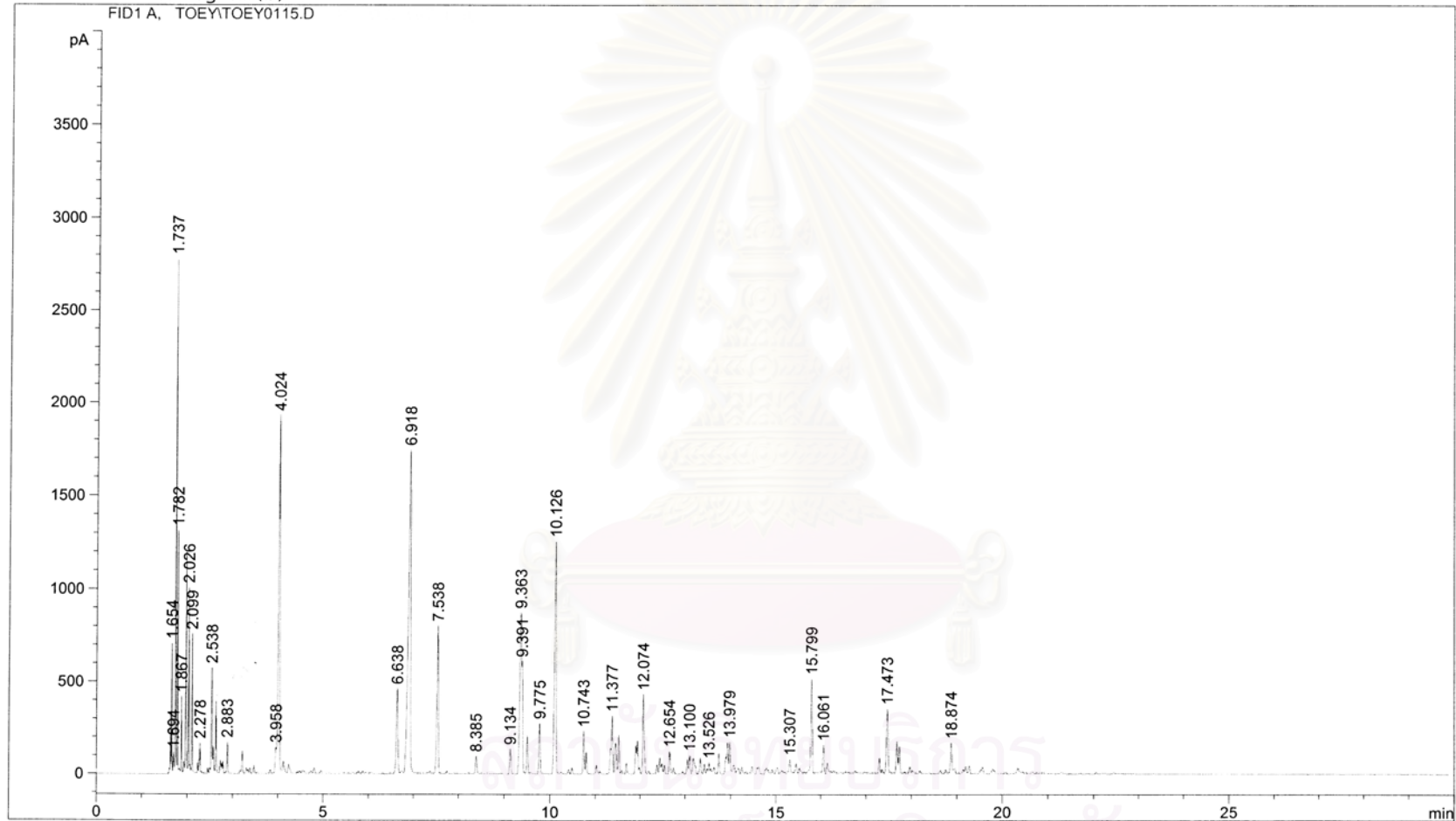
This spectrum was recorded on a JEOL X-ray powder diffractometer (model JDX-3530).



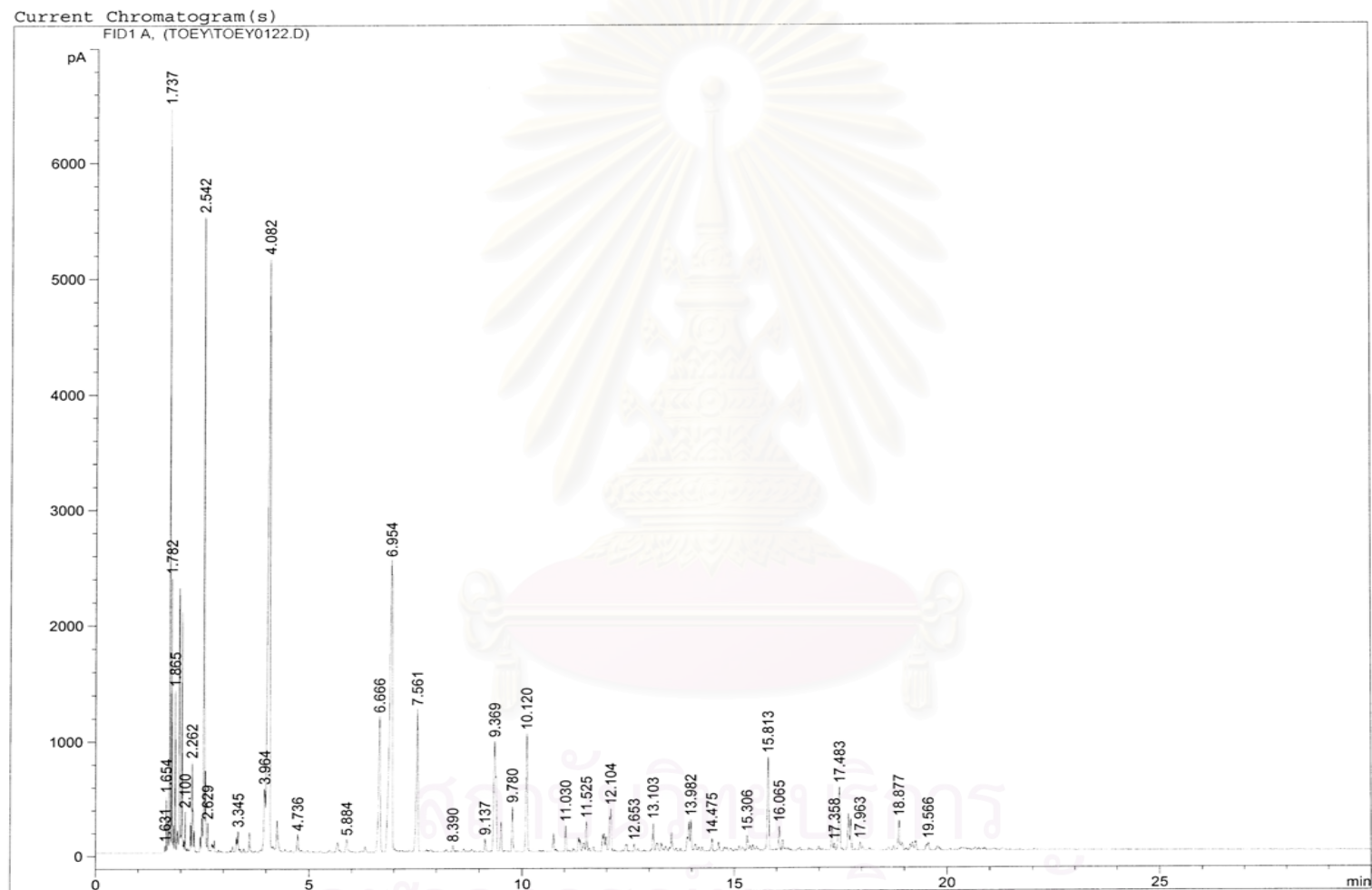
Appendix 1-3A: XRD spectrum of regenerated Pd/ZSM-5 catalyst

This spectrum was recorded on a JEOL X-ray powder diffractometer (model JDX-3530).

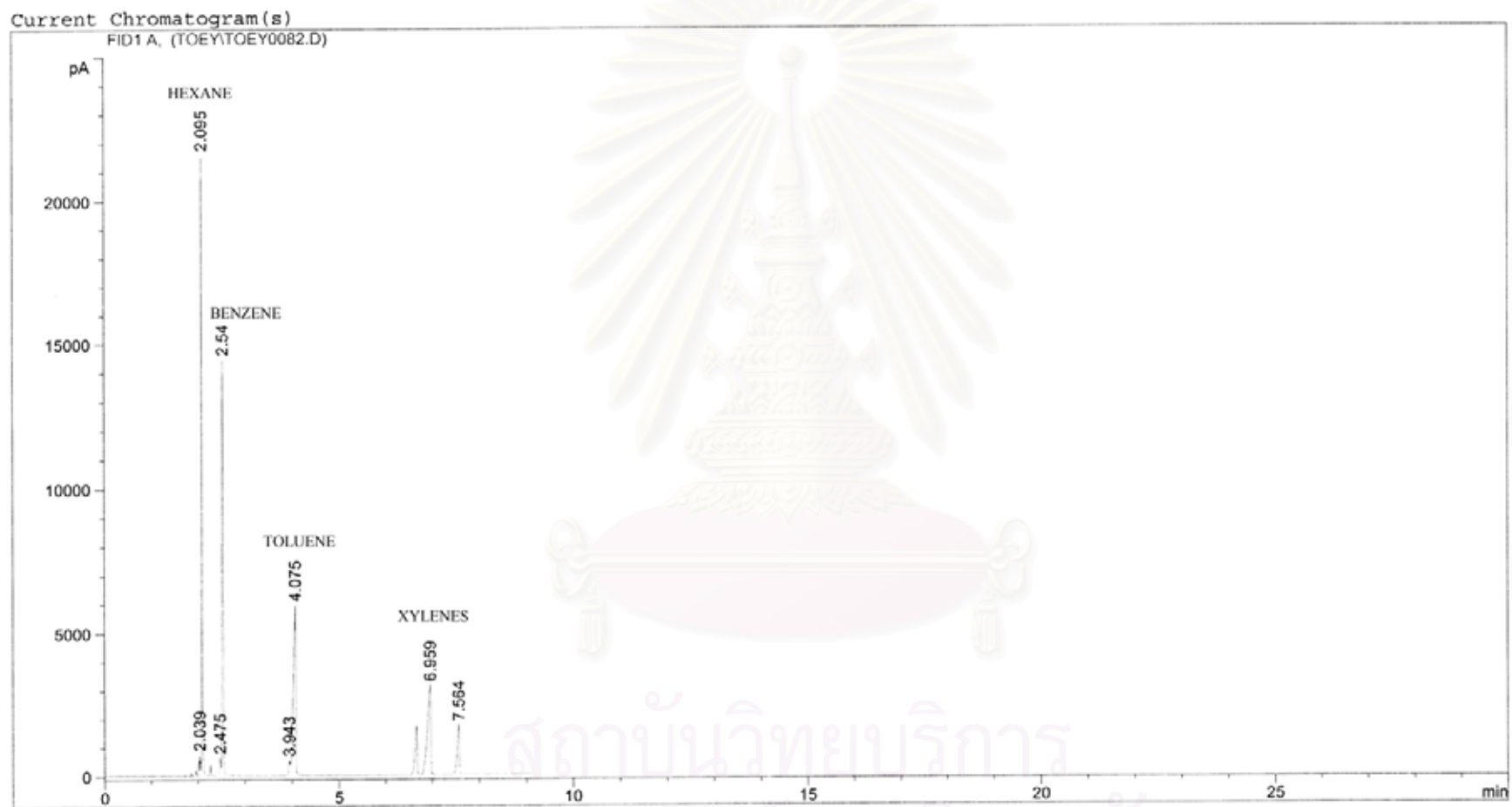
Current Chromatogram(s)
FID1 A, TOEYTOEY0115.D



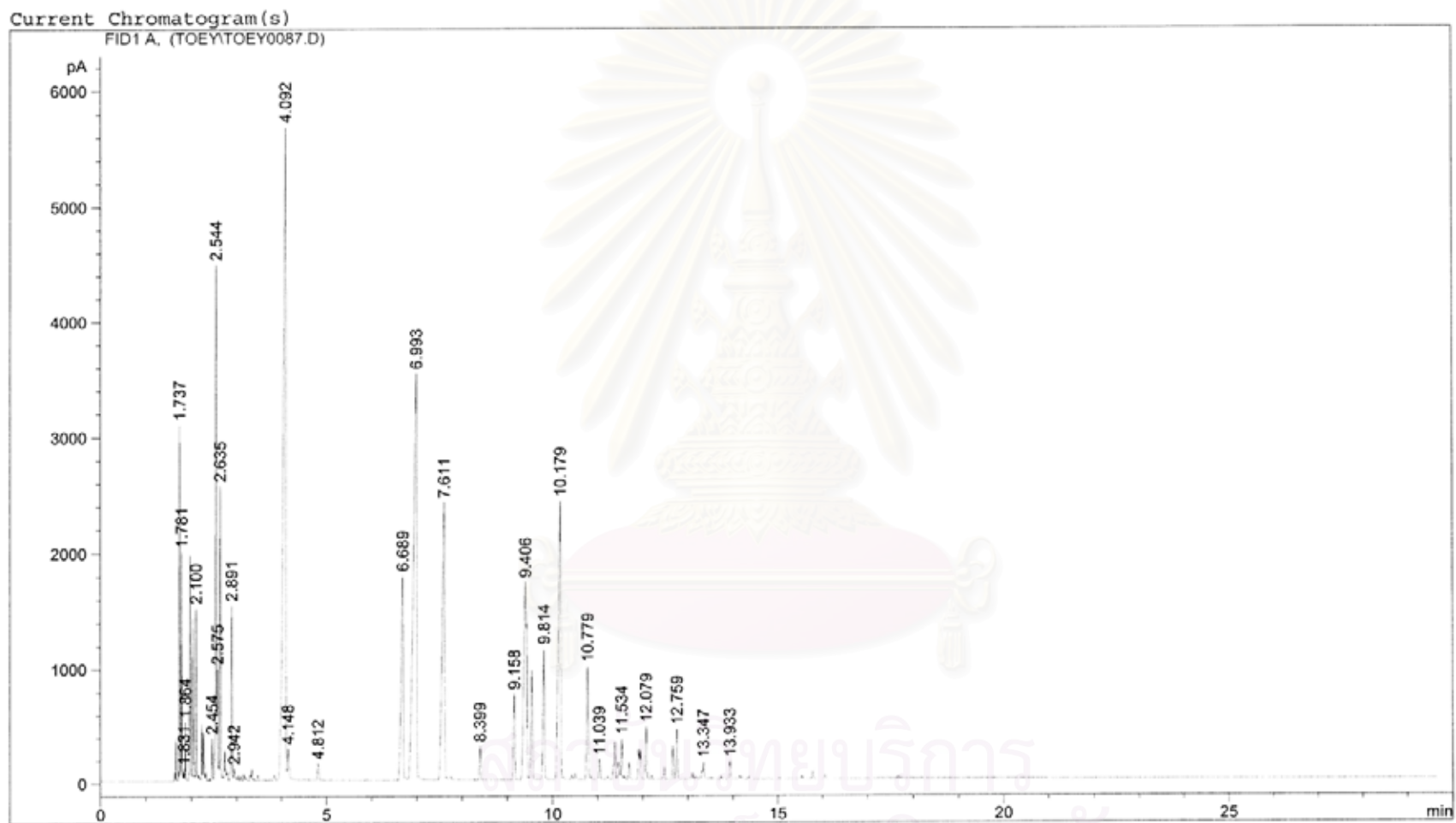
Appendix 1-4A: Typical GC chromatogram of products from *n*-hexane aromatization



Appendix 1-5A: Typical GC chromatogram of products from natural gasoline aromatization



Appendix 1-6A: GC chromatogram of standard compounds



Appendix 1-7A: GC chromatogram of commercial mixture of benzene, toluene, and xylenes

Appendix 2-1A: Correlation for the two-phase pressure drop calculation in cocurrent downflow and upflow fixed bed reactors (After Julcour [70])

a) Cocurrent downflow fixed bed reactor		
Reference	System, Catalyst, Column diameter, Bed porosity	Correlation, Application domain
Turpin and Huntington [69]	Air – water Cylindrical alumina particles: $7.6 < d_p < 8.3$ mm $6.2 < D_c/d_p < 20.0$	$\left(\frac{\Delta P}{\Delta H}\right)_f = \frac{2\rho_G u_G^2}{d_e} \times f_{LGG}$ $\ln f_{LGG} = 7.96 - 1.34 (\ln Z) + 0.0021 (\ln Z)^2 + 0.0078 (\ln Z)^3$ $Z = \frac{Re_G^{1.167}}{Re_L^{0.767}} \quad d_e = 4 \left(\frac{\varepsilon}{1-\varepsilon} \frac{V_p}{S_p} \right)$ $0.2 \leq Z \leq 500$ $0.02 < G < 6.5 \text{ kg/m}^2/\text{s}$ $6.5 < L < 54.2 \text{ kg/m}^2/\text{s}$ $P < 3.4 \text{ atm}$
Specchia and Baldi [72]	Air – water, air – aqueous solution of glycerol (9, 29 %), air – water + surfactant (8, 16 ppm) Glass beads: $d_p = 6$ mm Cylindrical glass particles: $2.7 \leq d_p \leq 5.4$ mm $D_c = 0.08$ m $0.37 \leq \varepsilon \leq 0.40$ $d_p = 2.7$ mm $k_1 = 4.60 \times 10^7$ $k_2 = 460$	Poor interaction regime $\left(\frac{\Delta P}{\Delta H}\right)_f = k_1 \frac{[1 - \varepsilon(1 - \beta_{LS} - \beta_{LD})]^2}{\varepsilon^3 (1 - \beta_{LS} - \beta_{LD})^3} \mu_G u_G + k_2 \frac{[1 - \varepsilon(1 - \beta_{LS} - \beta_{LD})]}{\varepsilon^3 (1 - \beta_{LS} - \beta_{LD})^3} \rho_G u_G^2$ k_1 and k_2 depend on the form and the size of catalyst: $1.36 \times 10^7 < k_1 < 9.65 \times 10^7 \text{ (m}^{-2}\text{)}$ $202 < k_2 < 1620 \text{ (m}^{-1}\text{)}$ $0.0023 \leq u_L \leq 0.022 \text{ m/s}$ $0.082 \leq u_G \leq 1.09 \text{ m/s}$ High interaction regime $\left(\frac{\Delta P}{\Delta H}\right)_f = \frac{2\rho_G u_G^2}{d_e} \times f_{LGG}$ $\ln f_{LGG} = 7.82 - 1.30 (\ln (Z/\psi^{1.1})) - 0.0573 (\ln (Z/\psi^{1.1}))^2$ $\psi = \frac{\sigma_W}{\sigma_L} \left[\frac{\mu_L}{\mu_W} \left(\frac{\rho_W}{\rho_L} \right)^2 \right]^{1/3}$ $0.0016 \leq u_L \leq 0.025 \text{ m/s}$ $0.011 \leq u_G \leq 2.46 \text{ m/s}$ $810 \leq \rho_L \leq 1070 \text{ kg/m}^3$ $0.7 \leq \rho_G \leq 1.2 \text{ kg/m}^3$ $0.001 \leq \mu_L \leq 0.005 \text{ Pa.s}$ $0.027 \leq \sigma_L \leq 0.072 \text{ N/m}$

Ellman <i>et al.</i> [73]	<p>Air – ethyleneglycol, air – gas oil, air – water, air – cyclohexane</p> <p>Spherical and cylindrical particles: $1.16 < d_p < 3.06$ mm</p> <p>$23 < D_c < 100$ mm $0.273 \leq \varepsilon \leq 0.489$</p>	<p>Conditions: $0.0001 \leq G \leq 10$ kg/m²/s $0.5 \leq L \leq 105$ kg/m²/s $0.1 \leq P \leq 10$ MPa</p> $\left(\frac{\Delta P}{\Delta H}\right)_f = \frac{2G^2}{d_h \rho_G} \times f_{LGG}$ <p>High interaction regime $f_{LGG} = \frac{6.96}{(X_G \xi_1)^2} + \frac{53.27}{(X_G \xi_1)^{1.5}} \quad X_G < 0.8$</p> <p>Poor interaction regime $f_{LGG} = \frac{200}{(X_G \xi_2)^{1.2}} + \frac{85}{(X_G \xi_2)^{0.5}} \quad X_G > 1.2$</p> $\xi_1 = \frac{Re_L^{0.25} We_L^{0.2}}{(1 + 3.17 Re_L^{1.65} We_L^{1.2})^{0.1}}$ $\xi_2 = \frac{Re_L^2}{(0.001 + Re_L^{1.5})}$ $d_h = \left(\frac{16\varepsilon^3}{9\pi(1-\varepsilon)^2}\right)^{0.33} d_p$ $X_G = \left(\frac{\rho_G}{\rho_L}\right)^{0.5} \frac{u_G}{u_L}$
Wammes <i>et al.</i> [74]	<p>Nitrogen, helium – water, ethanol, ethyleneglycol</p> <p>Glass beads: $d_p = 3$ mm Alumina extrudates: $d_p = 3.2$ mm</p> <p>$D_c = 51$ mm $0.39 \leq \varepsilon \leq 0.43$</p>	$\frac{\Delta P}{\frac{1}{2} \rho_G u_G^2} \left(\frac{d_p}{\Delta H}\right) = 155 \left(\frac{\rho_G u_G d_p \varepsilon}{\mu_G (1-\varepsilon)}\right)^{-0.37} \left(\frac{1-\varepsilon}{\varepsilon(1-\beta_{Lext})}\right)$ <p>$200 < Re_G < 5000, \beta_{Lext} > 0.25$</p> <p>$u_{L,max} = 16$ mm/s $u_{G,max} = 0.36$ m/s $P < 7.5$ MPa</p>
Larachi <i>et al.</i> [75]	<p>Nitrogen – water, helium – water, nitrogen–ethyleneglycol, nitrogen – water + 1% ethanol</p> <p>Glass beads: $1.4 \leq d_p \leq 2$ mm $D_c = 23$ mm $0.35 \leq \varepsilon \leq 0.38$</p>	$\left(\frac{\Delta P}{\Delta H}\right)_f = \frac{2\rho_G u_G^2}{d_h} \times f_{LGG}$ $f_{LGG} = \frac{1}{\kappa^{1.5}} \left(A + \frac{B}{\kappa^{0.5}}\right)$ <p>$\kappa = X_G (Re_L We_L)^{0.25}$ $A = 31.3 \pm 3.9 \quad B = 17.3 \pm 0.6$</p> <p>$0.003 \leq G \leq 3$ kg/m²/s $1.8 \leq L \leq 24.5$ kg/m²/s $0.2 \leq P \leq 8.1$ MPa</p>

b) Cocurrent upflow fixed bed reactor		
Reference	System, Catalyst, Column diameter, Bed porosity	Correlation, Application domain
Turpin and Huntington [69]	Air – water Cylindrical alumina particles: $7.6 < d_p < 8.3$ mm $6.2 < D_c/d_p < 20.0$	$\ln f_{LGG} = 8.0 - 1.12 (\ln Z) - 0.0769 (\ln Z)^2 + 0.0152 (\ln Z)^3$ $Z = \frac{Re_G^{1.167}}{Re_L^{0.767}} \quad 0.3 \leq Z \leq 500$ $0.02 < G < 6.5$ kg/m ² /s; $6.5 < L < 54.2$ kg/m ² /s $P < 3.4$ atm
Yang <i>et al.</i> [76]	Air, nitrogen – various hydrocarbons $2.2 \leq d_p \leq 2.8$ mm $0.05 \leq D_c \leq 0.225$ m $0.30 \leq \varepsilon \leq 0.34$ $\left(\frac{\Delta P}{\Delta H}\right)_t \leq 4 \times 10^4$ Pa/m $\left(\frac{\Delta P}{\Delta H}\right)_t > 3 \times 10^4$ Pa/m	$\left(\frac{\Delta P}{\Delta H}\right)_f = F_{GL} + F_{LS}$ $F_{LS} = \left[\frac{63.2}{\left(\frac{Re_L \varepsilon}{(1-\varepsilon)\varepsilon_{Lext}}\right)^{0.85}} + 1.07 \right] \frac{1-\varepsilon}{\varepsilon} \frac{\rho_L}{d_p} \left(\frac{u_L}{\varepsilon_{Lext}}\right)^2$ Nonfoaming liquid $F_{GL} = 1756 \sigma_L^{0.72} \times (Re_L'^{0.25} / Fr_G'^{1.11}) \times (u_G / \varepsilon_{Gext})^2 / d_p$ Foaming liquid $F_{GL} = 2945 \sigma_L^{0.72} \times (1 / Fr_G'^{1.11}) \times (u_G / \varepsilon_{Gext})^2 / d_p$ $Re_L' = Re_L / \varepsilon_{Lext} \quad Fr_G' = Fr_G / (\varepsilon_{Gext})^2$ $\log_{10} \left(\frac{\Delta P}{\Delta H}\right)_f = \frac{C_1}{(\log_{10} \chi)^2 + C_2} + \log_{10} \left(\left(\frac{\Delta P}{\Delta H}\right)_G + \left(\frac{\Delta P}{\Delta H}\right)_L \right)$ Nonfoaming liquid $C_1 = 0.082 (\sigma_L / \mu_L)^{0.61}$ $C_2 = 0.099 (\sigma_L / \mu_L)^{0.61}$ Foaming liquid $C_1 = 1.31 \quad C_2 = 1.14$ $\chi = \left(\frac{(\Delta P / \Delta H)_L}{(\Delta P / \Delta H)_G} \right)^{0.5}$ $0 \leq u_L \leq 0.04$ m/s $0 \leq u_G \leq 0.14$ m/s Atmospheric pressure

Larachi [71]	<p>Various systems</p> <p>$0.85 \leq d_p \leq 3.4 \text{ mm}$</p> <p>$D_c = 23 \text{ mm}$</p> <p>$0.32 \leq \varepsilon \leq 0.39$</p>	$f_{LGG} = \frac{1}{\kappa^{1.5}} \left(A + \frac{B}{\kappa^{0.5}} \right)$ <p>$\kappa = X_G (\text{Re}_L \text{We}_L)^{0.25}$</p> <p>$A = 53.4 \pm 5.0$</p> <p>$B = 18.2 \pm 1.0$</p> <p>$0.003 \leq G \leq 3 \text{ kg/m}^2/\text{s}$</p> <p>$1.8 \leq L \leq 24.5 \text{ kg/m}^2/\text{s}$</p> <p>$0.2 \leq P \leq 5.1 \text{ MPa}$</p>
--------------	--	---



สถาบันวิทยบริการ
จุฬาลงกรณ์มหาวิทยาลัย

Appendix 2-2A: Correlation for the calculation of liquid retention or liquid saturation in cocurrent downflow and upflow fixed bed reactors (After Julcour [70])

a) Cocurrent downflow fixed bed reactor		
Reference	System, Catalyst, Column diameter, Bed porosity	Correlation, Application domain
Turpin and Huntington [69]	Air – water Alumina cylindrical particles: $7.6 < d_p < 8.3$ mm $6.2 < D_c/d_p < 20.0$ volumetric method	$\beta_{LD} = 0.132 \left(\frac{L}{G} \right)^{0.24} - 0.017$ $1 < \left(\frac{L}{G} \right)^{0.24} < 6$ $0.02 < G < 6.5 \text{ kg/m}^2/\text{s}$ $6.5 < L < 54.2 \text{ kg/m}^2/\text{s}$ $P < 3.4 \text{ atm}$
Specchia and Baldi [72]	Air – water, air – aqueous solution of glycerol (9, 29 %), air – water + surfactant (8, 16 ppm) Glass beads: $d_p = 6$ mm Glass cylindrical particles: $2.7 \leq d_p \leq 5.4$ mm $D_c = 0.08$ m $0.37 \leq \varepsilon \leq 0.40$ volumetric method $u_{L,max} = 0.03$ m/s $u_{G,max} = 1.09$ m/s	Poor interaction regime $\beta_{LD} = 3.86 (\text{Re}_L)^{0.545} (\text{Ga}_L^*)^{-0.42} \left(\frac{a_c d_p}{\varepsilon} \right)^{0.65}$ $\text{Ga}_L^* = \frac{d_p^3 \rho_L (\rho_L g + (\Delta P / \Delta H)_f)}{\mu_L^2}$ $3 < \text{Re}_L < 3000$ High interaction regime for nonfoaming liquid $\beta_{LD} = 0.125 (Z / \psi^{1.1})^{-0.312} \left(\frac{a_c d_p}{\varepsilon} \right)^{0.65}$ $1 < Z / \psi^{1.1} < 500$
Fukushima and Kusaka [83]	Air – water Raschig rings: $d_p = 9.525$ mm Ceramic spherical particles: $12.7 \leq d_p \leq 25.4$ mm $0.114 \leq D_c \leq 0.2$ m tracer method	$\beta_{Lext} = 1 - 1.8 \chi^{0.15} \left(\frac{d_p}{D_c} \right)^{0.3}$ $3.5 \times 10^{-3} \left(\frac{d_p}{D_c} \right) \leq \chi \left(\frac{d_p}{D_c} \right)^2 < 1.5 \times 10^{-2}$ $\beta_{Lext} = 1 - 1.1 \times 10^2 \chi^{0.9} \left(\frac{d_p}{D_c} \right)^{1.1}$ $2 \times 10^{-5} < \chi \left(\frac{d_p}{D_c} \right)^2 < 3.5 \times 10^{-3} \left(\frac{d_p}{D_c} \right)$ $\chi = \phi^{0.5} \text{Re}_G^{0.4} \text{Re}_L^{-1}, \text{Re} = \frac{\rho u d_s}{\mu}, \phi = \frac{S_p}{d_p^2}$ $0.23 \leq G \leq 2.5 \text{ kg/m}^2/\text{s}$ $2.3 \leq L \leq 100 \text{ kg/m}^2/\text{s}$

Ellman <i>et al.</i> [81]	<p>Various systems</p> <p>Spherical and cylindrical particles: $1.16 < d_p < 3.06$ mm</p> <p>$23 < D_c < 100$ mm $0.273 \leq \varepsilon \leq 0.489$</p>	<p>Conditions: $0.0001 \leq G \leq 10$ kg/m²/s $0.5 \leq L \leq 105$ kg/m²/s $0.1 \leq P \leq 10$ MPa</p> <p>$\beta_{LD} = 10^\kappa$ $\kappa = 0.001 - R / \alpha^S$</p> <p>High interaction regime: $X_G < 0.8$ $\alpha = X_L^{0.5} Re_L^{-0.25} We_L^{0.2} \left(\frac{a_c d_h}{1 - \varepsilon} \right)^{0.25}$ $R = 0.16 \quad S = 0.65$</p> <p>Poor interaction regime: $X_G > 1.2$ $\alpha = X_L^{0.5} Re_L^{-0.3} \left(\frac{a_c d_h}{1 - \varepsilon} \right)^{0.3}$ $R = 0.42 \quad S = 0.48$</p>
Wammes <i>et al.</i> [84]	<p>Nitrogen, helium – water, ethanol, ethyleneglycol</p> <p>Glass beads: $d_p = 3$ mm Alumina extrudates: $d_p = 3.2$ mm</p> <p>$D_c = 51$ mm $0.39 \leq \varepsilon \leq 0.43$</p> <p>volumetric method</p>	$\beta_{LD} = 3.8 \left(\frac{\rho_L u_L d_p}{\mu_L} \right)^{0.55} \times$ $\left(\frac{d_p^3 \rho_L^2 g}{\mu_L^2} \left(1 + \frac{(\Delta P / \Delta H)}{\rho_L g} \right) \right)^{-0.42} \left(\frac{a_c d_p}{\varepsilon} \right)^{0.65}$ <p>$2 \leq Re_L \leq 55$ $3.2 \times 10^3 \leq Ga_L \leq 0.32 \times 10^6$ $0 \leq (\Delta P / (\Delta H \rho_L g)) \leq 16$</p> <p>$u_{L,max} = 16$ mm/s $u_{G,max} = 0.36$ m/s $P < 7.5$ MPa</p>
Larachi <i>et al.</i> [85]	<p>Nitrogen – water, helium – water, nitrogen – ethyleneglycol, nitrogen – water + 1% ethanol</p> <p>Glass beads: $1.4 \leq d_p \leq 2$ mm</p> <p>$D_c = 23$ mm $0.35 \leq \varepsilon \leq 0.38$ tracer method</p>	<p>$\beta_{Lext} = 1 - 10^{-\Gamma}$ $\Gamma = 1.22 \frac{We_L^C}{X_G^D Re_L^E}$ $C = 0.15 \pm 0.016$ $D = 0.15 \pm 0.008$ $E = 0.20 \pm 0.013$</p> <p>$0.003 \leq G \leq 3$ kg/m²/s $1.8 \leq L \leq 24.5$ kg/m²/s $0.2 \leq P \leq 8.1$ MPa</p>

b) Cocurrent upflow fixed bed reactor		
Reference	System, Catalyst, Column diameter, Bed porosity	Correlation, Application domain
Turpin and Huntington [69]	Air – water Alumina cylindrical particles: $7.6 < d_p < 8.3$ mm $6.2 < D_c/d_p < 20.0$ volumetric method	$\beta_{LD} = 0.182 \left(\frac{L}{G} \right)^{0.24} - 0.035$ $1 < \left(\frac{L}{G} \right)^{0.24} < 6$ $0.02 < G < 6.5 \text{ kg/m}^2/\text{s}$ $6.5 < L < 54.2 \text{ kg/m}^2/\text{s}$ $P < 3.4 \text{ atm}$
Stiegel and Shah [82]	Air – water Polyethylene extrudates: 2.8×5.6 mm and 3.12×3.12 mm $D_c = 0.05$ m $\varepsilon = 0.41$ tracer method	$\varepsilon_{Lext} = 1.47 \varepsilon \text{Re}_L^{0.11} \text{Re}_G^{-0.14} (a_s d_s')^{-0.41}$ $d'_s = \sqrt{d_p L_p + d_p^2/2}$ Re calculated with d'_s $0 < G < 0.7 \text{ kg/m}^2/\text{s}$ $3 < L < 25 \text{ kg/m}^2/\text{s}$
Yang <i>et al.</i> [86]	Air, nitrogen – water, various hydrocarbons (foaming and nonfoaming) $2 < d_p < 2.8$ mm $0.05 < D_c < 0.15$ m $0.30 \leq \varepsilon \leq 0.34$ various methods	$\varepsilon_{Lext} = \varepsilon - C_0 \frac{u_G}{u_G + u_L}$ $\frac{u_G}{u_G + u_L} \leq 0.93$ $C_0 = 0.16 \text{ for nonfoaming liquids}$ $C_0 = 0.28 \text{ for foaming liquids}$ $0 \leq u_L \leq 0.04 \text{ m/s}$ $0 \leq u_G \leq 0.14 \text{ m/s}$ Atmospheric pressure

Appendix 2-3A: Correlation for the calculation of mass transfer volumetric coefficient and the gas-liquid interfacial area in cocurrent downflow and upflow fixed bed reactors (After Julcour [70])

a) Cocurrent downflow fixed bed reactor		
Reference	System, Catalyst, Column diameter, Bed porosity	Correlation, Application domain
Reiss [96]	Air – water Raschig rings: $12.7 \leq d_p \leq 76.2$ mm $75 \leq D_c \leq 410$ mm $0.726 \leq \varepsilon \leq 0.883$ Desorption	$k_L a = 0.0173 E_L^{0.5}$ $E_L = \left(\frac{\Delta P}{\Delta H} \right)_f u_L$ $50 < E_L < 10^4$ W/m ³ Atmospheric pressure
Hirose <i>et al.</i> [97]	O ₂ – water Glass beads: $2.59 \leq d_p \leq 12.2$ mm $D_c = 65.8$ mm $0.370 \leq \varepsilon \leq 0.438$ Desorption	$k_L a = d_p^{-0.5} u_L^{0.8} u_G^{0.8}$ $0.05 \leq u_G \leq 1$ m/s $0.01 \leq u_L \leq 0.2$ m/s Bubble flow regime $\frac{k_L a}{\varepsilon} = 0.163 \left(\frac{u_G}{\varepsilon} \right)^{0.6} E_L'^{0.31}$ Pulsed flow regime $\frac{k_L a}{\varepsilon} = 0.135 \left(\frac{u_G}{\varepsilon} \right)^{0.6} E_L'^{0.31}$ $E_L' = \left(\frac{\Delta P}{\Delta H} \right)_f \frac{u_L}{\varepsilon_{Lext}}$ Atmospheric pressure
Goto <i>et al.</i> [98]	O ₂ – water Glass beads: $d_p = 4.13$ mm $\varepsilon = 0.371$ Catalyst particles: $0.541 \leq d_p \leq 2.91$ mm $0.441 \leq \varepsilon \leq 0.453$ $6.25 < D_c / d_p < 58.5$	Catalyst particle of 2.91 mm diameter: $k_L a = 9081 \times D_A \left(\frac{L}{\mu_L} \right)^{0.41} \left(\frac{\mu_L}{\rho_L D_A} \right)^{0.5}$ Catalyst particle of 0.541 mm diameter: $k_L a = 12900 \times D_A \left(\frac{L}{\mu_L} \right)^{0.39} \left(\frac{\mu_L}{\rho_L D_A} \right)^{0.5}$ Glass beads:

		$k_L a = 4438 \times D_A \left(\frac{L}{\mu_L} \right)^{0.4} \left(\frac{\mu_L}{\rho_L D_A} \right)^{0.5}$ $0 \leq u_G \leq 8 \times 10^{-3} \text{ m/s}$ $5 \times 10^{-4} \leq u_L \leq 5 \times 10^{-3} \text{ m/s}$
Charpentier [99]	Various systems	$k_L a = 0.0011 E_L \left(\frac{D_A}{2.4 \times 10^{-9}} \right)$ $5 < E_L < 100 \text{ W/m}^3$ $P \leq 4 \text{ bar}$
Fukushima and Kusaka [100]	<p>Air – Na₂SO₃ solution</p> <p>Raschig rings: d_p = 9.525 mm</p> <p>Ceramic sphericle particles: 12.7 ≤ d_p ≤ 25.4 mm</p> <p>0.114 ≤ D_c ≤ 0.2 m</p>	<p>Pulsed flow regime</p> $k_L a = \frac{D_A}{d_p^2} \left(1 - \frac{\varepsilon_{Lext}}{\varepsilon} \right) \times 1.1 \times 10^{-1} \text{Re}_L \text{Re}_G^{0.4} \text{Sc}_L^{0.5} \left(\frac{d_p}{D_c} \right)^{-0.3}$ <p>Bubble flow regime</p> $k_L a = \frac{D_A}{d_p^2} \left(1 - \frac{\varepsilon_{Lext}}{\varepsilon} \right) \times 6.1 \times 10^{-5} \phi^{-0.6} \text{Re}_L^{2.1} \text{Re}_G^{0.2} \text{Sc}_L^{0.5} \left(\frac{d_p}{D_c} \right)^{-1.5}$ <p>Trickle-flow regime</p> $k_L a = \frac{D_A}{d_p^2} \left(1 - \frac{\varepsilon_{Lext}}{\varepsilon} \right) \times 2.0 \phi^{0.2} \text{Re}_L^{0.73} \text{Re}_G^{0.2} \text{Sc}_L^{0.5} \left(\frac{d_p}{D_c} \right)^{1/5}$
Turek and Lange [101]	<p>Hydrogen – cumene, α-methylstyrene</p> <p>Crushed particles: 0.54 ≤ d_p ≤ 3 mm</p> <p>D_c = 0.034 m</p>	$\frac{k_L a}{D_A} = 16.8 \times 10^4 \text{Ga}^{-0.22} \text{Re}_L^{0.25} \text{Sc}_L^{0.5}$ $0 \leq F_G \leq 100 \text{ l/h}$ $0 \leq F_L \leq 1.5 \text{ l/h}$
Midoux <i>et al.</i> [102]	<p>CO₂ – CHA in toluene + 10% IPA, CO₂ – MEA in ethanol, CO₂ – DEA in ethylene glycol</p> <p>Beads: d_p = 2.4 mm</p>	$\frac{k_L a}{\varepsilon \sqrt{D_A}} = 7.22 \times 10^7 \times \left[\frac{\varepsilon^2 \xi_{LG}}{a_c \left(\frac{L}{\rho_L} + \frac{G}{\rho_G} \right)} \right]^{1.23}$ $= 7.22 \times 10^7 \times \tau_{LS}^{1.23}$

	<p>Cylindrical particles: 0.9 × 5 mm</p> <p>$D_c = 0.05$ m $0.385 \leq \varepsilon \leq 0.396$</p> <p>Absorption with chemical reaction</p>	$\frac{a}{\varepsilon} = 1.47 \times 10^5 \times \left[\frac{\varepsilon^2 \xi_{LG}}{a_c \left(\frac{L}{\rho_L} + \frac{G}{\rho_G} \right)} \right]^{0.65}$ <p>$2 \times 10^{-5} \leq \tau_{LS} \leq 1.5 \times 10^{-3}$</p> $\xi_{LG} = \frac{1}{\varepsilon} \left(\frac{L}{\rho_L} + \frac{G}{\rho_G} \right) \left(\frac{\Delta H_W}{\Delta Z} \right)_f + \frac{L+G}{\varepsilon \rho_W}$ <p>L (max) = 14 kg/m²/s G (max) = 0.25 kg/m²/s</p>
Hirose <i>et al.</i> [97]	<p>CO₂ – NaOH</p> <p>Glass beads: $2.59 \leq d_p \leq 12.2$ mm</p> <p>$D_c = 65.8$ mm $0.370 \leq \varepsilon \leq 0.438$</p> <p>Chemical absorption</p>	<p>$a = 175 d_p^{-0.8} u_L^{0.5} u_G^{0.6}$</p> <p>$0.01 < u_G < 0.6$ m/s $0.01 < u_L < 0.1$ m/s</p> <p>Atmospheric pressure</p>
Morsi [103]	<p>CO₂ – DEA in ethanol, CO₂ – DEA in ethylene glycol</p> <p>Catalyst particles: $d_p =$ 2.4 mm</p> <p>$D_c = 0.05$ m $\varepsilon = 0.385$</p> <p>Absorption with chemical reaction</p>	$\lambda_{LG} = g \left(\frac{L+G}{u_L + u_G} \right) + \left(\frac{\Delta P}{\Delta H} \right)_{LG}$ $\frac{k_L a}{\sqrt{D_A}} = 0.0014 \lambda_{LG}^{1.46}$ <p>$2000 < \lambda_{LG} < 50000$ Pa.m⁻¹</p> <p>$0.05 < G < 0.15$ kg/m²/s $6 < L < 8$ kg/m²/s</p> <p>Atmospheric pressure</p>
Larachi <i>et al.</i> [104]	<p>CO₂ – aqueous solution of DEA – ETG</p> <p>$0.85 \leq d_p \leq 3.37$ mm</p> <p>$D_c = 23$ mm $0.32 \leq \varepsilon \leq 0.39$</p> <p>Chemical absorption</p>	$a = a^\circ \frac{f_w}{f_w^\circ} \times \left\{ 1 + K \left(\frac{\mu_G}{\mu_L} \right)^{1/6} \frac{\mu_L u_L}{\sigma_L \varepsilon} \times \left(1 + 2.5 \left(1 - \frac{\beta_L}{\beta_L^\circ} \right) \right) \times \left(\frac{1}{\beta_L} - \frac{1}{\beta_L^\circ} \right) \right\}$ <p>β_L°, a°, and f_w° were estimated at 1 atm $K = 2.65 \times 10^4$</p> <p>$1.4 \leq L \leq 8$ kg/m²/s $0.3 \leq P \leq 3.2$ MPa</p>

b) Cocurrent upflow fixed bed reactor		
Reference	System, Catalyst, Column diameter, Bed porosity	Correlation, Application domain
Specchia <i>et al.</i> [78]	CO ₂ – NaOH solutions d _p = 6 mm Chemical absorption	$10^3 \frac{k_L \varepsilon}{u_L} = 7.96 \left(\left \frac{\Delta P}{\Delta H} \right \frac{g_c \varepsilon}{a_c \rho_L u_L^2} \right)^{0.275} - 9.41$ $\frac{a}{a_c} = 0.29 \left(\left \frac{\Delta P}{\Delta H} \right \frac{\varepsilon}{a_c} \right)^{1.17} + 0.61$ 0.0025 ≤ u _L ≤ 0.043 m/s 0.14 ≤ u _G ≤ 2.21 m/s
Saada [105]	CO ₂ – NaOH solution Spherical particles: 0.5 ≤ d _p ≤ 2.1 mm D _c = 45 mm Absorption with chemical reaction	$k_L a = 10.72 \frac{D_A}{d_p^2} \text{Re}_G^{0.22} \text{Re}_L^{0.32} \left(\frac{d_p}{D_c} \right)^{0.33}$ 4 ≤ Re _L ≤ 105 20 ≤ Re _G ≤ 450 m/s
Lara Marquez [106]	Air – Na ₂ SO ₃ solution; CO ₂ – DEA 1.2 ≤ d _p ≤ 3 mm D _c = 50 mm ε = 0.37 Chemical absorption	$\frac{a}{a_c} = 1.44(1 - \beta_L) d'_h \left(\frac{\rho_L}{\sigma_L^3} \right)^{0.2} \xi_{LG}^{0.4}$ $\xi_{LG} = \frac{1}{\varepsilon} \left(\frac{L}{\rho_L} + \frac{G}{\rho_G} \right) \left(\frac{\Delta P}{\Delta Z} \right)_f + \frac{L+G}{\varepsilon} g$ $d'_h = \left(\frac{2\varepsilon d_p}{3(1-\varepsilon)} \right)$ $\frac{k_L a}{\sqrt{D_A}} = 40 \xi_{LG}^{0.5}$ $k_L a = 1.026 d_p^{-0.51} u_L^{0.90} u_G^{0.42}$ 5.4 ≤ L ≤ 32.4 kg/m ² /s 0.01 ≤ G ≤ 0.15 kg/m ² /s

Appendix 2-4A: Properties of Marlotherm S (BRENNTAG SPECIALITES)

Marlotherm S is a mixture of dibenzyltoluene isomers. This hydrocarbon is water immiscible and does not react with water.

Chemical, physical, and thermal characteristics of Marlotherm S

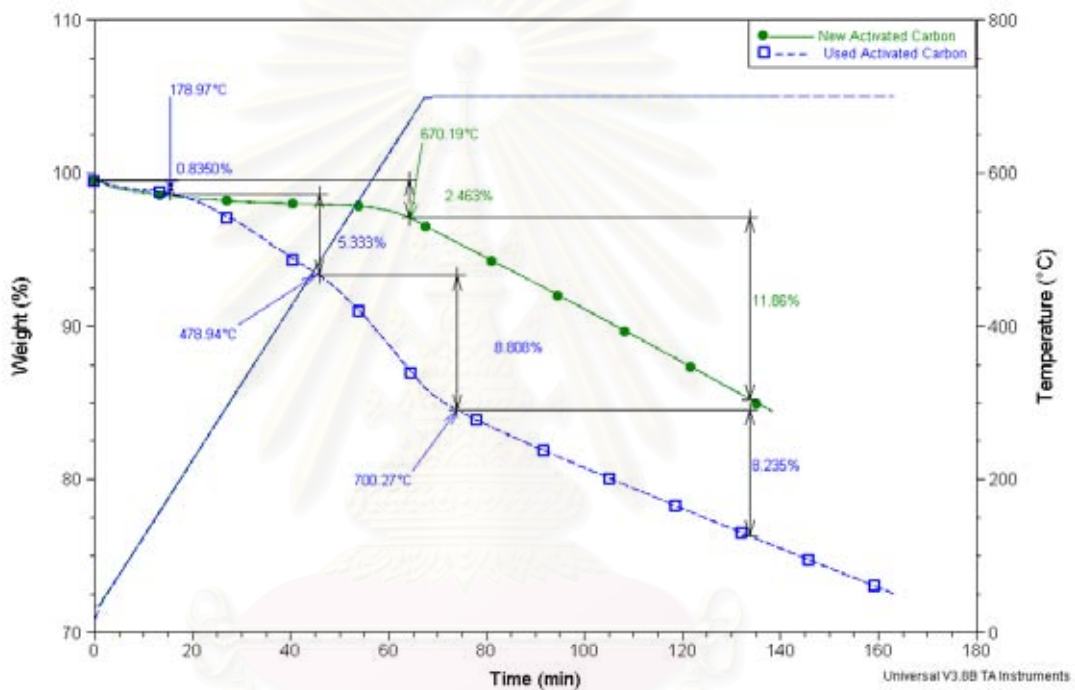
Properties	Value	Unit	Test Method
Molecular weight	272	g/mole	-
Appearance at 20 °C	Clear liquid	-	visual
Chloride contents	< 10	ppm	DIN 51408
Acid number	< 0.02	mg KOH/g	DIN EN ISO 3682
Density at 20 °C	1.04-1.05	g/mL	DIN 51757
Viscosity at 20 °C	42-52	mm ² /s	DIN 51562
Boiling point (at normal pressure)	Approx. 385-395	°C	ASTM D1078
Heat of vaporization (at normal boiling point)	264	kJ/kg	-
Pour point	< -34	°C	DIN ISO 3016
Freezing point	Approx. -35	°C	DIN 51583
Flash point	Approx. 200	°C	EN 22719
Ignition temperature	Approx. 450	°C	DIN 51794
Permissible heater outlet temperature	350	°C	-
Permissible heater film temperature	380	°C	-
Wall admissible temperature	Max. 370	°C	-
Inflammation group	G1	-	VDE 0165
Temperature class	T1	-	VDE 0171
Specific electrical conductivity at 20 °C	6.7×10^{-9}	$\mu\text{s/cm}$	DIN 53779

Evolution of physical characteristics of Marlotherm S at various temperatures

Temperature (K)	Vapor pressure (mbar)	Liquid density (kg/m³)	Liquid viscosity (10⁻³ Pa.s)	Thermal conductivity (W/m/K)	Specific heat capacity (kJ/kg/K)
253		1056	1100	0.136	1.44
273		1043	188	0.134	1.51
293		1029	41	0.132	1.58
313		1015	15	0.130	1.65
333		1001	7.6	0.128	1.71
353		988	4.3	0.126	1.78
373		974	2.9	0.123	1.85
393		959	2.3	0.120	1.92
413		945	1.6	0.119	1.99
433		931	1.3	0.117	2.06
453	1	918	1.0	0.115	2.13
473	4	904	0.86	0.113	2.20
493	8	890	0.73	0.110	2.27
513	17	876	0.62	0.108	2.34
533	33	862	0.54	0.106	2.41
553	64	848	0.47	0.104	2.48
573	114	834	0.42	0.102	2.55
593	190	820	0.38	0.100	2.62
613	326	806	0.34	0.098	2.69
633	513	792	0.32	0.096	2.76

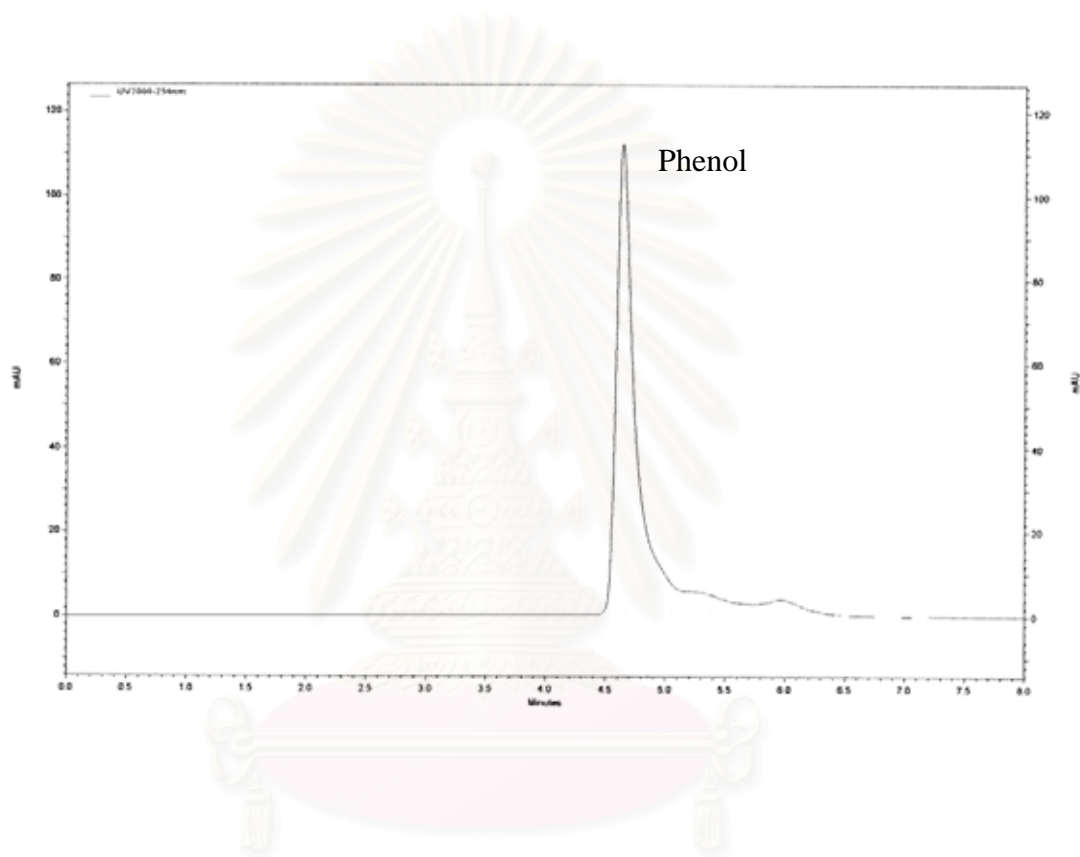
สถาบันวิทยบริการ
จุฬาลงกรณ์มหาวิทยาลัย

Appendix 2-5A: Thermogravimetric analysis of fresh and aged activated carbon
(TA Instrument, SDT Q 600)



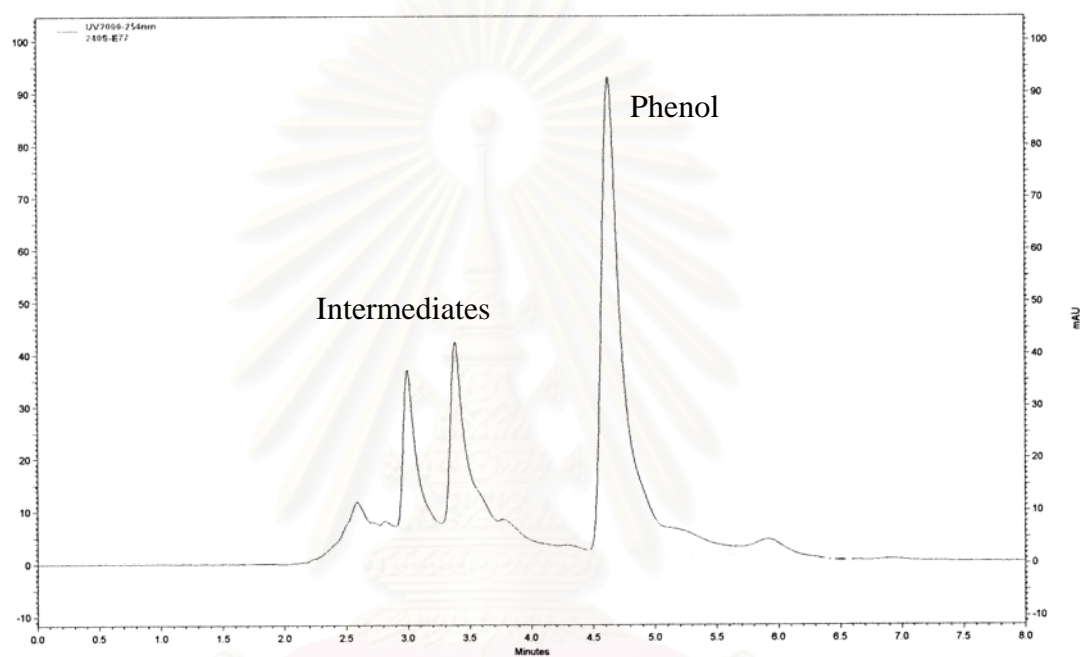
สถาบันวิทยบริการ
จุฬาลงกรณ์มหาวิทยาลัย

Appendix 2-6A: Typical HPLC chromatogram of fast analysis for phenol



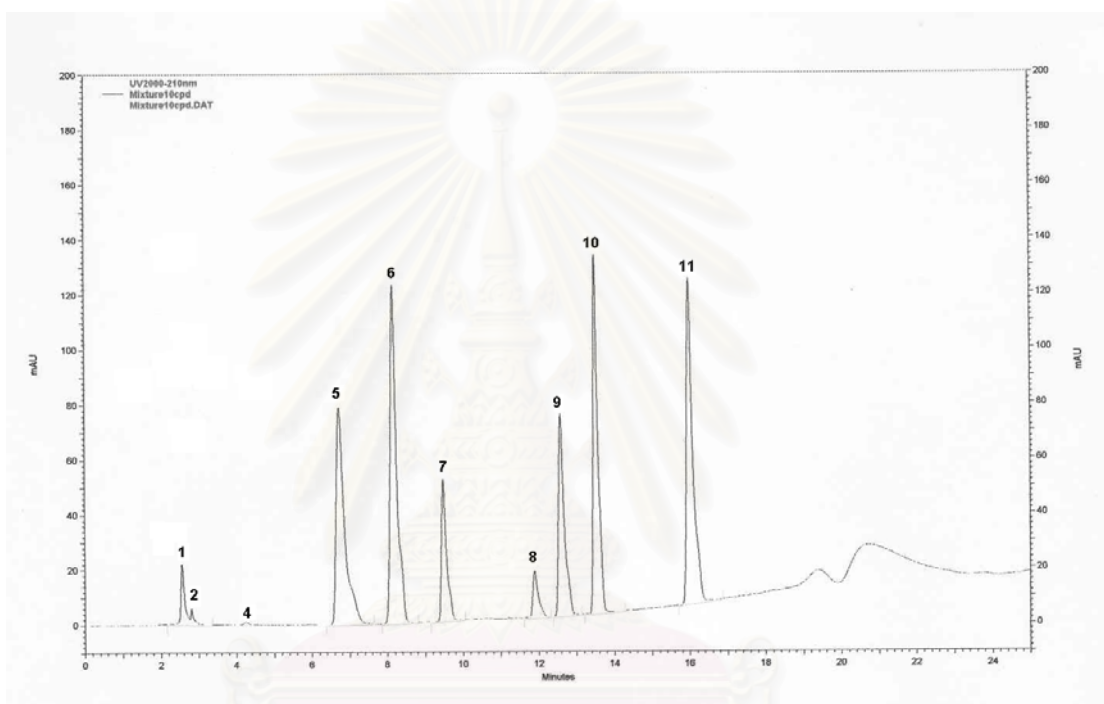
สถาบันวิทยบริการ
จุฬาลงกรณ์มหาวิทยาลัย

Appendix 2-7A: Typical HPLC chromatogram of fast analysis for phenol oxidation products



สถาบันวิทยบริการ
จุฬาลงกรณ์มหาวิทยาลัย

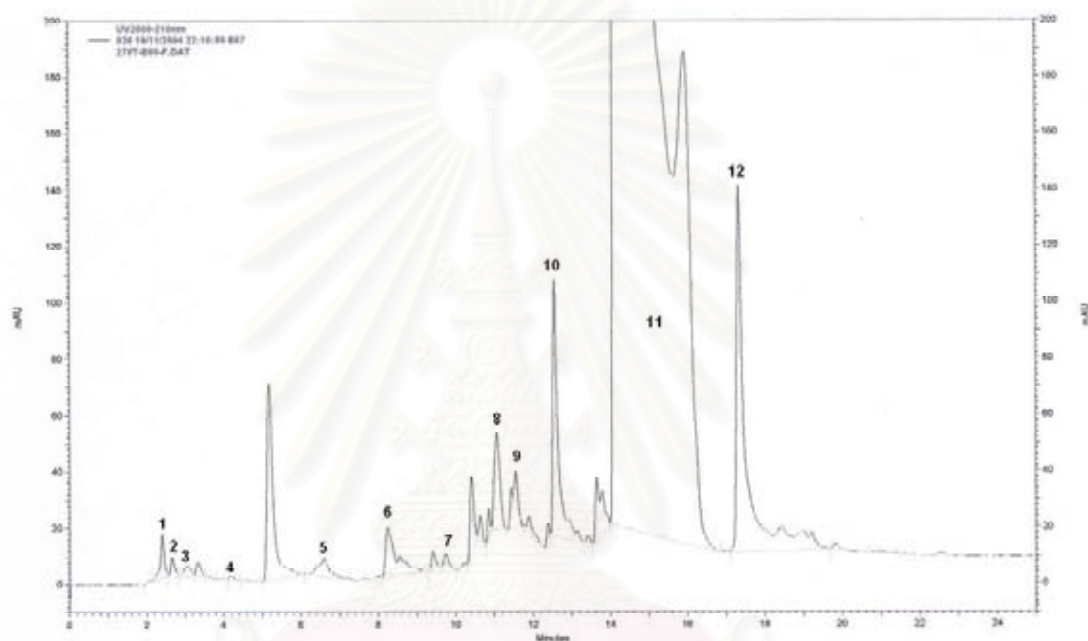
Appendix 2-8A: HPLC chromatogram of full analysis for standard solution (commercial compounds) including some of main phenol oxidation intermediates



1: oxalic acid, 2: formic acid, 4: acetic acid, 5: maleic acid, 6: fumaric acid, 7: hydroquinone, 8: benzoquinone, 9: pyrocatechol (1,2-dihydroxybenzene), 10: 4-hydroxybenzoic acid, 11: phenol.

จุฬาลงกรณ์มหาวิทยาลัย

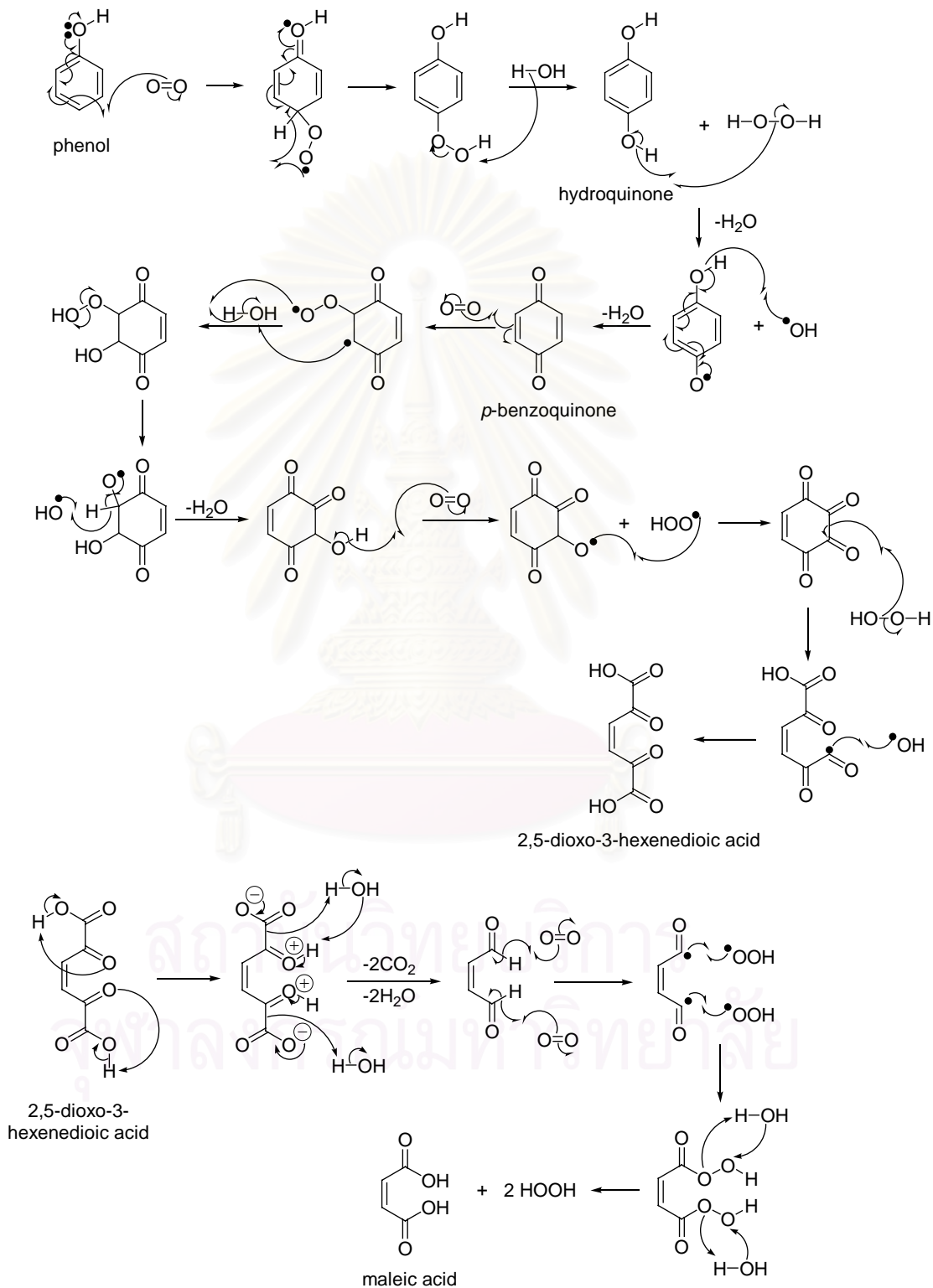
Appendix 2-9A: Typical HPLC chromatogram of full analysis of phenol oxidation products

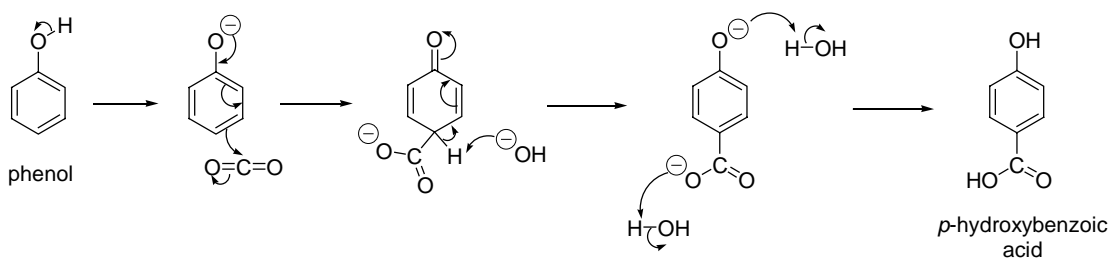
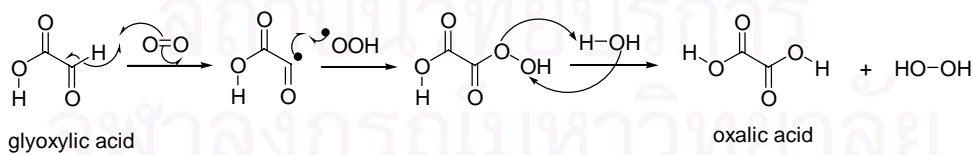
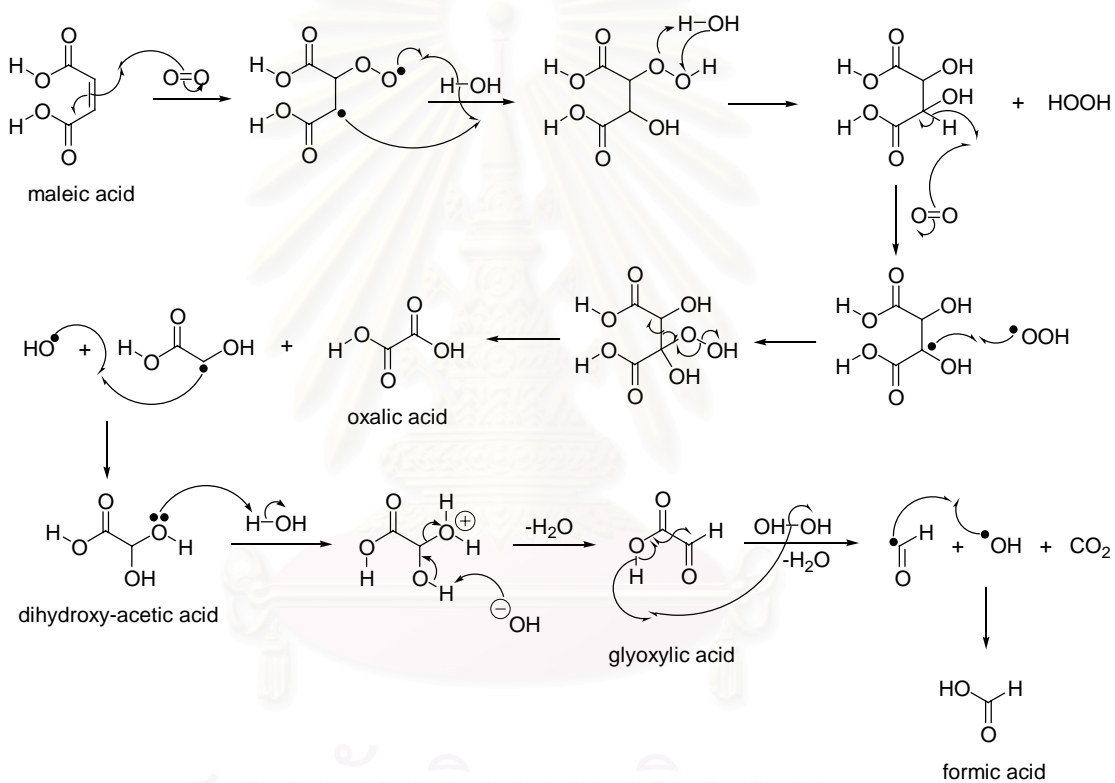
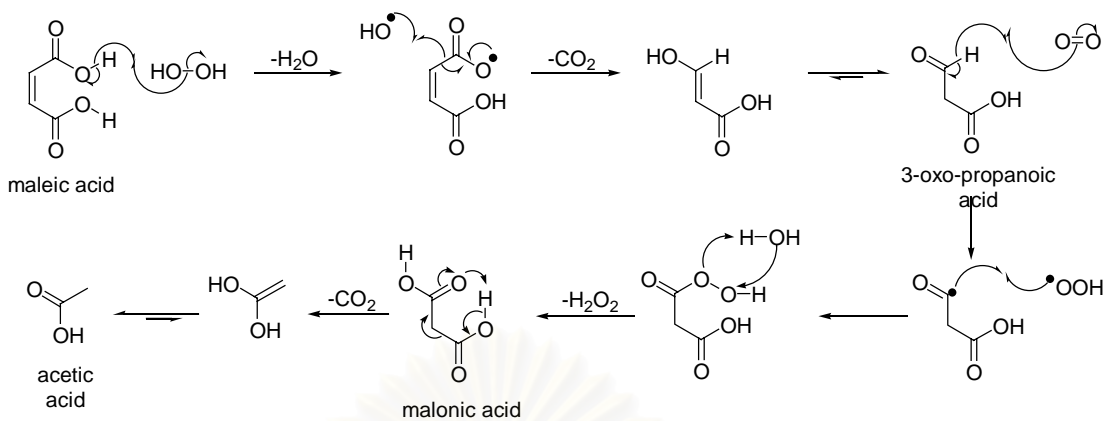


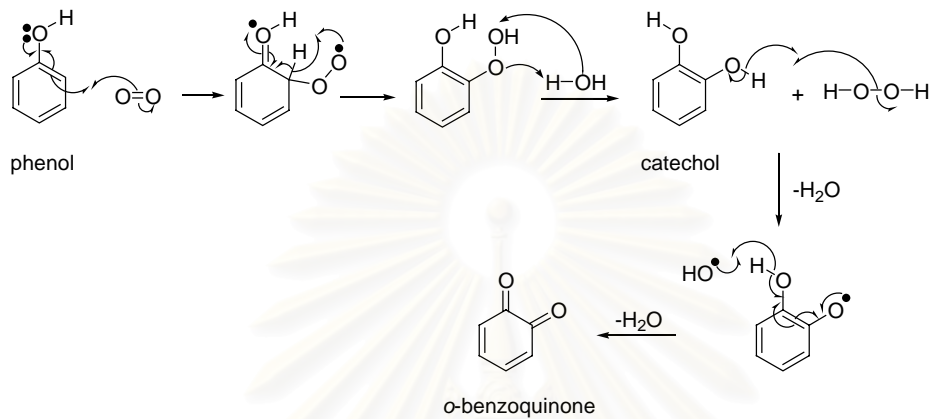
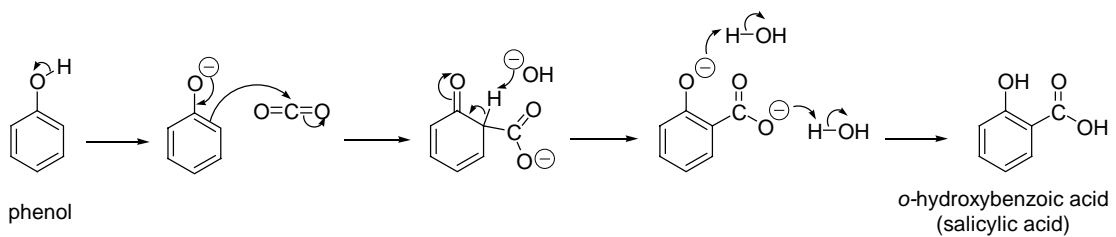
1: oxalic acid, 2: formic acid, 3: malonic acid, 4: acetic acid, 5: maleic acid, 6: fumaric acid, 7: hydroquinone, 8: benzoquinone, 9: pyrocatechol (1,2-dihydroxybenzene), 10: 4-hydroxybenzoic acid, 11: phenol, 12: 2-hydroxybenzoic acid.

จุฬาลงกรณ์มหาวิทยาลัย

Appendix 2-10A: Proposed reaction mechanism for phenol CWAO based on the identified intermediates in the reaction products.

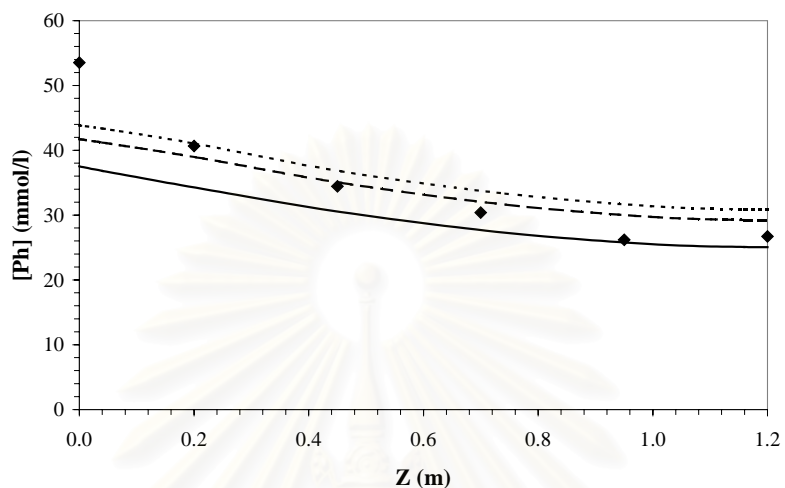




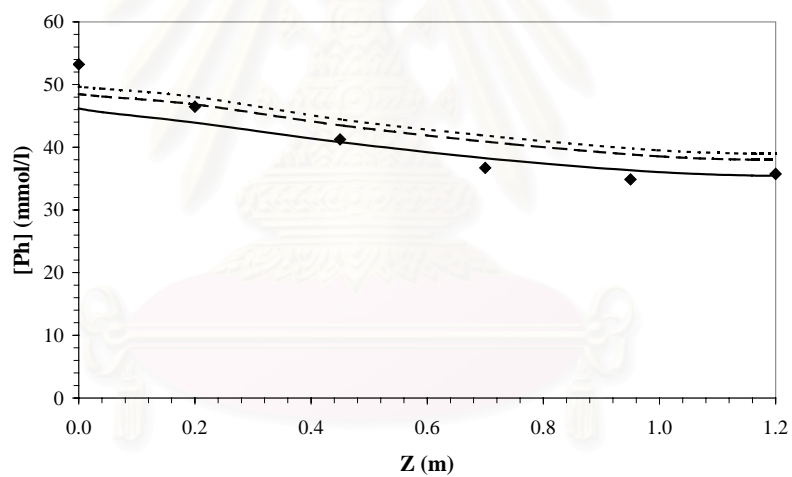


สถาบันวิทยบริการ
จุฬาลงกรณ์มหาวิทยาลัย

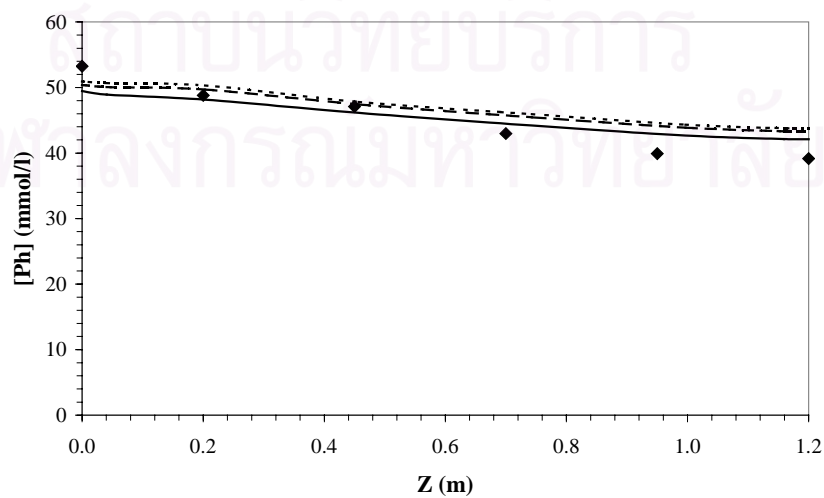
Appendix 2-11A: Axial phenol concentration profiles (1): experimental (\diamond) and corresponding simulations for fully wetted catalyst: $k_{Ga} = k_{La}$ (solid line), $k_{Ga} = 5 \times k_{La}$ (long dotted line), and instantaneous liquid-vapour equilibrium (short dotted line). $D^{ad} = 16.7 \times D^{ad}_{(Stüber)}$; $P_{O_2} = 0.5$ bar, $T_w = 140^\circ\text{C}$, $F_G = 100$ NI/h
 (a) $F_L = 0.5$ l/h; (b) $F_L = 1$ l/h; (c) $F_L = 2$ l/h.



(a)



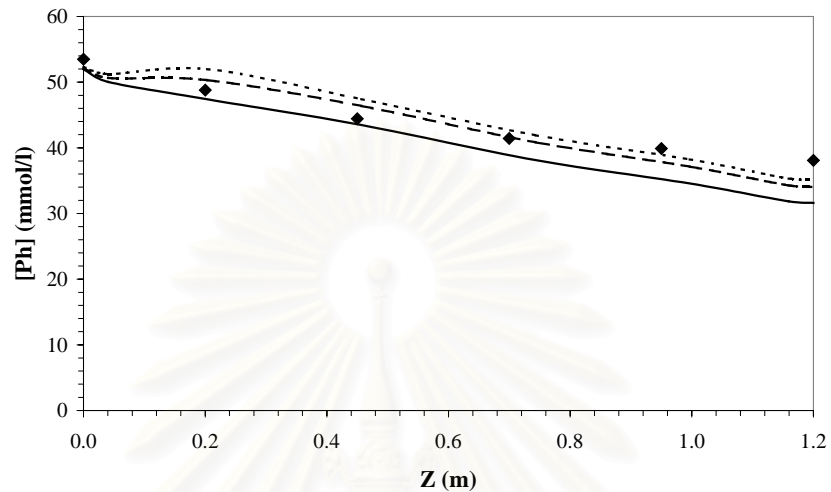
(b)



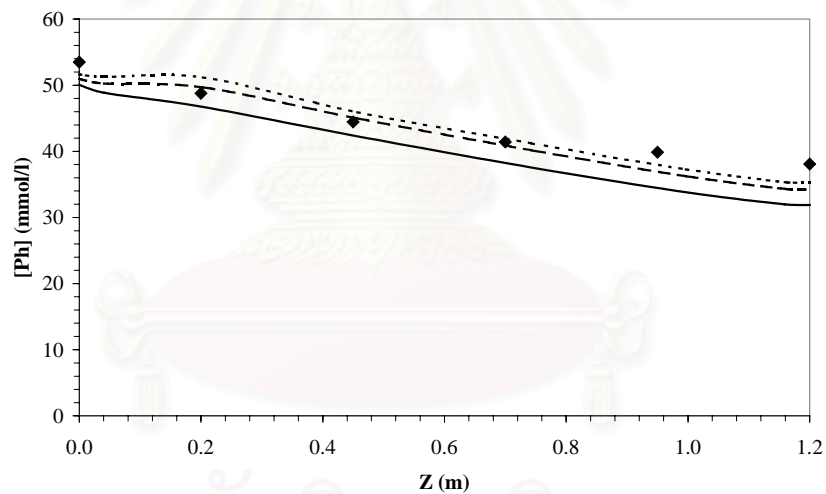
(c)

Appendix 2-12A: Axial phenol concentration profiles (2): experimental (\diamond) and corresponding simulations for fully wetted catalyst: $k_{Ga} = k_{La}$ (solid line), $k_{Ga} = 5 \times k_{La}$ (long dotted line), and instantaneous liquid-vapour equilibrium (short dotted line). $P_{O_2} = 2.0$ bar, $T_w = 140^\circ\text{C}$, $F_G = 100$ NI/h, $F_L = 1.3$ l/h

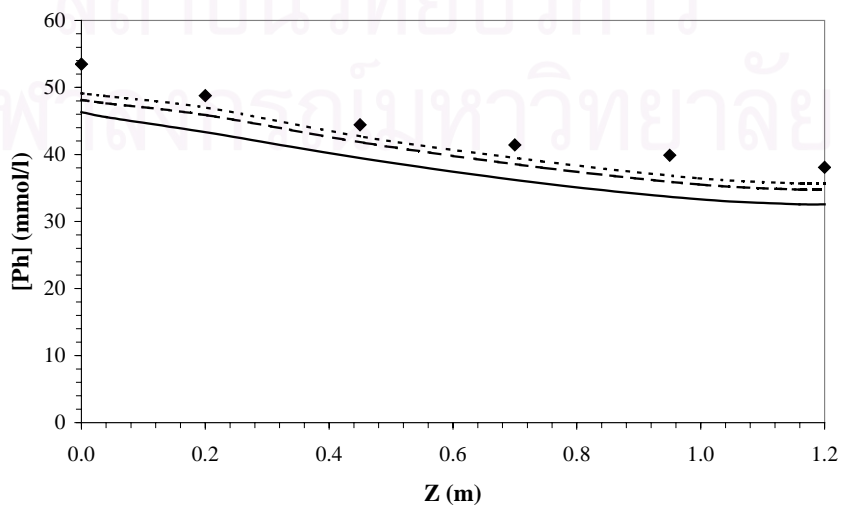
(a) $D^{ad} = D^{ad}_{(St\ddot{u}ber)}$; (b) $D^{ad} = 4.2 \times D^{ad}_{(St\ddot{u}ber)}$; (c) $D^{ad} = 16.7 \times D^{ad}_{(St\ddot{u}ber)}$.



(a)



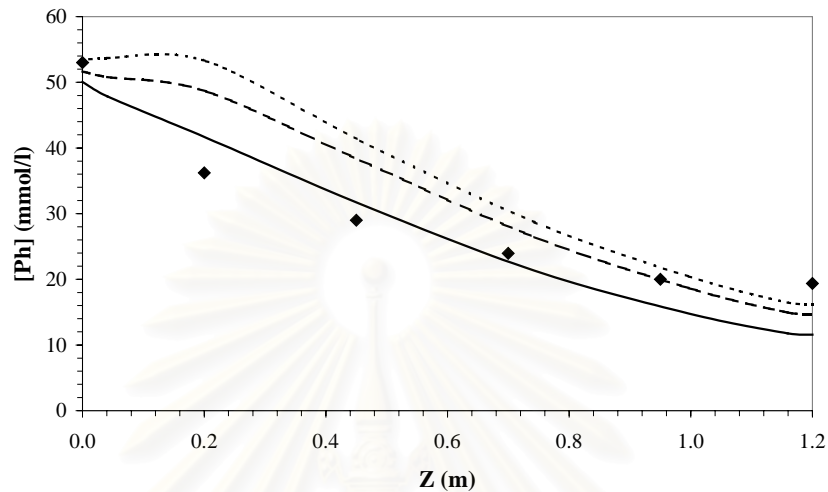
(b)



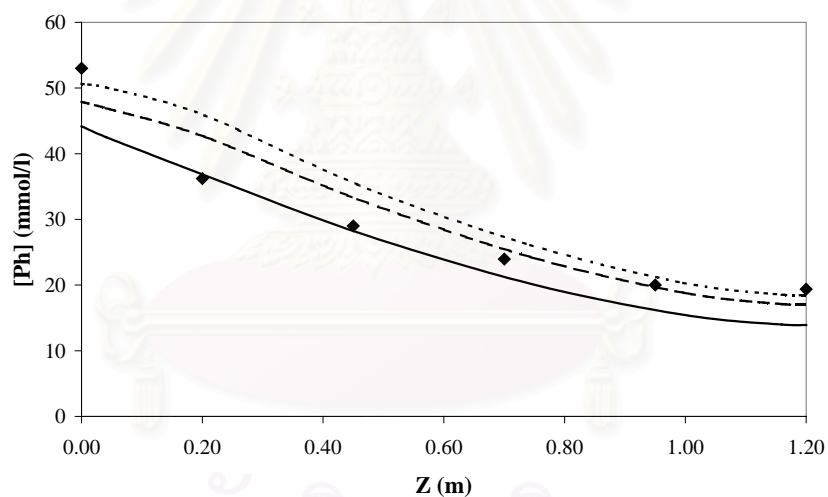
(c)

Appendix 2-13A: Axial phenol concentration profiles (3): experimental (\diamond) and corresponding simulations for fully wetted catalyst: $k_{Ga} = k_{La}$ (solid line), $k_{Ga} = 5 \times k_{La}$ (long dotted line), and instantaneous liquid-vapour equilibrium (short dotted line). $P_{O_2} = 2.0$ bar, $T_w = 140^\circ\text{C}$, $F_G = 100$ NI/h, $F_L = 0.5$ l/h

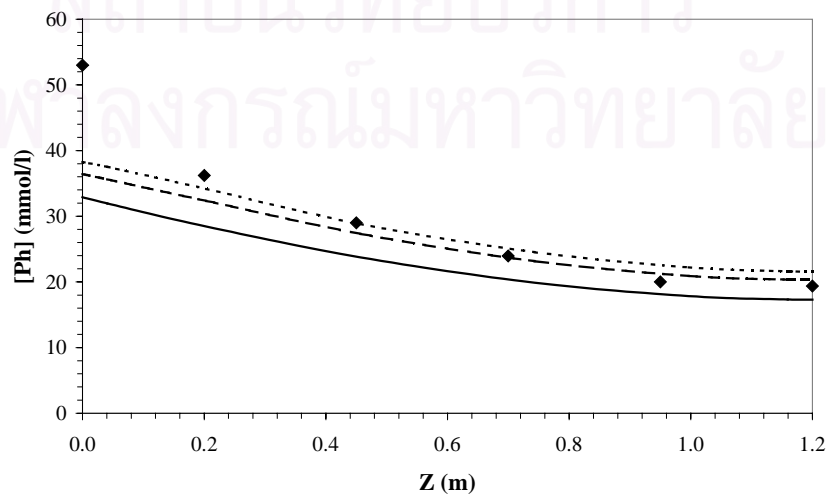
(a) $D^{ad} = D^{ad}_{(St\ddot{u}ber)}$; (b) $D^{ad} = 4.2 \times D^{ad}_{(St\ddot{u}ber)}$; (c) $D^{ad} = 16.7 \times D^{ad}_{(St\ddot{u}ber)}$.



(a)



(b)



(c)

VITA

Miss Somsaluay Suwanprasop was born on October 3, 1977, in Bangkok, Thailand. She received her Bachelor of Science degree (B.Sc.) in Chemistry in 1998, and her Master of Science degree (M.Sc.) in Petrochemistry and Polymer Sciences in 2000, from Chulalongkorn University. She continues her study as a Ph.D. candidate at Chulalongkorn University (Petrochemistry) and at Ecole National Supérieure des Ingénieurs en Arts Chimiques Et Technologiques (ENSIACET), Institut National Polytechnique de Toulouse (INPT), France. She received a Ph.D. student grant from the Royal Golden Jubilee Ph.D. Program and also from the French Embassy in Thailand.



สถาบันวิทยบริการ
จุฬาลงกรณ์มหาวิทยาลัย